CRITICAL SPEEDS OF AN HJ364 WATER JET ASSEMBLY

by

Ashley Edward Brittenden

A thesis submitted in partial fulfillment
of the requirements for the degree of

Master of Engineering

in the

Department of Mechanical Engineering
University of Canterbury
Christchurch, New Zealand

October, 2012

ABSTRACT

With a new range of water jet assemblies under development, CWF Hamilton & Co. Ltd. highlighted the need to establish a validated model for predicting critical speeds. A review of the relevant literature revealed a significant lack of information concerning the operating properties of a lightly loaded, water lubricated marine bearing. Therefore, an instrumented test rig based on a CWF Hamilton & Co. Ltd. 'HJ364' water jet assembly was established to evaluate critical speeds and validate the predictive models.

A number of analytical and numerical models for predicting critical speeds were investigated. Geometric modifications were made to the test rig and the changes in critical speeds were observed. The ability of the predictive models to measure these observed critical speeds was examined.

Driveline mass and driveline overhang were found to have the most significant effects on critical speeds. Modifications to the thrust bearing housing, the impeller mass, the tailpipe stiffness and the marine bearing resulted in no significant shift in critical speeds. However, a change to the geometry of the thrust bearing resulted in a significant shift. This indicated that the thrust bearing was not performing ideally in the test rig.

All three models predicted *changes* in critical speeds relatively accurately. However, the estimates of the critical speeds themselves were somewhat conservative; approximately 10 to 15 percent lower than those measured. Linearisation of the thrust bearing geometry is recommended if greater accuracy is to be achieved. Of all the predictive methods, the Myklestad-Prohl transfer-matrix and the Isolated-Mainshaft finite-element were deemed to be the most flexible and suitable for CWF Hamilton & Co. Ltd.

ACKNOWLEDGMENTS

I would like to express my sincere gratitude to the University of Canterbury and CWF Hamilton & Co. Ltd. for organising this opportunity. Thank you to the Ministry of Science and Innovation (MSI) for providing the funding to make this project possible.

Thank you to a number of people who helped me during this project including:

Dr John Pearse, Dr Stefanie Gutschmidt and Malcolm Lewis for establishing this project and providing ongoing supervision and guidance.

Brian Donahue, Jonathan Roebuck, Mladen Meduric and Stuart Stratton for their invaluable assistance, ideas and guidance.

Finally, I would like to thank my parents, Louise and Rob, and my partner, Annika – your ongoing support made this achievable.

CONTENTS

LIST OF FIGURES

LIST OF TABLES

1

INTRODUCTION

1.1 MOTIVATION AND OBJECTIVES

Spreadsheet calculations and prior testing had indicated that a number of water jet assemblies currently designed and manufactured by CWF Hamilton & Co. Ltd. were operating close to their first critical speed. With a new range of water jet assemblies under development, it was deemed an appropriate time to investigate this phenomenon. A project was undertaken with the University of Canterbury with the following key objectives:

1. Establish how accurately the models currently used by CWF Hamilton & Co. Ltd. predicted critical speeds of a water jet assembly.
2. Determine how the individual components on the mainshaft of a water jet assembly affected critical speeds.
3. Create a validated means of predicting critical speeds across the current and future CWF Hamilton & Co. Ltd. water jet range.

1.2 SCOPE

Experimental testing was carried out on a CWF Hamilton & Co. Ltd. 'HJ364' water jet assembly. Of the entire range, this model was deemed to be running the closest to its first critical speed. A range of analytical and numerical models were investigated; the most suitable of these subsequently compared to results from experimental testing. The scope of this work was limited as follows:

- Testing was carried out with a plain disc to represent the mass properties of the impeller (hence no thrust loads were present on the mainshaft or thrust bearing).
- The majority of testing was performed 'dry' with water trickling through the marine bearing and draining out the bottom of the intake. This was largely due to power limitations of the motor.
- The effects of driveline mass, driveline overhang, impeller mass, intake stiffness and bearing geometry on critical speeds were investigated.
- The effects of the mainshaft geometry (length and diameter) on critical speeds were excluded from the analysis.

This work was carried out between April 2011 and April 2012

1.3 BACKGROUND

1.3.1 Rotordynamics and Terminology

The field of rotordynamics was established almost 150 years ago; the first documented analysis of a spinning shaft was performed by W. J. M. Rankine in 1869 (Sam Samarasekera, 2005). The field is largely concerned with predicting and analysing the behavior of rotating

assemblies. By far the most common issue dealt with in the field of rotordynamics is that of critical speeds.

Any continuous structure has an infinite range of natural frequencies. If a periodic forcing function is applied to the structure at one of these frequencies, 'resonance' will occur[1]. This includes both static and rotating structures. However, rotating structures also encounter speed dependent properties such as gyroscopic terms and internal and external stiffness and damping. Therefore, the resonant frequency changes with the rotational speed of a rotating structure. Periodic forcing functions in rotating assemblies can arise from:

- synchronous effects (unbalance);
- sub-synchronous effects (oil whirl and bearing properties); and
- super-synchronous effects (uncommon).

The American Petroleum Institute (API) defines a critical speed as:

> "… a shaft rotational speed that corresponds to the peak of a non-critically damped (amplification factor > 2.5) rotor system resonance frequency. The frequency location of the critical speed is defined as the frequency of the peak vibration response as defined by a Bodé plot (for unbalance excitation)." (American Petroleum Institute, 1996)

Stability is another common issue in rotordynamics. The API defines stability as:

> "… a term referring to a unit's susceptibility to vibration at sub-synchronous frequencies due to cross-coupled/destabilizing forces produced by stationary critical clearance components (such as bearings and seals) and rotating shrunk-on parts (such as impellers and shaft sleeves)..." (American Petroleum Institute, 1996)

[1] The magnitude of this resonance is strongly coupled to the degree of modal damping present.

1.3.2 Modelling Options and Limitations

A number of models exist for determining critical speeds of rotor systems. Models can be split into two categories: analytical and numerical. While there is some cross-over between these categories, analytical models are generally simple and provide an explicit solution. Numerical methods generally require an iterative solution and, as such, are typically performed on a computer.

Most analytical and numerical models require the knowledge of the stiffness and damping properties of supports. However, at the time of preparing this thesis, there was a very limited range of information regarding these properties in a rubber marine bearing. This, and the largely unknown behavior of the spherical thrust bearing, the impeller and the effects of water on critical speeds, required experimental validation of any predictive models.

1.4 APPROACH

The requirement for experimental validation necessitated the construction of an instrumented HJ364 test rig. The critical speeds obtained from this test rig would be compared to those predicted by the analytical and numerical models with the aim of achieving a correlation.

With this test rig, the ‘real world’ effects of unbalance and repeatability could be assessed (see Section 5). In addition, the effects of modifying individual components on the test rig could be investigated and again compared to the models.

The geometry deemed the most suitable for observing effects on critical speeds included:

- the ‘driveline mass’ (a mass used to emulate the mass of a driveshaft);
- the overhang of this driveline mass from the spherical thrust bearing;

- the stiffness of the thrust bearing housing
- the mass of the impeller disc (a disc used to represent the mass and inertia effects of an impeller);
- the stiffness of the tailpipe which houses the marine bearing;
- the marine bearing; and
- the thrust bearing.

A modification was made to each of these components and applied individually to the test rig. In Sections 6 to 11, the effects of these modifications are presented, whereby the performance of the predictive models is discussed.

1.5 SECTION SUMMARY

This section introduced the issues CWF Hamilton & Co. Ltd. currently faces in terms of critical speeds of their current water jet assemblies. A brief introduction into the field of rotordynamics and a review of modelling techniques was provided. Finally, the project scope and the investigative approach were described.

2

ANALYTICAL MODELING

2.1 INTRODUCTION

There are a number of analytical models available to assess critical speeds of rotating shaft assemblies. The most basic of these models approximate the critical speed as the first natural frequency of vibration. Examples of these include the ‘Rayleigh-Ritz’ and ‘Dunkerley’ methods. A method based upon Timoshenko beam theory is currently utilised by CWF Hamilton & Co. Ltd; herein referred to as the ‘Timoshenko-Beam’ model.

More complex models incorporate support stiffness, inertia and gyroscopic terms and directly evaluate the critical speed(s) of the system. These models generally require an iterative solver and are typically carried out on a computer. Common examples are transfer matrix methods (TMM) and finite element methods (FEM). Numerical assessment of damping on critical speeds was considered out of scope for this study; it was not included in any of the models.

Basic and complex models were assessed for their suitability in determining the critical speeds of an HJ364 water jet assembly. Descriptions and evaluations are provided in this section.

2.2 GEOMETRY

A number of geometric simplifications of the HJ364 water jet assembly were required to facilitate modelling. All methods (excluding the 'Complete-System' finite element method) required complete isolation of the mainshaft from the intake. The Rayleigh-Ritz, Dunkerley and Timoshenko-Beam methods required rigid supports and simplified mainshaft geometry.

Problems arose when assessing the effective location of the thrust bearing support. The centre of rotation of a spherical thrust bearing on flexible supports cannot be determined without experimental data. Therefore two limiting cases are presented; rotation about the thrust roller plane, or, rotation about the thrust bearing geometric centre. For an illustration of this, observe Figure 2.1 and Figure 2.2. Case 1 (Figure 2.1) was deemed to provide the most accurate representation of the bearing behavior in an HJ364 water jet assembly.

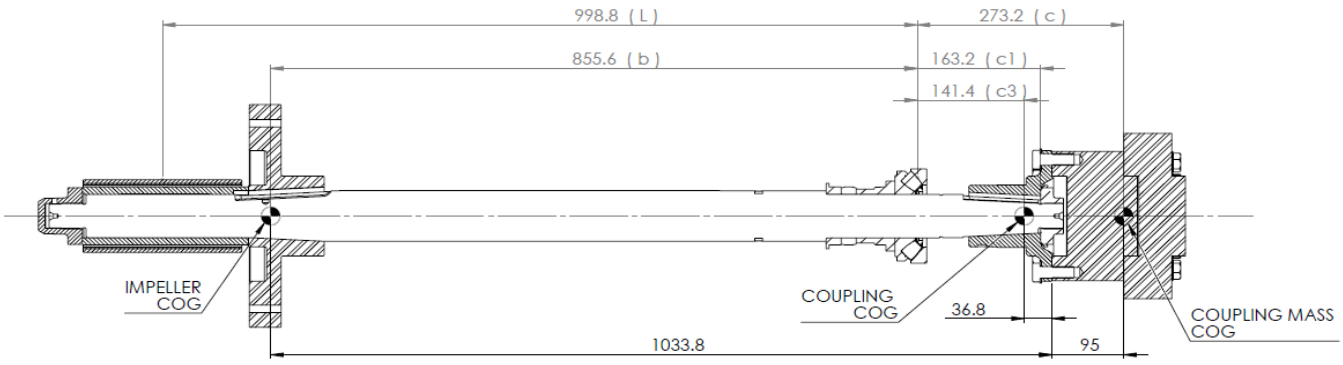

Figure 2.1 – Thrust Bearing Modelling Options: Case 1 (Effective centre in thrust bearing roller plane)

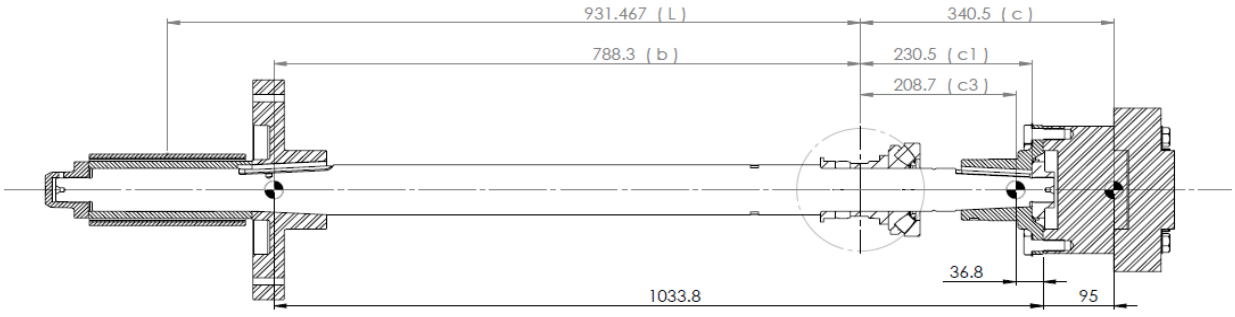

Figure 2.2 – Thrust Bearing Modelling Options: Case 2 (Effective centre at geometric centre of bearing)

2.3 MODELLING

2.3.1 Rayleigh-Ritz Method

The Rayleigh-Ritz method is a traditional method that utilises a known mode 'shape' to predict the corresponding modal frequency. The method is commonly used for basic rotordynamic analyses and uses the deflection shape under a uniform acceleration field (typically 9.81 m/s^2). This deflection shape can be used to determine the first modal frequency and subsequently predict the first critical speed (Budynas-Nisbett, 2008, p374).

However, little literature regarding the use of this method with overhung shaft assemblies has been obtained. Under a uniform acceleration field, the overhung mass will counteract the mass between the bearings (Figure 2.3). In practice, the two masses will act together resulting in a lower energy and lower frequency mode shape (Figure 2.4). Therefore, the Rayleigh-Ritz method may be unsuitable for the HJ364 mainshaft geometry and was not pursued.

Figure 2.3 – High Energy Deflection Shape of a Beam under a Uniform Acceleration Field

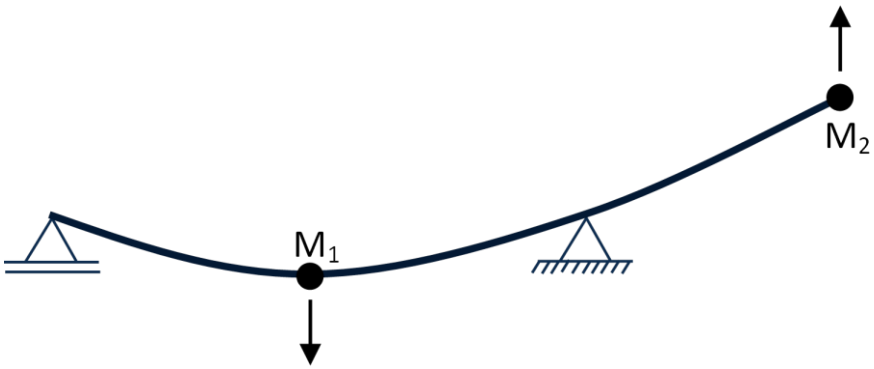

Figure 2.4 – Lower Energy Deflection Shape of a Beam Undergoing Whirling

2.3.2 Dunkerley Method

The Dunkerley method works in a similar manner to the Rayleigh-Ritz method. Crucially however, the deflection of the mainshaft is determined for each mass individually and the result summed using 'influence coefficients'. Therefore, the issues with the application of the Rayleigh-Ritz model do not apply here.

This method relies on superposition of the critical speed of individual masses. It assumes rigid supports; ignores damping, inertia and gyroscopic terms; and uses the calculated first natural frequency to assess the first critical speed of the system.

For an n-body shaft, the first natural frequency ω_1 is approximated by (Budynas-Nisbett, 2008):

$$\frac{1}{\omega_1^2} = \sum_{i=1}^{n} \frac{1}{\omega_{ii}^2} \tag{2.1}$$

where ω_{ii} is the critical speed of the nth body on the shaft and is calculated from the mass, m_i and the deflection of the shaft d_{ii} at the nth body resulting from an applied unit load:

$$\omega_{ii} = \sqrt{\frac{1}{m_i d_{ii}}} \tag{2.2}$$

It should be noted that the assumption $\omega_1 \ll \omega_2 \ll \cdots \ll \omega_n$ has been made. Therefore, the Dunkerley method will tend to estimate a lower first critical speed than is actually the case. Due to the complex mainshaft geometry of the HJ364 water jet assembly, influence coefficients were determined numerically. The results of the analysis are presented in Table

2.1. Clearly, driveline mass was predicted to have the most significant effect on critical speed. The mainshaft mass was expected to have some effect[2]. Impeller and coupling masses were predicted to have a negligible effect. The *trends* predicted by the Dunkerley method were expected to prove relatively accurate. However, the critical speeds were predicted to be less accurate due to the over-simplified nature of the model.

Table 2.1 - Results from the Dunkerley Method Analysis of the HJ364 Mainshaft

Mass Component	**Mass [kg]**	**Individual Critical Speed**	
		[Hz]	**[RPM]**
Impeller	22.0	281	16900
Mainshaft Mid-span	18.3	136	8180
Mainshaft Overhang	4.4	505	30300
Coupling	6.0	245	14700
Driveline	38.0	55	3300
CRITICAL SPEED		49	2940

2.3.3 'Timoshenko-Beam' Method

This method also utilised the first natural frequency to approximate the first critical speed and was obtained through Timoshenko beam theory. While a derivation is not presented here, the formulae are presented below. For further information, consult pages 514 to 519 of 'The Marine Engineer's Handbook' (Sterling, 1920). This approach is currently used by CWF Hamilton & Co. Ltd. to assess mainshaft critical speeds across the full water jet range.

$$N_{c1}\ and\ N_{c2} = \sqrt{\frac{1}{2A}\left[U^2 + V^2 \pm \sqrt{(U^2 + V^2)^2 - 4AU^2\,V^2}\right]} \qquad (2.3)$$

[2] A hollow mainshaft may be worth consideration in future designs.

Where N_{c1} and N_{c2} are the first and second critical speed estimates respectively and:

$$A = 1 - \frac{9}{16}\frac{L}{L+c} \tag{2.4}$$

$$U = 207114\frac{d^2}{L\sqrt{W_1 L}} \tag{2.5}$$

$$V = 51778\frac{d^2}{c\sqrt{W_2(L+c)}} \tag{2.6}$$

Here, L is the shaft length between bearings; c is the overhung length; d is the shaft diameter; W_1 is the 'mid-span' mass between the bearings and W_2 is the overhung mass. The mainshaft self-mass, impeller mass and coupling mass must be summed to equivalent mid-span and overhung masses. An assumption of uniform shaft geometry was required to employ this method. The inputs and outputs of the solution process are provided in Table 2.2 and Table 2.3 respectively.

Table 2.2 - Inputs to the Timoshenko-Beam Method (HJ364 Mainshaft Geometry)

L	c	d	W_1	W_2
931.5 mm	340.5 mm	70 mm	24.2 kg	42.4 kg

Table 2.3 - Outputs from the Timoshenko-Beam Method (HJ364 Mainshaft Geometry)

A	U	V	N_{c1}	N_{c2}
0.5881	7255	3207	**3072 RPM**	**9877 RPM**

This method does not take into account full shaft geometry, distributed shaft mass, support stiffness, inertia, or gyroscopic terms. Therefore, the results were not expected to be accurate. Interestingly, $N_{c1} \ll N_{c2}$ thereby satisfying the requirements of Section 2.3.2.

2.4 ASSESSMENT AND CONCLUSIONS

A summary of the performance and predicted accuracy of the various analytical models is provided in Table 2.4. Comparisons with the numerical modelling options are made in the following section.

Table 2.4 - Assessment of Analytical Methods for CWF Hamilton & Co. Ltd.

Method	Applicable	Ease of Use	Accuracy	Solution Times
Rayleigh-Ritz	No	Excellent	Poor	Excellent
Dunkerley	Yes	Good	Good	Poor
Timoshenko-Beam	Yes	Good	Good	Good

2.5 SECTION SUMMARY

A range of analytical critical-speed models of rotating shaft assemblies on rigid supports were investigated in this section. The classical ‘Rayleigh-Ritz’ approach proved inapplicable; however the ‘Timoshenko-Beam’ and ‘Dunkerley’ models performed relatively well. The Dunkerley model highlighted the driveline mass as having the most significant effect on the fundamental critical speeds. However, as solution times with this method were excessive, only the Timoshenko-Beam method was pursued.

3

NUMERICAL MODELLING

3.1 INTRODUCTION

Due to their ability to incorporate complicated geometry and other effects, numerical methods are becoming the methods of choice in rotordynamic analyses. Packages such as ANSYS Workbench v14.1 now allow for the simple inclusion of asymmetric support properties and damping; Campbell plots and critical speeds are readily obtained.

This section initially deals with the Myklestad-Prohl transfer-matrix method then considers two independent finite-element models: 'Isolated-Mainshaft' and 'Complete-System'. The Isolated-Mainshaft model used only the geometry of the mainshaft and attached masses on spring supports; the stiffness of these supports was determined by a numerical deflection analysis of the intake. The Complete-System model used the geometry of the intake, mainshaft and attached masses to directly assess the critical speeds.

At the end of this section, the various predictive models are compared and selected for experimental validation.

3.2 MYKLESTAD-PROHL TRANSFER-MATRIX MODEL (TMM)

Lumped-parameter models are particularly appropriate for the analysis of rotor system. Rotors can be modelled as a set of rigid bodies which are connected by massless, flexible beam elements; the rigid bodies incorporate the distributed mass and inertia properties of the shaft while the beam elements incorporate the stiffness properties. As each rigid body only interacts with adjacent rigid bodies, transfer-matrix methods lend themselves particularly well to solving these systems (Childs, 1993).

A wide range of transfer-matrix methods exist and a detailed survey of these methods was carried out entitled "Matrix Methods in Elastomechanics" (Pestel & Leckie, 1963). However, of all these methods, the Myklestad-Prohl method was considered the most appropriate for the requirements of this analysis: "…the Myklestad-Prohl transfer-matrix format has historically been employed for analysis of lumped-parameter models of flexible rotors, viz., Eigen analysis, synchronous response, and stability analysis." (Childs, 1993, p104)

The general approach undertaken with the Myklestad-Prohl transfer-matrix method (herein referred to as the Myklestad-Prohl TMM) is to:

1. discretise the shaft into finite lengths with point masses;
2. make or refine a 'guess' at the critical speed of the system;
3. calculate the linear and angular deflections, shear forces and moments at each section;
4. determine whether the known support/end conditions are met.

Steps 2, 3 and 4 are iterated until a critical speed is obtained within the required tolerance. This would typically be performed on a computer. A brief overview of the Myklestad-Prohl TMM is provided here. A full derivation can be found in Childs (p105 – p111).

The station transfer-matrix relates the linear displacements, angular displacements, internal shear forces and internal bending moments before and after each lumped mass. It incorporates self-mass and inertia, support forces and moments, and forces resulting from imbalance and gyroscopic effects. At station 'i', the station transfer-matrix and state vectors are provided in equation (3.1):

$$\begin{Bmatrix} R_i \\ \beta_i \\ M_i \\ V_i \end{Bmatrix}^r = \begin{bmatrix} 1 & 0 & 0 & 0 \\ 0 & 1 & 0 & 0 \\ 0 & K_i - (J_i - \overline{J_\iota})\omega^2 & 1 & 0 \\ k_i - m_i\omega^2 & 0 & 0 & 1 \end{bmatrix} \begin{Bmatrix} R_i \\ \beta_i \\ M_i \\ V_i \end{Bmatrix}^l \tag{3.1}$$

Where: $m_i, k_i, K_i, J_i, \overline{J_\iota}$ and ω are the mass, linear (radial) support stiffness, rotational (diametral) support stiffness, diametral moment of inertia, polar moment of inertia, and angular velocity (axial) of the point mass respectively. The state vector components R_i, β_i, M_i and V_i are the linear (radial) displacement, angular (diametral) displacement, internal bending moment and internal shear force respectively. The superscripts on the state vector indicate whether immediately prior to ('l') or immediately after ('r') the station.

In a more compact form, equation (3.1) becomes:

$$\{ Q \}_i^r = [T_{si}] \{ Q \}_i{}^l \tag{3.2}$$

Knowledge of the elastic and geometric properties of the massless beam elements leads to the development of the field transfer-matrix and state vector provided in equation (3.3):

$$\begin{Bmatrix} R_{i+1} \\ \beta_{i+1} \\ M_{i+1} \\ V_{i+1} \end{Bmatrix}^{l} = \begin{bmatrix} 1 & L_i & L_i^2/2EI_i & -L_i^3/6EI_i \\ 0 & 1 & L_i/EI_i & -L_i^2/2EI_i \\ 0 & 0 & 1 & -L_i \\ 0 & 0 & 0 & 1 \end{bmatrix} \begin{Bmatrix} R_i \\ \beta_i \\ M_i \\ V_i \end{Bmatrix}^{r} \tag{3.3}$$

where L_i, E and I_i are the length, elastic modulus and second moment of area of the beam-element respectively. This can also be stated more compactly as:

$$\{ Q \}_{i+1}{}^{l} = [T_{fi}] \{ Q \}_i{}^{r} \tag{3.4}$$

and combined with equation (3.2) to produce the complete transfer-matrix:

$$\{ Q \}_{i+1}{}^{l} = [T_{fi}] [T_{si}] \{ Q \}_i{}^{l} = [T_i] \{ Q \}_i{}^{l} \tag{3.5}$$

Finally, to relate the first station to the n[th] station, the transfer-matrix for each station is combined as shown:

$$\{ Q \}_n{}^{r} = [T_{sn}][T_{n-1}][T_{n-2}] \cdots [T_1] \{ Q \}_1{}^{l} = [T] \{ Q \}_1{}^{l} \tag{3.6}$$

Expansion of the global transfer-matrix [T] yields:

$$\begin{Bmatrix} R_n \\ \beta_n \\ M_n \\ V_n \end{Bmatrix}^{r} = \begin{bmatrix} T_{11} & T_{12} & T_{13} & T_{14} \\ T_{21} & T_{22} & T_{23} & T_{24} \\ T_{31} & T_{32} & T_{33} & T_{34} \\ T_{41} & T_{42} & T_{43} & T_{44} \end{bmatrix} \begin{Bmatrix} R_1 \\ \beta_1 \\ M_1 \\ V_1 \end{Bmatrix}^{l} \tag{3.7}$$

For the generalised case, the shear force V_n and bending moment M_n is zero at each end of the beam (massless dummy elements can be included to achieve this if necessary). Hence:

$$M_1^l = M_n^r = V_1^l = V_n^r = 0 \tag{3.8}$$

This requires that:

$$0 = T_{31}R_1^l + T_{32}\beta_1^l \tag{3.9}$$

$$0 = T_{41}R_1^l + T_{42}\beta_1^l \tag{3.10}$$

which is satisfied for a non-trivial solution to the determinant:

$$\begin{vmatrix} T_{33} & T_{34} \\ T_{43} & T_{44} \end{vmatrix} = 0 \tag{3.11}$$

Therefore, a value of ω that satisfies this equation is a critical speed of the system.

A script was developed in Matlab R2011b to receive the geometry of the mainshaft, apply loads and supports; discretise and apply dummy end sections; and locate the first critical speed within a specified tolerance. This script is provided in Appendix B4.

In Figure 3.1, the input geometry as rendered in Matlab R2011b is shown. The driveline point mass was attached with a rigid, massless element on the right-hand side. Included in the analysis were four additional ‘slices’ where supports and point masses were applied. The properties of these slices are given in Table 3.1. A range of uniform discretisation lengths were trialled to obtain mesh independence. The results of the analysis with these inputs are provided in Table 3.2. Mesh independence was achieved with a discretisation length of approximately 1mm.

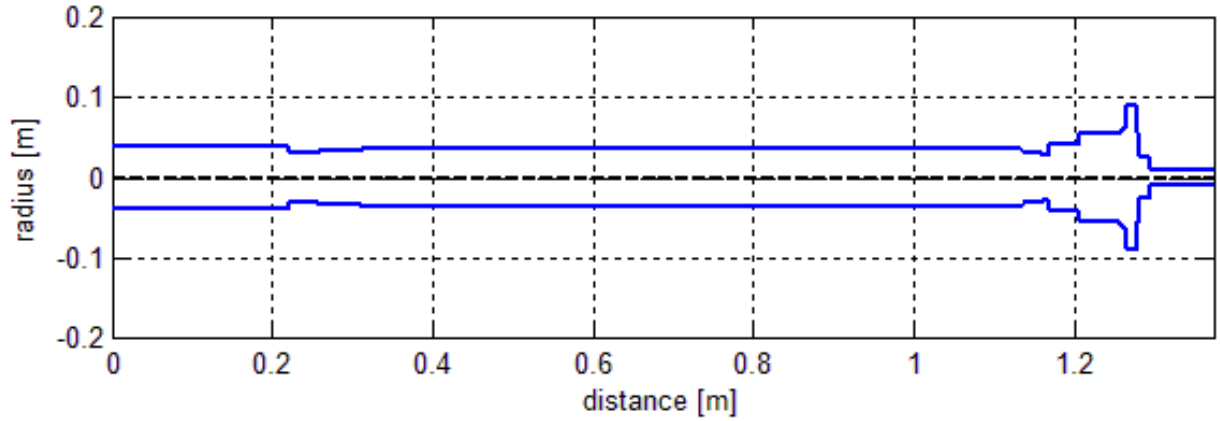

Figure 3.1 - Mainshaft Geometry Input to the Myklestad-Prohl TMM

Table 3.1 - Locations and Properties of Individual 'Slices' in the Myklestad-Prohl TMM

Slice Name	**Position [m]**	**Mass [m]**	**Polar Inertia [kgm^2]**	**Diametral Inertia [kgm^2]**	**Radial Stiffness[3] [N/m]**	**Rotational Stiffness [Nm/rad]**
'Water Bearing Support'	0.110	0	0	0	1.1e7	0
'Impeller Mass'	0.244	22.3	0.27	0.14	0	0
'Thrust Bearing Support'	1.033	0	0	0	1e12	0
'Driveline Mass'	1.373	39.1	0.21	0.19	0	0

Table 3.2 – Critical Speed and Mesh Dependence Results from the Myklestad-Prohl TMM Script

Discretisation Length [mm]	**Evaluated Critical Speed**		**Solution Time [s]**
	[Hz]	**[RPM]**	
10	47.9	2873	0.32
1	48.9	2935	2.73
0.1	48.9	2937	37.6

[3] Radial stiffness is determined later in this section. The 'Thrust Bearing Support' stiffness was set to 1e12 to imitate a rigid support. The reasons for this are discussed later in this section.

3.3 ISOLATED-MAINSHAFT FINITE ELEMENT MODEL (FEM)

A common means of characterising a rotor-system is with a shaft on flexible supports and a pre-determined stiffness. To fully characterise the critical speeds of the HJ364 water jet assembly, the following steps were required:

1. Evaluate the stiffness of the intake at each of the bearing locations (thrust bearing and tailpipe).
2. Determine the behavior of the thrust bearing and the most appropriate means of modelling it.
3. Apply this information to the 'isolated-mainshaft' model and extract the relevant critical speeds.

3.3.1 Support Stiffness Evaluation

Prior to meshing, simplifications to the base-frame and intake geometries were made to achieve a satisfactory, convergent mesh. This required the removal of fillets, chamfers, threads and fasteners (leading geometry and wall thicknesses were conserved). Minimal modifications were made around the bearing housings themselves. While details of the geometry are not shown here, an overview of the simplified geometry is provided in Figure 3.2. In Figure 3.3, an overview of the meshed intake is provided.

To determine the stiffness of the supports, a deflection study of the intake was performed in ANSYS Workbench v14.1. Assuming small deflections, the support stiffness could be determined from the following equation:

$$K = \frac{df}{dx} \tag{3.12}$$

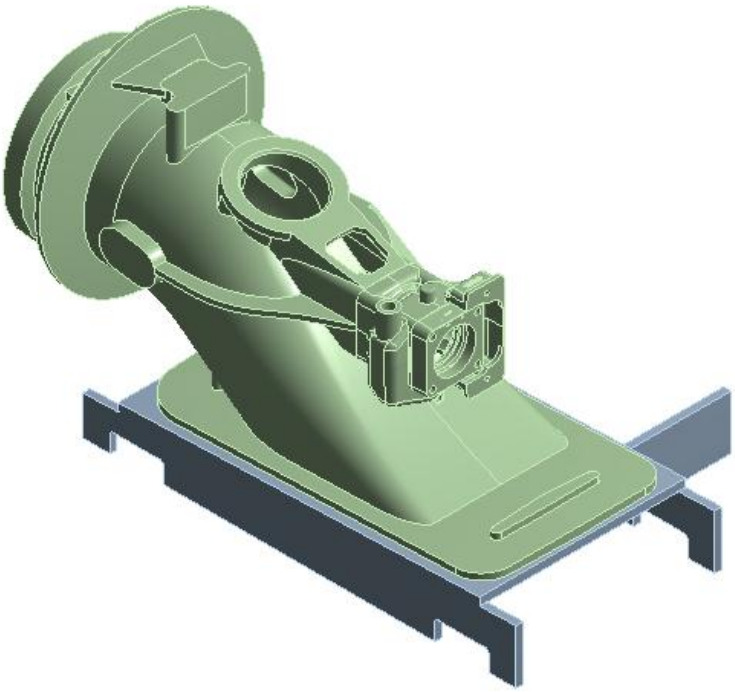

Figure 3.2 - Simplified HJ364 Geometry for Deflection Testing (ANSYS Workbench v14.1)

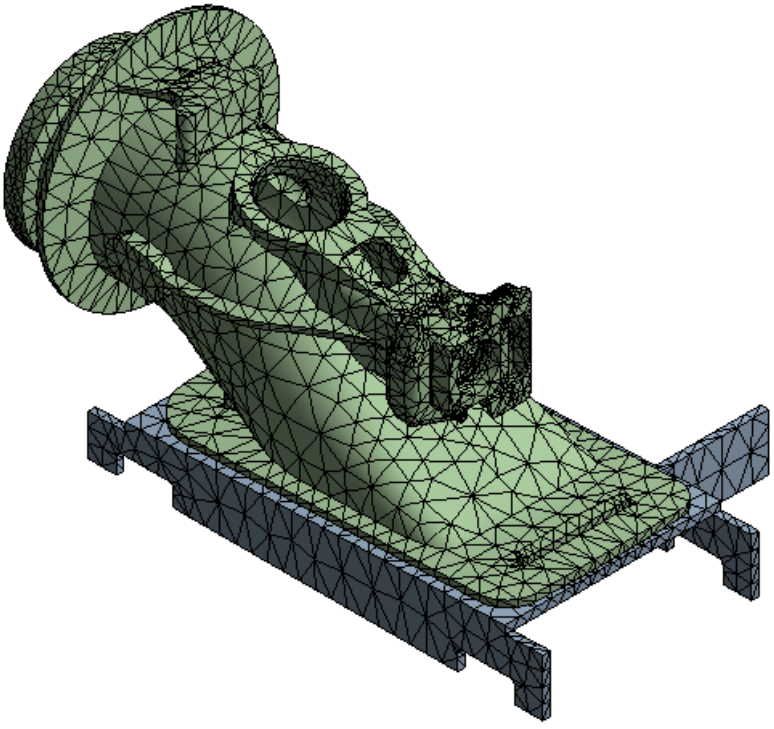

Figure 3.3 - Meshed Intake for Deflection Testing
(95900 nodes, 54700 elements, 4 minute solve time, ANSYS Workbench v14.1)

Here, df is the applied force; dx is the resultant displacement in the direction of the applied force; and K is the stiffness in the direction of the applied force. A unit radial load was independently applied at each of the bearing locations[4] in increments of 15 degrees. At each increment, the displacement in the direction of the applied force was extracted. The results of the deflection testing of the thrust bearing and the marine bearing housings are provided in Figure 3.4 (A) and (B) respectively.

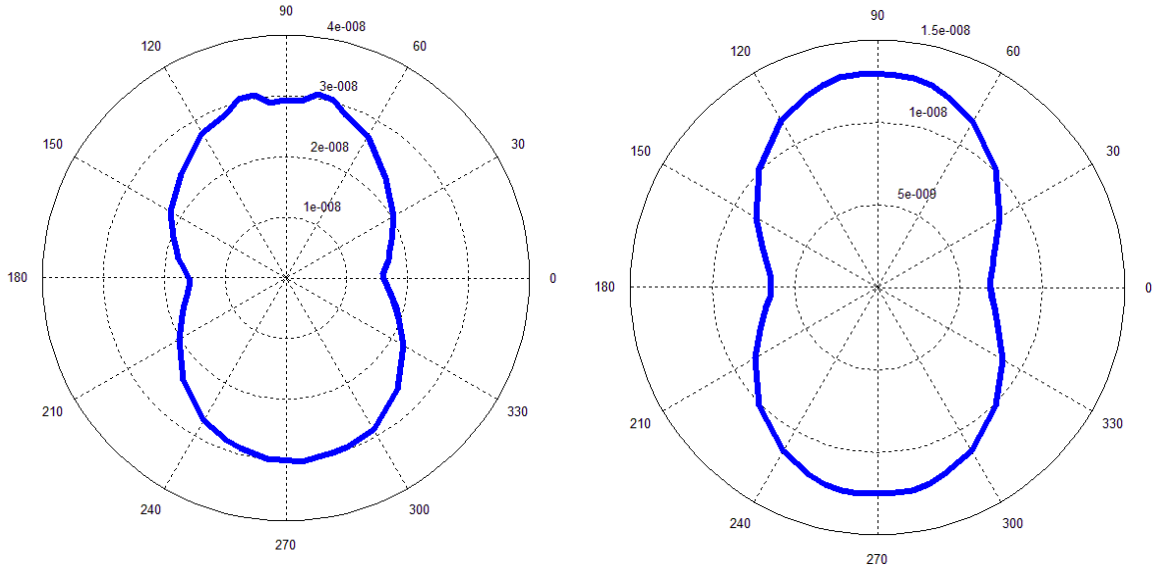

Figure 3.4 – Polar Deflection Plots of the Intake
(A) Deflection of the Thrust Bearing Seat with a Unit Load Applied Radially through 360 degrees
(B) Deflection of the Marine Bearing Seat with a Unit Load Applied Radially through 360 degrees

Evidently, both housings presented a maximum deflection in the vertical plane and a minimum deflection in the horizontal plane. Through equation (3.12), the maximum and minimum stiffness values were found to be in the horizontal and vertical planes respectively.

In Table 3.3, these derived peak stiffness values are summarised. The stiffness of the rubber marine bearing (determined in Section 9) was added to that of the marine bearing support to

[4] These include the spherical thrust bearing housing behind the coupling and the marine bearing housing (tailpipe) at the rear of the water jet assembly unit. A detailed geometric description of these housings is not provided.

achieve the "Combined Marine Bearing Stiffness". These combined values were used for all subsequent analyses (where not stated otherwise). The "Thrust Bearing Centre Plane" stiffness values were determined through the thrust bearing geometric centre and were also added to this table.

It should be noted that support stiffness asymmetry typically gives rise to a separation in the first two modes (the separation being dependent on the asymmetry ratio). The lower frequency of these will be a 'backward' mode; the higher frequency a 'forward' mode (Greenhill & Cornejo, 1995). A mode shape would be expected in each of these planes; the mode in the vertical plane occurring at a lower frequency.

Table 3.3 – Summary of the Evaluated Support Stiffness Values (ANSYS Workbench v14.1)

Feature	**Maximum Stiffness** (angle from horizontal)	**Minimum Stiffness** (angle from horizontal)
Thrust Bearing Roller Plane	6.35×10^7 N/m (0,180°)	3.26×10^7 N/m (± 90°)
Thrust Bearing Centre Plane	1.11×10^8 N/m (0,180°)	6.23×10^7 N/m (± 90°)
Marine Bearing Housing	1.56×10^8 N/m (0,180°)	7.72×10^7 N/m (± 90°)
Combined Marine Bearing Stiffness	1.2×10^7 N/m (0,180°)	1.11×10^7 N/m (± 90°)

3.3.2 Thrust Bearing Characterisation

As discussed in Section 2.2, a thrust bearing supported on flexible mounts is inherently difficult to model; the centre of rotation during bending does not occur in the same plane as the restoring force from the rollers. To analyse this behavior, a model was created incorporating the mainshaft geometry and a sleeve to model the thrust bearing surface. An overview of this is provided in Figure 3.5. A close up of the mesh at the bearing interface is

shown in Figure 3.6. A high degree of refinement was necessary to ensure that the 'no-separation' contact applied during the solution process was maintained.

In ANSYS Workbench v14.1, a frictionless contact was applied to the right hand face of the bearing surface. "Thrust Bearing Roller Plane" stiffness values (see Table 3.3) were applied radially and orthogonally to the outer edge of the bearing surface. "Combined Marine Bearing Stiffness" values (see Table 3.3) were applied in the same manner to the mainshaft.

Figure 3.5 - Geometry Description of the Thrust Bearing Characterisation Model (ANSYS Workbench v14.1)

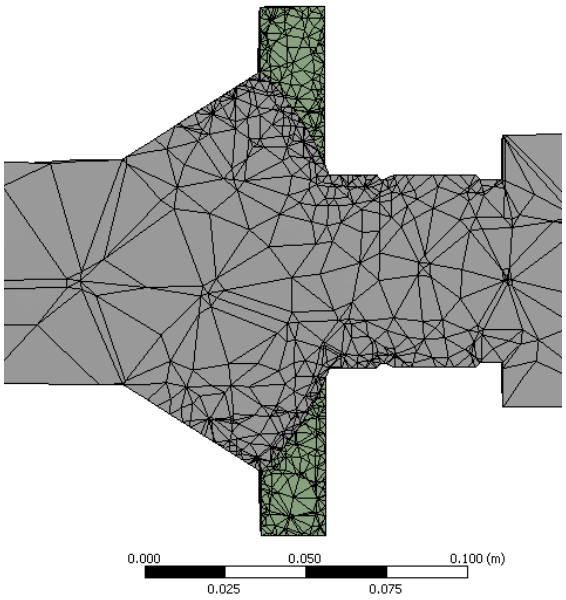

Figure 3.6 – Geometry of Mainshaft and Bearing (no Intake, ANSYS Workbench v14.1)

A modal analysis was performed using a ‘qrdamp’ solver in ANSYS Workbench v14.1. Coriolis effects were activated and a remote displacement was applied to the end of the mainshaft to prevent axial motion. Modal frequencies were extracted over five equally spaced intervals from 1 to 5000 RPM. Finally, a Campbell diagram was generated and the first two critical speeds were extracted assuming synchronous excitation from unbalance. The mode shape of this analysis is presented in Figure 3.7.

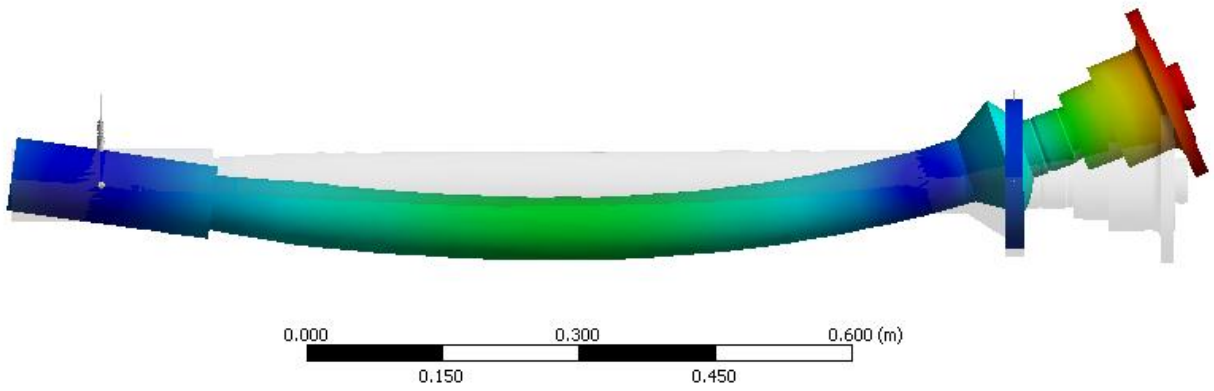

Figure 3.7 – Deflected Mainshaft and Bearing Geometry (no Intake, ANSYS Workbench v14.1)

This approach was computationally intensive and the solution time was large. It was deemed necessary to approximate the system by more conventional means. Four options were trialed:

- pinned flexible or rigid supports in the thrust bearing roller plane; or
- pinned flexible or rigid supports at the thrust bearing geometric centre.

An example of the deflection curve with one of these simplified conditions is shown in Figure 3.8. A summary of the results and the respective deviations is shown in Table 3.4. It should be noted that the exact geometry of the HJ364 mainshaft was not modelled (due to modelling limitations). Therefore, these results were for first estimation and comparative purposes only.

Evidently, the best approximation of the thrust bearing support was a rigid, pinned support at the rotational centre of the thrust bearing (as described in Section 2). This indicated that the thrust bearing housing and intake was far more rigid than the mainshaft itself; also evident in the small ratio of bearing to mainshaft deflection in Figure 3.7. This 'pinned thrust centre' approximation is used in the remainder of this thesis. Assessment of the ratio of thrust housing stiffness to mainshaft stiffness will be required before this approximation can be applied to other water jet assemblies in the CWF Hamilton & Co. Ltd. range.

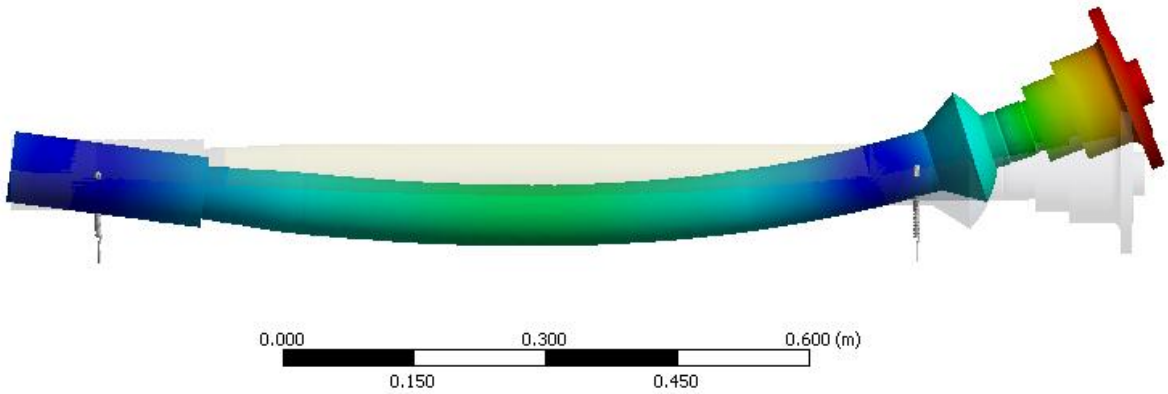

Figure 3.8 - Deflection Curve of the Mainshaft Model with Flexible Supports in the Thrust Bearing Centre Plane (Horizontal and Vertical Support Stiffness of $1.11x10^8$ and $6.23x10^7$ respectively)

Table 3.4 - Comparison of Thrust Bearing Characterisations (Critical Speed Figures for Comparitive Purposes Only)

Model Type	**Critical Speed 1 [RPM]**	**Critical Speed 2 [RPM]**	**Deviation from 'Full'**
Full	2963	3131	
Flexible Roller Plane	3191	3224	+7.70% and +3.00%
Rigid Roller Plane	3475	3756	+17.3% and +20.0%
Flexible Roller Centre	2834	2995	-4.35% and -4.34%
Rigid Roller Centre	2952	3122	-0.37% and -0.29%

3.3.3 The 'Isolated-Mainshaft' Finite-Element Model

With the work carried out in Section 3.3.2, the final geometry of the 'Isolated-Mainshaft' finite element model (herein referred to as the Isolated-Mainshaft FEM) was selected. This involved the full mainshaft and coupling geometry, point impeller and driveline masses and simple spring supports at the water bearing and a pinned support at the thrust bearing location. A 70mm sleeve acted in place of the thrust bearing and sleeve assembly. A render of the geometry in ANSYS Workbench v14.1 is provided in Figure 3.9. Not shown is the rigid element connecting the driveline point mass to the coupling face. The 'pinned thrust centre' was modelled as two springs.

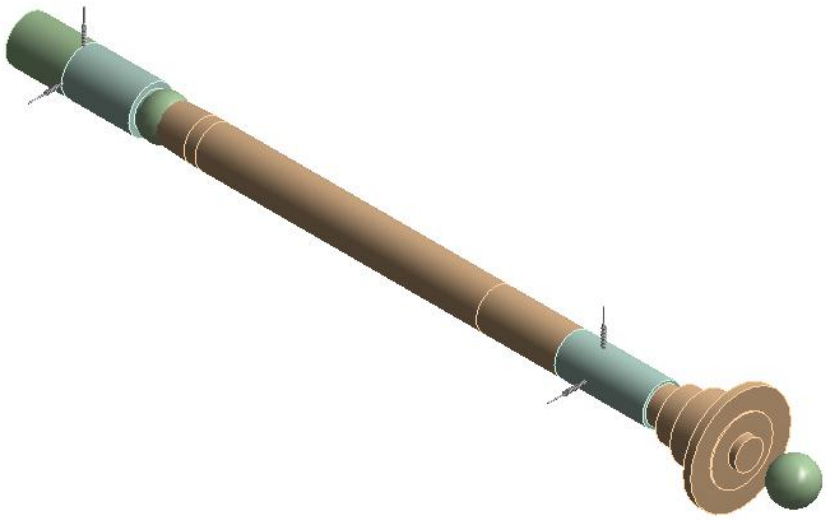

Figure 3.9 – Render of the Isolated-Mainshaft geometry
(ANSYS Workbench v14.1)

With the same modal analysis setup described in Section 3.3.2, the final results of the 'Isolated-Mainshaft' model were obtained. Observe Figure 3.10 for an example of the deflection 'shape' of the first two modes. A Campbell diagram was generated (Figure 3.11) and the first two critical speeds were extracted assuming synchronous excitation from unbalance. These results are provided in Table 3.5 and are compared to the results from a basic modal analysis; useful for determining the extent of gyroscopic 'stiffening' present.

Table 3.5 - Summary of the 'Isolated-Mainshaft' Critical Speed Analysis

Number	Critical Speed [Hz]	Modal Frequency [Hz]	Deviation	Orientation
1	2809	2869	+2.1%	Vertical
2	2951	2886	-2.2%	Horizontal

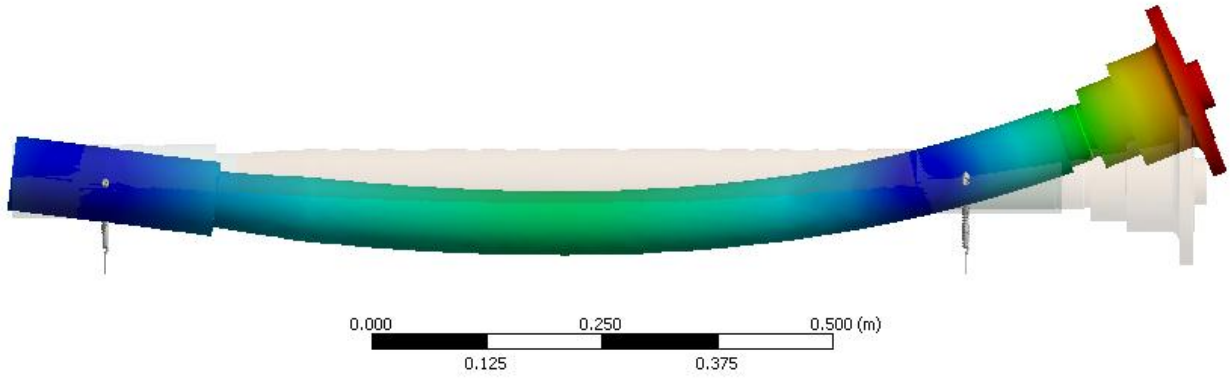

Figure 3.10 – 'Shape' of Modes 1 and 2 of the HJ364 Mainshaft (not to scale). Un-deformed geometry shown in background

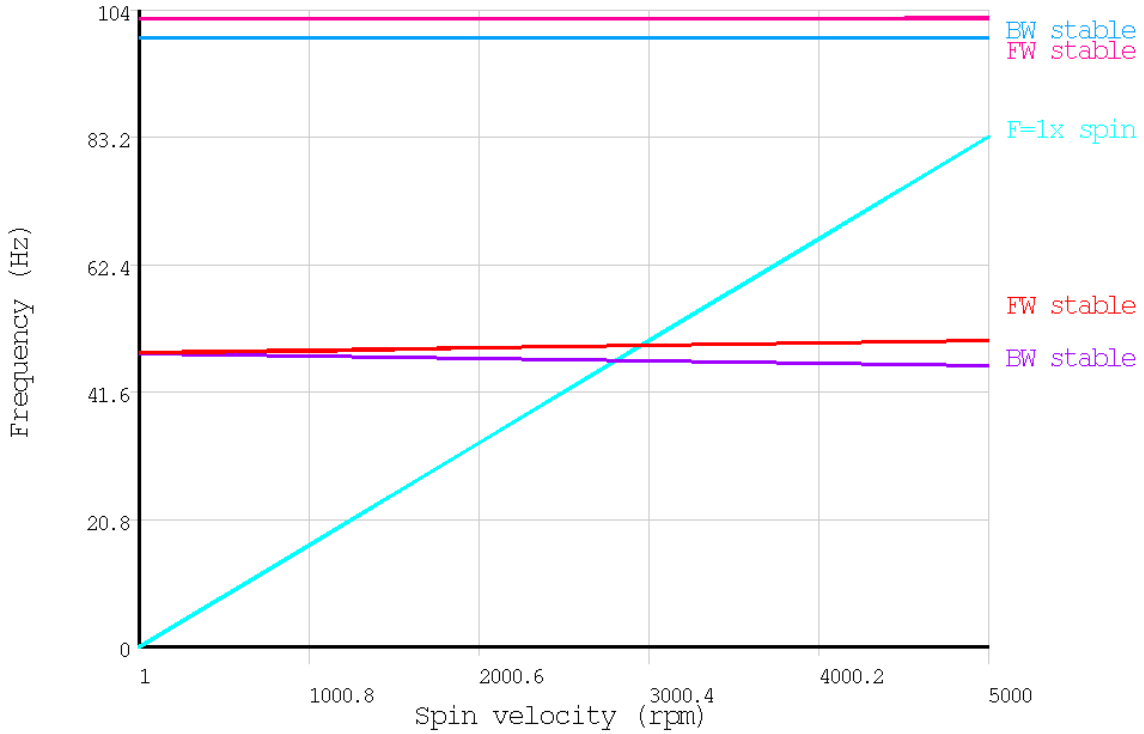

Figure 3.11 – Campbell Diagram from the Modal Analysis of the 'Isolated-Mainshaft' model.

Clearly, only a small deviation was present between the first two critical speeds and the first two modal frequencies. This was apparent in the Campbell diagram shown in Figure 3.11; it can be seen that the first two modes do not separate significantly with speed. This behavior indicated that gyroscopic effects played a relatively small role in determining the first critical speeds of the system. Therefore, first two modal frequencies provide a reasonable approximation for the first two critical speeds of the HJ364 water jet assembly. This result could be particularly useful for CWF Hamilton & Co. Ltd. to reduce solution times in future analyses.

3.4 COMPLETE-SYSTEM FINITE ELEMENT MODEL (FEM)

The alternative means of characterizing this rotor-system was by using a 'Complete-System' finite-element model (herein referred to as the Complete-System FEM). To perform this, the geometries of the base-frame, intake and mainshaft were modelled in their entirety in ANSYS Workbench v14.1. Due to computational limitations, only the natural frequencies could be extracted (not the critical speeds themselves).

The geometry used in this model was effectively a direct combination of the geometry in Figure 3.2 and Figure 3.10. However, issues arose in modelling the thrust bearing interface. The bearing was modelled as two coincident spherical surfaces with a 'no-separation' contact condition applied. An overview of the geometry and mesh is provided in Figure 3.12; a close up of the bearing mesh is shown in Figure 3.13. A refinement was required at the bearing interface to ensure the contact condition was being maintained. However, performing this resulted in a non-convergent solution. Due to computational and time limitations, only a modal frequency could be evaluated. With these limitations, the results in Table 3.6 were obtained. Only mode 1 could be assessed.

Table 3.6 - Results from the Modal Analysis of the Complete-System FEM Model of the HJ364 Intake (Full Intake Geometry)

Mode Number	Modal Frequency [Hz]	Orientation	Number of Nodes	Solution Time [mins]
1	51.69	Vertical	93 520	15

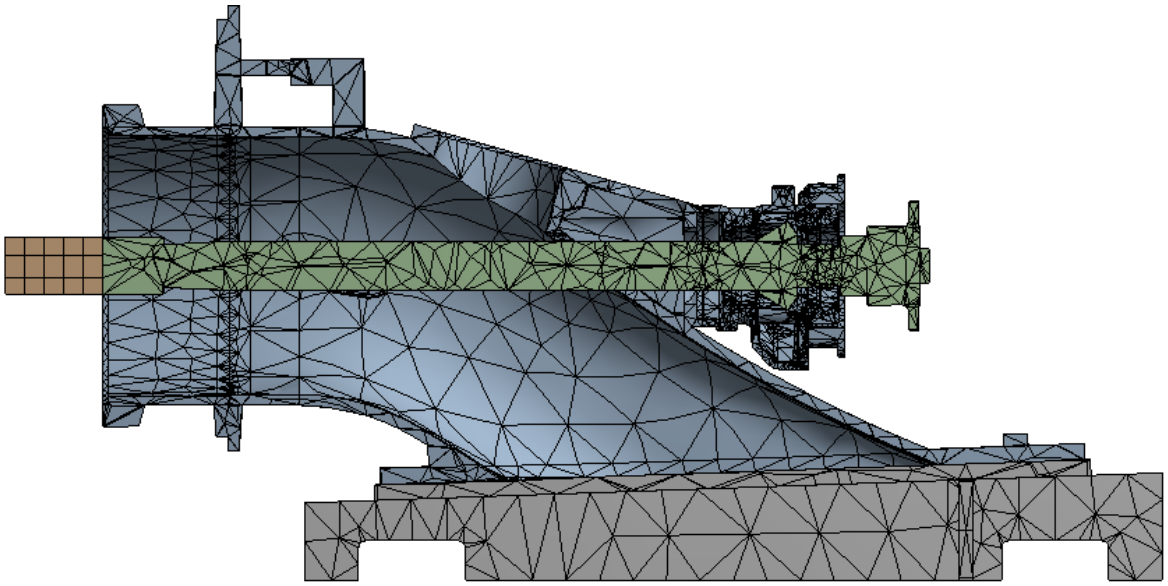

Figure 3.12 – Cross-Section of the Complete-System FEM Model of the HJ364 Water Jet Assembly (ANSYS Workbench v14.1)

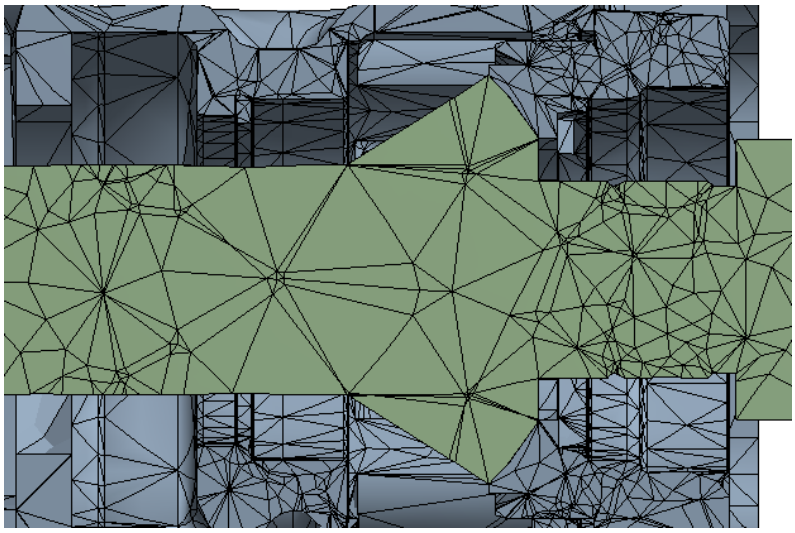

Figure 3.13 – Detailed View of the Simplified Spherical Thrust Bearing Contact (ANSYS Workbench v14.1)

Evidently, the Complete-System FEM approach imposed significant limitations in assessing critical speeds. Meshing difficulty at the bearing interface led to results where mesh independence could not be achieved. Large solution times, poor accuracy and modelling limitations eliminate this approach as a means of assessing critical speeds for CWF Hamilton & Co. Ltd.

3.5 NEGLECTED EFFECTS

3.5.1 Spring Carrier Assembly

The 'spring-carrier' in an HJ364 water jet assembly is located behind the spherical thrust bearing. It is used to add a pre-load to the spherical thrust bearing to maintain alignment. Within, there are sixteen 24.5 kN/m pre-load springs, equally spaced around the circumference at a 50mm radius. A simplified geometry of this spring-carrier was modelled and added to the geometric description of the mainshaft in Figure 3.14.

A critical speed analysis of the system was performed in ANSYS Workbench v14.1 with the same setup described in Section 3.3.2. A small increase in the first two critical speeds of +1.88% and +2.00% was recorded. The spring carrier had the additional effect of providing a restoring moment to any angular (diametral) deflections of the mainshaft. Since the first two modes were bending modes and not rigid body modes, the spring carrier had a small effect on critical speeds.

However, this slight increase in critical speed was considered negligible. It was deemed satisfactory to ignore the geometric complication and it was not considered further.

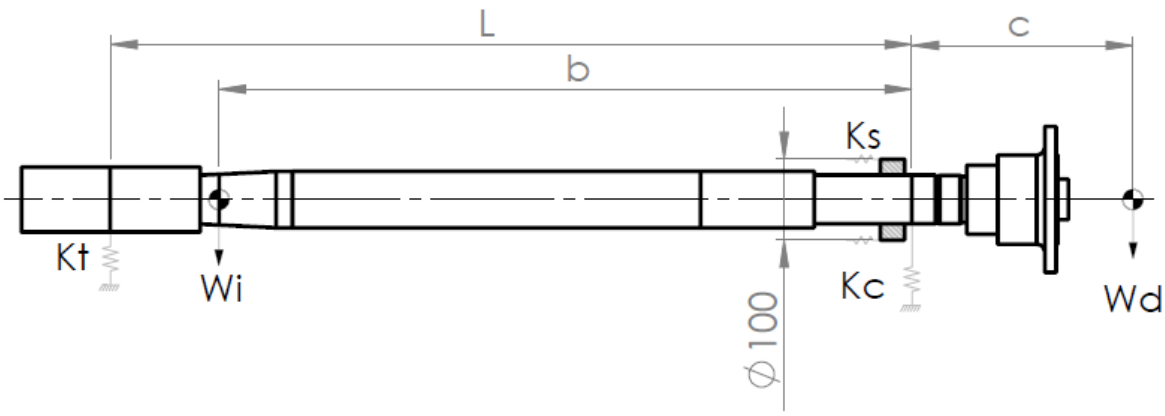

Figure 3.14 - Geometry Description of the Spring Carrier Assembly
(Ks is the stiffness of each individual pre-load spring).

3.5.2 Distributed Water Bearing Support

It was considered necessary to test whether the water bearing could be reliably modelled as a flexible-point support. In operation, a hydrodynamic journal bearing should give rise to a pressure over the entire surface of the journal. Therefore, ideally the bearing should be modelled as a 'uniformly distributed spring' support.

No such 'distributed-support' element exists in the ANSYS Workbench v14.1 element library. However, to assess the effect, it was deemed satisfactory to split the spring 'Kt' into five parallel springs of individual stiffness 'Kt/5' as shown in Figure 3.15. This distributed support had the added effect of:

- providing a restoring moment to any angular (diametral) deflections of the mainshaft about the bearing centre; and
- 'stiffening' by applying a restoring force to any bending of the mainshaft.

A change in the first two critical speeds of +0.63% and +0.00% was recorded. This difference was considered negligible. Therefore, a single flexible support was deemed sufficient to approximate the water bearing.

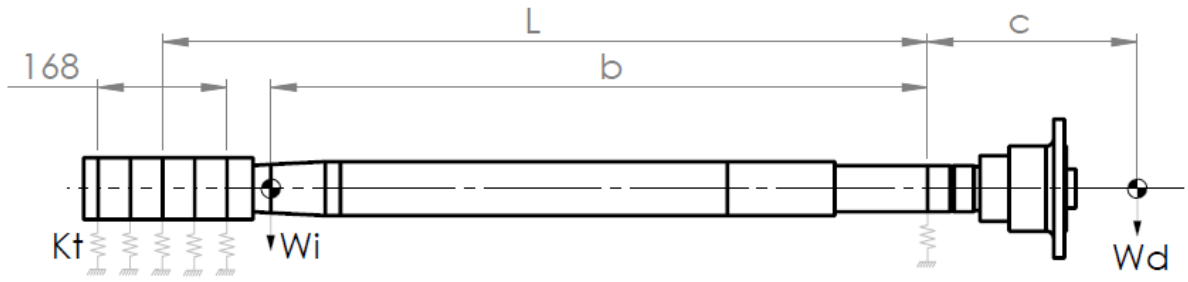

Figure 3.15 - Distributed Water Bearing Support Geometry

3.6 ASSESSMENT AND CONCLUSIONS

In Table 3.7, a basic comparison of the Isolated-Mainshaft FEM and Myklestad-Prohl TMM methods is provided. Overall the two methods gave very similar results. This was expected as both approaches take into account support properties, gyroscopic effects and inertia terms. Both methods directly calculated critical speeds instead of approximation through modal frequencies.

Table 3.7 - Comparison of Selected Analytical and Numerical Methods

Method	Critical Speed 1 [RPM]	Critical Speed 2 [RPM]	Solution Time
Isolated-Mainshaft FEM	2809	2951	4 minutes
Myklestad-Prohl TMM	2922	2954	2.8 seconds

The slight deviations noted between the two methods cannot be entirely explained; both models were validated at a basic level. It is likely that some minor non-conformity in geometry of the two models gave rise to this deviation. Some further investigation will be required in the future. Overall, the percentage deviation between the values provided by the two models was deemed slight enough to proceed.

In terms of application, both models have their advantages. The Isolated-Mainshaft FEM should have higher accuracy yet the Myklestad-Prohl TMM approach should yield much faster solution times.

In Table 3.8, an assessment of all the analytical and numerical methods presented in Section 2 and Section 3 is made. The Timoshenko-Beam, Myklestad-Prohl TMM and isolated mainshaft models appear the most appropriate for use by CWF Hamilton & Co. Ltd. Comparisons between these models and the experimental results will be drawn in the following sections.

Table 3.8 - Assessment of Analytical and Numerical Methods for CWF Hamilton & Co. Ltd.

Method	**Applicable**	**Ease of Use**	**Accuracy**	**Solution Times**
Rayleigh-Ritz	No	Excellent	Poor	Excellent
Dunkerley	Yes	Good	Good	Poor
Timoshenko-Beam	Yes	Excellent	Good	Good
Myklestad-Prohl TMM	Yes	Good	Excellent	Excellent
Isolated Mainshaft FEM	Yes	Good	Excellent	Good
Complete System FEM	Yes	Good	Poor	Very Poor

3.7 SECTION SUMMARY

An investigation into the various models used to predict critical speeds of shaft assemblies was performed. Both analytical and numerical methods were investigated. While a range of models were investigated, the Timoshenko-Beam, Myklestad-Prohl TMM and Isolated-Mainshaft FEM methods were deemed to be the most suitable for assessing the critical speeds of an HJ364 water jet assembly. The accuracy of these predictive models will be assessed in the rest of this thesis.

4

TEST RIG AND CRITICAL SPEEDS

4.1 INTRODUCTION

The second part of this work involved gathering critical speed data from an HJ364 water jet assembly. An instrumented test rig was established and a means of extracting critical speeds was determined.

The aim of this was twofold: to validate the analytical and numerical models described in the first part of this thesis (namely the Timoshenko-Beam, the Myklestad-Prohl TMM and the Isolated-Mainshaft FEM approaches); and analyse the effect of individual components on critical speeds including unbalance, driveline mass and overhang, support stiffness, impeller mass, bearing properties and water level.

The test rig, the instrumentation and the means of extracting critical speed data is detailed in this section.

4.2 TEST RIG

Testing was carried out on a modified HJ364 water jet assembly located in the old impeller facility at CWF Hamilton & Co. Ltd. These modifications are annotated on Figure 4.1 and included:

1. a steel base frame bolted to the bottom of the intake and the concrete floor of the test facility with a 40mm drain hole in the bottom;
2. an 11kW WEG motor, bolted to the base frame on a sliding platform and used to drive the mainshaft with a toothed belt at 11:10 speed ratio;
3. a shroud to cover the motor belts;
4. a shroud to cover the coupling and driveline mass;

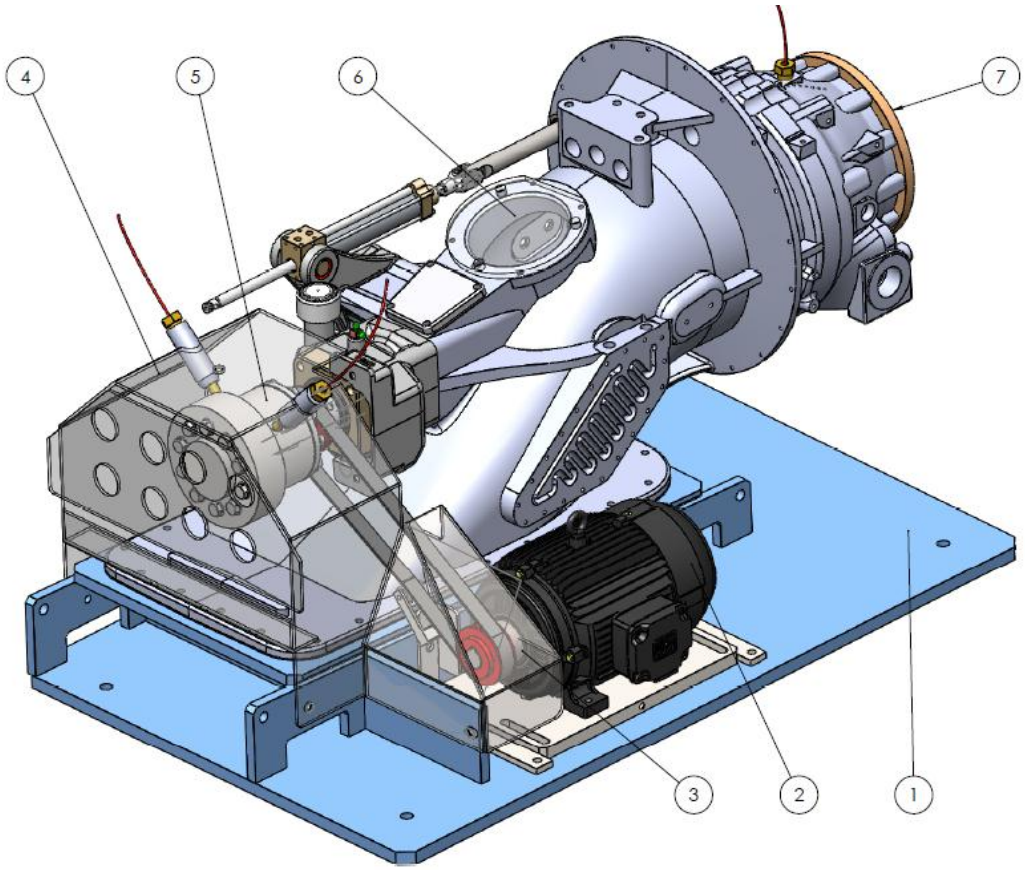

Figure 4.1 - Overview of the HJ364 Water Jet Assembly Test Rig

5. masses bolted to the coupling to emulate the mass and inertia of a driveshaft;
6. a see-through inspection cover to view the water level in the intake;
7. a blanking plate with a water feed, bolted to the end of the tailpipe to prevent water loss and allow water to be fed into the marine bearing; and
8. a steel disc to represent the mass and inertia properties of the impeller.

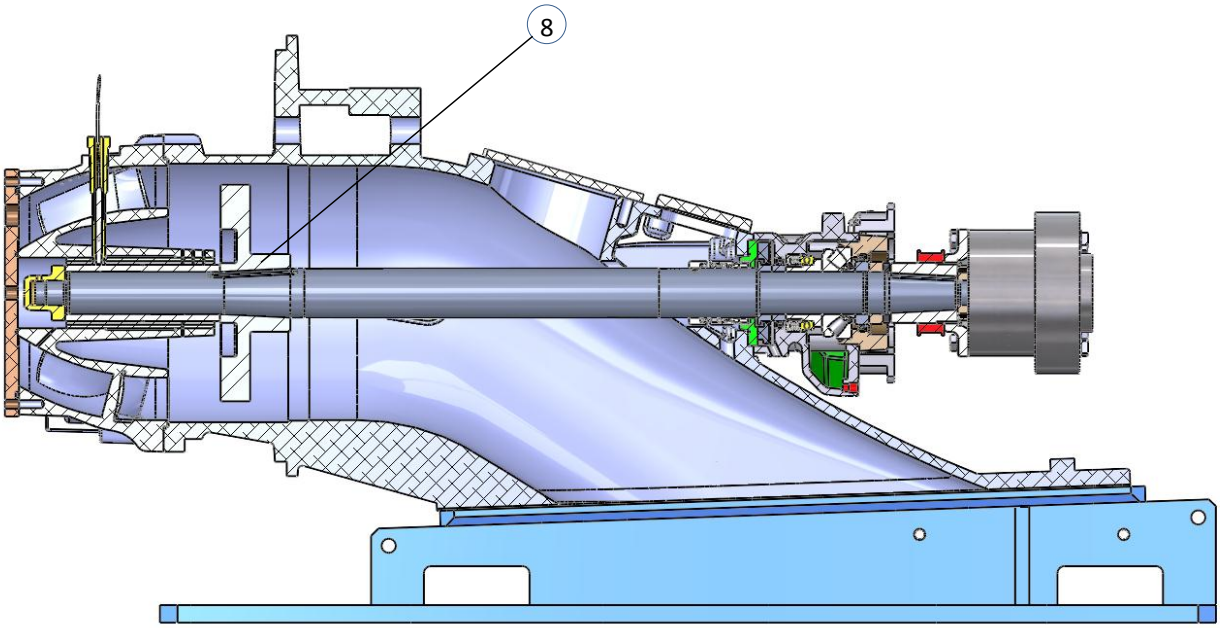

Figure 4.2 – Cross Section of the HJ364 Water Jet Assembly Test Rig

4.3 INSTRUMENTATION

4.3.1 Equipment

The test rig was instrumented with motion transducers in three separate locations in an attempt to gain a complete picture of the test rig operation including:

- a pair of displacement transducers (Brüel and Kjær IN – 081), aligned at 45º and -45º from the vertical and located at the coupling mass (Figure 4.3 and Figure 4.4);

- a pair of displacement transducers (Brüel and Kjær IN – 081), aligned horizontally and vertically and located within the tailpipe at the midpoint of the water bearing (Figure 4.5); and
- a pair of general purpose shear accelerometers (Brüel and Kjær 352C03) aligned horizontally and vertically and attached to the top of the thrust bearing housing (Figure 4.6).

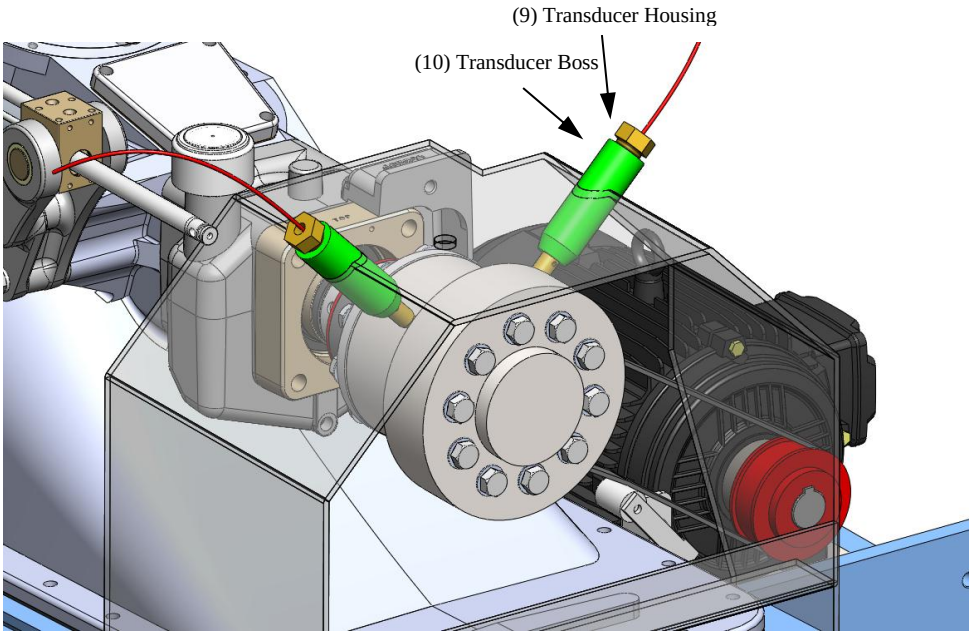

Figure 4.3 - Overview of the Displacement Transducers on the Driveline Mass

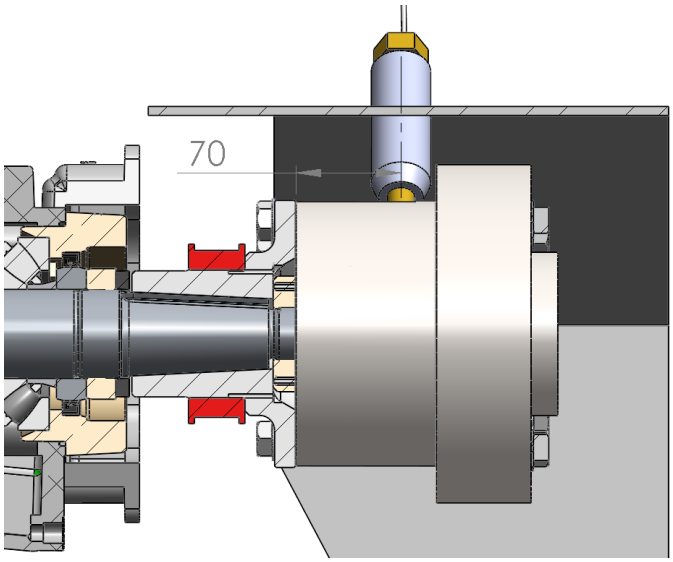

Figure 4.4 - Location of the Displacement Transducers on the Driveline Mass

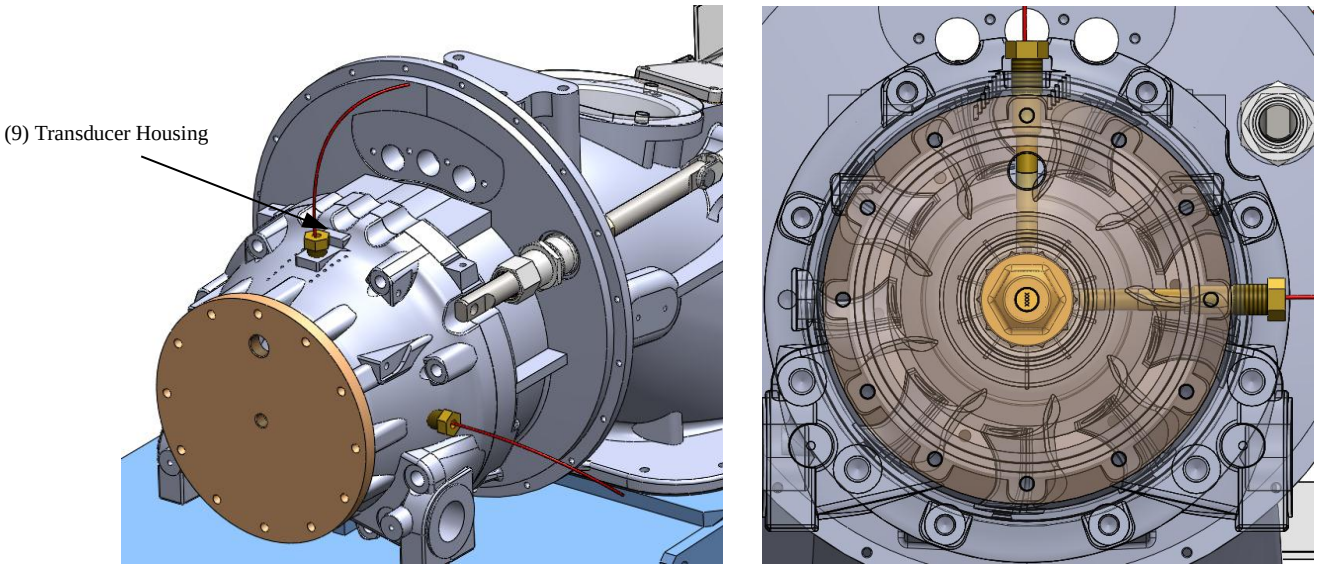

Figure 4.5 – Tailpipe Displacement Transducers
(A) Overview of the Displacement Transducers in the Tailpipe
(B) Detailed view of the Displacement Transducers in the Tailpipe

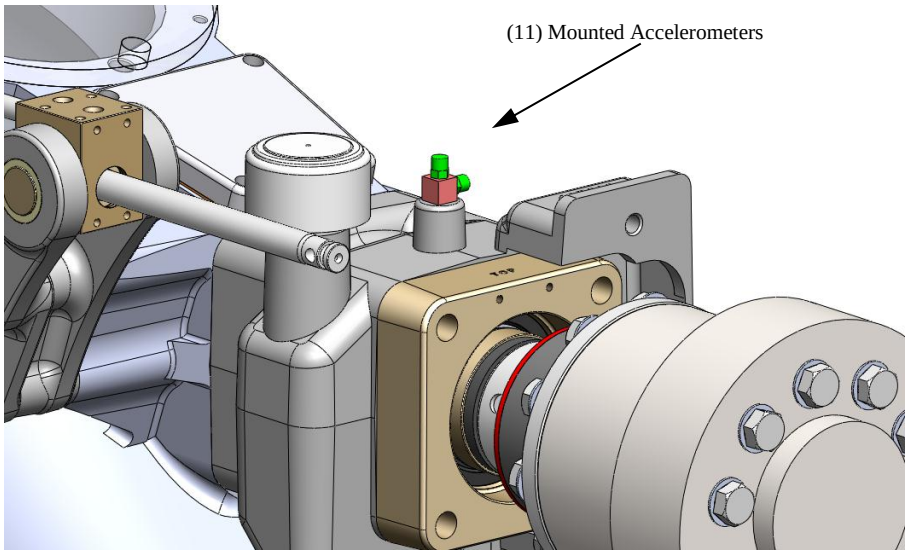

Figure 4.6 - Location of the Accelerometers on the Thrust Bearing Housing

4.3.2 Speed Control

Speed control was performed with a WEG 'CFW-11 Frequency Inverter' speed controller. A National Instruments 'NI 9263' (4-Channel, 100 kS/s, 16-bit, ±10 V) analog output module was used to provide a DC signal to the speed controller. A linear relationship between DC voltage and shaft speed was established with a digital photo tachometer (model RM-1500) and a maximum combined error of ±2 RPM was recorded across the range.

4.3.3 Data Conversion, Acquisition and Calibration

Analogue to digital conversion was performed primarily with University of Canterbury National Instruments equipment. This comprised:

- a 'NI 9234' (4-channel, 24-bit, 51.2 kS/s) analogue input module to sample and perform analogue to digital conversion of the output signals from the displacement transducers;
- a 'NI 9234' (4-channel, 24-bit, 51.2 kS/s) analogue input module to sample and perform analogue to digital conversion of the output signals from the accelerometers; and
- a 'NI 9178' CompactDAQ 8-slot chassis to allow serial transmission of the sampled data.

Data acquisition was performed using a script prepared in National Instruments LabVIEW (2009 release) and run on a Dell 'Latitude D630' laptop computer. All sampling was performed at a rate of 5 kHz. A circuit schematic and a screenshot of the 'Front Panel' of the LabVIEW script are provided in Figure 4.7 and Figure 4.8 respectively.

Calibration of the displacement transducers was performed by creating an output voltage versus displacement plot for each transducer and extracting the gradient in the linear range.

These gradients were then used to scale data during the acquisition process. Care was taken to ensure that each transducer was operating in the linear range at all times.

The two accelerometers were provided with calibration data from the manufacturer. Hence, no further calibration of these was required.

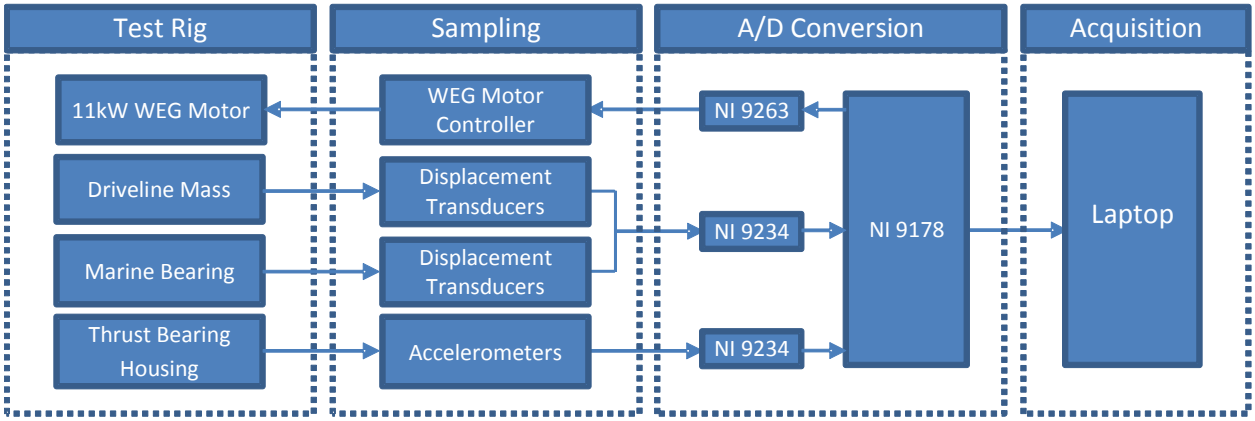

Figure 4.7 - Instrumentation Circuit Schematic

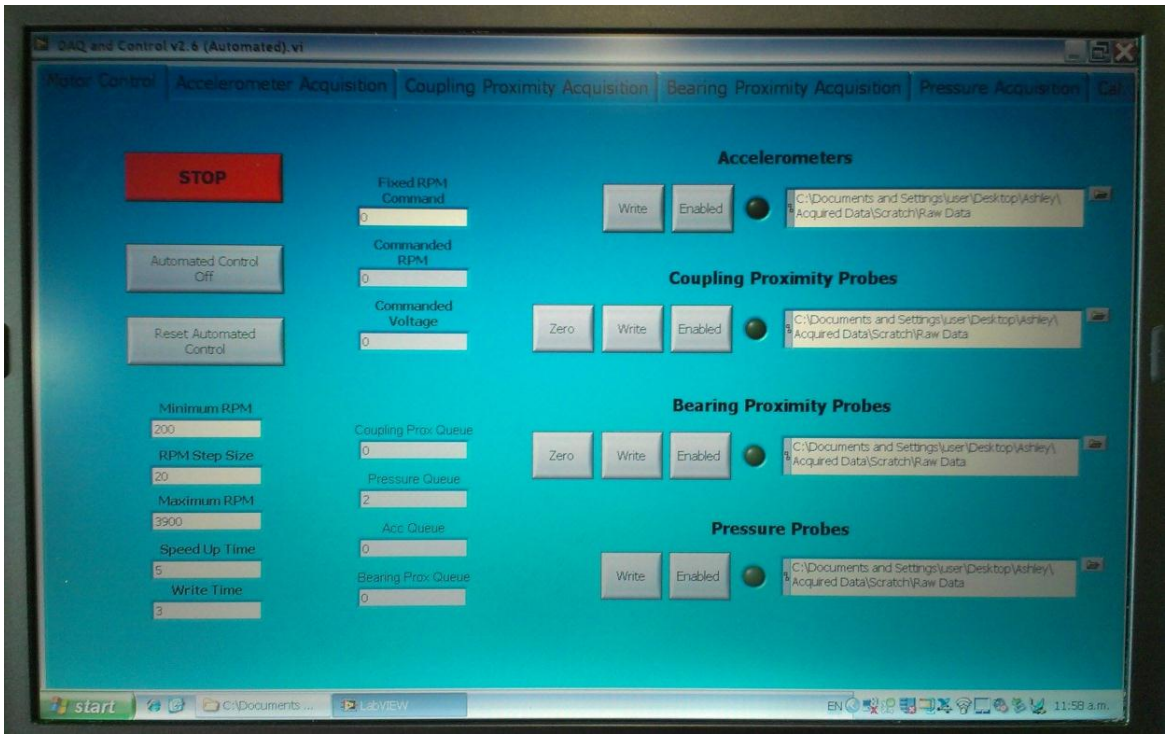

Figure 4.8 - Acquisition VI Front Panel as Displayed in LabVIEW

4.4 EXTRACTING CRITICAL SPEEDS

4.4.1 Determining Orbit Shapes from Data

Due to the arrangement of the displacement transducers, a 2-dimensional mapping of the shaft position with time could be created. This is commonly called an 'Orbit Plot'. Scripts were generated in Matlab (R2011b release) to convert the acquired data into a native Matlab format and create orbit plots. However, it was found that surface roughness added significant errors resulting in a poor representation of the shaft orbit (see Figure 4.9).

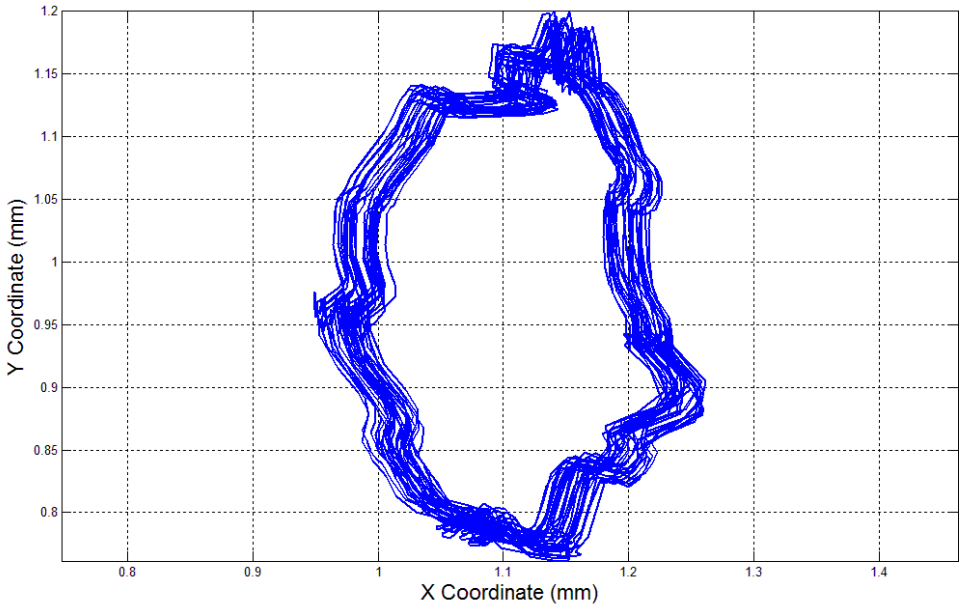

Figure 4.9 – An Example of a Poor Representation of an Orbit at the Driveline Mass (Standard Configuration, 1500 RPM)

Eliminating surface roughness from the Orbit Plot would have proven very difficult. However, it was realised that each displacement transducer should output a sinusoidal voltage with some noise. A Fourier series is a common means of estimating a periodic signal and since a sinusoidal output was expected, a first order series of the form:

$$X(t) = X_0 + a_1 sin(wt) + b_1 cos(wt) \quad (4.1)$$

$$Y(t) = Y_0 + a_2 sin(wt) + b_2 cos(wt) \quad (4.2)$$

was fitted to each data set. The results of this on an individual proximity probe can be viewed in Figure 4.10.

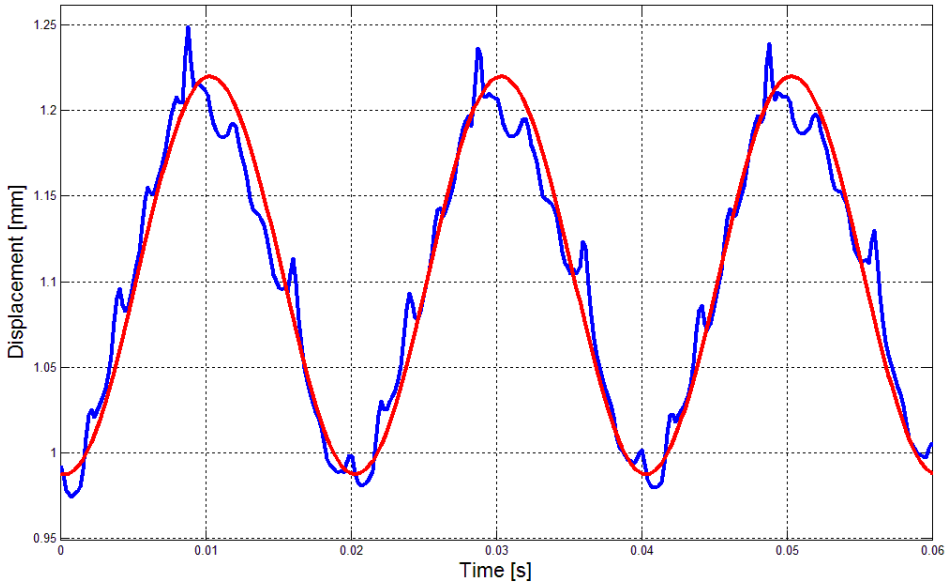

Figure 4.10 – First Order Fourier Approximation of the 'X' Proximity Probe Output at the Driveline Mass Approximation is shown in Red; Original Measurement in Blue
(Standard Configuration, 1500 RPM)

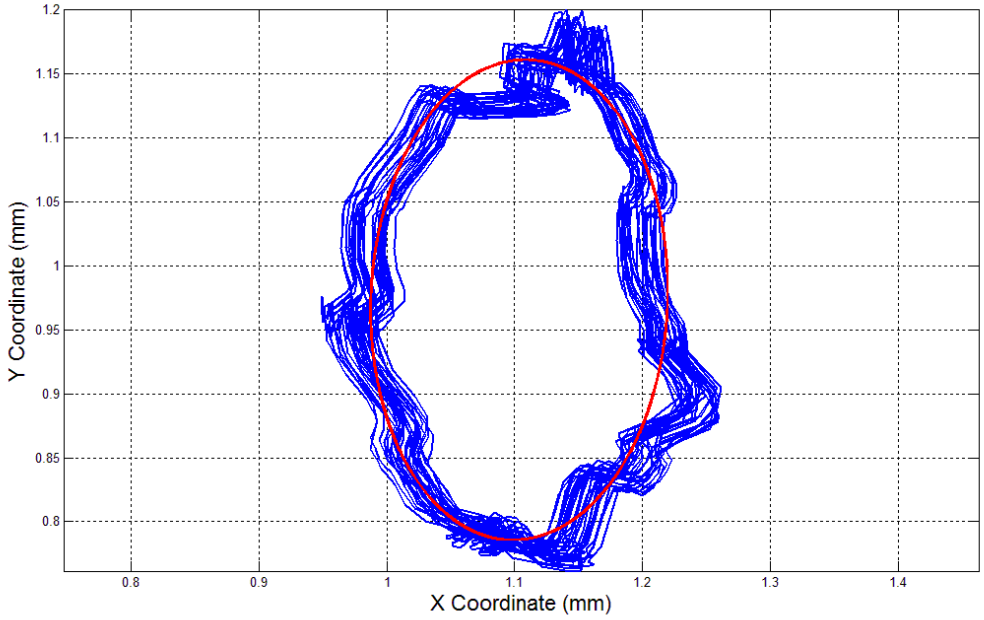

Figure 4.11 – First Order Fourier Approximation of the Whirl Orbit at the Driveline Mass Approximation is Shown in Red; Original Measurement in Blue
(Standard Configuration, 1500 RPM)

When re-mapped as an orbit plot, the results proved far more satisfactory (Figure 4.11). Although the peak values were not captured perfectly, the estimation was adequate for extracting critical speeds.

4.4.2 Determining Critical Speeds from Orbit Shapes

The most common method of determining a stable critical speed from experimental data involves finding the rotational speed at which a peak deflection of the whirling body occurs. The first order Fourier series (4.1) and (4.2) can be compared to the parametric equations of an ellipse:

$$X(t) = X_c + A\cos(\omega t)\cos(\vartheta) - B\sin(\omega t)\sin(\vartheta) \tag{4.3}$$

$$Y(t) = Y_c + A\cos(\omega t)\sin(\vartheta) + B\sin(\omega t)\cos(\vartheta) \tag{4.4}$$

Where: $[X_c, Y_c]$ is the centre of the ellipse; A is the major axis; B is the minor axis; and ϑ is the angle between the x-axis and the major axis of the ellipse. Comparison of terms yields:

$$[X_0, Y_0] = [X_c, Y_c] \tag{4.5}$$

$$a_1 = -B\sin(\vartheta) \tag{4.6}$$

$$b_1 = A\cos(\vartheta) \tag{4.7}$$

$$a_2 = B\cos(\vartheta) \tag{4.8}$$

$$b_2 = A\sin(\vartheta) \tag{4.9}$$

With the symmetric behavior of trigonometric functions:

$$\cos(\vartheta) = \cos(-\vartheta) \tag{4.10}$$

$$sin(\vartheta) = sin(\pi - \vartheta) \tag{4.11}$$

Thus, the maximum deflection (A), the minimum deflection (B) and the phase angle (ϑ) can be determined from each individual orbit plot. A script was prepared in Matlab (R2011b) to perform this process automatically and is provided in Appendix B2.

4.4.3 Determining Critical Speeds from Accelerometers

A less conventional means of establishing critical speeds comes from determining the peak unbalance response. When a body experiences static unbalance, the centre of mass is not aligned with the axis of rotation. Therefore the radial acceleration 'a' experienced by the mass 'm' at an angular velocity 'ω' is:

$$a_{radial} = -e\,\omega^2 \tag{4.12}$$

and the unbalance force (acting radially along the vector connecting the centre of mass and the centre of rotation) is:

$$f_{unbalance} = -m\,e\,\omega^2 \tag{4.13}$$

This unbalance force will be partially opposed by the nearest support and 180º out of phase.

A Fast Fourier Transform (FFT) was taken of each data set obtained from the accelerometers. This was repeated for each rotational speed and plotted into a three-dimensional figure called a 'Waterfall' plot. An example is provided in Figure 4.12. A script was prepared to extract the peak acceleration magnitude at the driven frequency for each data set (that is, the first

'peak' of the waterfall plot). This data was re-plotted on a two-dimensional axis and is shown in Figure 4.13. The peak magnitude of this plot should indicate a critical speed.

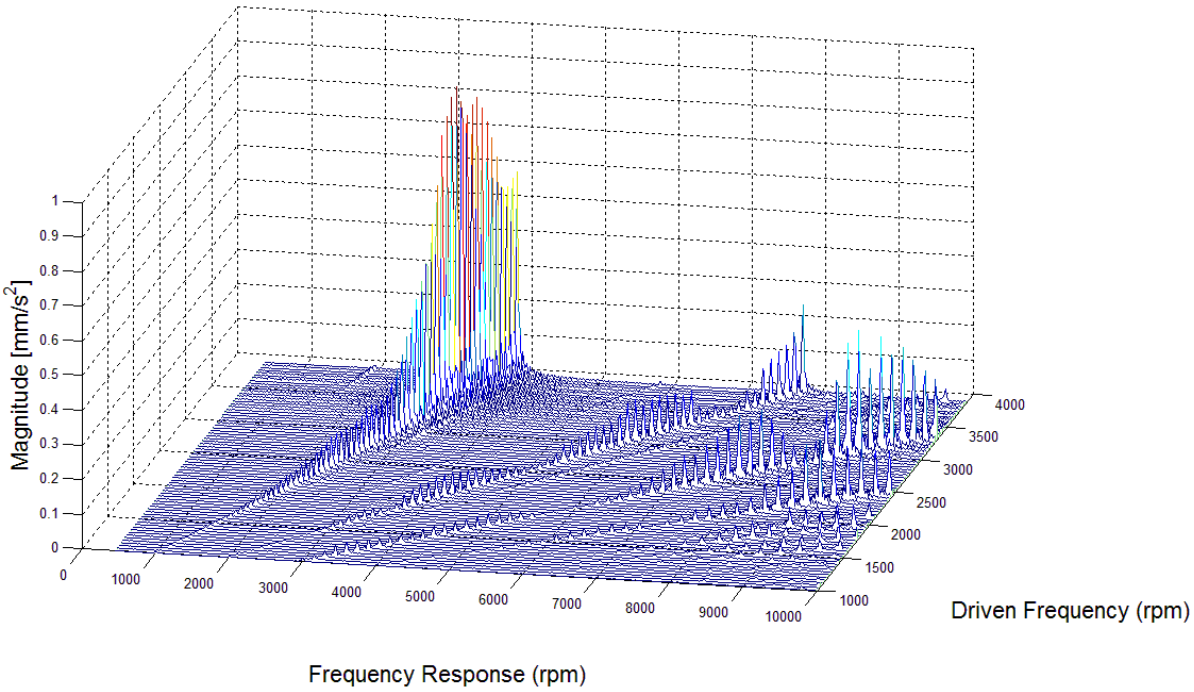

Figure 4.12 – Waterfall Plot derived from the Vertically Aligned Accelerometer Data
(Standard Configuration; 1000 to 3900 RPM in 20 RPM intervals)

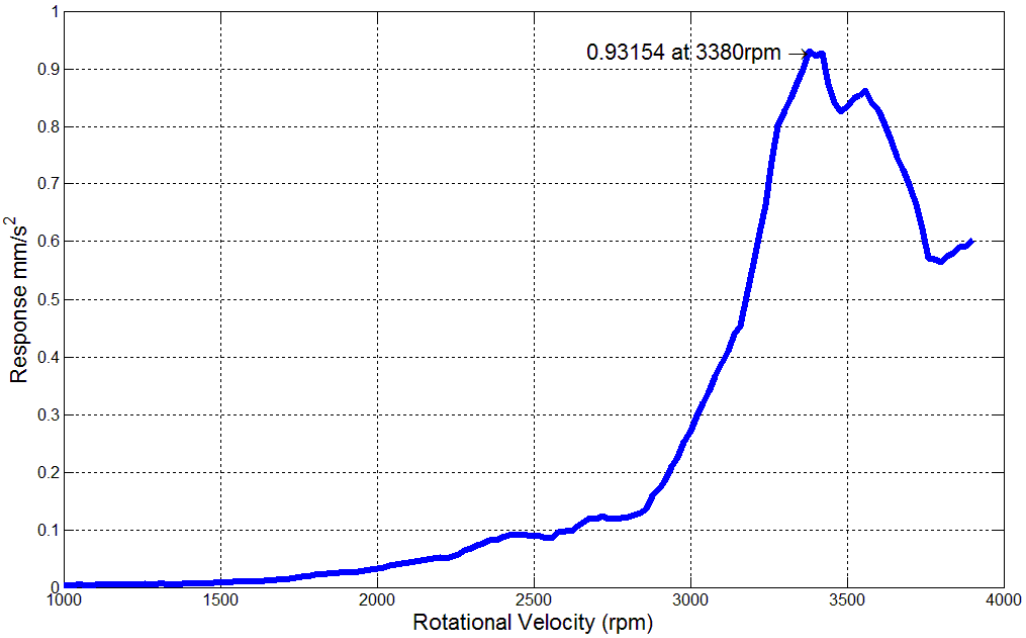

Figure 4.13 – Plot of Peak Acceleration at Driven Frequency for Each Rotational Speed
(Standard Configuration, 1000 to 3900 RPM in 20 RPM intervals)

4.5 SECTION SUMMARY

Initially, this section provided an overview of the test facility including the test rig, instrumentation, speed control and data acquisition procedures. Subsequently, a detailed explanation of the data processing requirements was provided; fitting a first order Fourier series to the displacement data allowed repeatable and accurate measurement of critical speeds. Finally, it was shown that accelerometer data could be used to approximate critical speeds; however, this was found to be useful for a first estimate only.

5

UNBALANCE, REPEATABILITY AND INITIAL RESULTS

5.1 INTRODUCTION

To overcome damping and excite all of the primary modes, it was necessary to apply a mass unbalance. As the driveline mass was calculated to play a significant role in the first two modes, the unbalanced mass was applied to it. The effect that the degree of unbalance played on the system was reviewed then measured.

With the selected unbalanced mass, the critical speeds were measured from the system in its standard configuration. Repetition of these measurements allowed the repeatability of the process to be assessed and the overall measurement error to be determined.

5.2 UNBALANCE EFFECTS

5.2.1 Theoretical Effects on Critical Speeds

Under ideal conditions, the addition of unbalance (with no change in system mass) will cause no changes in the critical speeds of a system. "The value of the speed is fixed … In particular, the main flexural critical speeds do not depend on the amount of unbalance, but the amplitude increases with increasing unbalance" (Genta, 2008). This agrees with the theoretical models described in Section 2; no unbalance term is present when evaluating critical speeds.

It should be noted that "external damping causes the rotor's motion to be bounded at the critical speed" (Childs, 1993). The steady state solution of the 'Jeffcott Model' including damping as provided by Childs (1993, p5) is

$$\boldsymbol{R} = |C_{(\omega)}|\boldsymbol{A}e^{j\psi} \tag{5.1}$$

where

$$\left|C_{(\omega)}\right| = \frac{\omega^2}{\sqrt{(\lambda^2 - \omega^2)^2 + 4\zeta_e^2\lambda^2\omega^2}} \tag{5.2}$$

$$\tan\psi = \frac{-2\zeta_e\lambda\omega}{\lambda^2 - \omega^2} \tag{5.3}$$

and the complex displacement and rotor-imbalance vectors are respectively

$$\boldsymbol{R} = R_x + jR_y \tag{5.4}$$

$$\boldsymbol{A} = A_x + jA_y \tag{5.5}$$

Here, ω is the angular velocity of the shaft, λ is the critical speed and ζ_e is the damping factor. Observation of equation (5.1) shows that an increase in damping leads to a reduction

in rotor response. Therefore, the rotor-imbalance vector must be increased to produce the same displacement.

Hence, any heavily damped modes can be overcome with adequate unbalance. Therefore, it was deemed appropriate to apply the largest unbalanced mass available that would not cause the mainshaft to yield.

5.2.2 Unbalanced Mass Design

Since the degree of system damping was unknown, it was not possible to calculate the required unbalanced mass. Instead, a range of unbalanced masses were trialled and the response compared.

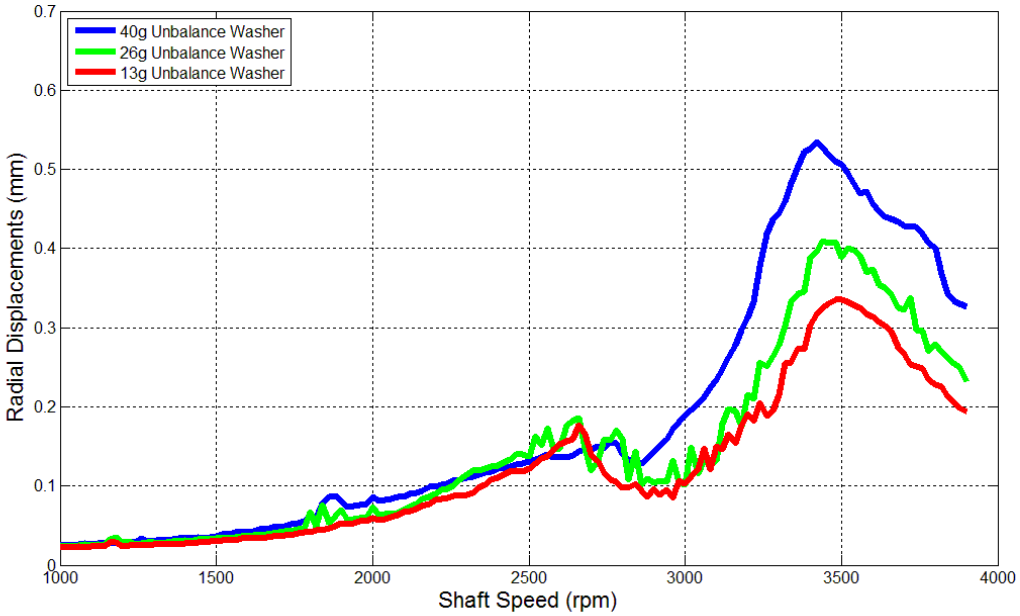

Figure 5.1 – Maximum Displacement of the Driveline Mass during Unbalanced Mass Testing (Standard Configuration, 1000 to 3900 RPM)

The results of the unbalanced mass testing are provided in Figure 5.1; a plot of the maximum driveline mass displacement over the full speed range. As indicated, washers were used to provide mass eccentricities of 1014g-mm, 2028g-mm and 3120g-mm. A larger, 60g unbalanced mass led to excessive whirling and instability.

For the reasons outlined in Section 5.2.1, the 40g washer was selected for critical speed excitation in all testing. The slight reduction noted in the critical speed with larger unbalance is predicted by equation (5.1). In Table 5.1, a summary of these results is provided.

Table 5.1 - Summary of Unbalanced Mass Testing Results

Washer Mass [g]	Mass-Eccentricity [g-mm]	Peak Driveline Mass Displacement [mm]	Stable
13	1014	0.34	Yes
26	2028	0.41	Yes
40	3120	0.54	Yes
60	4680	-	No

5.3 REPEATABILITY AND MEASUREMENT ERROR

5.3.1 Repeatability

To assess the measurement error present in the system, repeatability was assessed with the 40g unbalanced washer. Three runs of this configuration are presented in Figure 5.2. A minor reduction in critical speed was present with each run along with a minor increase in response. This is indicative of a reduction in damping. Since the oil-filled thrust bearing housing adjacent to the driveline mass heated up significantly during testing, the viscosity of the oil would have reduced. This reduction in viscosity would have led to a reduction in damping. However, since the overall effect on critical speed was small, this was not considered problematic.

5.3.2 Measurement Error

The results obtained in Section 5.3.1 and Section 5.3.2 allowed the combined measurement error to be assessed. Each error could be combined linearly to create a cumulative result. A summary of these values is provided in Table 5.2. These results should also be applicable for the tests that involved geometric modifications to the test rig. They will be referred to in the following sections unless otherwise stated.

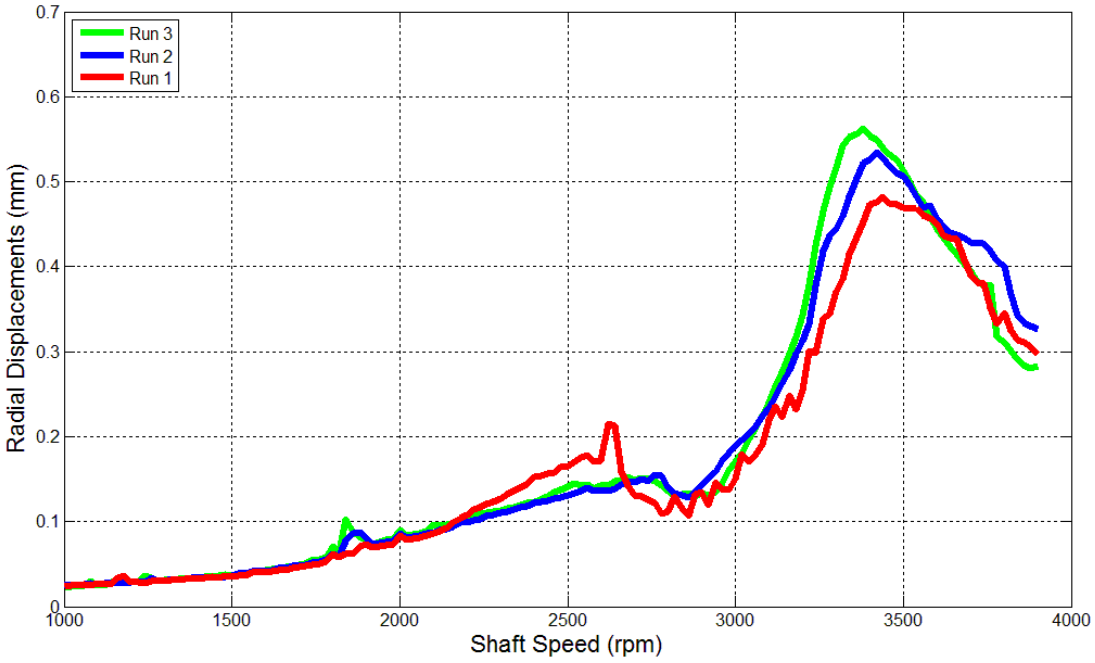

Figure 5.2 – Max. Displacement of the Driveline Mass during Repeatability Testing with a 3120g-mm Eccentricity (Standard Configuration, 1000 to 3900 RPM)

Table 5.2 – Summary of Individual and Cumulative Error of Critical Speed Measurements

Error Type	**Associated Error [RPM]**
Resolution (RPM step size)	± 10
Unbalance	± 20
Repeatability	± 30
Zero	NEG
Cumulative	± 60

5.4 INITIAL RESULTS

To conclude this section, the peak displacement and peak acceleration plots from the test rig in its standard configuration are provided in Figure 5.3, Figure 5.4 and Figure 5.5 respectively. In Table 5.3, they are compared with the predictions of the Timoshenko-Beam, Myklestad-Prohl TMM and Isolated-Mainshaft FEM methods.

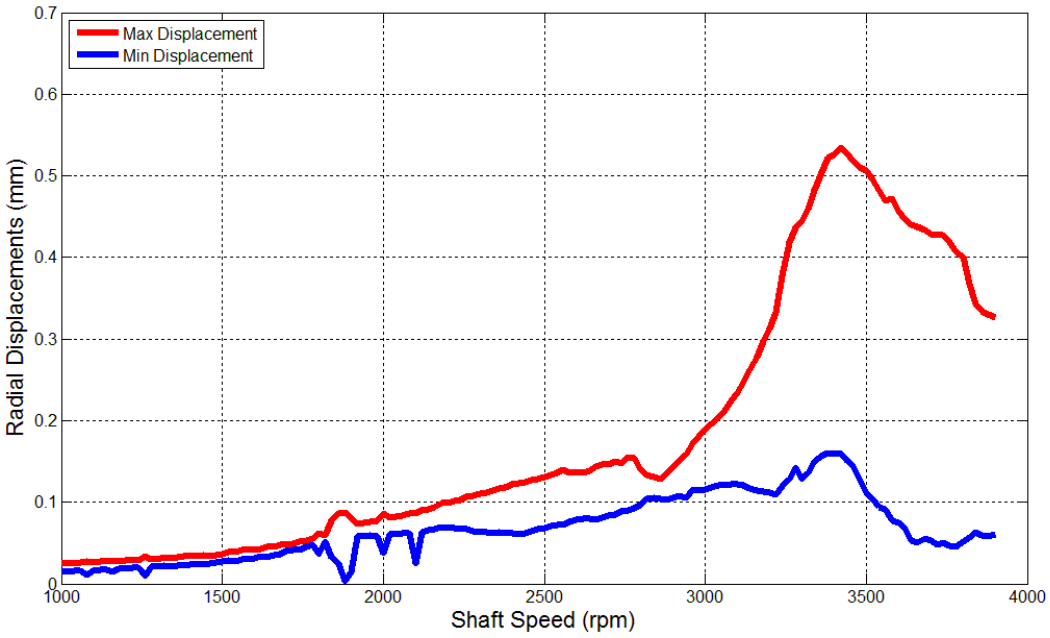

Figure 5.3 – Maximum and Minimum Displacement of the Driveline Mass
(Standard Configuration, 1000 to 3900 RPM, 3120g-mm unbalance)

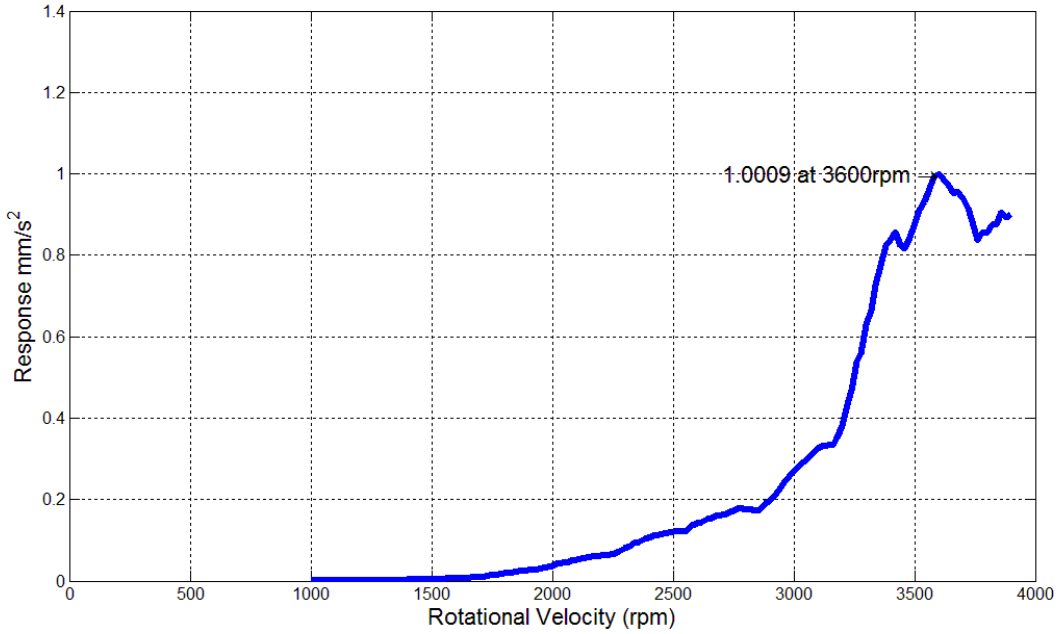

Figure 5.4 – Response from the Horizontally Aligned Accelerometer along the Synchronous Excitation Peak (Standard Configuration, 1000 to 3900 RPM, 3120g-mm unbalance)

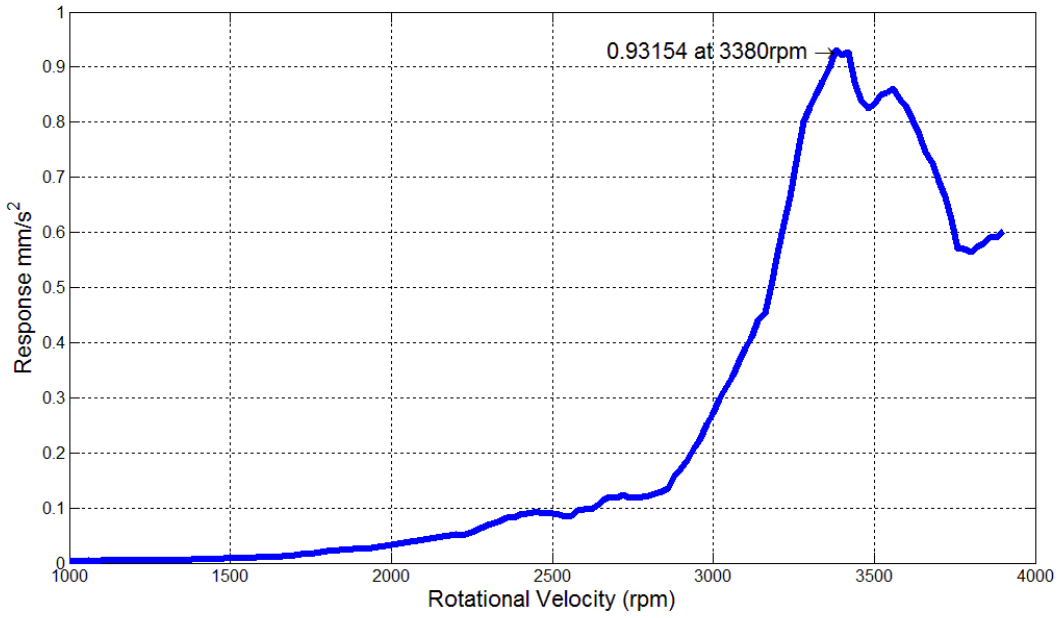

Figure 5.5 - Response from the Vertically Aligned Accelerometer along the Synchronous Excitation Peak (Standard Configuration, 1000 to 3900 RPM, 3120g-mm unbalance)

5.5 DISCUSSION

Overall, the predicted and experimentally determined critical speeds compared favorably. Some unexplained phenomena at 1800 and 2750 RPM were apparent (Figure 5.3). Otherwise, the results appeared to follow the predicted trend. The accelerometer results could not be used directly as they required superimposition. However, they were useful for a first estimate.

Table 5.3 - Comparison of Experimental, Analytical and Numerical Results
of the HJ364 Water Jet Assembly (Standard Configuration)

Method	First Critical Speed	Second Critical Speed
Experimental	3420 ± 60	3420 ± 60
Timoshenko-Beam	3072	3072
Myklestad-Prohl TMM	2921	2935
Isolated-Mainshaft FEM	2931	3098

Observation of Table 5.3 indicates that there were some large deviations between the experimental and predicted results. Both the accelerometers and the displacement transducers indicated a critical speed approximately 500 RPM higher than the analytical and numerical models. As the models were extensively investigated and refined, this was considered an inexplicable deviation. The behavior is further investigated in Section 11.

The second point of interest is the lack of deviation between the first two measured critical speeds. A difference of approximately 200 RPM was predicted by the numerical models due to support asymmetry. However, this did not appear in the displacement measurements. Interestingly, the peak magnitudes indicated by the accelerometers (Figure 5.4, Figure 5.4 and Figure 5.5) differed by approximately this speed range.

Cross-coupled stiffness is common in hydrodynamic journal bearings and the effect “reduces the effective amount of asymmetry by coupling the response in both lateral planes”

(Greenhill & Cornejo, 1995). Therefore, the marine bearing in the HJ364 water jet assembly was considered to be the reason for the coincidence of the first two critical speeds. It is further investigated in Section 10.

5.6 SECTION SUMMARY

In this section, the repeatability and unbalance response of the HJ364 water jet assembly was measured from which a measurement error of ± 60 RPM was determined. With the selected 3120g-mm mass unbalance, initial critical speed measurements were taken. The experimental method proved reliable. However, the experimentally determined critical speeds were approximately 500 RPM higher than those predicted. This phenomenon was left unexplained and is further investigated in Section 11.

6

DRIVELINE MASS AND OVERHANG EFFECTS

6.1 INTRODUCTION

In Section 2, it was determined that the driveline mass[5] and its overhang from the coupling had the largest effect on critical speeds. To experimentally validate this result, a range of driveline masses were designed such that coupling mass and overhang could be modified independently. These masses were attached to the test rig, critical speeds were measured and comparisons were made to the predicted values. This work is detailed in this section.

[5] The 'driveline mass' was attached to the coupling and was used to emulate the mass and inertia properties of a driveshaft

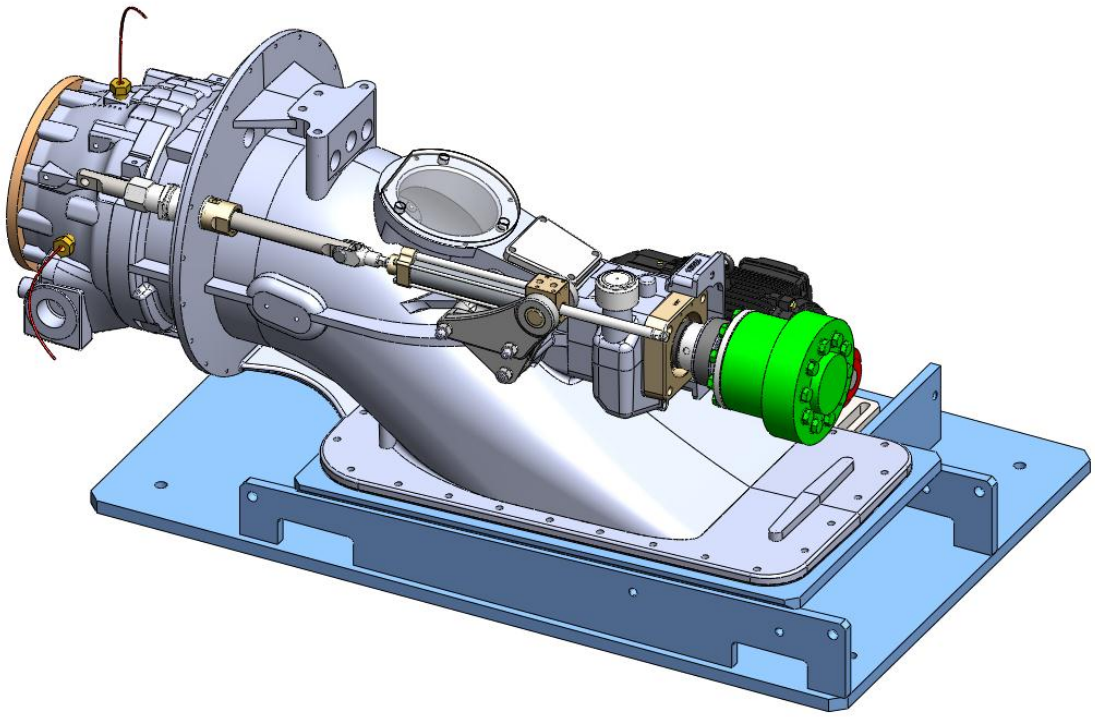

Figure 6.1 - Overview of HJ364 Test Rig at CWF Hamilton & Co. Ltd.
(Driveline Mass Highlighted in Green)

6.2 CRITICAL SPEED MODELLING

Analytical and numerical modelling work was carried out to determine a suitable alternative driveline mass and an alternative driveline overhang. To achieve this, the effect of driveline mass and driveline overhang on critical speeds was evaluated through first principals and subsequently through the Timoshenko-Beam method.

The driveline mass and mainshaft assembly could be tentatively approximated as a cantilever with an end mass. The first natural frequency ω_n of a system such as this is given in equation (6.1).

$$\omega_n = 1.875^2 \sqrt{\frac{EI}{mL^4}} \tag{6.1}$$

Evidently, a reduction in mass, m or a reduction in overhang, L, should lead to an increase in natural frequency. This approximation is backed up by the Timoshenko-Beam simulations provided in Figure 6.2 and Figure 6.3.

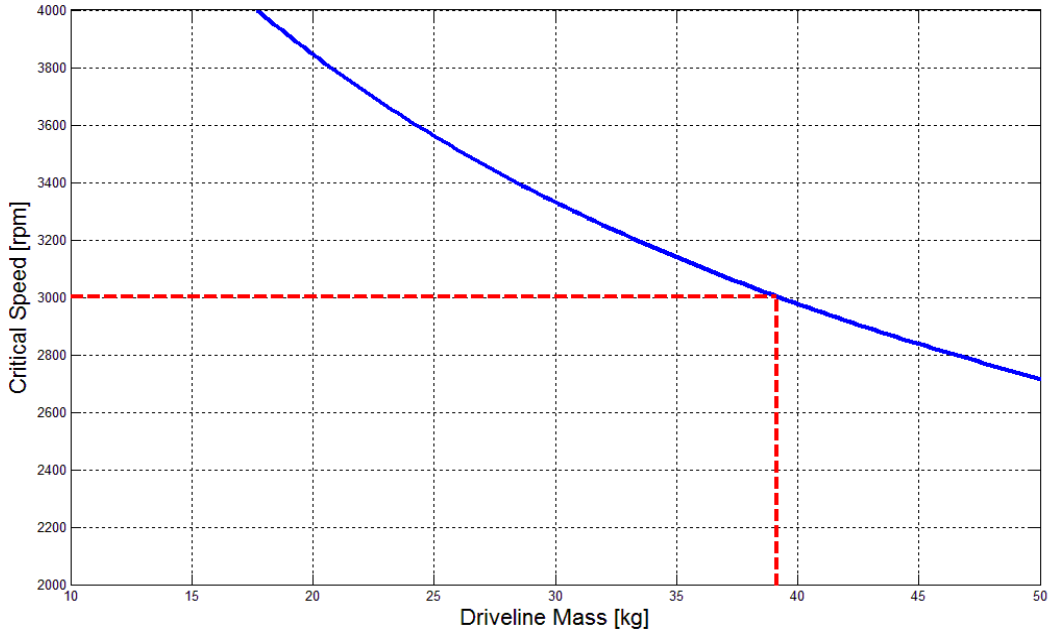

Figure 6.2 –Effect of Driveline Mass on Critical Speeds as evaluated by the Timoshenko-Beam Method
Dashed Red Line: 39kg, 3003 RPM (standard configuration)

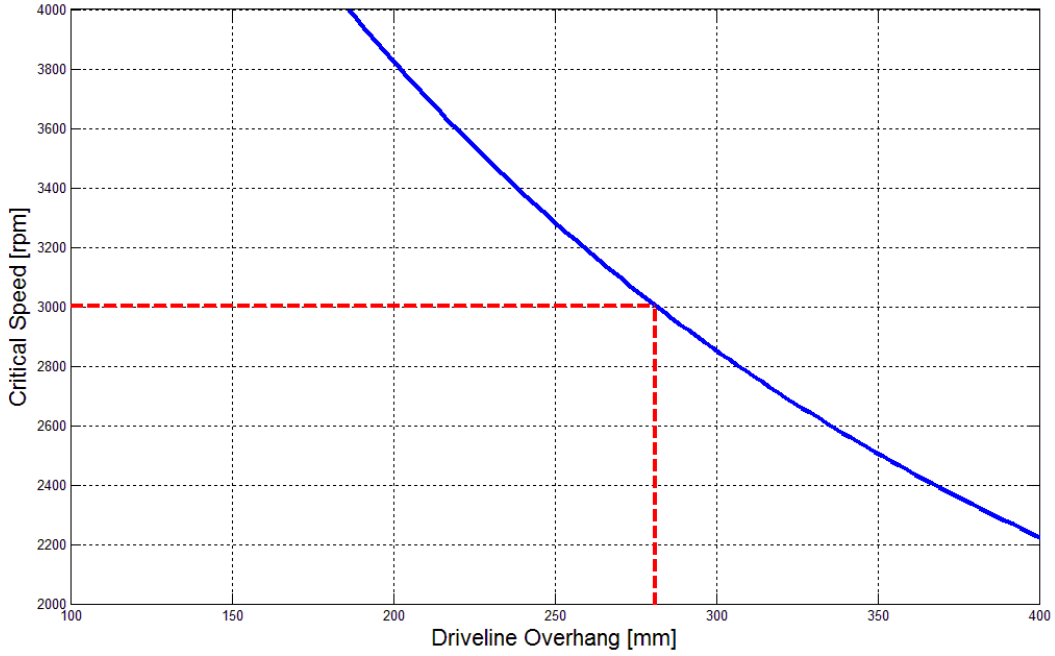

Figure 6.3 - Effect of Driveline Overhang on Critical Speeds as evaluated by the Timoshenko-Beam Method
Provided as Overhang from the Spherical Thrust Bearing
Dashed Red Line: 281mm, 3003 RPM (standard configuration)

6.3 ALTERNATIVE DRIVELINE MASS DESIGNS

As the damping properties of the system were unknown, stability of the system could not be evaluated. Therefore to ensure instability did not occur, only lighter driveline masses and smaller overhangs were investigated. Two masses were designed such that driveline mass and driveline overhang could be varied independently.

6.3.1 Alternative Driveline Mass

While the aim was that the diametral moment of inertia would be held constant, material and clearance limitations mean that this could not be entirely achieved. The alternative driveline mass was designed iteratively in "Solidworks 2010" to obtain the largest reduction in mass possible while maintaining the standard overhang of 281mm.

The overview of the optimal design is provided in Figure 6.4. This was fabricated by the tool room at CWF Hamilton & Co. Ltd. A detailed drawing is provided in Appendix A1. In Figure 6.5, the theoretical critical speed of the new mass was evaluated using the Timoshenko-Beam method. In Table 6.1 and Table 6.2, the mass properties and predicted effects on critical speeds are provided.

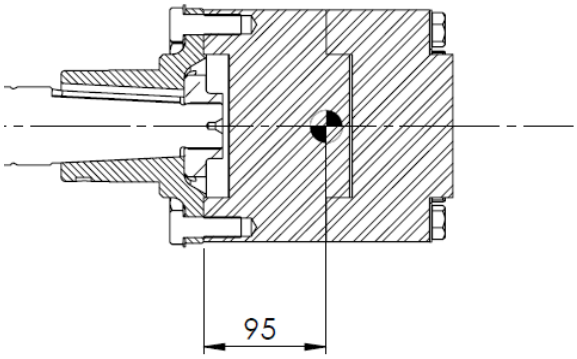

Figure 6.4 – Alternative Driveline Mass Configuration
Total Mass: 32kg
Overhang: 281mm (standard)

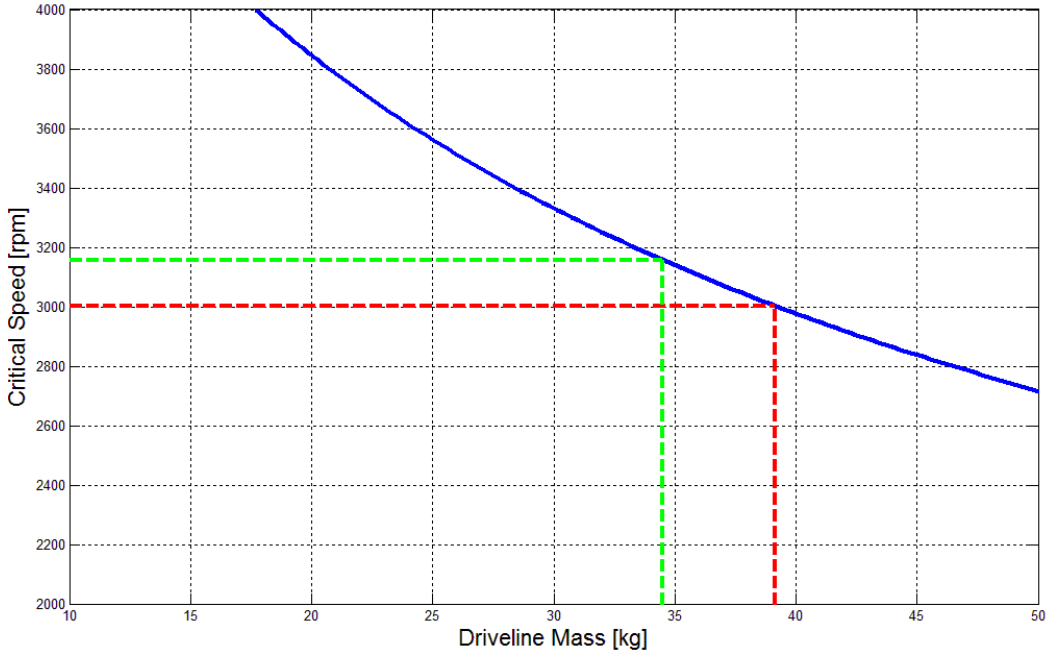

Figure 6.5 –Effect of Driveline Mass on Critical Speeds as evaluated by the Timoshenko-Beam Method
Dashed Red Line: 39kg, 3003 RPM (standard configuration)
Dashed Green Line: 34.5kg, 3158 RPM (reduced mass configuration)

Table 6.1 – Mass Properties of the Alternative Driveline Mass

Property	**Value**	**Change**
Mass	34.5 kg	-4.7 kg
COM from Thrust Bearing	273.2 mm	0.0 mm
Rotational Inertia	0.14 kgm^2	-0.7 kgm^2
Diametral Inertia	0.17 kgm^2	+0.02 kgm^2

Table 6.2 – Critical Speed Properties of the Alternative Driveline Mass

Method	**Predicted Critical Speed**	**Change in Critical Speed**
Timoshenko-Beam	3158 RPM	+155 RPM
Myklestad-Prohl TMM	3064 RPM	+142 RPM
Isolated-Mainshaft FEM	2963 and 3081 RPM	+154 and +130 RPM

6.3.2 Alternative Driveline Overhang

The alternative driveline overhang was also designed iteratively in "Solidworks 2010" to obtain the largest reduction in mass possible while maintaining the standard driveline mass of 39kg. Again, the aim was that the diametral moment of inertia and driveline mass would be held constant. This was once again restricted by the material and clearance limitations and could not be entirely achieved.

An overview of the optimal design is provided in Figure 6.6. Only modifications to the inner mass were required to achieve this shift in overhang. It was fabricated by the tool room at CWF Hamilton & Co. Ltd. A detailed drawing is provided in Appendix A2. In Figure 6.7, the theoretical critical speed of the new driveline overhang was evaluated using the Timoshenko-Beam method. In Table 6.3 and Table 6.4, the mass properties and predicted effects on critical speeds are provided.

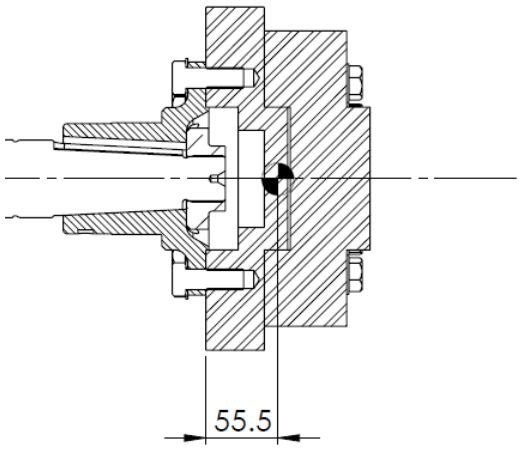

Figure 6.6 - Alternative Driveline Overhang Configuration
Total Mass: 39kg (standard)
Overhang: 242mm

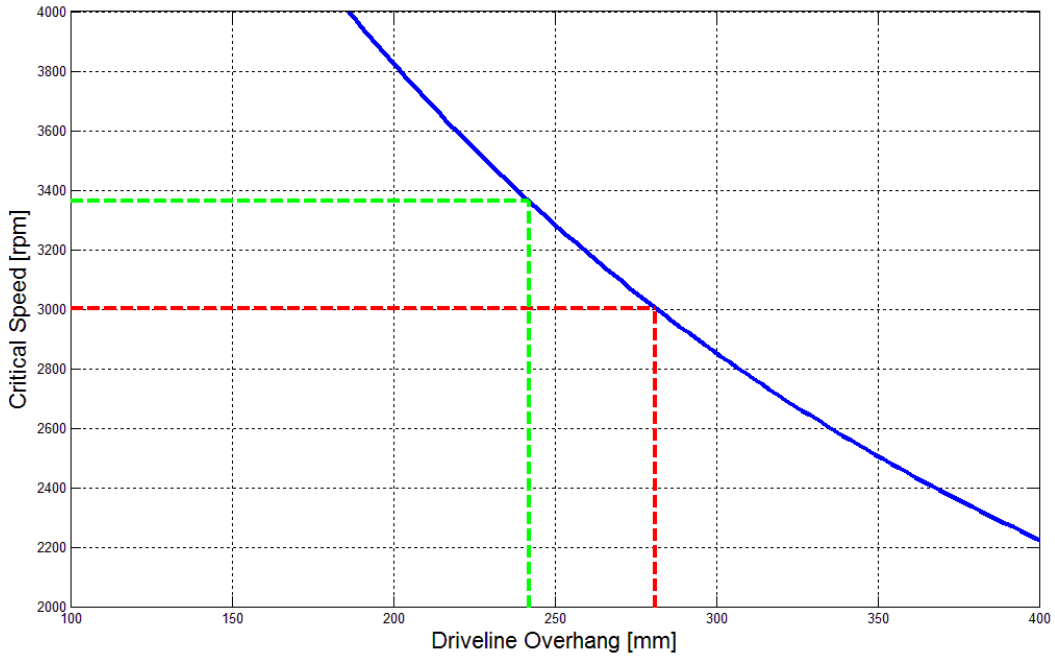

Figure 6.7 - Effect of Driveline Overhang on Critical Speeds as evaluated by the Timoshenko-Beam Method
Provided as Overhang from the Spherical Thrust Bearing
Dashed Red Line: 281mm, 3003 RPM (standard configuration)
Dashed Green Line: 242mm, 3363 RPM (reduced overhang configuration)

Table 6.3 – Mass Properties of the Alternative Driveline Overhang

Property	**Value**	**Change**
Mass	39 kg	- 0.1 kg
COM from Thrust Bearing	242 mm	- 39 mm
Rotational Inertia	0.30 kgm^2	+ 0.09 kgm^2
Diametral Inertia	0.21 kgm^2	+ 0.02 kgm^2

Table 6.4 – Critical Speed Properties of the Alternative Driveline Overhang

Method	**Predicted Critical Speed**	**Change in Critical Speed**
Timoshenko-Beam	3363 RPM	+ 360 RPM
Myklestad-Prohl TMM	3220 RPM	+298 RPM
Isolated-Mainshaft FEM	3047 and 3293 RPM	+238 and +342 RPM

6.4 TEST RESULTS

6.4.1 Alternative Driveline Mass Testing

With the alternative mass assembly shown in Figure 6.4, critical speed testing was carried out in accordance with the methodology described in Section 4. For reasons of conciseness, the results from the accelerometers have not been plotted here. However, the displacement results at the driveline mass are provided in Figure 6.8.

Observation of this figure indicates some strange behavior. While there was a well-defined critical speed at 3580 RPM, there was also a secondary peak at 2680 RPM (approximately 75%). This secondary peak appeared to increase exponentially with speed as would be expected with unbalance. However, above 2680 RPM, the displacement suddenly decreased in magnitude. There was also a strange response at around 2000 RPM where the response suddenly became planar then returned to elliptical. Clearly, the system was exhibiting some non-linear behavior. The displacement response is compared to that of the standard shaft configuration in Figure 6.9.

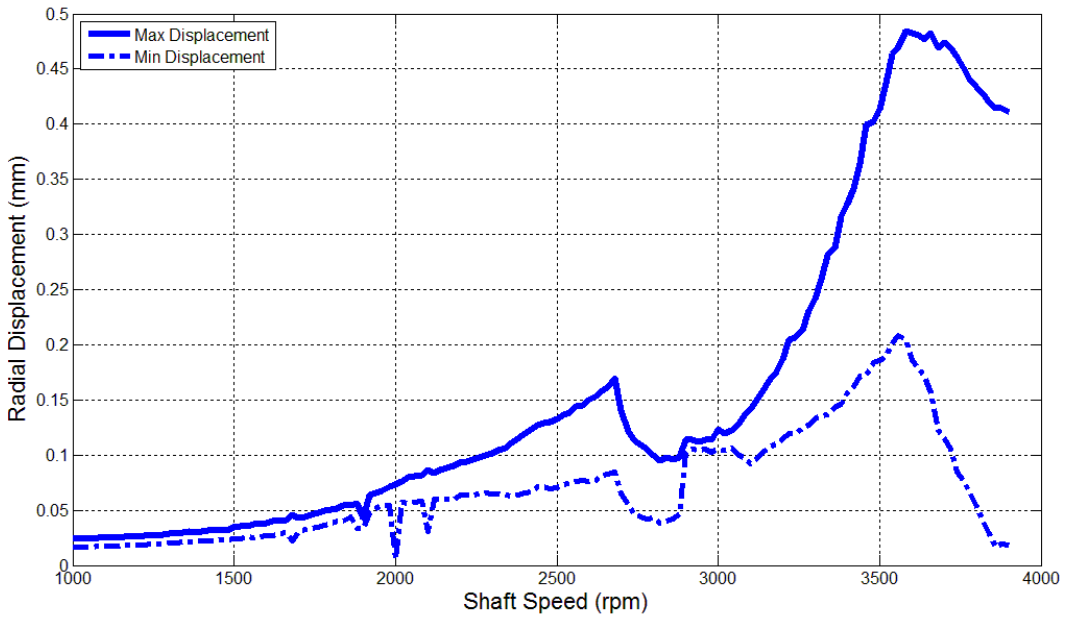

Figure 6.8 – Peak Radial Displacements of the Alternative Driveline Mass
(34.5kg Driveline Mass, 1000 to 3900 RPM, 20 RPM sampling)

Evidently the results are somewhat consistent with the predictions made in Section 6.3.1; the critical speed increased by approximately 160 RPM. The general 'trend' of the response was conserved between tests. Peak deflections and accelerations (not shown) also decreased with the increase in critical speed. In Table 6.5, the measured critical speed data from the alternative driveline mass testing is provided.

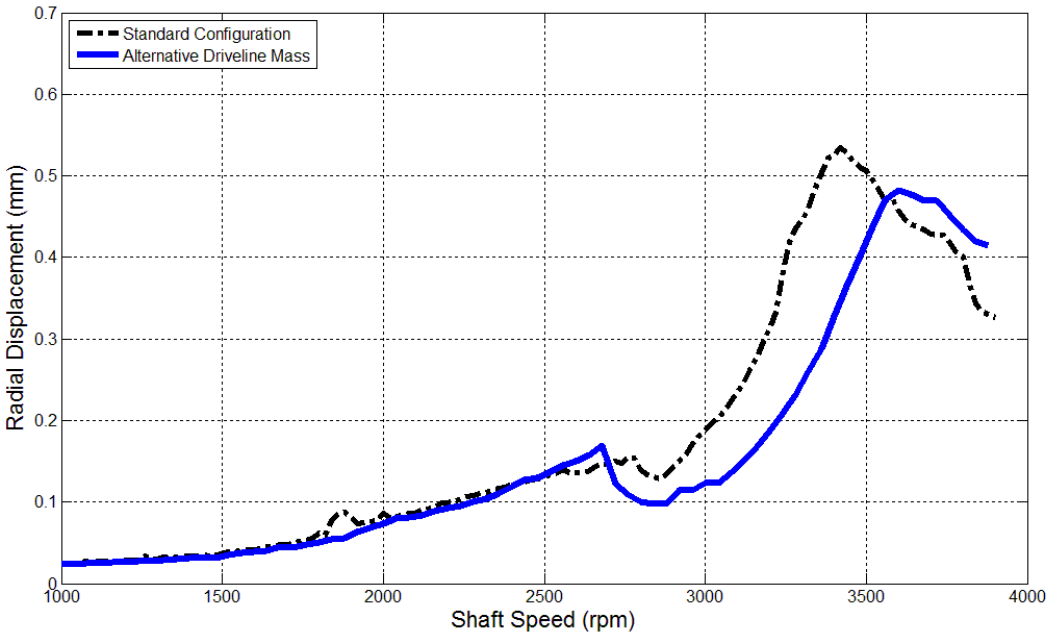

Figure 6.9 – Comparisons of Maximum Radial Displacement at the Driveline Mass
(34.5kg Driveline Mass, 1000 to 3880 RPM, 20 RPM sampling)

Table 6.5 - Critical Speed Data from the Alternative Driveline Mass Testing (Summary)

Evaluation Method	Measured Critical Speed	Change in Critical Speed
Maximum Deflection	3580 ± 60 RPM	+ 160 ± 120 RPM
Maximum Vertical Accel.	3640 ± 60 RPM	+ 260 ± 120 RPM
Maximum Horizontal Accel.	3900 ± 60 RPM	+ 300 ± 120 RPM

6.4.2 Alternative Driveline Overhang Testing

With the alternative mass assembly shown in Figure 6.6, critical speed testing was again carried out in accordance with the methodology described in Section 4. The displacement results at the driveline mass are provided in Figure 6.10.

As with the alternative mass testing, observation of this figure indicates some similar strange behavior. There was a well-defined peak at 3760 RPM. However, the maximum displacement appeared to vary somewhat sporadically between 1700 and 3500 RPM. Interestingly, the misalignment observable at 1000 RPM appeared to reduce with speed up to 1700 RPM. At 1900 and 2200 RPM there were two peaks with a planar displacement shape. Finally there appeared to be a strong peak at around 2750 RPM (approximately 73% of the main peak). Evidently, the system was again exhibiting some non-linear behavior. The displacement response is compared to that of the standard shaft configuration in Figure 6.11.

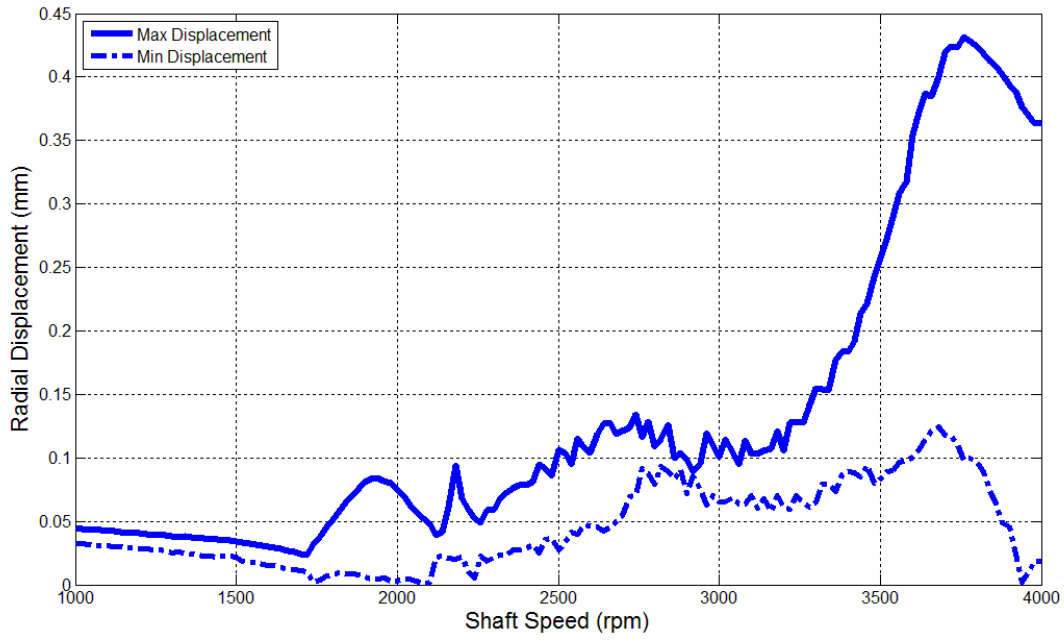

Figure 6.10 – Peak Radial Displacements of the Alternative Driveline Overhang
(242mm Driveline Overhang, 1000 to 3900 RPM, 20 RPM sampling)

The results are somewhat consistent with the predictions made in Section 6.3.2; the critical speed increased by approximately 520 RPM. Despite the unusual behavior of the driveline

mass, the general ‘trend’ of the response was conserved between tests. Predictably, maximum deflections and accelerations (not shown) decreased with the reduction in driveline overhang. In Table 6.6, the measured critical speed data from the alternative driveline overhang testing is provided.

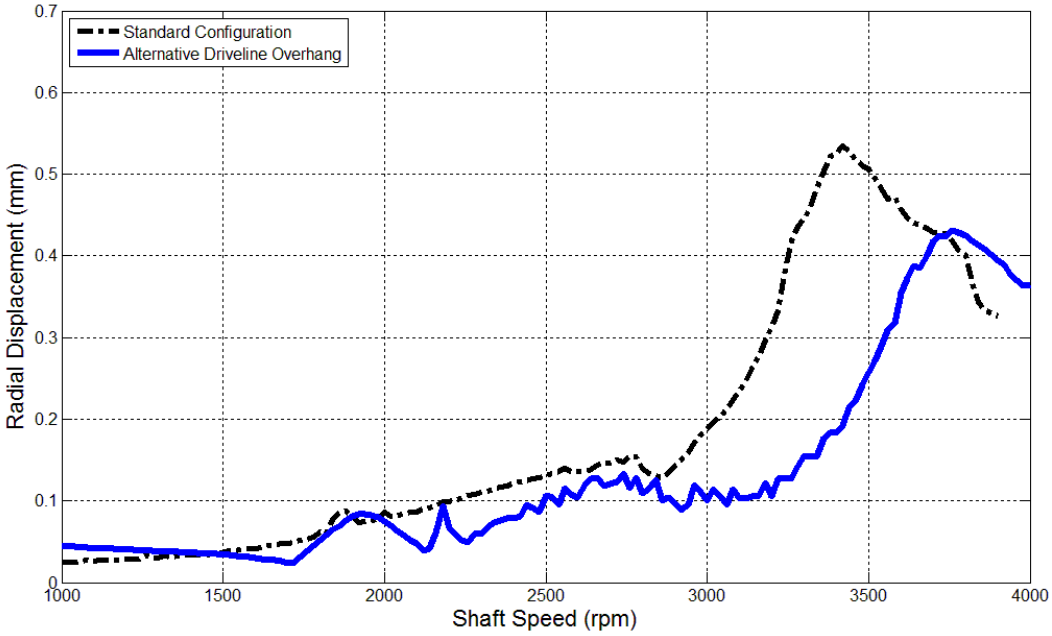

Figure 6.11 – Comparisons of Maximum Radial Displacement at the Driveline Mass
(242mm Driveline Overhang, 1000 to 3900 RPM, 20 RPM sampling)

Table 6.6 - Critical Speed Data from the Alternative Driveline Overhang Testing

Evaluation Method	Measured Critical Speed	Change in Critical Speed
Maximum Deflection	3760 ± 60 RPM	+ 520 ± 120 RPM
Maximum Vertical Accel.	3720 ± 60 RPM	+ 340 ± 120 RPM
Maximum Horizontal Accel.	3880 ± 60 RPM	+ 280 ± 120 RPM

6.5 COMPARISONS AND DISCUSSION OF RESULTS

To summarise the results of this section and draw comparisons, Table 6.7 and Table 6.8 have been provided. Observation of both these tables indicates that the experimentally determined critical speeds were significantly higher than those predicted. Both the accelerometers and the displacement transducers indicated a critical speed approximately 400 to 700 RPM higher than the analytical and numerical models. This unexpected behavior was also noted in the initial results displayed in Section 5. It is further investigated in Section 11.

Interestingly, the predicted and measured changes in critical speed (from the standard configuration) for both tests; the 'alternative driveline mass' testing coinciding almost perfectly. The change predicted for the 'alternative driveline overhang' testing is slightly less accurate. Evidently, the problem lies with the assumptions made in regards to overhang length. Despite this, the similarity between the predicted and measured changes indicates that all three models account for the effects of driveline mass and overhang relatively well.

The non-linear behavior observed in both the alternative driveline mass and overhang tests was not predicted in the modeling work. This is largely because the rotordynamic analyses described can only be used on linear systems. Therefore, the non-linear aspects of the system could not be modelled. The predominant non-linearities present in the test rig were the water-lubricated rubber marine bearing and the spherical thrust bearing.

Work carried out in Section 10 showed that the marine bearing was behaving poorly; largely due to the very small radial loading present. This bearing was noted to add a small degree of random behavior to the system. However, since the marine bearing was located so far from the driveline mass, this was not expected to be the root cause of the non-linear behavior.

Table 6.7 – Experimental and Modelled Critical Speed Data from the Alternative Driveline Mass

Method	Evaluated Critical Speed	Change in Critical Speed
Experimental	3580 ± 60 RPM	+ 160 ± 120 RPM
Timoshenko-Beam	3158 RPM	+155 RPM
Myklestad-Prohl TMM	3064 RPM	+142 RPM
Isolated-Mainshaft FEM	2963 and 3081 RPM	+154 and +130 RPM

Table 6.8 – Experimental and Modelled Critical Speed Data from the Alternative Driveline Overhang

Method	Evaluated Critical Speed	Change in Critical Speed
Experimental	3760 ± 60 RPM	+520 ± 120 RPM
Timoshenko-Beam	3363 RPM	+ 360 RPM
Myklestad-Prohl TMM	3220 RPM	+298 RPM
Isolated-Mainshaft FEM	3047 and 3293 RPM	+238 and +342 RPM

While the spherical thrust bearing should operate in a linear manner, its application in the HJ364 water jet assembly lends itself to non-linear behavior. A standard, 200kg pre-load was applied through a spring carrier to ensure that the thrust bearing maintained alignment[6]. However, the residual misalignment observed at 1000 RPM in both Figure 6.8 and Figure 6.10 indicated that this pre-load was not sufficient and that the bearing was not operating correctly. A limitation of the spring carrier design is that the amount of axial and angular float of the spherical thrust bearing is severely restricted. With significant mainshaft deflection, this 'float' could be taken up, impact made with the spring carrier and a non-linearity produced. This complex behavior is further investigated in Section 11.

Further to these non-linearities, the peak evident at 2700 RPM in Figure 6.9 could not be explained. All tests discovered this peak (at approximately 70% of the first main critical

[6] In practice a further thrust load would be provided by the impeller; no thrust load was produced by the impeller disc used in the test rig and was a limitation of the testing.

speed) to some degree. Since it varied with the configuration of the mainshaft, it could not be a natural frequency of the intake or the proximity probe housing. Therefore it was considered to be a combined natural frequency of the entire test-rig. However, the model was not extended to investigate this with the time available. Therefore the '70% peak' was labeled a phenomenon for further investigation at a later date.

6.6 SECTION SUMMARY

The effects of the driveshaft (approximated by a dummy mass) on critical speeds were investigated in this section. Comparisons were made between various mass configurations and the predictive models described in Section 2 and Section 3. It was found that the models incorrectly predicted the critical speeds of the test rig although predicted the effects of mass changes relatively accurately. It was surmised that some non-linearities present in the test-rig were leading to these results. These non-linearities are further investigated in Section 10 and Section 11.

For future water jet assembly designs, the driveshaft mass and overhang should be reduced as much as possible to increase critical speeds. CWF Hamilton & Co. Ltd. should take regard of this for all future designs.

7

THRUST BEARING HOUSING STIFFNESS

7.1 INTRODUCTION

In Section 3, it was determined that the stiffness of the thrust bearing housing had little effect on the critical speeds of the system; it could be approximated as infinite for modelling purposes. To validate this characteristic, a stiffener plate was added to the thrust bearing housing. If the assumption was correct, then the stiffener plate should have no measurable effect on critical speeds.

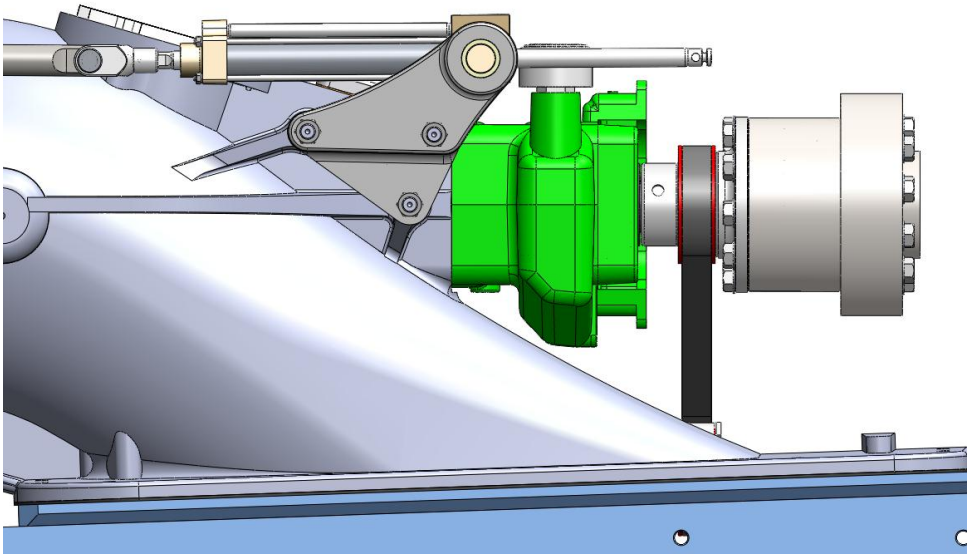

Figure 7.1 - Close up View of the Cantilevered Thrust Bearing Housing
(Thrust Bearing Housing Highlighted in Green)

7.2 BEARING HOUSING STIFFNESS MODIFICATIONS

In Figure 7.1, a close up view of the thrust bearing housing is provided. Note that the bearing housing (highlighted in green) is cantilevered from the intake. The design of the cantilevered thrust bearing housing readily leant itself to stiffness modifications. A cross-section of the design provided in Figure 7.3 was deemed the most suitable. This design consisted of:

- a 20mm thick 'aluminium boss' (highlighted in red) with 5 equally spaced M16 tapped holes, fitted and welded to the intake; and
- a 20mm mild steel 'stiffener plate' with a 10mm mild steel spacer (highlighted in green) bolted to the aluminium boss and the thrust bearing housing.

In Figure 7.3, a complete overview of the stiffened HJ364 test rig is provided. The stiffener plate was fastened to the thrust bearing housing using pre-existing studs. Substantial torque was applied to each bolt to prevent any relative motion between the plate and intake. Detailed drawings of the aluminium boss and the stiffener plate are provided in Appendix A3.

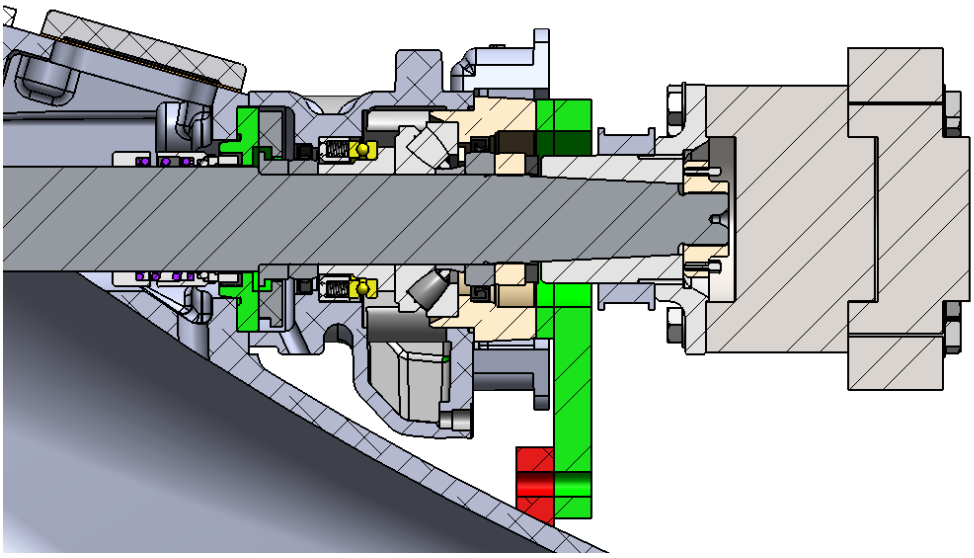

Figure 7.2 – Cross-Section of the Thrust Bearing Housing
(aluminium boss welded to intake; all other parts bolted)

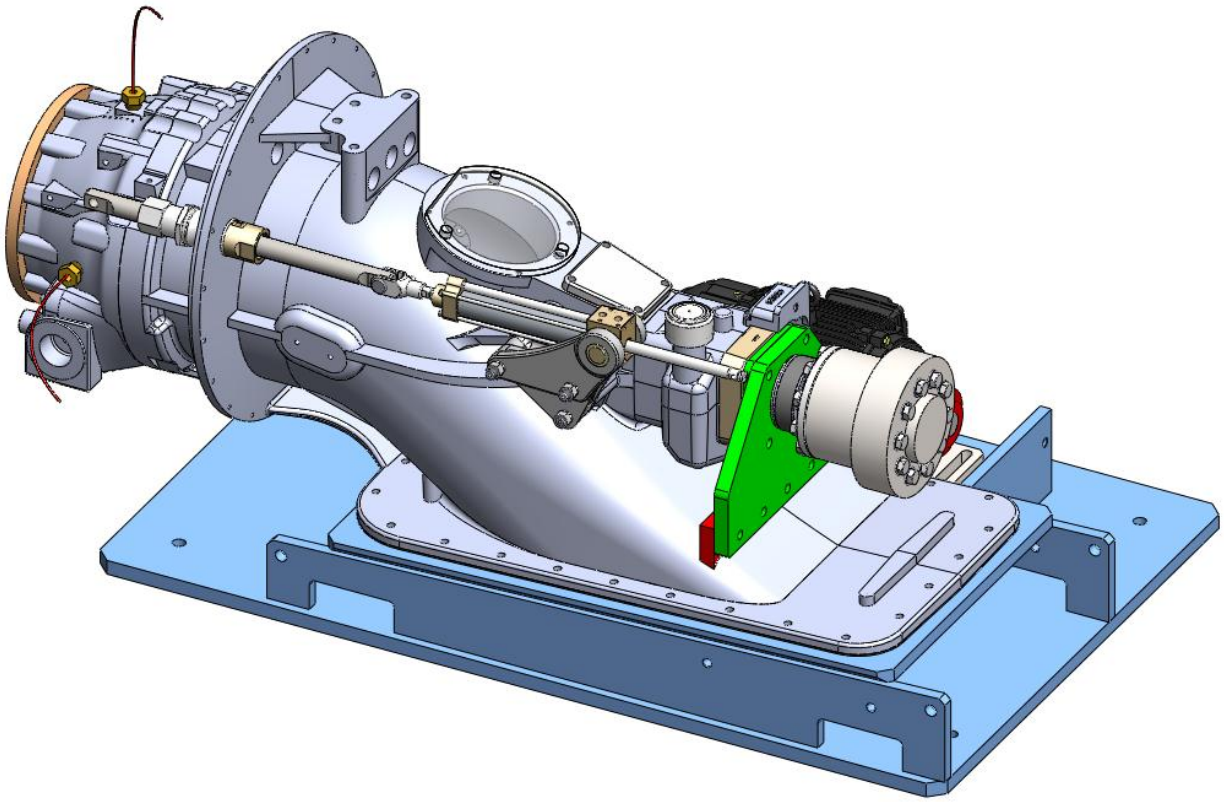

Figure 7.3 - Final Design of Housing Stiffener Plate Attached to the Test Rig.
The steel plate and spacer are shown in green; the aluminium boss in red.

7.3 ANALYTICAL AND NUMERICAL MODELLING

The numerical modelling work carried out in Section 3 determined that the most appropriate means of approximating the thrust bearing was with a point support on the mainshaft at the virtual centre of the bearing. It was also determined that the support stiffness at this location had little to no effect on critical speeds. Therefore a support of infinite rigidity was selected for modelling purposes.

However, in practice, it was considered possible that the thrust bearing may not behave ideally. With the addition of friction and misalignment, the virtual centre of the bearing could have been closer to the plane of the rollers. If this were the case, the support stiffness would reduce; as would the effective overhang of the driveline mass.

With the same methodology used in Section 3, a numerical deflection analysis of the stiffened thrust bearing housing was carried out. A polar plot of the deflection results (under unit load) is provided in Figure 7.4 (A). The deflection results from the unmodified intake are provided in Figure 7.4 (B) for comparison purposes.

With reference to these figures, it is evident that the stiffness properties at the thrust bearing housing changed significantly. The location of maximum deflection occurred at approximately 45 degrees either side of vertical plane whereas the location of minimum deflection occurred in the vertical plane. The effects of the stiffener plate on the support stiffness at the tailpipe were assumed negligible.

A summary of these mesh independent results and their corresponding extracted stiffness values are provided in Table 7.1. As stated earlier, the stiffness values derived from this analysis should be very accurate. This is because nodal deflections are the primary output of a finite element numerical solution. Therefore, once mesh independence was achieved, no

experimental validation of the stiffness values was considered necessary. However, this does rely on accurate geometry modelling which can be an issue with cast parts.

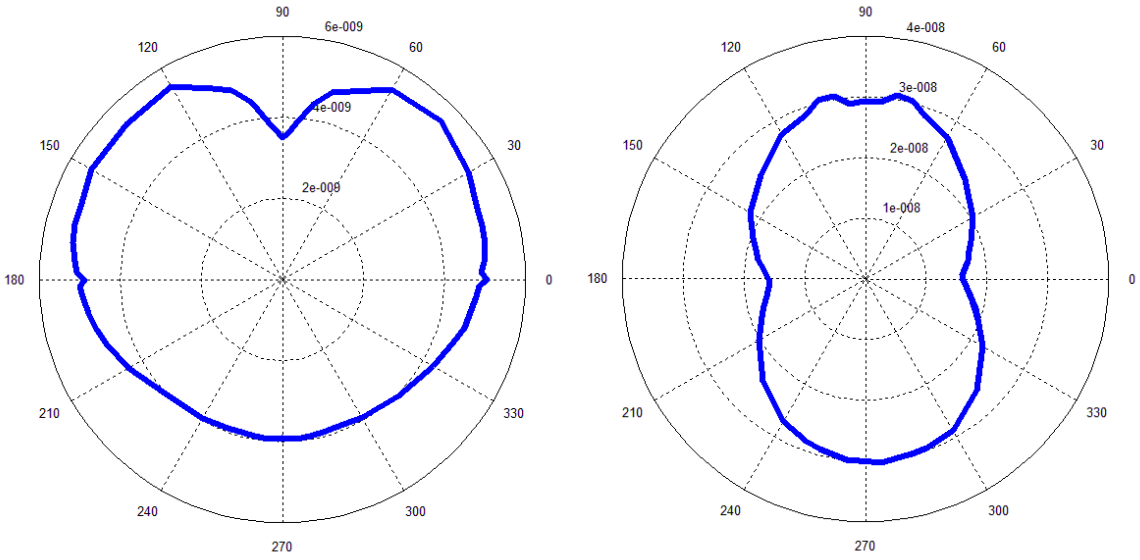

Figure 7.4 – Stiffened Housing Polar Deflection Plots
(A) Polar Deflection Plot of the Stiffened Thrust Bearing Housing;
(B) Polar Deflection Plot of the Non-Stiffened Thrust Bearing Housing

Table 7.1 –Deflection Testing of the Stiffened Thrust Bearing Housing Results

Maximum Deflection (angle)	5.54×10^{-9} m/N (± 45°)
Minimum Deflection (angle)	3.51×10^{-9} m/N (0 , 180°)
Maximum Stiffness (angle)	2.85×10^{8} N/m (0 , 180°)
Minimum Stiffness (angle)	1.80×10^{8} N/m (± 45°)
Increase in Minimum Stiffness	4.5 times
Increase in Maximum Stiffness	3.5 times

With the uncertainties outlined at the start of this section, the critical speeds of the HJ364 test rig were evaluated using two limiting cases. These included:

- Case 1: a rigid support at the effective centre of the thrust bearing (therefore resulting in no change from the standard configuration); and
- Case 2: a flexible support in the plane of the thrust bearing rollers (therefore resulting in an increase in stiffness of 3.5 times to 4.5 times).

As a flexible Timoshenko-Beam support was not achievable for Case 2, a rigid support was used instead. The results of these analyses are presented in Table 7.2 and Table 7.3. The aim of these limiting cases was to compare the predicted changes in critical speeds with those measured and determine how to model the experimental system most appropriately. This is discussed in Section 7.5.

Table 7.2 – Modelled Critical Speed Data of the Alternative Thrust Bearing Housing
(Limiting Case 1: Rigid Support at Thrust Bearing Centre)

Method	**Evaluated Critical Speed**	**Change in Critical Speed**
Timoshenko-Beam	3072 RPM	0 RPM
Myklestad-Prohl TMM	2922 and 2954 RPM	0 RPM
Isolated-Mainshaft FEM	2809 and 2951 RPM	0 RPM

Table 7.3 – Modelled Critical Speed Data of the Alternative Thrust Bearing Housing
(Limiting Case 2: Flexible Support in the Plane of the Thrust Roller Bearing)

Method	**Evaluated Critical Speed**	**Change in Critical Speed**
Timoshenko-Beam	3680 RPM	0 RPM
Myklestad-Prohl TMM	3427 and 3463 RPM	+232 and +109 RPM
Isolated-Mainshaft FEM	3241 and 3445 RPM	+162 and +141 RPM

7.4 TEST RESULTS

The peak deflections of the driveline mass (obtained with the stiffened thrust bearing housing) are provided in Figure 7.5. A steady increase in displacement up to 3000 RPM can be observed and, as before, was attributed to unbalance. The maximum displacement can be observed at 3800 RPM. In Figure 7.6, Figure 7.7 and Figure 7.8 the peak displacement and acceleration plots (as described in Section 4) were compared with the original test results. Overall a significant shift in the measured critical speed can be observed.

In Figure 7.6, the response of the stiffened housing below 3100 RPM was very similar to the original test. Above this speed, the 'shape' of the stiffened housing response remained similar although the critical speed occurred approximately 350 RPM higher. The peak magnitude of the response was very similar to the original test. This was attributed to the higher level of residual unbalance present in the system (observable at 1000 RPM).

In Figure 7.7 and Figure 7.8, a significant reduction in the peak acceleration at the thrust bearing housing is evident. The response in the vertical plane was significantly reduced across all rotational speeds; the change in the horizontal response was not as large. This agreed well with the predicted changes in stiffness in these two orientations (see Section 7.3). In Table 7.4, a summary of the results from the critical speed testing is provided.

Table 7.4 - Critical Speed Data from the Thrust Bearing Housing Stiffness Modifications

Performance Metric	**Peak Coupling Response**	**Peak Vertical Acceleration**	**Peak Horizontal Acceleration**
Measured Critical	3800 RPM	3640 RPM	3880 RPM
Increase	380 RPM	260 RPM	280 RPM
	10 %	7.1%	7.2%

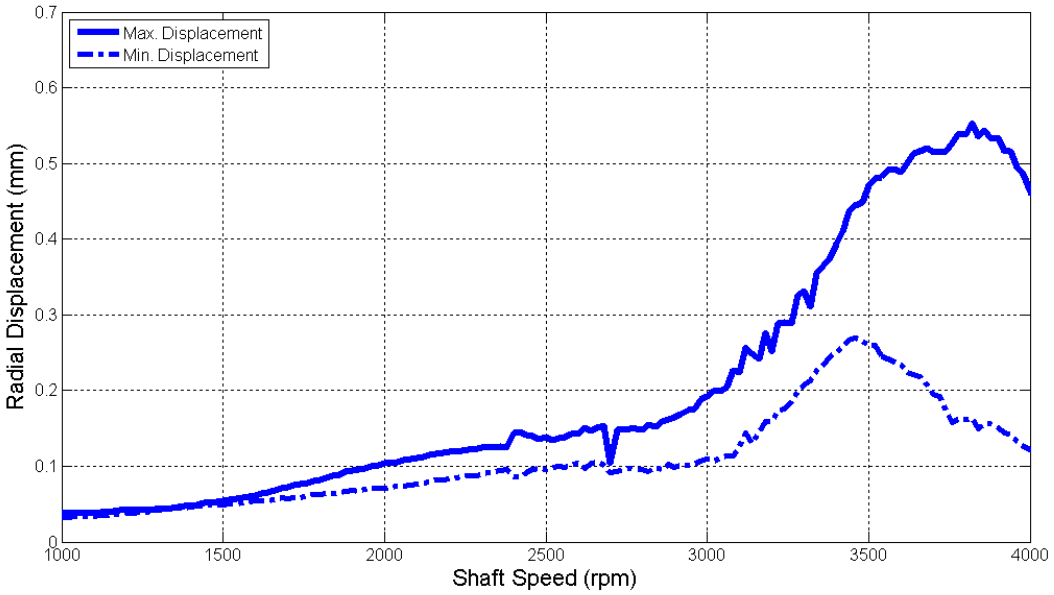

Figure 7.5 - Maximum and Minimum Radial Displacement at the Driveline Mass
(Alternative Thrust Stiffness Configuration, 1000 to 4000 RPM, 20 RPM sampling)

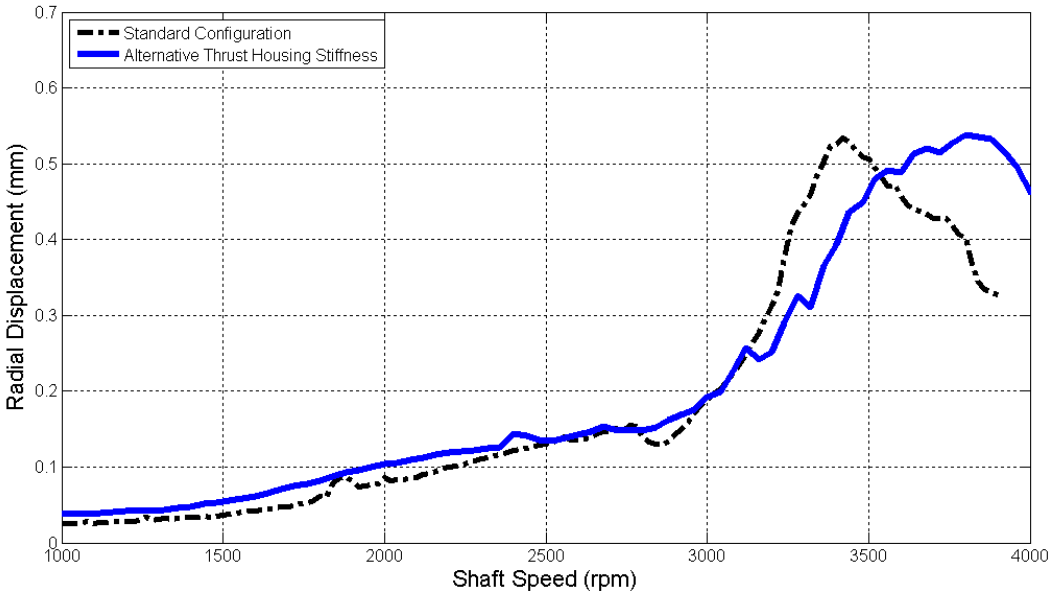

Figure 7.6 - Comparisons of Maximum Radial Displacement at the Driveline Mass
(Alternative Thrust Stiffness Configuration, 1000 to 4000 RPM, 20 RPM sampling)

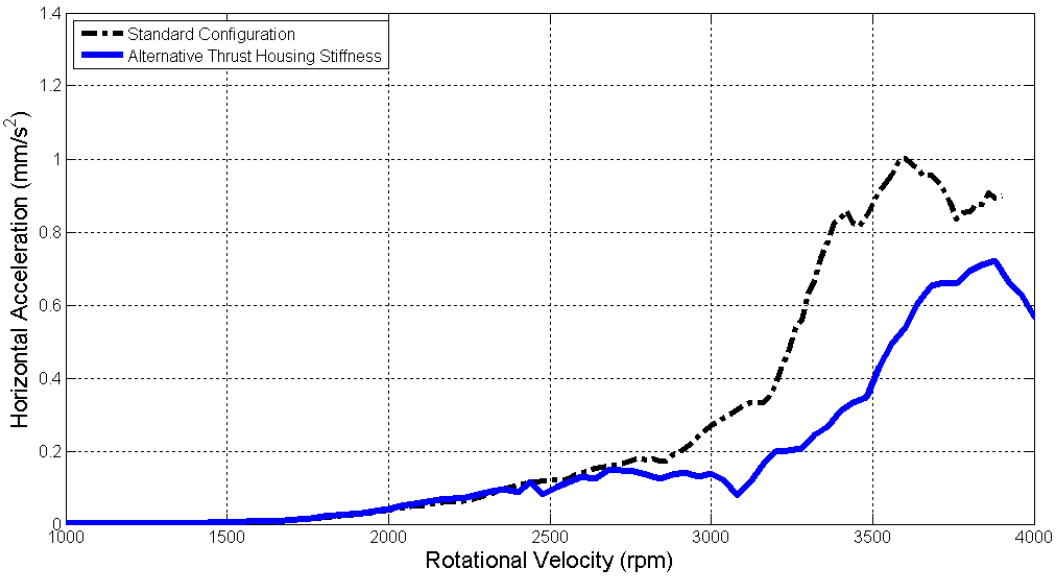

Figure 7.7 - Response from the Horizontally Aligned Accelerometer along the Synchronous Excitation Peak (Alternative Thrust Stiffness Configuration, 1000 to 4000 RPM, 20 RPM sampling)

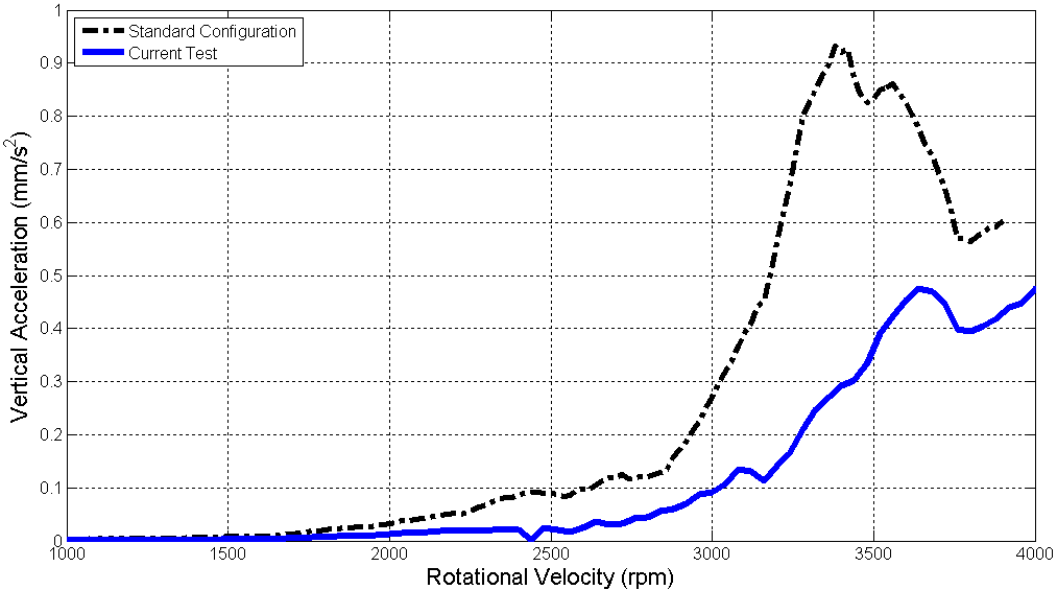

Figure 7.8 - Response from the Vertically Aligned Accelerometer along the Synchronous Excitation Peak (Alternative Thrust Stiffness Configuration, 1000 to 4000 RPM, 20 RPM sampling)

7.5 DISCUSSION

In Table 7.5 and Table 7.6, the experimental results from the alternative thrust bearing housing geometry are compared to 'Limiting Case 1' and 'Limiting Case 2' respectively. Observation of Table 7.5 shows that the assumption of a rigid support at the centre of the thrust bearing is not suitable for predicting critical speeds; the model 'under-predicted' the first critical speed and change in critical speed. The flexible support in the plane of the roller bearing was expected to put an upper limit on the measured critical speed. However, observation of Table 7.6 shows that this was not the case. Again, the model 'under-predicted' the first critical speed and change in critical speed.

To assess the validity of these findings, the test was run with the alternative mass designs described in Section 6. The results of the critical speed testing are provided in Table 7.5. For all three mass configurations, a large increase in critical speed was observed from the standard configuration.

As the analytical and numerical models were well validated in Section 2 and Section 3, this disparity in results indicated that some strongly influential characteristic(s) of the test rig was/were not being taken into account. Possibilities included:

- incorrect stiffness assumptions;
- damping and stiffening effects from the marine bearing;
- rubbing against the spring carrier; and/or
- spherical thrust bearing misalignment issues due to insufficient pre-load;

Re-calculation with an infinitely rigid support at the thrust bearing plane was performed though this still did not provide an upper bound on the measured critical speeds. This indicated that the stiffness assumptions were not the reason for this deviation. The marine and spherical thrust bearings are investigated in Section 10 and Section 11 respectively.

Table 7.5 – Modelled Critical Speed Data with the Alternative Housing Stiffness
(Limiting Case 1: Rigid Support at Thrust Bearing Centre)

Method	**Evaluated Critical Speed**	**Change in Critical Speed**
Experimental	3800 ± 60 RPM	+380 ± 120 RPM
Timoshenko-Beam	3072 RPM	0 RPM
Myklestad-Prohl TMM	2922 and 2954 RPM	0 RPM
Isolated-Mainshaft FEM	2809 and 2951 RPM	0 RPM

Table 7.6 – Modelled Critical Speed Data with the Alternative Housing Stiffness
(Limiting Case 2: Flexible Support in the Plane of the Thrust Roller Bearing)

Method	**Evaluated Critical Speed**	**Change in Critical Speed**
Experimental	3800 ± 60 RPM	+380 ± 120 RPM
Timoshenko-Beam	3680 RPM	0 RPM
Myklestad-Prohl TMM	3427 and 3463 RPM	+232 and +109 RPM
Isolated-Mainshaft FEM	3241 and 3445 RPM	+162 and +141 RPM

Table 7.7 – Comparisons with Alternative Driveline Configurations

Method	**Critical Speed** (Standard Thrust Bearing Housing)	**Critical Speed** (Stiffened Thrust Bearing Housing)	**Deviation**
Standard Mass Configuration	3420 ± 60 RPM	3800 ± 60 RPM	+380 ± 120 RPM
Alt. Mass Configuration	3580 ± 60 RPM	4000 ± 60 RPM	+420 ± 120 RPM
Alt. Overhang Configuration	3760 ± 60 RPM	4280 ± 60 RPM	+520 ± 120 RPM

7.6 SECTION SUMMARY

The effect of increasing the thrust bearing housing stiffness on critical speeds was tested. With a 4.5 times increase in minimum stiffness, a 380 RPM increase in critical speed was observed. This was significantly higher than predicted by the numerical and analytical models and indicated that some key characteristic(s) of the test rig was/were not being modelled.

A relatively simple modification to the intake led to a significant increase in the first critical speed. While the reasons for this are not entirely understood at this stage, the information should prove useful for future water jet assembly designs. Further investigations into the causes are carried out in Section 10 and Section 11.

8

IMPELLER MASS EFFECTS

8.1 INTRODUCTION

In this section, the mass effects of the impeller on critical speeds are evaluated. In Section 2, it was determined that the mass of the impeller should have a negligible effect on critical speeds. This was largely due to the close proximity of the impeller to the marine bearing. To test this prediction, an additional mass was fabricated and bolted to the back of the original impeller mass. Critical speeds were measured and comparisons were made to the predicted values.

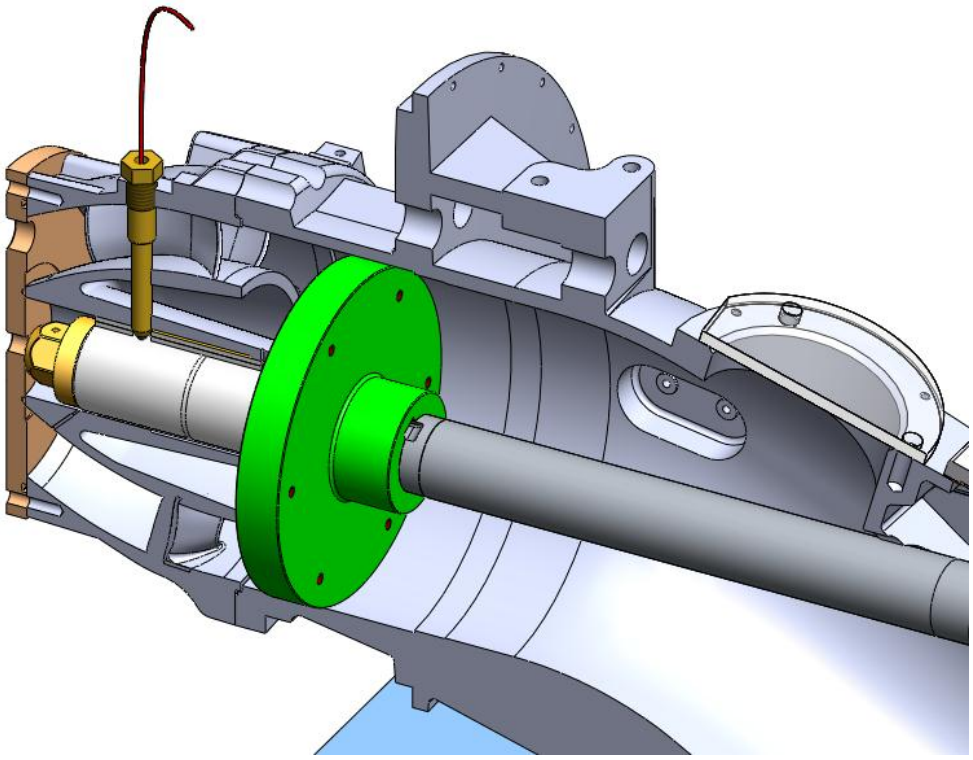

Figure 8.1 – Section View of the HJ364Test Rig showing the Impeller Mass
(Impeller Mass Highlighted in Green)

8.2 CRITICAL SPEED MODELLING

The results from the Dunkerley analysis in Section 2 indicated that the impeller mass should have very little effect on critical speed. This compared well to the predictions obtained from the Timoshenko-Beam method shown in Figure 8.2. Observation of this figure shows how little effect the impeller mass should have on critical speeds; a 60kg impeller would lead to a reduction in critical speed of only 100 RPM.

It should be noted that the Timoshenko-Beam method does not take into account inertial terms. Since inertia of the impeller mass would increase with an increase in mass, so too would the degree of gyroscopic ‘stiffening’ present. However, this ‘stiffening’ was predicted to be relatively small due to the relatively low running speeds of the mainshaft.

8.3 ALTERNATIVE IMPELLER MASS DESIGN

8.3.1 Impeller Mass Selection

A significant change in impeller mass was required to validate the modeling predictions. However, a reduction in impeller mass would have led to further instability within the marine bearing and reduced the energy in the system. This would have made it much harder to experimentally determine critical speeds.

Therefore, an alternative mass of 42.0 kg was deemed satisfactory to obtain a measurable shift in results. The close proximity to the heavily damped marine bearing meant that the stability of the system should not be affected despite this mass increase. In Figure 8.3, the first critical speeds of the 42kg mass and the 21.5kg mass are compared (evaluated by the Timoshenko-Beam method).

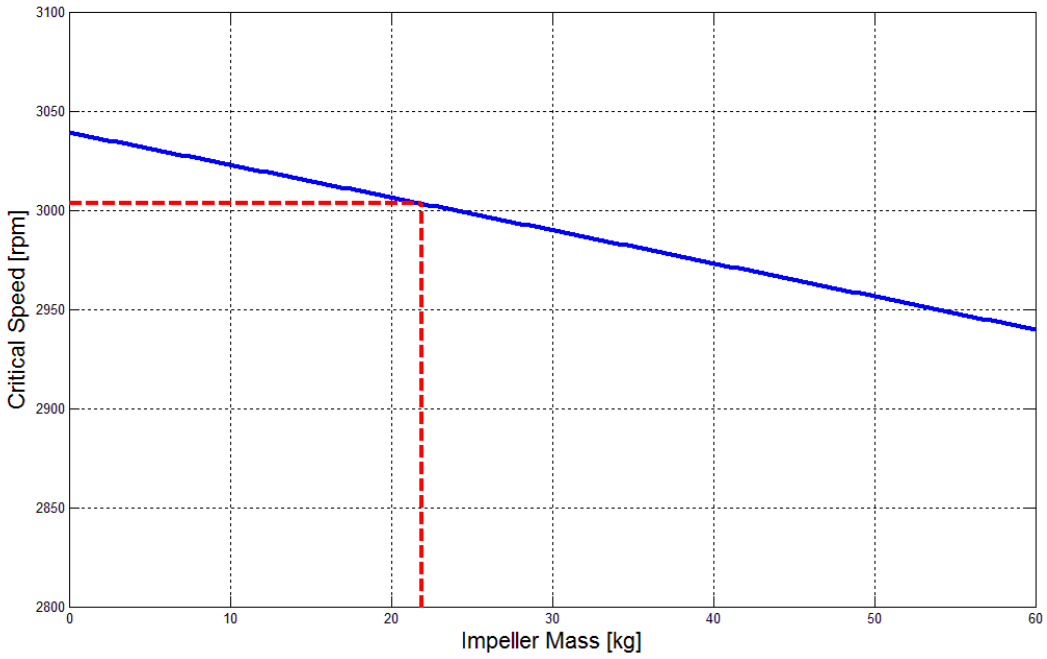

Figure 8.2 - Effect of Impeller Mass on Critical Speeds Evaluated by the Timoshenko-Beam Method
Dashed Red Line: 21.5kg impeller, 3003 RPM (standard configuration)

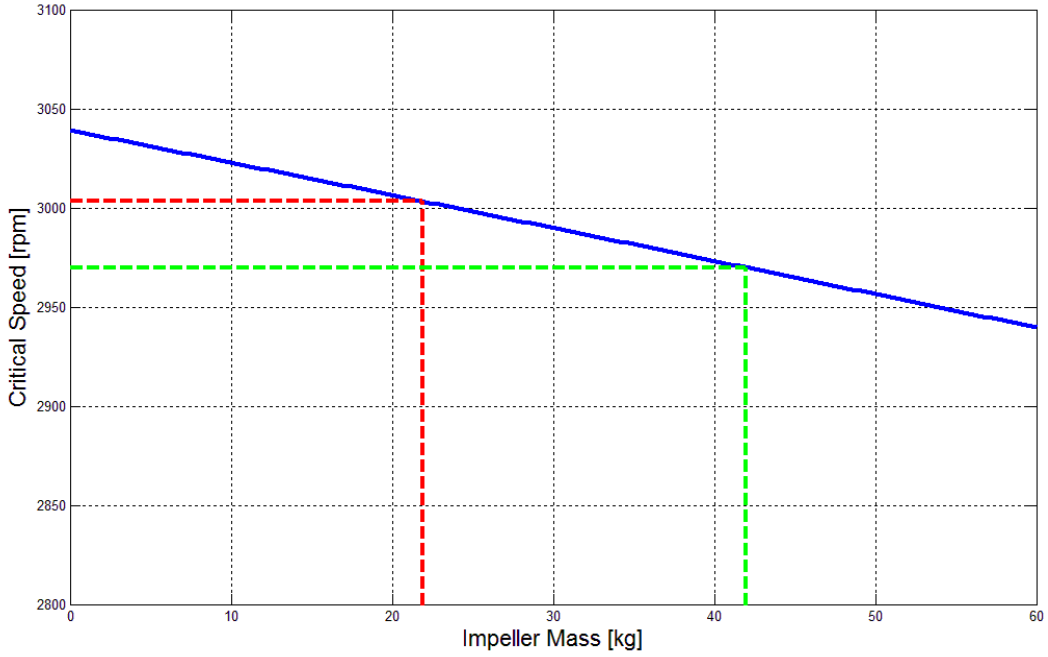

Figure 8.3 - Effect of the Impeller Mass on Critical Speeds as evaluated by the Timoshenko-Beam Method
Dashed Green Line: 42.0kg impeller, 2970 RPM (increased mass configuration)

8.3.2 Impeller Mass Design

In Table 6.1 and Table 6.2, a summary of the alternative impeller mass properties is given. In Figure 8.4, a cross-section of the HJ364 water jet assembly with the additional impeller mass is shown. A detailed drawing of the alternative mass is provided in Appendix A4.

Table 8.1 – Mass Properties of the Alternative Impeller Mass

Property	Value	Change
Mass	42.0 kg	+ 19.7 kg
COM from Water Bearing	254 mm	+ 10 mm
Rotational Inertia	0.54 kgm2	+ 0.27 kgm2
Diametral Inertia	0.29 kgm2	+ 0.15 kgm2

Table 8.2 – Critical Speed Properties of the Alternative Impeller Mass

Method	Predicted Critical Speed	Change in Critical Speed
Timoshenko-Beam	2970 RPM	-33 RPM
Myklestad-Prohl TMM	2829 RPM	-93 RPM
Isolated-Mainshaft FEM	2735 and 2869 RPM	-74 and -82 RPM

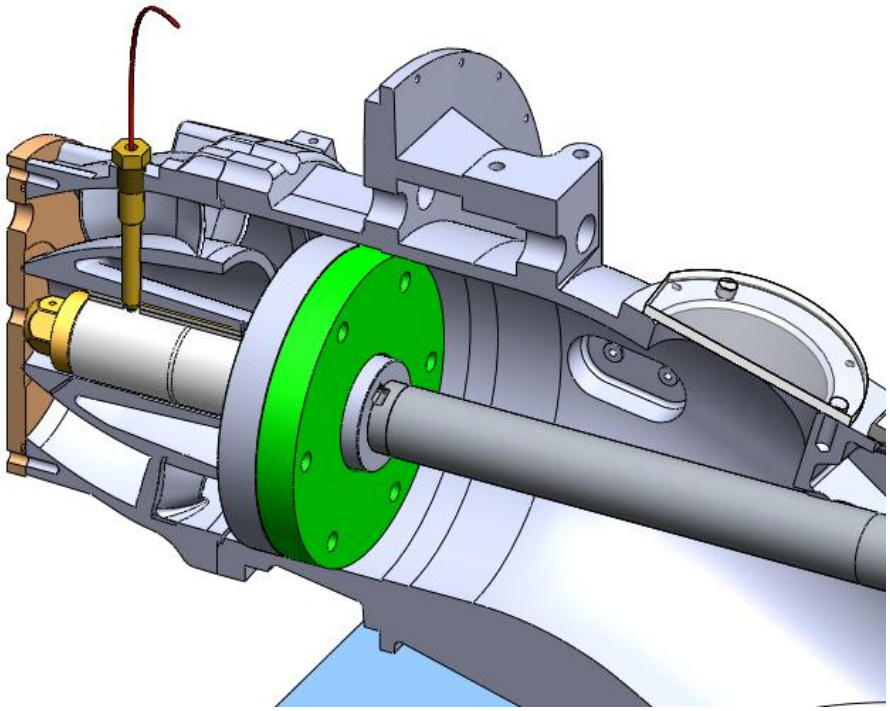

Figure 8.4 - Final Design of the Additional Impeller Mass Attached to the Test Rig (shown in green)

8.4 TEST RESULTS

With the alternative mass assembly shown in Figure 8.4, critical speed testing was carried out in accordance with the methodology described in Section 4. The displacement results at the driveline mass are provided in Figure 6.8.

It appears that the test rig was behaving in a relatively ideal manner; minimal deflection below 2700 RPM and the strongly evident critical speed at 3420 RPM. This critical speed

was highly ‘planar’. Despite the large response, no separation of the first two critical speeds was apparent. Once again, some degree of misalignment was present in the system (observable at 1000 RPM). Finally, some fluctuation in the response could be observed between 2200 and 3000 RPM although the magnitude of the fluctuation was relatively small.

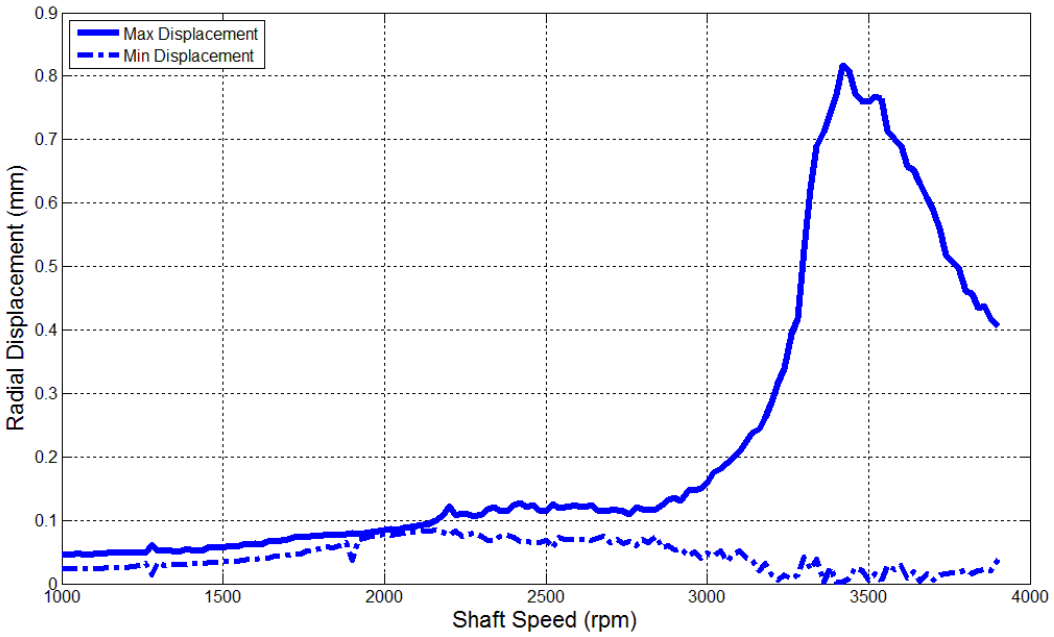

Figure 8.5 – Peak Radial Displacements of the Alternative Driveline Mass
(42.0kg Impeller, 1000 to 3900 RPM, 20 RPM sampling)

Graphical comparisons of the displacement and accelerometer responses for each impeller mass are provided in Figure 8.6, Figure 8.7 and Figure 8.8. Observation of Figure 8.6 indicates that the driveline mass response for the two impellers was very similar below 2500 RPM. The original peak at 2750 RPM did not occur in the alternative configuration. However, the magnitude of the displacement at the first critical speed was much greater.

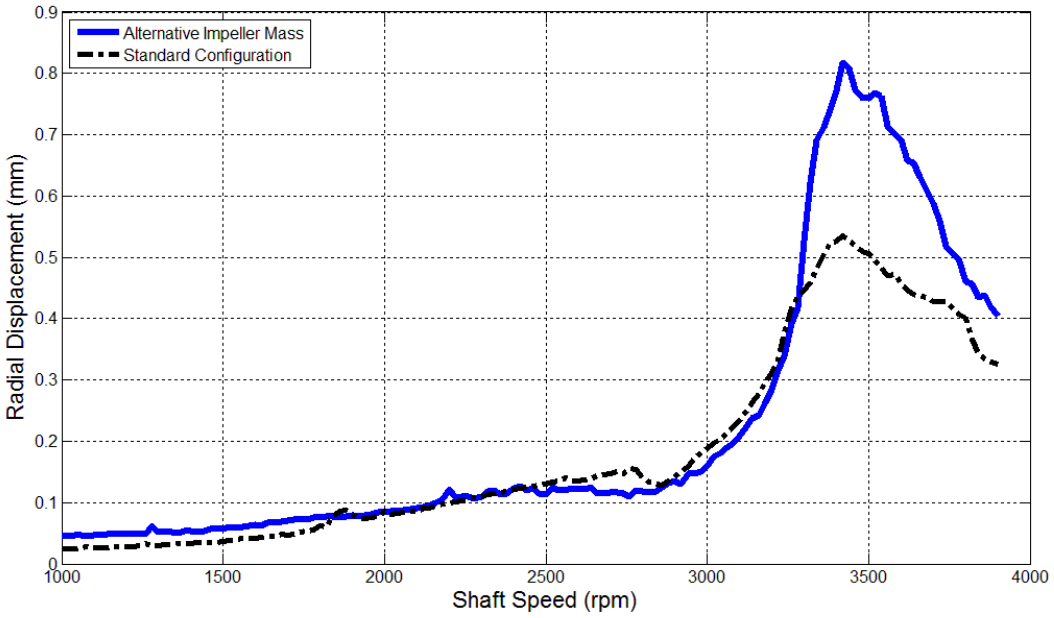

Figure 8.6 –Comparisons of Maximum Radial Displacement at the Driveline Mass
(42.0kg Impeller Mass, 1000 to 3900 RPM, 20 RPM sampling)

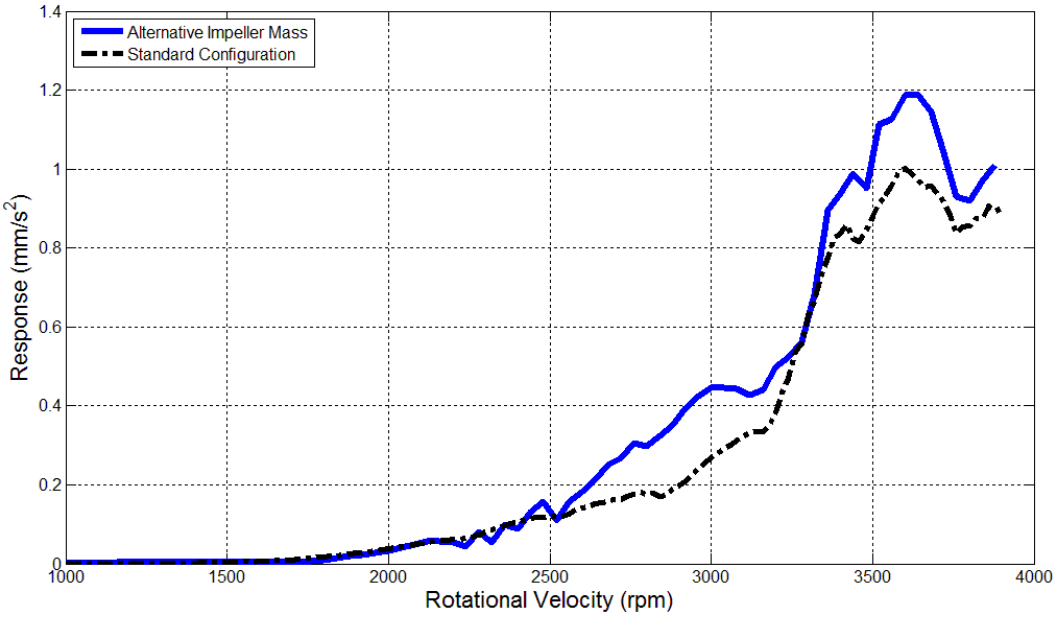

Figure 8.7 –Max Horizontal Acceleration Comparisons at the Thrust Bearing Housing
(42.0kg Impeller Mass, 1000 to 3900 RPM, 20 RPM sampling)

The acceleration response at the thrust bearing housing also changed with the alternative impeller mass (see Figure 8.7 and Figure 8.8). However the 'shape' of the response was conserved. While the horizontal acceleration response increased with the alternative mass, the vertical response actually reduced. Despite the change in displacement and acceleration response magnitudes, the value of the critical speed remained unchanged.

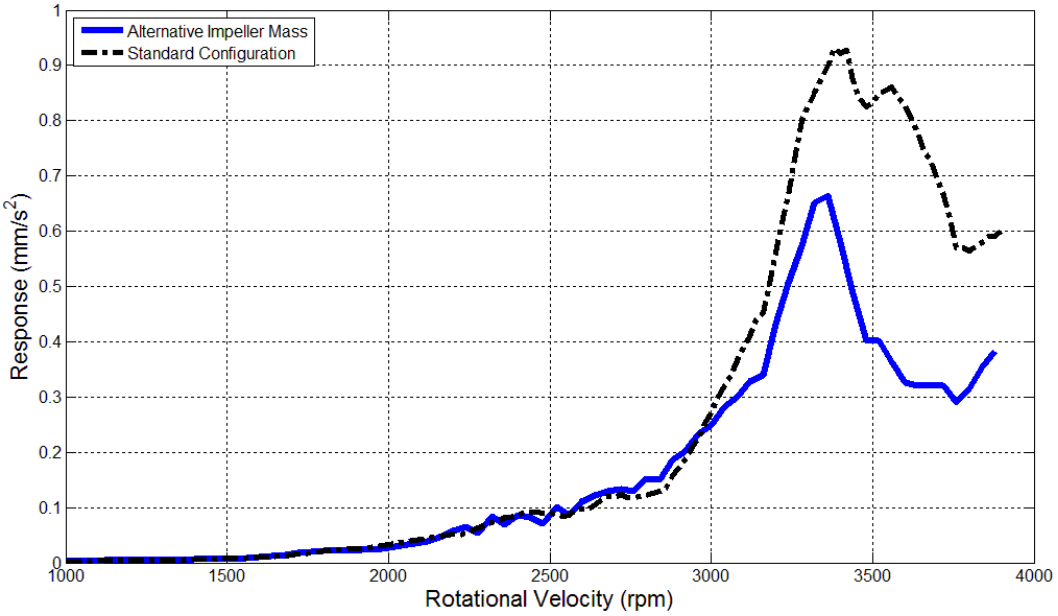

Figure 8.8 – Max Vertical Acceleration Comparisons at the Thrust Bearing Housing
(42.0kg Impeller Mass, 1000 to 3900 RPM, 20 RPM sampling)

8.5 COMPARISONS AND DISCUSSION

A comparison of the predicted and measured critical speeds is provided in Table 8.3. Once again, the peak displacement response of the driveline mass was considered to be the most accurate means of evaluating critical speeds. As observed in the previous sections, the measured critical speeds were significantly higher than those predicted (the reasons for this

deviation were discussed in Section 5). Interestingly, the predicted and measured changes in critical speed were very similar.

Table 8.3 – Critical Speed Properties of the Alternative Impeller Mass

Method	Predicted Critical Speed	Change in Critical Speed
Experimental	3420 ± 60 RPM	0 ± 120 RPM
Timoshenko-Beam	2970 RPM	-33 RPM
Myklestad-Prohl TMM	2829 RPM	-93 RPM
Isolated-Mainshaft FEM	2735 and 2869 RPM	-74 and -82 RPM

This similarity indicates that the models accurately took into account the effects of the impeller mass on critical speeds. This was somewhat surprising due to the close proximity of the impeller mass to the marine bearing; it was expected that the increased radial load (effectively double) at the marine bearing would lead to a significant change in bearing performance. However, this was not the case and indicates that the stiffness characteristics of the marine bearing were relatively insensitive to the degree of radial load.

The magnitude of the displacement response is controlled purely by damping at a critical speed (Weisstein, 2012). However, Figure 6.9 indicates that the displacement response at the driveline mass was greater with the larger impeller mass. This indicates that the larger impeller gave rise to a reduced level of system damping; possibly a behavior of the marine bearing. During operation of a real HJ364 water jet assembly, it is expected that the much higher degree of system damping present would significantly reduce the magnitude of this response trend.

While the increase in response at the driveline mass should have given rise to increased accelerometer response, this was not the case for the vertically aligned accelerometer (see Figure 8.8). Here, a significant reduction in response was observed indicating that the motion

of the mainshaft in the vertical plane was reduced. Due to the close proximity of the impeller mass and the marine bearing, this behavior was again attributed to the marine bearing. The performance of the marine bearing and its effects on the system are considered further in Section 10.

It is possible that the spherical thrust bearing may have played some role in the observed system performance. The larger residual bearing misalignment present in the 42.0kg impeller mass test (see Figure 6.9 at 1000 RPM) could have added to the observed trends. However, the agreement between the predicted and measured changes in critical speeds indicates that the effect of this was relatively small.

8.6 SECTION SUMMARY

A two-fold increase of the impeller mass to 42.0kg led to a very small increase in measured critical speed. Critical speed predictions from the analytical and numerical models matched these observations very well; the small deviations were largely attributed to the characteristics of the marine bearing and are investigated further in Section 10.

The mass of the impeller in the HJ364 water jet assembly had a negligible effect on critical speeds. However, the response did increase with the additional impeller mass. Therefore it would be worth minimising the mass of the impeller to some degree in future water jet assembly designs.

9

TAILPIPE STIFFNESS EFFECTS

9.1 INTRODUCTION

In Section 2 and Section 3, it was determined that the stiffness of the tailpipe would have a negligible effect on critical speeds. This was due to the large separation from the spherical thrust bearing and the driveline mass; considered largely responsible for defining critical speeds of the HJ364 test rig. Stiffness modifications were made to the tailpipe, critical speeds were measured and comparisons were made to the predicted values.

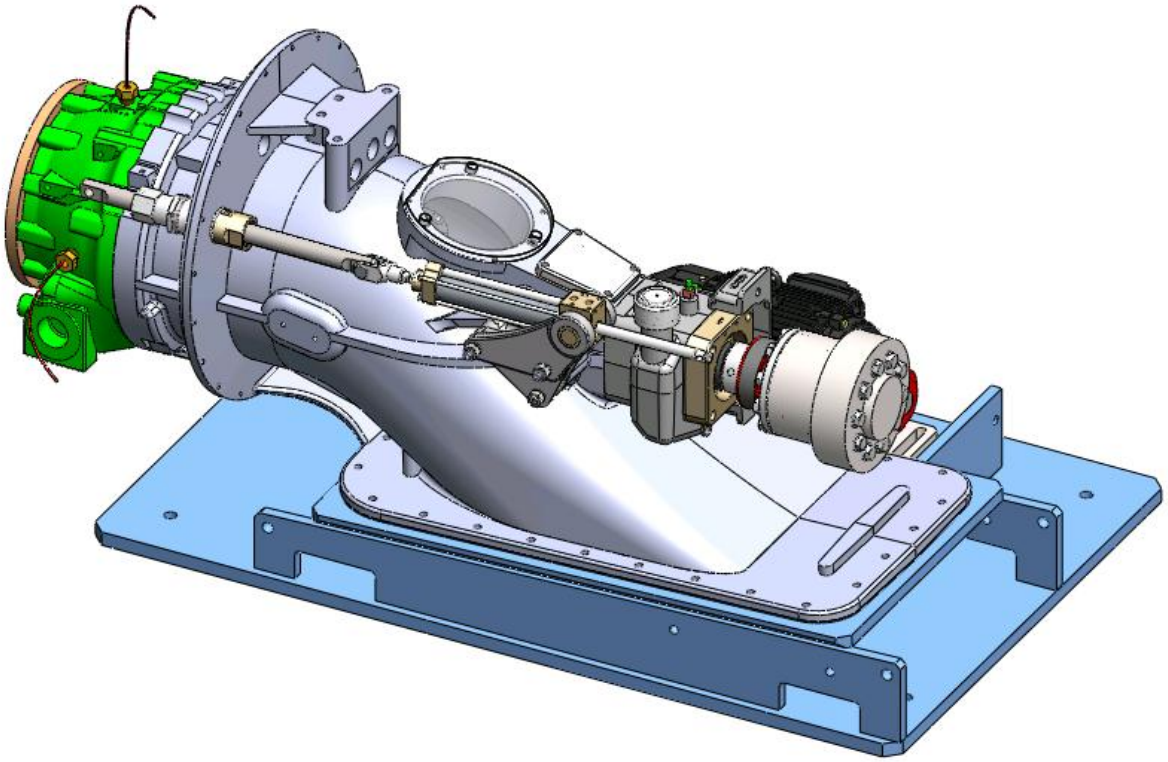

Figure 9.1 – Overview of the HJ364 Test Rig
(Tailpipe Highlighted in Green)

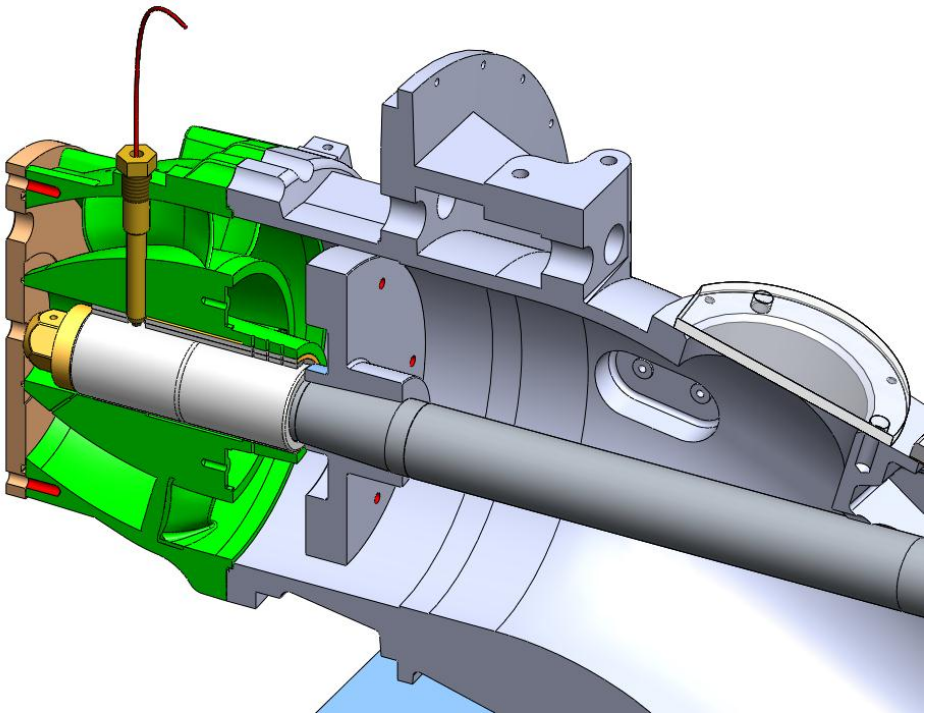

Figure 9.2 – Section View of the HJ364 Test Rig
(Tailpipe Highlighted in Green)

9.2 TAILPIPE STIFFNESS MODIFICATIONS

The results of the analytical work suggested that significant modifications to the tailpipe stiffness would be required to have any measureable effect on critical speeds. Removing all but three of the stator blades from the tailpipe would not have resulted in a significant change in radial stiffness. Hence, the project scope was modified slightly to determine the effect that removal of the internal ribs in the tailpipe would have on performance (see Figure 9.3). This was a test considered more relevant to future designs.

In Figure 9.4, a detailed view of the tailpipe with the internal ribs removed is shown. These were machined from a new HJ364 tailpipe using a 5-axis CNC milling machine. Approximately 5 to 10mm could not be removed from the bottom of each rib due to geometric limitations. In Figure 9.5, a partial section view of the HJ364 test rig with the modified tailpipe geometry is provided.

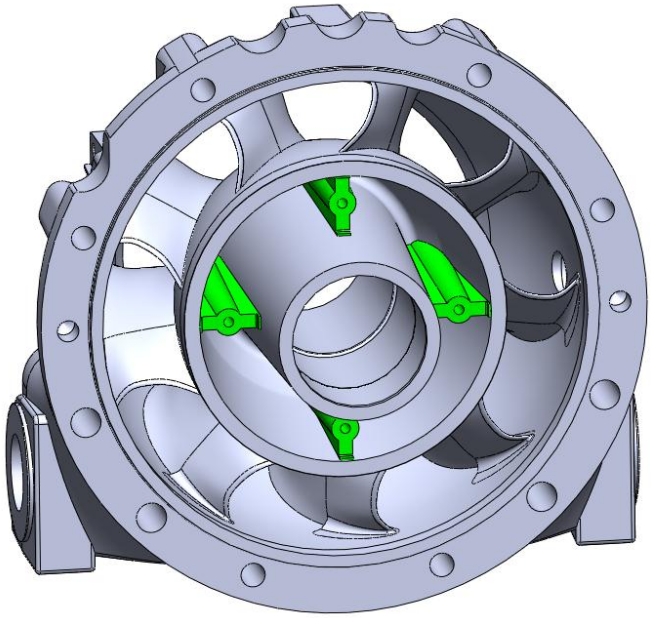

Figure 9.3 - Detailed View of Tailpipe with the Internal Ribs Highlighted

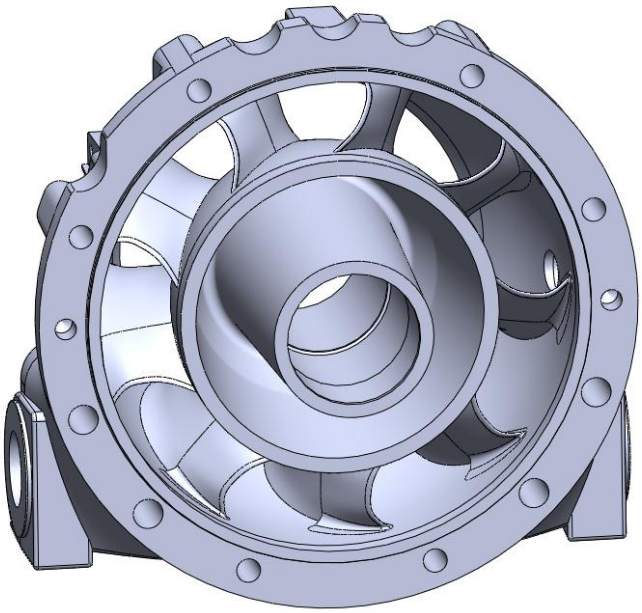

Figure 9.4 - Detailed View of Tailpipe with the Internal Ribs Removed

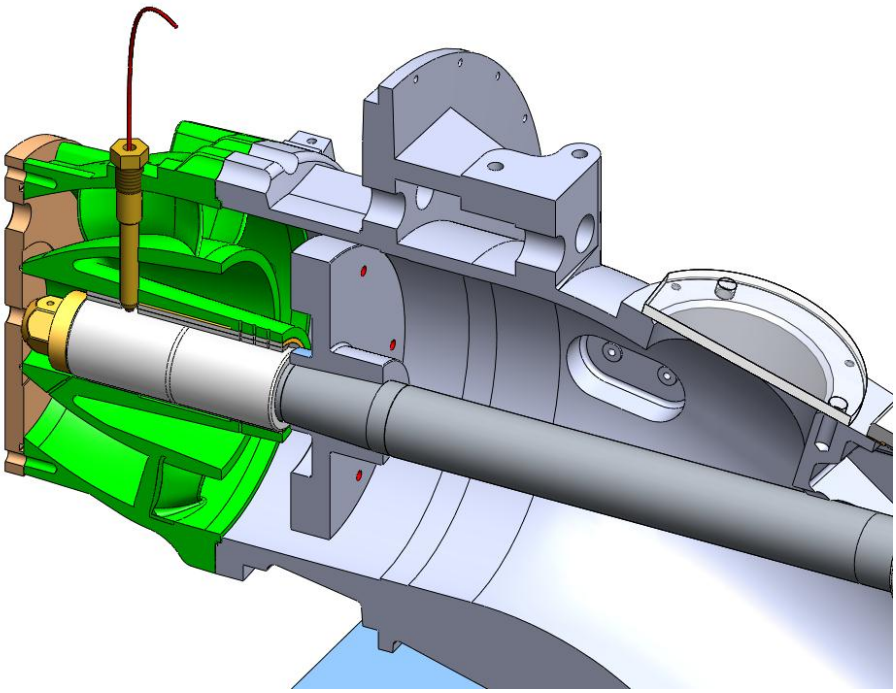

Figure 9.5 – Partial Section View of the HJ364 Test Rig with the New Tailpipe Geometry
(Modified Tailpipe Highlighted in Green)

9.3 ANALYTICAL AND NUMERICAL MODELLING

With the same methodology used in Section 3, a numerical deflection analysis of the modified tailpipe geometry was carried out. A polar plot of the deflection results (under unit load) is provided in Figure 9.6 (A). The deflection results from the unmodified tailpipe are provided in Figure 9.6 (B) for comparison purposes. With reference to these figures, it is evident that the stiffness of the tailpipe reduced quite significantly. However, the maximum and minimum deflections still occurred in the horizontal and vertical planes respectively.

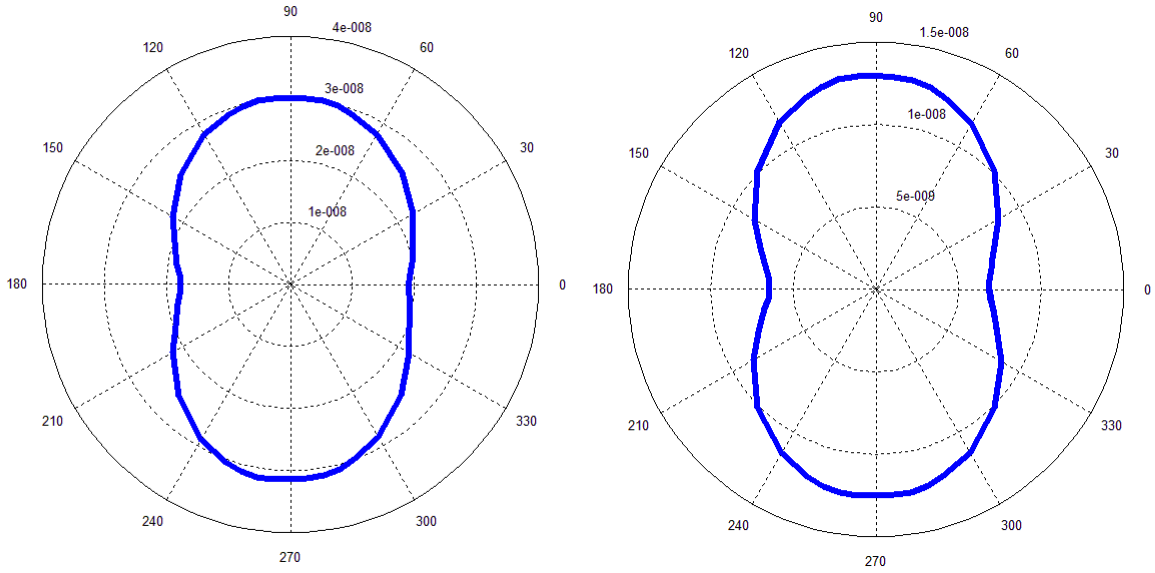

Figure 9.6 – Polar Deflection Plots of the Modified Tailpipe Geometry
(A) Polar Deflection Plot of the Tailpipe with No Internal Ribs;
(B) Polar Deflection Plot of the Standard Tailpipe (with ribs)

A summary of these mesh independent results and their corresponding stiffness values are provided in Table 9.1. In Table 9.2, the stiffness values have been combined with the properties of the rubber marine bearing. Evidently, only a small reduction in tailpipe stiffness could be achieved. As stated earlier, the stiffness values derived from this analysis should be very accurate as nodal deflections are the primary output of a finite element numerical solution. Again, due to this, no experimental validation of these stiffness values was

considered necessary. In Table 9.3, the critical speed predictions from the various analytical and numerical methods are provided. A very small reduction in critical speed was expected due to the small changes in minimum and maximum stiffness and remoteness from the driveline mass.

Table 9.1 –Deflection Testing of the Modified Tailpipe Geometry
(Without Rubber Marine Bearing Properties)

Maximum Deflection **(angle)**	3.16×10^{-8} m/N (± 90 °)
Minimum Deflection **(angle)**	1.77×10^{-8} m/N (0, 180 °)
Maximum Stiffness **(angle)**	5.65×10^{7} N/m (0, 180 °)
Minimum Stiffness **(angle)**	3.17×10^{7} N/m (± 90 °)
Change in Minimum Stiffness	64 % reduction
Change in Maximum Stiffness	59 % reduction

Table 9.2 –Deflection Testing of the Modified Tailpipe Geometry
(With Rubber Marine Bearing Properties)

Maximum Stiffness **(angle)**	1.06×10^{7} N/m (, °)
Minimum Stiffness **(angle)**	9.22×10^{6} N/m (± °)
Change in Minimum Stiffness	18 % reduction
Change in Maximum Stiffness	12 % reduction

Table 9.3 - Modelled Critical Speed Data with the Modified Tailpipe Geometry

Method	Evaluated Critical Speed	Change in Critical Speed
Timoshenko-Beam	3072 RPM	0 RPM
Myklestad-Prohl TMM	2880 and 2927 RPM	-42 and -27 RPM
Isolated-Mainshaft FEM	2779 and 2917 RPM	-31 and -34 RPM

9.4 TEST RESULTS

The peak deflections of the driveline mass (obtained with the modified tailpipe geometry) are provided in Figure 9.7. A ‘steep’ but steady increase in displacement up to 3000 RPM can be observed. This was attributed to the high level of residual misalignment present in the system (observable at 1000 RPM). Two peaks corresponding to the first two critical speeds can be observed at 3180 and 3480 RPM.

In Figure 9.8, the maximum deflection of the driveline mass has been compared to those of the standard configuration. Immediately evident is the significantly larger misalignment present in the modified tailpipe testing. Upon investigation it was found that the spherical thrust bearing was running out of alignment (the mainshaft was re-measured and found to be within straightness tolerance). Unfortunately due to time limitations, this test could not be repeated. Therefore, the conclusions that can be drawn from the test data are somewhat limited.

In Figure 9.9 and Figure 9.10, the first harmonic responses from the vertically and horizontally aligned accelerometers are provided respectively. These have been compared to the results from the standard configuration. For the same reasons outlined above, the conclusions that can be drawn from this data are again limited.

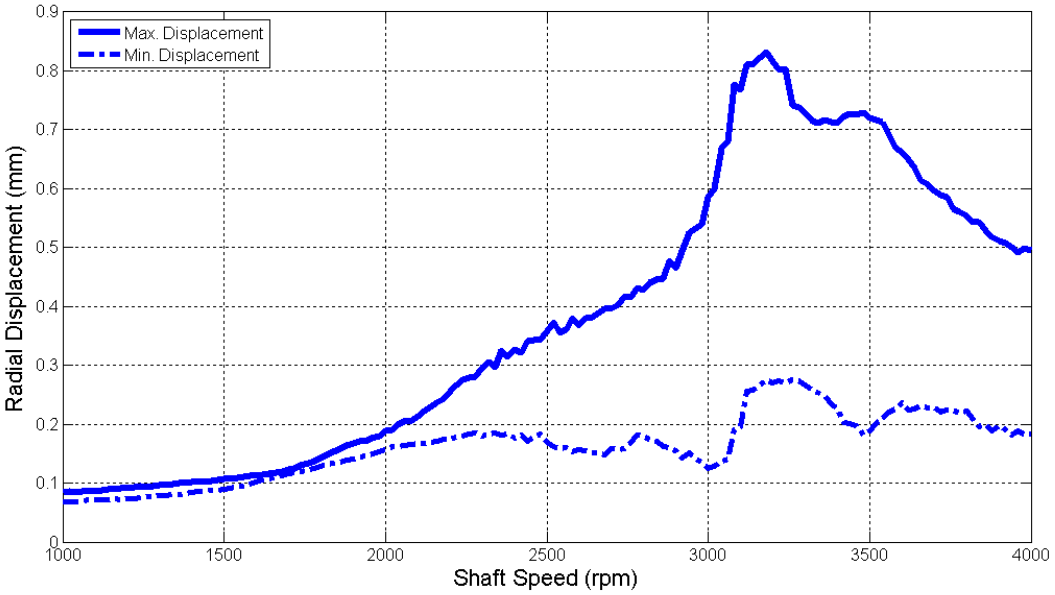

Figure 9.7 - Peak Radial Displacements of the Driveline Mass
(Alternative Tailpipe Geometry, 1000 to 4000 RPM, 20 RPM sampling)

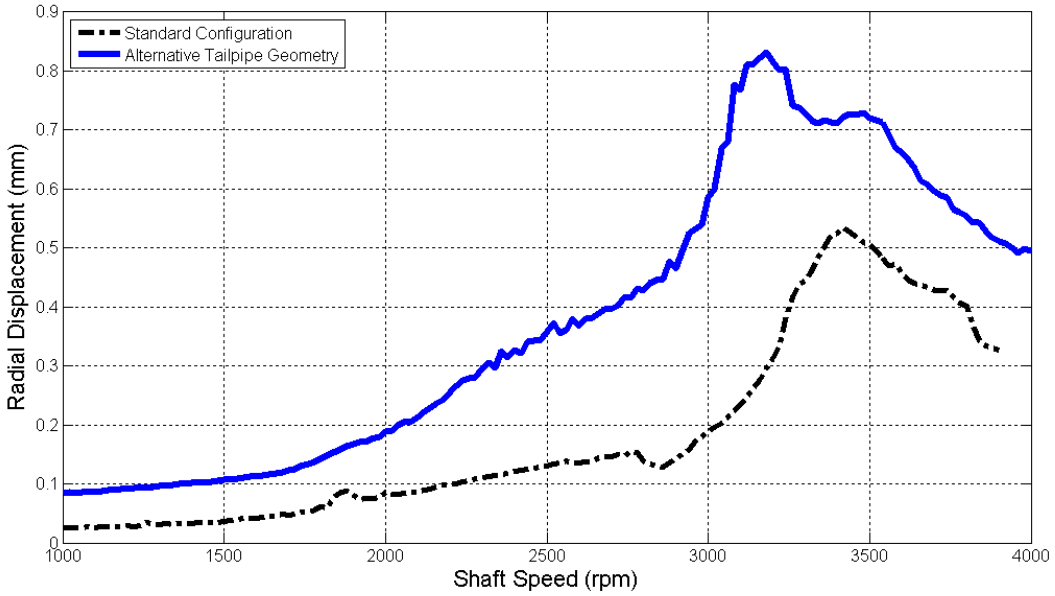

Figure 9.8 - Comparisons of Maximum Radial Displacement at the Driveline Mass
(Alternative Tailpipe Geometry, 1000 to 4000 RPM, 20 RPM sampling)

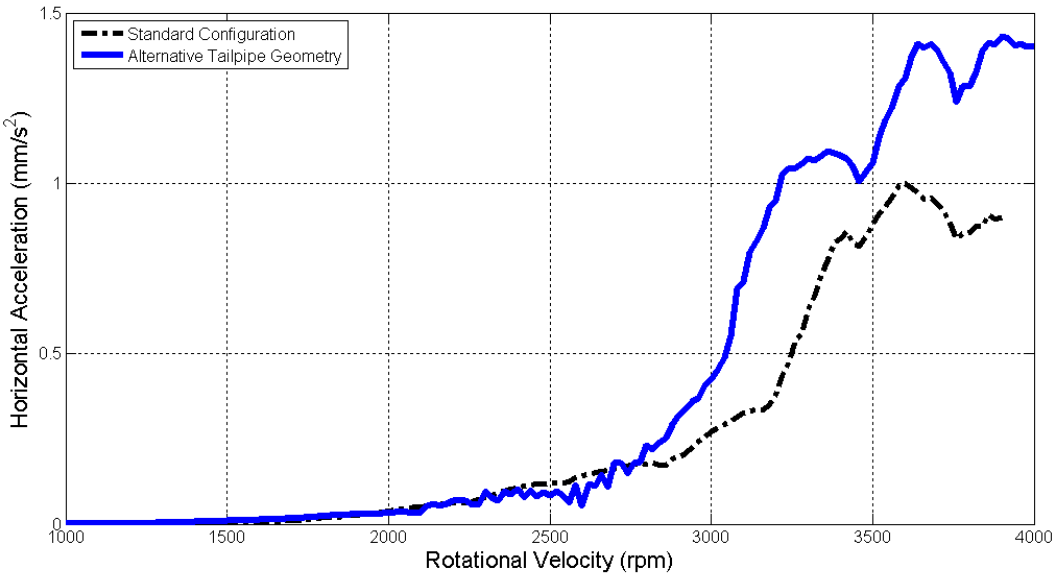

Figure 9.9 - Response from the Horizontally Aligned Accelerometer along the Synchronous Excitation Peak (Alternative Tailpipe Geometry, 1000 to 4000 RPM, 20 RPM sampling)

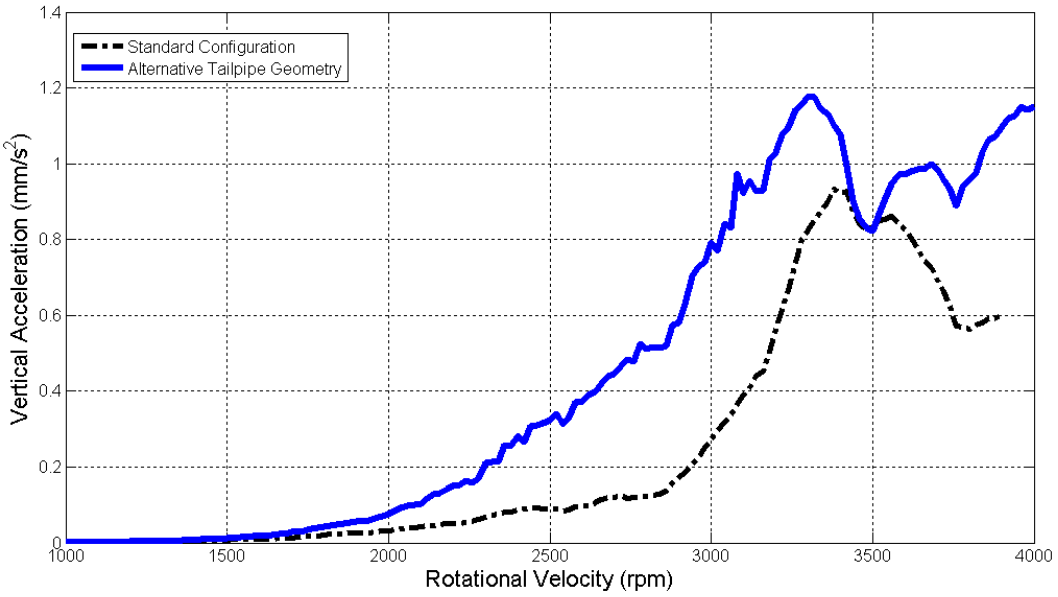

Figure 9.10 - Response from the Vertically Aligned Accelerometer along the Synchronous Excitation Peak (Alternative Tailpipe Geometry, 1000 to 4000 RPM, 20 RPM sampling)

9.5 DISCUSSION

The critical speed data from the modified tailpipe testing was compared to those predicted and is provided in Table 9.4. As stated in Section 9.4, the conclusions that can be drawn from the experimental data are somewhat limited due to the significant misalignment present.

This misalignment gave rise to two critical speeds. These were located slightly above and slightly below the first critical speed of the standard configuration. The separation between these first two measured critical speeds was larger than that predicted by the Myklestad-Prohl TMM and Isolated-Mainshaft FEM methods.

Table 9.4 – Experimental and Modelled Critical Speed Data with the Alternative Tailpipe Geometry

Method	Evaluated Critical Speed	Change in Critical Speed
Experimental	3180 and 3480 RPM ± 60 RPM	-240 and +60 RPM ± 120 RPM
Timoshenko-Beam	3072 RPM	0 RPM
Myklestad-Prohl TMM	2880 and 2927 RPM	-42 and -27 RPM
Isolated-Mainshaft FEM	2779 and 2917 RPM	-31 and -34 RPM

The accelerometer data in Figure 9.9 and Figure 9.10 is probably more reliable and suggests that no obvious shift in the critical speed occurred. A number of ‘turning-points’ can be observed that correspond between the two tests which differ only in magnitude and not rotational velocity.

Overall, these results appeared to indicate that removing the internal ribs from the tailpipe should have no measurable effect on critical speed. This conclusion matches well with the numerical simulations performed and the work carried out in Section 10 (in regards to marine bearing stiffness). For completeness, it is strongly recommended that the test be performed again. This was prevented due to time restrictions.

9.6 SECTION SUMMARY

Stiffness modifications were made to an HJ364 tailpipe to evaluate the effect on critical speeds. Limited conclusions could be drawn from the experimental data due to misalignment issues. Qualitatively however, all three comparison plots show a similar trend. The data 'shape' was conserved between tests indicating that; overall, the critical speeds of the system were largely unmodified. Numerical simulations and the work carried out in Section 9 agreed with this observation. It is strongly recommended that this testing be performed again once alignment of the spherical thrust bearing can be achieved.

For future designs, it is evident that the internal ribs in the tailpipe can be removed. This will have a negligible effect on critical speeds.

10

MARINE BEARING EFFECTS

10.1 INTRODUCTION

To assess the overall support stiffness at the rear end of the HJ364 water jet assembly, it was deemed necessary to determine the stiffness of the marine bearing during operation. Also of interest was the effect that different marine bearings could have on critical speeds. Marine bearings are difficult to model due to their complicated geometry and the low viscosity of the lubricant (water).

With the time constraints imposed, an approach was undertaken in which the performance of two different marine bearings was compared with that of a basic spherical roller support. In this way the damping and stiffness properties of the marine bearings could be ignored. This approach was considered valid due to the remoteness of the marine bearing from the driveline mass; considered largely responsible for dictating critical speeds of the test rig.

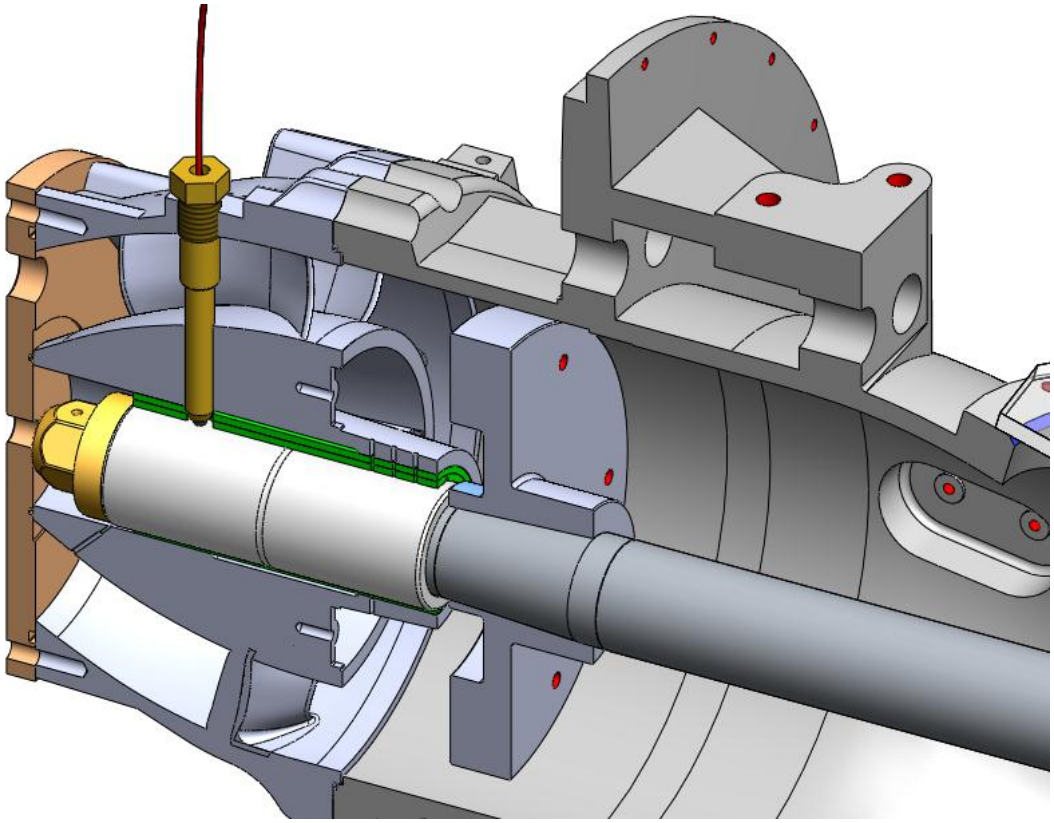

Figure 10.1 – Partial Section View of the HJ364 Test Rig
(Marine Bearing Highlighted in Green)

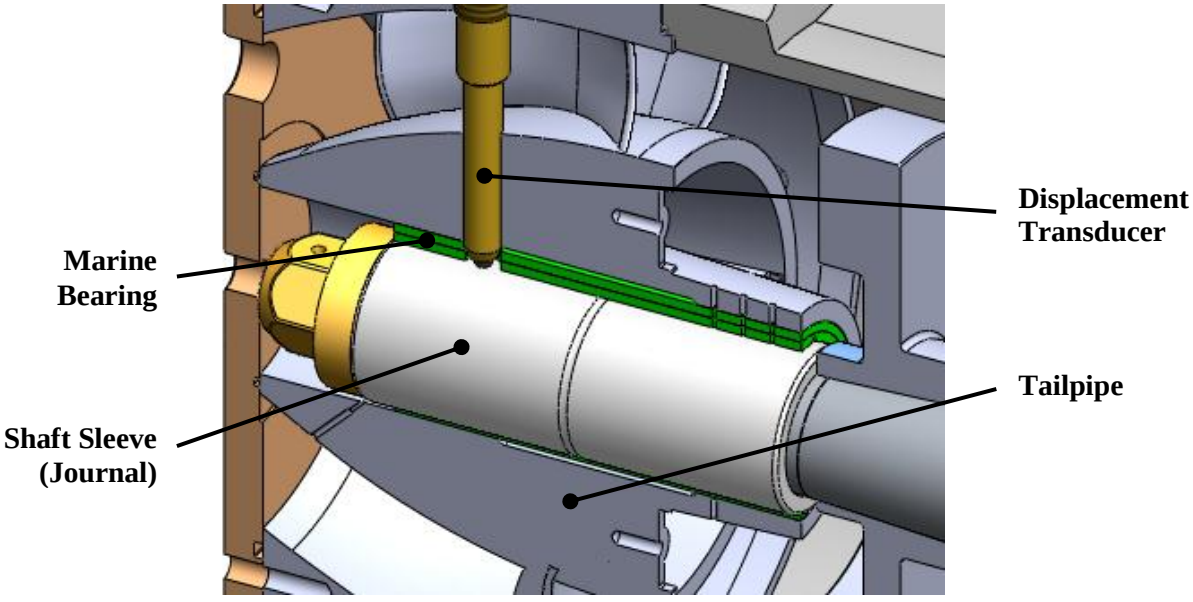

Figure 10.2 – Annotated Partial Section View of the HJ364 Test Rig
(Marine Bearing Highlighted in Green)

10.2 LITERATURE REVIEW

10.2.1 Background

Marine bearings (water lubricated bearings) come under the wider category of Hydrodynamic Journal (HDJ) bearings. This category of bearing uses a fluid film to provide a low-friction interface the journal and the bearing. The fluid film is only established once significant relative motion between the journal and the bearing is achieved. Therefore the bearings typically perform poorly at low speeds and have a recommended operating speed range.

According to Budynas-Nisbett (2008) an ideal hydrodynamic journal bearing has:

- a smooth, rigid and featureless circular journal;
- a smooth, rigid and featureless circular bearing race;
- speed dependent stiffness and damping properties and a high level of cross-coupling
- a lubricating fluid with a relatively high viscosity; and
- a significant radial load on the journal (with a fixed orientation).

The operation of an ideal HDJ bearing is relatively predictable and well understood. A number of analytical and numerical models exist for oil lubricated journal bearings; many software packages exist to predict their stiffness and damping properties. However, marine bearings typically deviate significantly from the ideal model. The marine bearing in the HJ364 water jet assembly has:

- axial grooves along the bearing race (for lubrication purposes);
- a compressible construction material - nitrile rubber;
- a relatively low viscosity lubricant (fresh or salt water); and
- a light, time-variant and orientation-variant radial load due to unbalance, critical speeds and external hydrodynamic effects

These deviations and the limited amount of relevant literature required an investigation. This was carried out by the author in parallel to the work reported here.

10.2.2 HJ364 Marine Bearing Investigations

A report was prepared by the author in March, 2012 entitled "Operating Characteristics of a Water Lubricated Hydrodynamic Journal Bearing" (provided in Appendix C for reference). Through the use of 10 pressure-tappings around the circumference of the marine bearing and two proximity probes to measure journal displacements, the performance of the bearing was assessed. It was found that the journal/mainshaft was:

- Not obtaining a stable centre of rotation and whirling at high angular velocities;
- Highly unstable and compressing the rubber bearing significantly from 400 RPM to 1000 RPM; and
- Never obtaining full-film development indicating that rubbing was occurring at all angular velocities.

These results matched well with the observations provided by the bearing manufacturer Duramax®. The highly non-ideal behavior of the marine bearing resulted in a termination of any further work to establish the stiffness and damping properties. Thus, an approximation was made that the stiffness of the bearing was the same regardless of rotational speed; reasonable as the fluid film was very small and could be assumed infinitely rigid. Hence, the bearing stiffness could be established from the stiffness of the nitrile rubber alone.

10.3 APPROACH

As the marine bearing was found to be performing poorly and unpredictably, an alternative means of assessing the effect of the marine bearing properties on critical speeds was required.

This was achieved through comparative testing. Three bearing configurations were tested including:

- the standard Duramax® rubber marine bearing;
- a Thordon SXL polymer marine bearing (a marine bearing with significantly different geometry and a harder construction material); and
- a spherical roller bearing applied in place of the tailpipe and marine bearing assembly (the closest approximation to a simple pinned support)

The comparative performance of the three bearing types was assessed and is described below.

10.4 DESIGN

10.4.1 Duramax® Rubber Marine Bearing

In Figure 10.3, a cross-section of the Duramax® rubber marine bearing with the mainshaft/sleeve is provided (not to scale). This bearing is standard issue with an HJ364 water jet assembly and was used unless otherwise stated across all tests on the HJ364 test rig. In Table 10.1, the main dimensions of the bearing and its operating parameters are provided; these were specified by the manufacturer Duramax®. The radial stiffness of the bearing K_r was determined in Section 10.5.1.

Table 10.1 - Dimensions of the Duramax® Marine Bearing

Bearing Inner Diameter (ID)	80.26mm
Mainshaft Diameter (OD)	79.92mm
Running Diametral Clearance	0.34mm
Groove Width (approx.)	5mm
Groove Depth (approx.)	2mm
Number of Grooves	10
Bearing Length	210mm

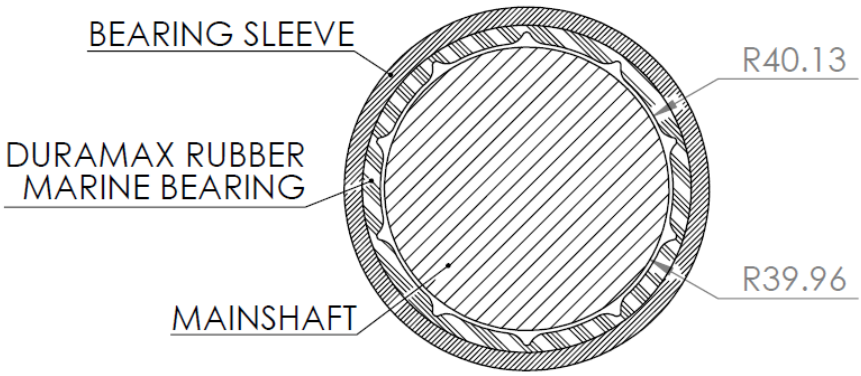

Figure 10.3 – Annotated Cross-Section of the Duramax® Rubber Marine Bearing
(not to scale)

10.4.2 Thordon SXL Marine Bearing

'SXL' is the specification of a polymer based marine bearing manufactured by *Thordon Bearings* in Canada. Of polymer construction, it has a much greater modulus of elasticity than nitrile rubber. It was considered necessary to determine the effect of this greater modulus on critical speeds and evaluate whether the bearing could be suitable for future water jet assembly designs.

On specification of leading dimensions and loads, the bearing manufacturer designed and fabricated an SXL marine bearing to suit the HJ364 test rig; these communications are

provided in Appendix A5. In Figure 10.4, a cross-section of the SXL bearing and mainshaft is provided (not to scale). In Table 10.2, the dimensions of the SXL marine bearing are provided. A detailed drawing of the bearing fitted to the tailpipe is provided in Appendix A6.

A bearing sleeve was designed and submitted for manufacture to fit the SXL bearing to the tailpipe (not shown). This was a standard production part manufactured by CWF Hamilton & Co. Ltd. and was machined to fit the new bearing. As with the Duramax® marine bearing, two 18mm diameter holes were drilled at right angles into the rear end of the bearing for the proximity probes.

Table 10.2 - Dimensions of the SXL Marine Bearing

Bearing Inner Diameter (ID)	81.06mm
Mainshaft Diameter (OD)	79.92mm
Running Diametral Clearance	1.14mm
Groove Width	6mm
Groove Depth	2.90mm
Number of Grooves	8
Bearing Length	160mm

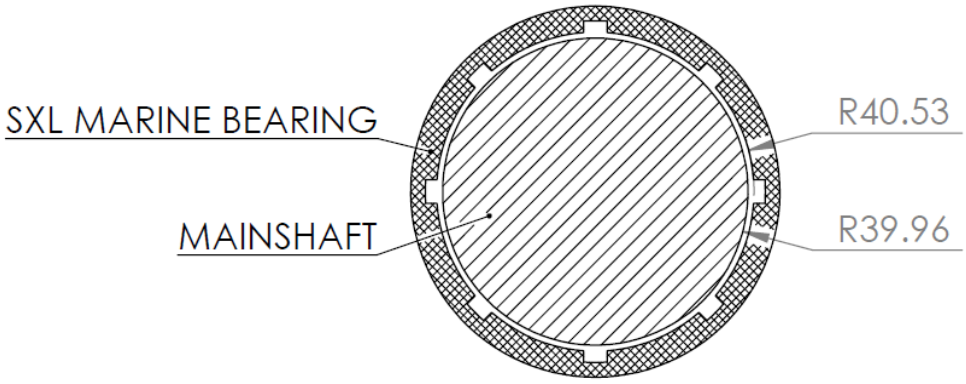

Figure 10.4 – Annotated Cross-Section of the SXL Marine Bearing
(not to scale)

10.4.3 Spherical Roller Tailpipe Bearing

To perform as a close approximation to a pinned support; free axial float, free rotation about all axes and a fixed radial displacement were required. The assembly in Figure 10.5 was chosen after a number of design iterations. An annotated cross-section of the alternative bearing housing is provided in Figure 10.6. This assembly allowed for free rotation about all axes; had a limited axial travel (within the confines of the housing); prevented radial motion and bolted in the existing stud pattern. The final model is shown in Figure 10.7. Drawings are provided in Appendix A7.

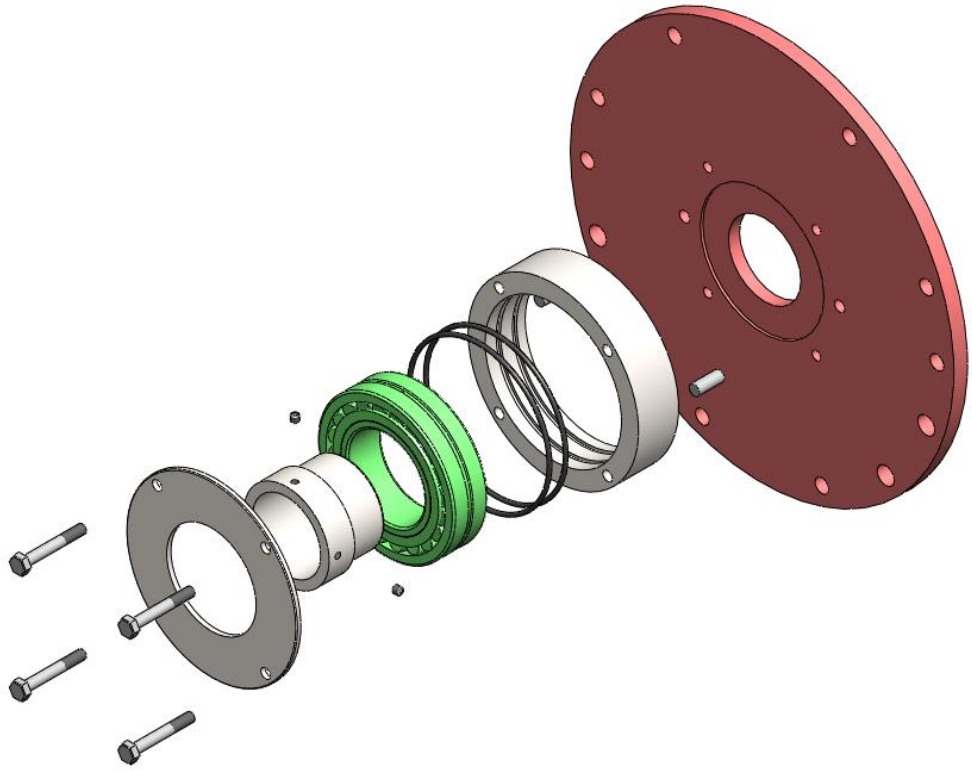

Figure 10.5 – Exploded View of the Spherical Roller Tailpipe Bearing Assembly

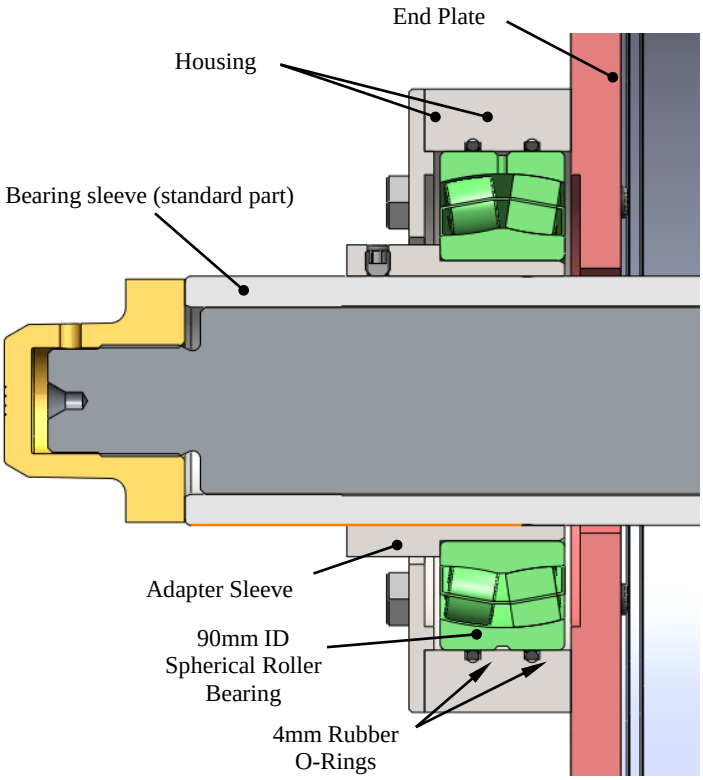

Figure 10.6 – Annotated Partial Section View of the Spherical Roller Tailpipe Bearing Assembly

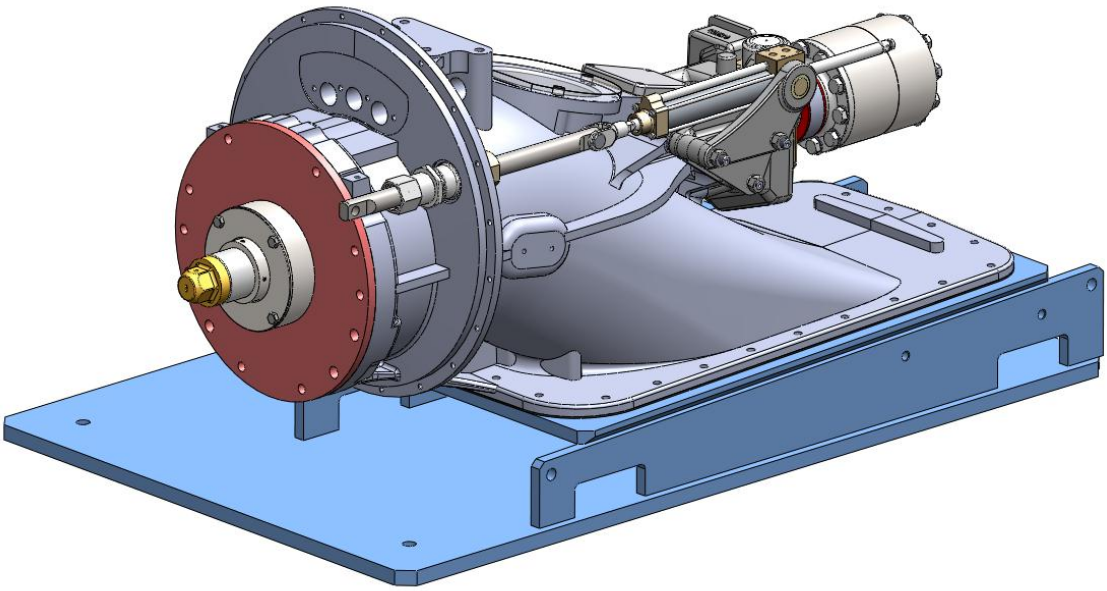

Figure 10.7 - Alternative Bearing Assembly Fitted to the HJ364 Test Rig

10.5 ANALYTICAL AND NUMERICAL MODELLING

10.5.1 Duramax® Rubber Marine Bearing Stiffness

Under the approximation made in Section 10.2.2 that the stiffness of the marine bearing during operation is the stiffness of the rubber alone, the effective bearing stiffness could be derived. The following is an excerpt from a spreadsheet calculation provided by Duramax®.

A straight fluted bearing can be considered to be fabricated from a number of inclined shear mounts. Calculate the radial stiffness of each pair of flutes and sum the total

$$K_r = \frac{F}{x} = 2\ (\ K_c \cos(\vartheta)^2 + K_s \sin(\vartheta)^2\ ) \tag{10.1}$$

Where: K_r is the radial stiffness; x is the radial deflection; K_c is the compression stiffness of an individual bearing land; K_s is the shear stiffness of an individual bearing land and ϑ is the angle of a pair of land faces to the horizontal.

Equation (10.1) can be simplified by ignoring the contribution of the shear stiffness as this is likely to be very low, particularly in operation as the friction coefficient is low. Therefore, equation (10.1) becomes:

$$K_r\ =\ 2\ (\ K_c \cos(\vartheta)^2\ ) \tag{10.2}$$

For a long strip of rubber, the strain in the direction of its length will be negligible:

$$S\ = \frac{b}{t} \tag{10.3}$$

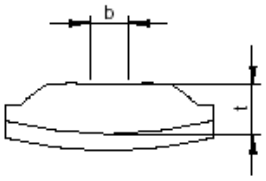

Figure 10.8 - Geometric Description of a Bearing 'Land'
(Provided by the Duramax® Calculation Spreadsheet)

Where: S is the shape factor; b is the width of the ground surface; and t is the total thickness of the rubber wall

The compression stiffness of a rubber strip (bearing land) is given by:

$$K_c = E_c \, I \frac{b}{t} \tag{10.4}$$

Where: E_c is the compression modulus of an individual land (from the E_c versus S curves for a given rubber hardness); and I is the bearing length.

In Table 10.3 and Table 10.4, the inputs and outputs of the bearing stiffness calculation for a ten-fluted bearing are provided respectively. Note that K_r (the radial stiffness) is given for static conditions. The stiffness of rubber is typically strain sensitive and therefore the calculation of K_r may be somewhat low.

Table 10.3 - Inputs to Duramax® Rubber Marine Bearing Stiffness Calculation

Bearing Size	80mm x 100mm x 210mm
Ground Surface Width, *b*	10mm
Rubber Wall Thickness, *t*	4.95mm
Bearing Length, *l*	210mm
Number of Groves, *n*	10

Table 10.4 - Outputs from Duramax® Rubber Marine Bearing Stiffness Calculation

Shape Factor, S	1.0
Compression Modulus, E_c	12 MPa *(as provided by* Duramax®*)*
Compression Stiffness, K_c	5.1kN/mm
Shear Stiffness, K_r	13kN/mm *(static stiffness)*

10.5.2 Thordon SXL Marine Bearing Stiffness

As no data was provided by the bearing manufacturer and no detailed experimental work was carried out, the stiffness properties of the SXL Marine Bearing during operation could not be determined. However, under the assumption that the nitrile rubber and SXL bearings operate in a similar manner, the lubricating film thickness could be assumed very thin and very rigid (see Section 10.2.2). Therefore, the radial stiffness of the SXL bearing during operation could be assumed approximately equal to that under static conditions.

Based on this assumption the manufacturer provided a means of calculating the radial stiffness of the material alone (Thordon Bearings Inc., 2006):

$$K_r = \frac{L\ D\ E_o}{t} \tag{10.5}$$

Here, L is the length of the bearing, D the diameter, E_o the Young's Modulus and t the wall thickness. These values and the evaluated radial stiffness K_r are provided in Table 10.5.

Table 10.5 - Inputs to Thordon SXL Marine Bearing Stiffness Calculation

Bearing Length, L	160 mm
Bearing Diameter, D	81.06 mm
Young's Modulus, E_o	440 MPa
Wall Thickness, t	5 mm
Radial Stiffness, K_r	1140 kN/mm

This derived stiffness was significantly higher than that of the intake indicating that the stiffness of the bearing could effectively be ignored. This agrees well with suggestions from the manufacturer:

> "When rubber bearings are being specified, due to the low stiffness characteristics of rubber (20% to 25% of that of Thordon), shaft line designers may be accustomed to considering the bearing flexibility when making whirling vibration calculations. However, this is not the case with Thordon XL, SXL, COMPAC or HPSXL where, due to a much higher stiffness, the Thordon bearing can be assumed to be as stiff as the bearing support structure" (Thordon Bearings Inc., 2006)

In addition:

> "…the stiffness of the bearing material is normally not considered in shaft whirling vibration calculations" (Thordon Bearings Inc., 2006)

The main purpose of this testing was performance comparison with the Duramax® rubber marine bearing. Therefore the precise value of this bearing stiffness was not considered critical.

10.5.3 Spherical Roller Tailpipe Bearing Stiffness

Based on the findings of Section 10.5.2, it was deemed unnecessary to perform any stiffness calculations of the spherical roller bearing. Since steel (the spherical bearing material) has a much greater Young's modulus than the SXL polymer, the dominant stiffness would again be that of the intake. The stiffness of the rubber 'O-rings' could be neglected as the outer race of the bearing could slide with a precision fit inside the housing.

10.5.4 Combined Stiffness Summary

The final step in determining the support stiffness for critical speed predictions was the incorporation of the intake properties. In Table 10.6, the combined horizontal and vertical stiffness values are provided for the Duramax® marine, Thordon SXL marine and spherical roller bearings. As the stiffness of each of the bearings was independent of angle (axially), the maximum and minimum stiffness remained in the horizontal and vertical planes respectively.

Table 10.6 – Combined Stiffness of the Various Marine Bearing Alternatives

Rear Bearing Type	**Maximum Combined Stiffness** (Horizontal)	**Minimum Combined Stiffness** (Vertical)
Duramax® Marine Bearing	1.2×10^7 N/m	1.1×10^7 N/m
Thordon SXL Marine Bearing	1.4×10^8 N/m	7.2×10^7 N/m
Spherical Roller Bearing	1.6×10^8 N/m	7.7×10^7 N/m

10.5.5 Critical Speeds

With the values provided in Table 10.6, critical speeds of the SXL marine bearing and the spherical roller bearing configurations were predicted. These are provided in Table 10.7and Table 10.8 respectively. As expected, the Timoshenko-Beam model did not indicate any change in critical speed as it does not incorporate a support stiffness term. Both the Myklestad-Prohl TMM and Isolated-Mainshaft FEM methods predicted a slight increase in critical speed.

Table 10.7 – Critical Speed Properties of the SXL Marine Bearing Installation

Method	Critical Speed	Change in Critical Speed
Timoshenko-Beam	3003 RPM	0 RPM
Myklestad-Prohl TMM	3090 and 3102 RPM	+150 and +162 RPM
Isolated-Mainshaft FEM	2948 and 3120 RPM	+139 and +169 RPM

Table 10.8 – Critical Speed Properties of the Spherical Roller Bearing

Method	Critical Speed	Change in Critical Speed
Timoshenko-Beam	3003 RPM	0 RPM
Myklestad-Prohl TMM	3090 and 3102 RPM	+150 and +162 RPM
Isolated-Mainshaft FEM	2948 and 3120 RPM	+139 and +169 RPM

10.6 TEST RESULTS

10.6.1 Critical Speeds

In Figure 10.9, the peak deflections of the driveline mass (obtained with the various tailpipe bearing geometries) are provided and compared. The Thordon SXL bearing showed a very similar response across all rotational speeds to the Duramax® marine bearing. It exhibited a reduced response between 2000 and 3800 RPM. Between 2800 and 3100 RPM and speeds below 2000 RPM, the response of the two bearings was largely the same. Overall, there was no observable shift in critical speed with the SXL marine bearing.

The spherical roller bearing exhibited a greater response than both marine bearings across all rotational speeds. In addition, two critical speeds could be observed at 3300 and 3700 RPM. These peaks also had a significantly larger magnitude. This was expected as the internal damping in a roller bearing is significantly lower than that in a marine bearing.

The accelerometer data provided in Figure 10.10 and Figure 10.11 showed a similar trend. Overall the spherical roller gave rise to the highest peak accelerations and the Thordon SXL bearing gave the lowest. A further peak was observed at approximately 3940 RPM. This resonance did not appear in Figure 10.9. Therefore, it was likely to be a resonance of the intake and not of the mainshaft.

Finally, there was a small peak observed between 2000 and 2500 RPM. This was evidently a heavily damped mode as it only appeared in the spherical roller bearing data. On a repeat test of the spherical bearing with a higher level of unbalance (Figure 10.12), the mode at 2400 RPM was highly evident. This is further investigated in Section 11. In Table 10.9, the critical speed data from the three tailpipe bearing configurations is provided.

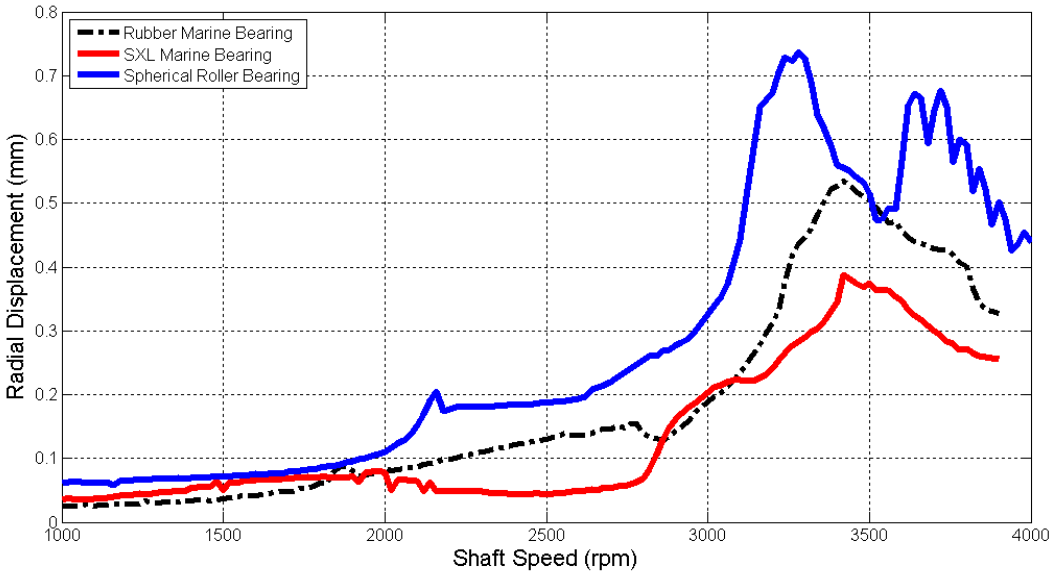

Figure 10.9 - Comparisons of Maximum Radial Displacement at the Driveline Mass
(Alternative Tailpipe Bearing Geometry, 1000 to 4000 RPM, 20 RPM sampling)

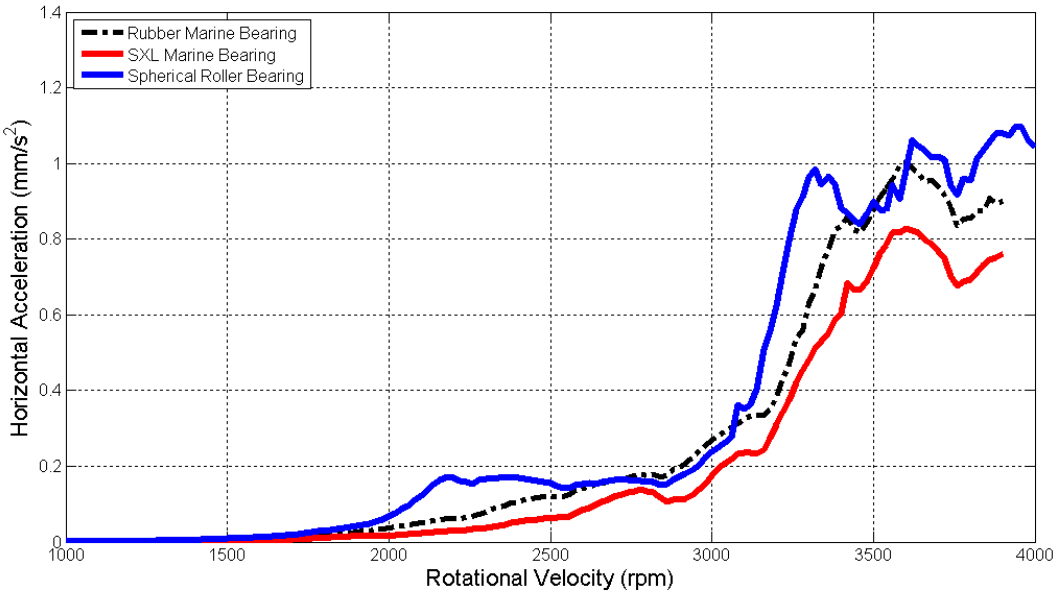

Figure 10.10 - Response from the Horizontally Aligned Accelerometer along the Synchronous Excitation Peak (Alternative Tailpipe Bearing Geometry, 1000 to 4000 RPM, 20 RPM sampling)

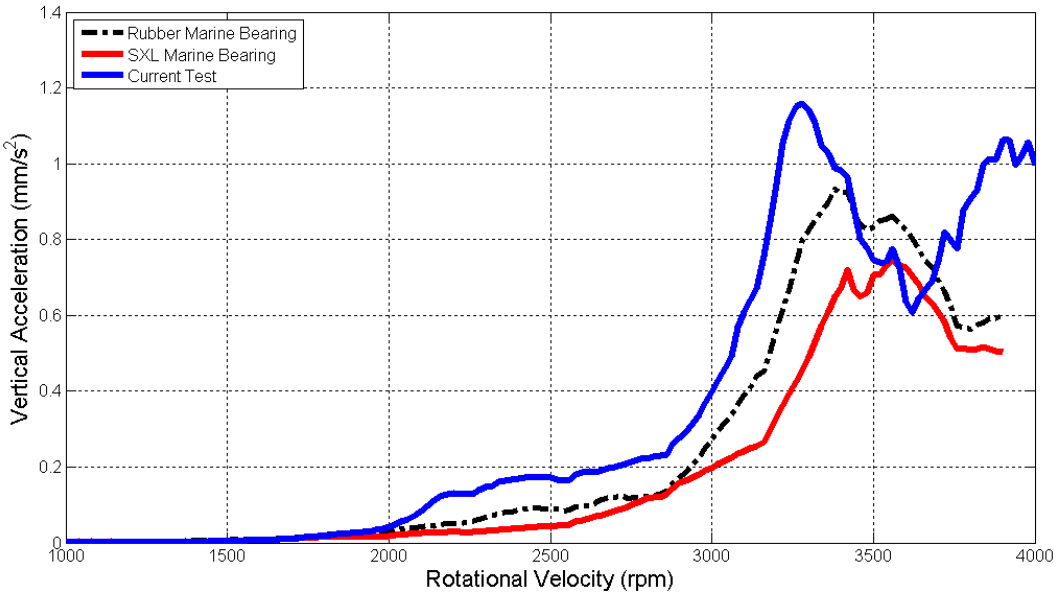

Figure 10.11 - Response from the Vertically Aligned Accelerometer along the Synchronous Excitation Peak (Alternative Tailpipe Bearing Geometry, 1000 to 4000 RPM, 20 RPM sampling)

Table 10.9 - Experimental Critical Speed Data for the Different Bearing Configurations

Bearing Configuration	**Critical Speed** [RPM]
Duramax® Rubber Bearing	3420 ± 60
Thordon SXL Bearing	3420 ± 60
Spherical Roller Bearing	3350 ± 60 and 3700 ± 60

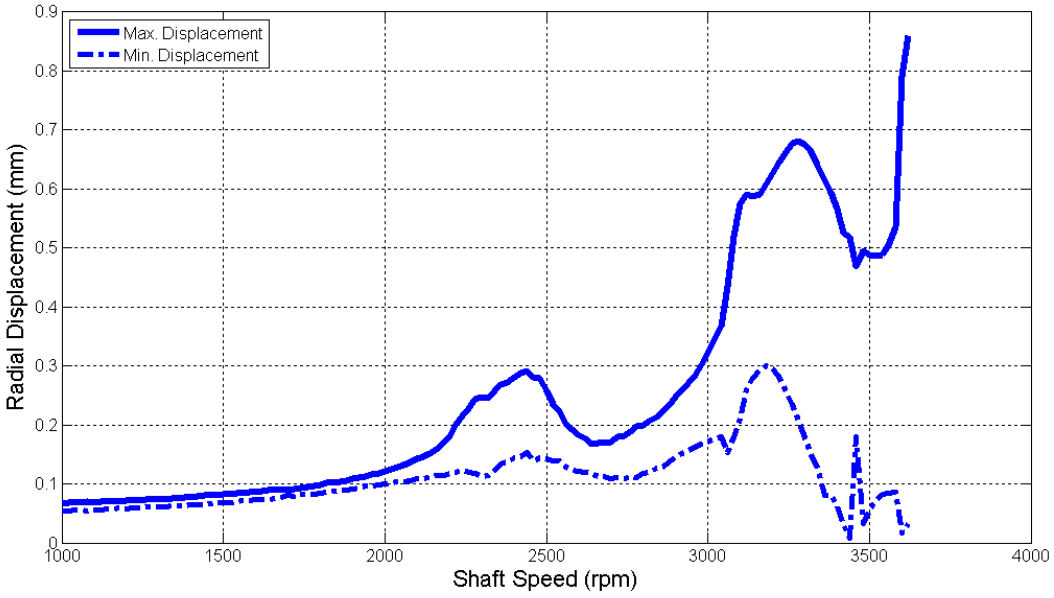

Figure 10.12 - Peak Radial Displacements of the Driveline Mass – Test Repeat
(Spherical Bearing Geometry, 1000 to 3640 RPM, 20 RPM sampling)

10.6.2 Bearing Performance

In Figure 10.13, Figure 10.14 and Figure 10.15, the waterfall plots from the vertically aligned accelerometer on the thrust bearing housing are provided. These provide a means of assessing the bearing performance.

In Figure 10.13 there was a strong first order resonance which peaked at 3240 RPM. The 2nd, 3rd and 4th order harmonics are also observable. There was also some indication of ½ and 1½ order modes at higher rotational speeds consistent with lubricant 'whirl'. In Figure 10.14, the Thordon SXL bearing exhibited a similar behavior. There was a strong first order resonance

at 3240 RPM and 2nd, 3rd, 4th and higher order resonances. ½ and 1½ and 2½ order resonances were also clearly visible at higher rotational speeds; again, consistent with lubricant 'whirl'.

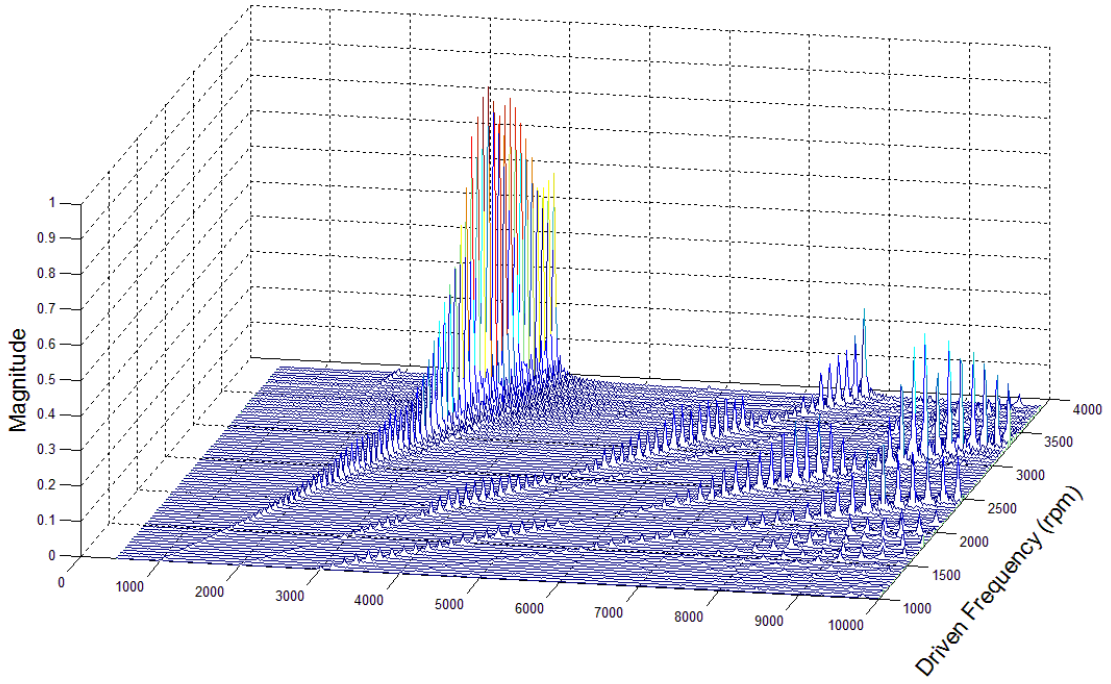

Figure 10.13 – Waterfall Plot from the Vertically Aligned Accelerometer
(Duramax® Marine Bearing, 500 to 4000 RPM, 20 RPM sampling)

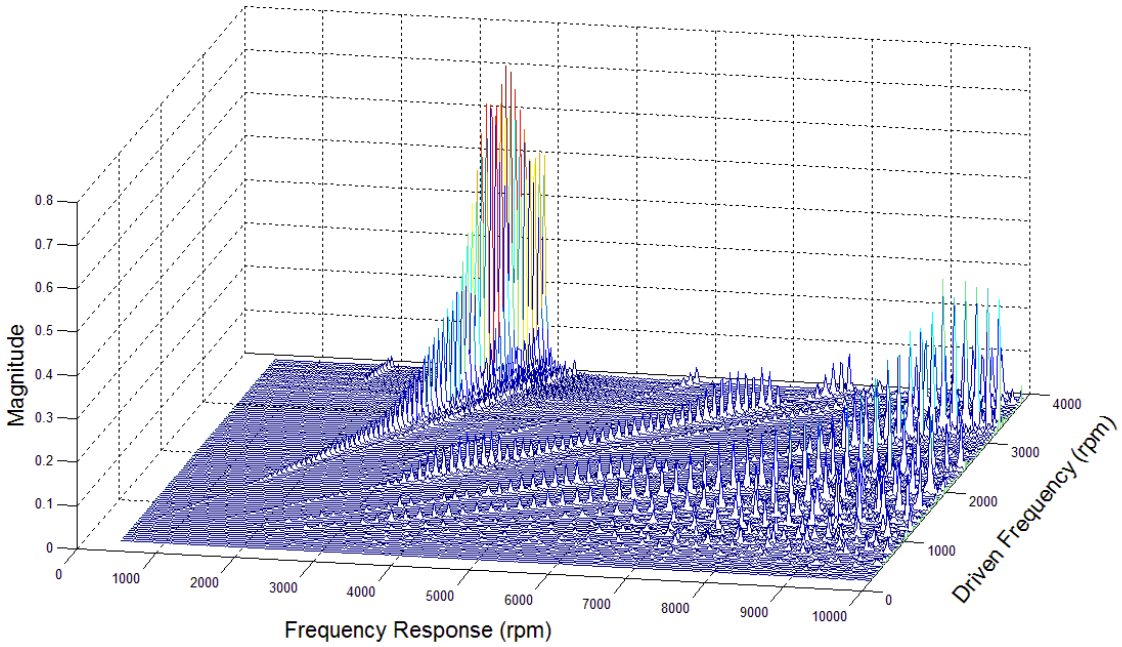

Figure 10.14 - Waterfall Plot from the Vertically Aligned Accelerometer
(Thordon SXL Marine Bearing, 500 to 4000 RPM, 20 RPM sampling)

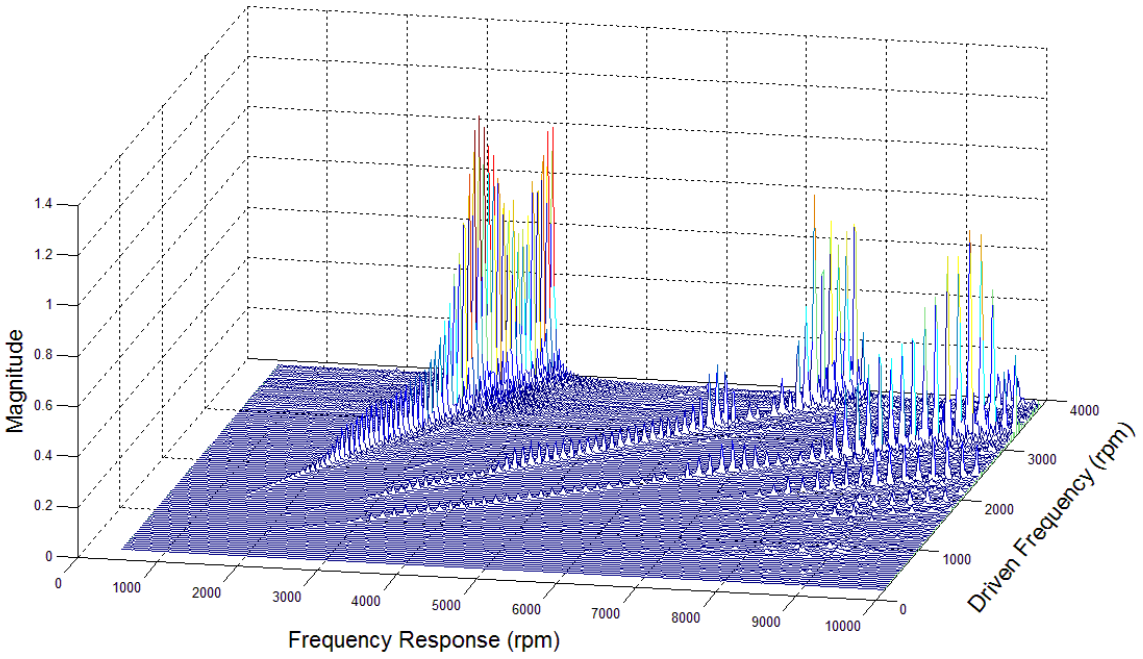

Figure 10.15 - Waterfall Plot from the Vertically Aligned Accelerometer
(Spherical Roller Bearing, 500 to 4000 RPM, 20 RPM sampling)

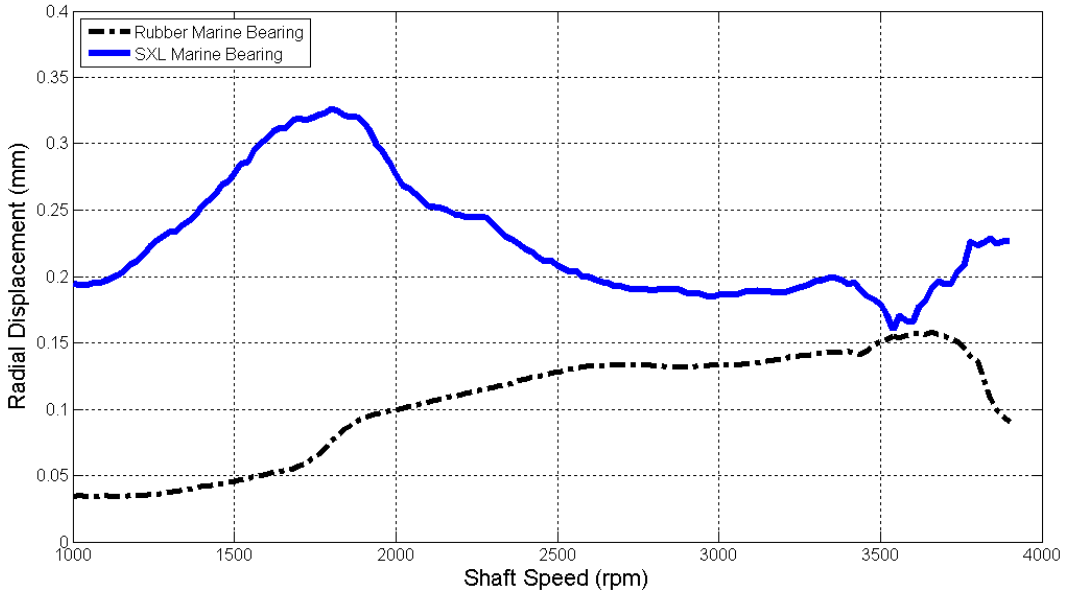

Figure 10.16 - Peak Deflection Comparisons at Marine Bearing

In Figure 10.15, the two peaks in the first order mode are clearly visible. The 2nd and 3rd order harmonics had a larger magnitude around the critical speed than either of the marine bearings. A very slight ½ and 1½ order resonance was also observable at higher rotational speeds. This is typical of rolling element bearings as the bearing 'race' rotates at half the speed of the journal.

In Figure 10.16, a comparison of the peak deflections within each of the marine bearings is provided. Clearly, the Thordon SXL bearing experienced the largest displacement across all rotational speeds. This is indicative of a poorer bearing performance.

10.7 DISCUSSION

10.7.1 Critical Speeds

Marine bearings (as with all hydrodynamic journal bearings) tend to have a high degree of cross-coupled stiffness and damping during operation. Khan and Khan (2003) showed that the direct and cross-coupled terms were approximately identical for a rigid rotor running on fluid film bearings. This 'cross-coupling' effectively reduces support asymmetry, bringing the first two critical speeds closer to the same value. As the spherical roller bearing has significantly less cross-coupling present, the separation between the first two critical speeds is significantly larger. Damping reduced the magnitude of the response for both marine bearings (and was considered responsible for eliminating the peak at 2400 RPM).

There is internal clearance present in any rolling element bearing. The journal will tend to 'chatter' during operation which acts to separate forward and backward modes (Johnson, 1962). This effect will add to the separation of the first two critical speeds of the spherical roller bearing in the test rig.

Finally, the length of the marine bearings will give rise to a restoring moment to any deflections of the shaft. This will tend to increase the critical speeds slightly higher than the spherical roller bearing (which provides no restoring moment).

In Table 10.10 and Table 10.11, the predicted and experimentally determined critical speeds for the Thordon SXL and the spherical roller bearing are provided respectively. As observed in previous sections, an accurate prediction of the critical speed was not obtained. Again, the reasons for this are investigated in Section 11.

Observation of Table 10.10 indicates that the Timoshenko-Beam model was the most accurate predictor of change in critical speed. However, this appears coincidental. The Myklestad-Prohl TMM and Isolated-Mainshaft FEM methods predicted an increase in critical speed which did not occur. It is expected that the lack of damping and cross coupling terms in the models were partially responsible for this; the poor performance of the Thordon SXL marine bearing also somewhat responsible.

The spherical bearing behaved in a more typical manner; it exhibited two critical speeds as predicted by the Myklestad-Prohl TMM and Isolated-Mainshaft FEM methods. The deviation of these two critical speeds was actually larger in the experimental data (420 RPM compared to 170 RPM predicted by the Isolated-Mainshaft FEM model). This may have been due to incorrect intake stiffness values or bearing ‘chatter’ described earlier. The critical speed, on average, only increased slightly in the experimental data (by 70 RPM).

These results indicated that, overall, the type and geometry of the tailpipe bearing had very little effect on critical speeds. As expected, the individual stiffness and damping properties of these tailpipe bearings can be ignored. Instead, the stiffness of the intake alone is sufficient for evaluation.

Table 10.10 – Critical Speed Properties of the Thordon SXL Marine Bearing Installation

Method	Critical Speed	Change in Critical Speed
Experimental	3420 RPM	0 RPM
Timoshenko-Beam	3003 RPM	0 RPM
Myklestad-Prohl TMM	3090 and 3102 RPM	+150 and +162 RPM
Isolated-Mainshaft FEM	2948 and 3120 RPM	+139 and +169 RPM

Table 10.11 – Critical Speed Properties of the Spherical Roller Bearing

Method	Critical Speed	Change in Critical Speed
Experimental	3280 and 3700 RPM	-140 and +280 RPM
Timoshenko-Beam	3003 RPM	0 RPM
Myklestad-Prohl TMM	3090 and 3102 RPM	+150 and +162 RPM
Isolated-Mainshaft FEM	2948 and 3120 RPM	+139 and +169 RPM

10.7.2 Bearing Performance

Both marine bearings appeared to perform in a similar manner with a high first order peak and low magnitude harmonics. However, the Thordon SXL bearing had an increased scatter of harmonics. The Thordon SXL bearing was made of a material with a higher elastic modulus and had a much larger internal clearance than the Duramax® rubber bearing. This possibly resulted in higher inertial effects and increased ‘chatter’.

The ½ and 1½ order modes in the marine bearings were attributed to lubricant ‘whirl’ as they appeared at higher rotational speeds. Lubricant whirl is commonly caused by (Berry, 2005):

- light dynamic and preload forces;
- excessive bearing wear or clearance;
- a change in lubricant properties (primarily shear viscosity);
- an increase or decrease in lubricant temperature or pressure;

- improper bearing design (over design for actual shaft loading);
- fluid leakage;
- change in internal damping; and
- gyroscopic effects, especially on overhung rotors with excessive overhang.

Since each of these factors was relevant to the HJ364 test rig to some degree, lubricant whirl was very likely to occur. However, the magnitude of the vibration relative to the first order harmonic was very small and occurred only at speeds higher than standard operational.

The Thordon SXL bearing appeared to perform poorly at low rotational speeds (see Figure 10.16); a large eccentricity occurred at 1700 RPM. Light loading and the larger internal clearance in the Thordon SXL bearing may have given rise to instability at this speed. Alternatively, there may have been a resonance within the mainshaft-bearing assembly at this rotational speed. Further testing will be required to evaluate this.

The Thordon SXL bearing performance improved between 2000 and 3500 RPM. Above these speeds, instability appeared to occur again. In contrast, the performance of the Duramax® rubber bearing appeared to worsen with rotational speed up to 3700 RPM. Above this speed, performance began to improve.

The spherical roller bearing exhibited a greater response in the higher order harmonics than the two marine bearings. This was attributed to the lower damping present in the system. The ½ order harmonics present also came about from the spherical roller bearing and were due to the bearing cage rotating at exactly half the speed of the journal.

Overall, the Duramax® rubber marine bearing appeared to perform the best. Re-design of the Thordon SXL bearing with a smaller running clearance should eliminate this performance deviation.

10.8 SECTION SUMMARY

The design of the marine bearing appears to have little to no effect on critical speeds. When compared to a standard spherical roller bearing, the marine bearing acted to damp out a sub-harmonic at 2400 RPM; combine the first two critical speeds into one due to cross-coupling; reduce the magnitude of the first critical speed due to damping; and slightly increase the critical speed due to a restoring moment that arose from the length of the bearing.

The Thordon SXL bearing appeared to perform worse than the Duramax® marine bearing and experienced a resonance or instability at 1700 RPM. While this had no noticeable effect on the vibration of the overall HJ364 water jet assembly, further investigation into performance and a bearing re-design may be required by CWF Hamilton & Co. Ltd.

11

THRUST BEARING EFFECTS

11.1 INTRODUCTION

As highlighted throughout this thesis, it was determined that a significant and unexplained deviation was present between the modelled and experimental data. It was surmised that the spherical thrust bearing was not operating ideally and was accountable for this deviation.

In Figure 11.2, a partial section view of the thrust bearing housing assembly is provided. In operation, a pre-load is applied to the thrust bearing (green) by a spring carrier and a plain thrust bearing (yellow). Angular deflection of the spherical thrust bearing is limited by the clearance in the spring carrier of 0.1mm. Once this clearance is taken up then rubbing will occur and the housing will deflect resulting in a non-linear system.

Preliminary calculations indicated that this rubbing may be occurring. It was also determined that insufficient pre-load on the thrust bearing would result in poor alignment. Therefore, a modification was made to the bearing assembly to increase this running clearance and improve alignment. The effects on critical speeds were observed.

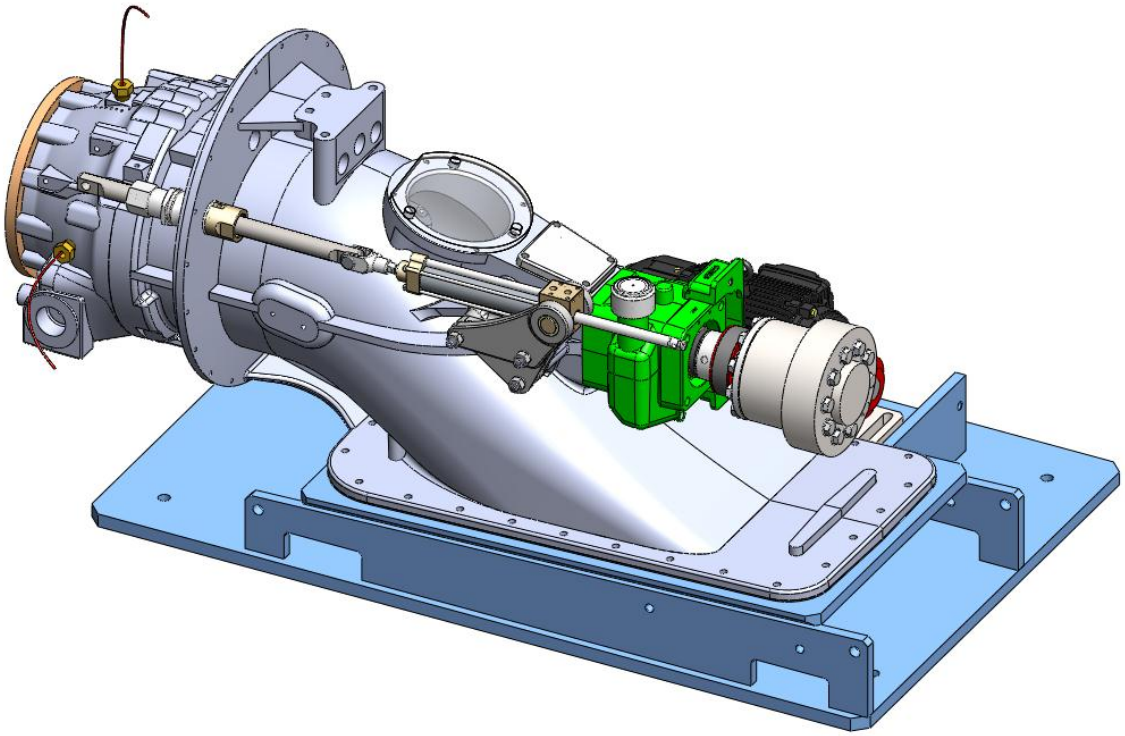

Figure 11.1 - Overview of the HJ364 Test Rig
(Thrust Bearing Housing Highlighted in Green)

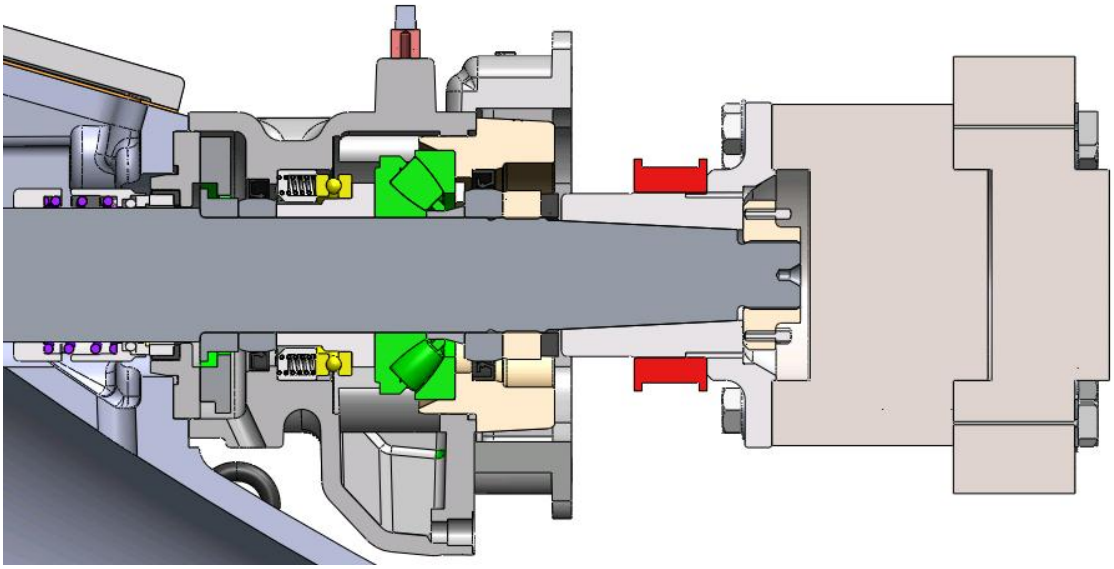

Figure 11.2 – Partial Section View of the Alternative Thrust Bearing Assembly in the HJ364 Test Rig
(Spherical Thrust Bearing Highlighted in Green)

11.2 DESIGN AND ANALYSIS

A design was required in which the thrust bearing would maintain alignment and have sufficient clearance to operate ideally. The selected design is provided in Figure 11.3. This was extracted from an existing design at CWF Hamilton & Co. Ltd. A plain spherical bearing (green) was put in place of the plain thrust bearing and spring carrier. This ensured alignment of the spherical thrust bearing (red) and allowed for significant angular (diametral) deflection of the mainshaft. A plain spherical bearing was also used in place of the marine bearing.

Modelling was carried out in the same manner as described in Section 3 and Section 4. In Table 11.1, the critical speeds as predicted by the various models are provided.

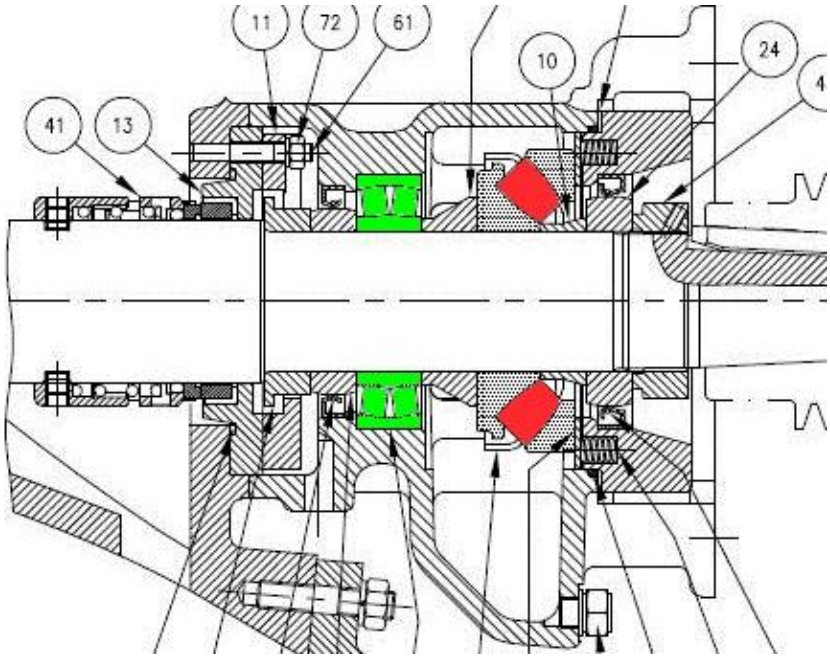

Figure 11.3 – Description of the Additional Spherical Bearing in the Thrust Bearing Housing (Additional Spherical Bearing in Green; Standard Thrust Bearing in Red)

Table 11.1 – Experimental and Modelled Critical Speed Data from the Alternative Thrust Bearing Arrangement

Method	Evaluated Critical Speed	Change in Critical Speed
Timoshenko-Beam	3072 RPM	+155 RPM
Myklestad-Prohl TMM	2922 and 2954 RPM	+142 RPM
Isolated-Mainshaft FEM	2809 and 2951 RPM	+154 and +130 RPM

11.3 TEST RESULTS

The peak deflections of the driveline mass (obtained with the stiffened thrust bearing housing) are provided in Figure 11.4. Two strong peaks were immediately evident; one at 2140 and one at 3000 RPM. These corresponded to two independent critical speeds. While significant misalignment was still present in the system (observable at 1000 RPM), the results appear reasonable. A 'triple-peak' occurred around 3000 RPM. This is most likely an indication of the separation of the forward and backward modes; the backward mode was excited due to significant support asymmetry. This phenomenon was explained by Greenhill and Cornejo (1995).

Comparisons between these results and those from the standard configuration are provided in Figure 11.5. A number of deviations were present including:

- a significantly higher first critical speed in the standard configuration;
- a significantly higher radial displacement of the driveline mass with the alternative thrust bearing assembly across all rotational speeds less than 3300 RPM;
- a lower response in the standard configuration at the first critical speed; and
- no indication of a critical speed around 2100 RPM in the standard configuration.

Evidently, the minor change in bearing geometry inside the thrust bearing housing had a significant effect on the system as predicted. This indicates that in earlier tests, the spherical

thrust bearing was running out of alignment and/or rubbing was occurring. Clearly, some redesign of the thrust bearing housing is required to ensure correct operation.

The second of these two points can be explained by damping and misalignment. The alternative thrust bearing assembly used two plain spherical bearings which would have had significantly less damping than the marine – thrust bearing configuration used in the standard test. As the peak response is purely controlled by damping at a critical speed (Weisstein, 2012), the maximum value was obtained by the alternative thrust bearing assembly. The larger degree of misalignment present in the alternative bearing configuration (observable at 1000 RPM) should have had no significant effect on the location of the critical speed. The misalignment was due to bearing clearance and the straightness of the mainshaft.

The final of these points can also be partially explained by damping. Observation of Figure 11.4 shows that the maximum and minimum displacements at 2140 RPM were quite similar. This indicates that the 'orbit shape' of the driveline mass was roughly circular; a phenomenon typically observed in heavily damped modes. As the standard configuration had a significantly higher level of damping, this first peak was almost entirely eliminated (a small trace of it can be observed at 2750 RPM). Reasons for this additional critical speed are discussed in Section 11.4.

Unfortunately, accelerometer data proved unreliable for the alternative thrust bearing testing. This data could prove useful in the future as comparisons could be drawn with the deflection of the thrust bearing housing.

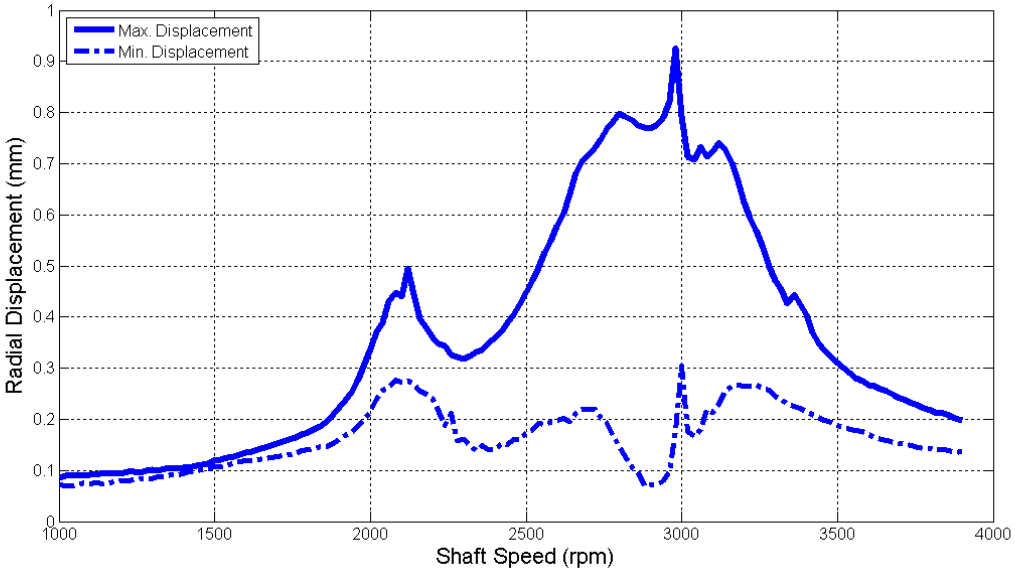

Figure 11.4 – Peak Radial Displacements of the Alternative Thrust Bearing Assembly
(1000 to 3900 RPM, 20 RPM sampling)

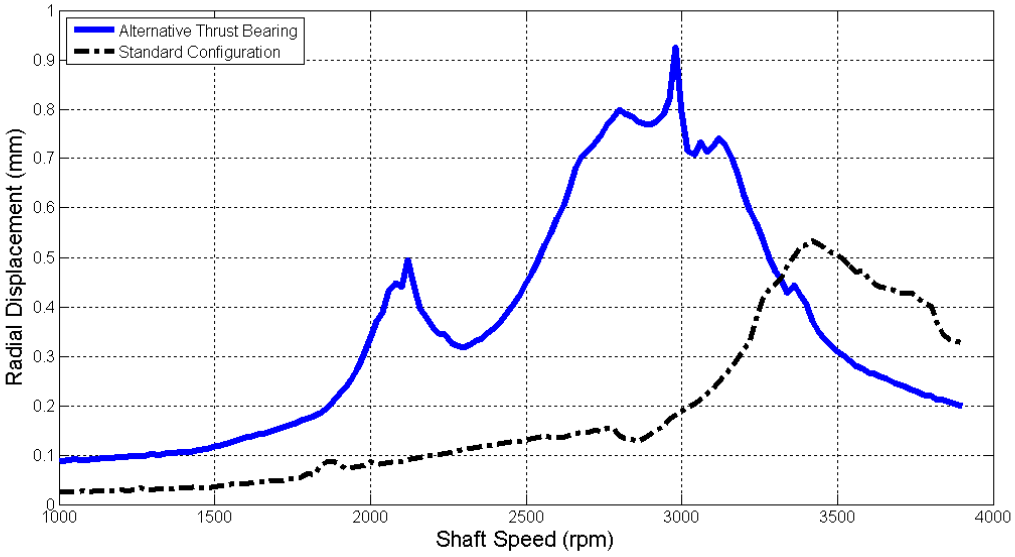

Figure 11.5 - Comparisons of Maximum Radial Displacement at the Driveline Mass
(1000 to 3880 RPM, 20 RPM sampling)

11.4 DISCUSSION

In Table 11.2, the results from the critical speed testing of the alternative thrust bearing assembly are compared to those predicted. Due to the accuracy of the predicted values, the deviations from the experimental data are also provided.

Table 11.2 – Experimental and Modelled Critical Speed Data from the Alternative Thrust Bearing Arrangement

Method	Evaluated Critical Speed	Deviation from Experimental
Experimental	3000 RPM	
Timoshenko-Beam	3072 RPM	+2.4%
Myklestad-Prohl TMM	2922 and 2954 RPM	-2.6% and -1.5%
Isolated-Mainshaft FEM	2809 and 2951 RPM	-6.4% and -1.6%

Immediately evident is the strong correlation between the predicted and experimentally determined critical speeds. The Timoshenko-Beam model appeared to make a slight 'over-prediction' of the first critical speed; this was attributed to the simplified geometry and rigid support assumptions. The Myklestad-Prohl TMM and Isolated-Mainshaft FEM methods made a slight 'under-prediction' of the first critical speed; this was attributed to the lack of damping effects in the models. However, any of these models could be used by CWF Hamilton & Co. Ltd. to make very accurate predictions of the critical speeds for configurations such as this.

This validation of the analytical and numerical models means that they can be used to consistently provide a conservative prediction of critical speeds in an HJ364 water jet assembly. In practice, the addition of thrust loads from an impeller will tend to reduce critical speeds toward the predicted value.

The reason for the lower critical speed with the alternative thrust bearing geometry cannot be explained. With the geometry used in the alternative thrust bearing configuration, a model of

a shaft with pin supports should have proven very accurate. However, none of the analytical or numerical models predicted this additional critical speed. Clearly, this phenomenon was indicative of some modelling limitation and is potentially a rigid body mode. However, due to time and scope limitations, it was not assessed further. For the purposes of CWF Hamilton & Co. Ltd., this critical speed should not prove problematic as it is heavily damped in practice.

Finally, a repeat was trialed with the alternative thrust bearing assembly and the 32kg driveline mass described in Section 5 (the experimental plots are not shown as this was performed primarily to test reliability). The results from this test are provided in Table 11.3. Clearly, a much improved prediction of the experimentally determined critical speeds was obtained.

Table 11.3 – Experimental and Modelled Critical Speed Data of the Alternative Driveline Mass

Method	Evaluated Critical Speed	Change in Critical Speed
Experimental	3140 ± 60 RPM	+ 140 ± 120 RPM
Timoshenko-Beam	3158 RPM	+155 RPM
Myklestad-Prohl TMM	3064 RPM	+142 RPM
Isolated-Mainshaft FEM	2963 and 3081 RPM	+154 and +130 RPM

11.5 SECTION SUMMARY

This section, while originally considered out of scope, investigated the effects of the thrust bearing on critical speeds and modelling. It was determined that the spherical thrust bearing was running out of alignment and/or rubbing within the housing. This behavior was giving rise to a significant deviation between the modelled and experimentally determined critical speed data.

Finally, this section provided final validation of the Timoshenko-Beam, Myklestad-Prohl TMM and Isolated-Mainshaft FEM methods used in this thesis. They can be used to provide a consistent, conservative prediction of the critical speeds of an HJ364 water jet assembly. Extension to the wider CWF Hamilton & Co. Ltd. water jet assembly range should be relatively straightforward.

Re-testing of the previous sections should be performed with this idealized configuration and comparisons made. The time and scope limitations of this work resulted in this not being performed.

12

CONCLUSIONS AND RECOMMENDATIONS

12.1 CONCLUSIONS

With a new range of water jet assemblies under development, CWF Hamilton & Co. Ltd. had highlighted the need to establish a validated model for predicting critical speeds. A review of the relevant literature had revealed a significant lack of information in regards to the operating properties of a lightly loaded, water lubricated marine bearing. Therefore, experimental critical speed data was considered necessary to validate the predictive models.

A test rig based on a CWF Hamilton & Co. Ltd. 'HJ364' water jet assembly was prepared; this particular model operates close to its first critical speed. Instrumentation was applied to measure the two-dimensional displacement and acceleration of the shaft with time. Through software, the data was acquired, smoothed and plotted to obtain whirl orbits and waterfall plots; critical speeds were then established from these.

A number of analytical and numerical models for predicting critical speeds were investigated. Comparisons were drawn between an analytical model (currently in use by CWF Hamilton & Co. Ltd.), a Myklestad-Prohl TMM model and an Isolated-Mainshaft FEM model. A number of geometric modifications were made to the test rig. These included changes to the: driveline mass, driveline overhang, thrust bearing housing stiffness, impeller mass, tailpipe stiffness,

marine bearing and thrust bearing. The changes in critical speeds were measured. Subsequently, comparisons were drawn between this data and the critical speeds established by the predictive models.

In terms of critical speeds, it was determined that driveline mass and driveline overhang had the most significant effects on critical speeds. A minor change to either of these properties resulted in a significant shift in critical speed. Modifications to the thrust bearing housing, the impeller mass, the tailpipe stiffness or the marine bearing resulted in no significant shift in critical speeds. However, changes to the thrust bearing configuration resulted in a significant shift. This indicated that the thrust bearing was not performing ideally in the test rig.

In terms of modelling, all three models predicted changes in critical speeds relatively accurately. However, all three models predicted critical speeds to be approximately 10 – 15% lower than those measured. This was explained when modifications were made to the thrust bearing assembly; the thrust bearing was operating in a non-linear manner and could not be modelled as a simple pinned support. However, the models consistently provided a conservative estimation of critical speeds.

Any of the three predictive models can be used to provide this conservative estimation of critical speeds. However, the Myklestad-Prohl TMM and Isolated-Mainshaft FEM methods are the most flexible and user-friendly. It is expected that the thrust-load from the impeller during operation would improve the operation of the thrust bearing. This would give rise to a more accurate prediction of critical speeds.

12.2 RECOMMENDATIONS

As discussed in the previous section, the driveline mass and driveline overhang had the most significant effect on critical speeds. These should be taken into account in the design of future water jet assemblies. Improvements could be made by:

- reducing the distance between the coupling and the thrust bearing;
- reducing the mass of the coupling; and/or
- reducing the length and/or mass of the attached driveshaft;

Modifications to the thrust bearing housing, the impeller mass, the tailpipe stiffness or the marine bearing had no significant shift in critical speeds. If no significant changes to the overall geometry are made in future water jet assembly designs, then changes to these parameters will have no measurable effect on critical speeds.

It is recommended that the thrust bearing geometry be investigated in more detail. While out of scope of this thesis, the various tests described in this thesis should be re-performed with the alternative thrust bearing geometry.

12.3 FUTURE INVESTIGATIONS

A small number of tests still present themselves for future testing on the HJ364 test rig located at CWF Hamilton & Co. Ltd. The following were considered out of scope of this thesis though would still prove useful to obtain full validation of the analytical and numerical models.

12.3.1 Water Level Testing

The effects of water level on critical speeds should be assessed. While tests were performed with the intake full of water, no useful data could be obtained as the power limitations of the motor prevented traversal of the first critical speed. A more powerful motor could achieve this; however, boat trials are potentially more suitable. See Section 12.3.5.

12.3.2 Experimentally Determine Intake Stiffness

The actual values of intake stiffness were never experimentally validated throughout this testing. It was initially considered unnecessary to validate this as the finite-element predictions were predicted to be relatively accurate. However, imperfections in the casting could lead to deviations from the actual value. Validation could be performed through:

- direct deflection testing with a load cell, hydraulic cylinder and displacement sensor;
- testing with a large unbalanced mass on the mainshaft at a speed significantly below a critical speed (geometric limitations would potentially prevent this approach); or
- detailed measurements of the geometry of the intake and thrust bearing housing.

12.3.3 Sensitivity to Mainshaft Geometry

Not included in this analysis was the effect of the changing the geometry of the mainshaft in the test rig. This should yield some new information although it may prove unnecessary; it is expected that the models should readily take into account any geometry changes.

12.3.4 Location of Bearing Supports

This test may also prove somewhat useful. Changing the location of either the spherical thrust bearing or the marine bearing axially will have a significant effect on critical speeds. Again,

as this is a geometric property (not a stiffness or damping property), the current models should accurately predict the corresponding change in critical speeds.

12.3.5 Boat Trials

Boat trials are the most important of the possible future tests as they take into account many of the 'real-world' effects that cannot be taken into account on the test rig. These include:

- thrust loads which provide a compression on the mainshaft, adding additional load to the spherical thrust bearing and increasing the likelihood of mainshaft buckling;
- the damping effects resulting from an intake full of water during operation;
- the effects of water entering the intake at a high velocity and an angle (adding an additional radial load to the mainshaft);
- the effects of coupling an engine through a driveshaft instead of a radial belt load (vibration from the engine may increase the response of the critical speed if not properly isolated);
- the effects of a semi-rigid coupling as opposed to a pinned universal coupling; and/or
- the effects of changing the water jet assembly type to verify the scalability of the model.

13

REFERENCES

American Petroleum Institute. (1996, February). Tutorial on the API Standard Paragraphs Covering Rotor Dynamics and Balancing: An Introduction to Lateral Critical and Train Torsional Analysis and Rotor Balancing. (First). Washington, DC, United States of America.

Budynas-Nisbett. (2008). *Shigley's Mechanical Engineering Design, Eigth Edition.* New York City: McGraw-Hill.

Childs, D. (1993). *Turbomachinery Rotordynamics.* New York City: John Wiley & Sons, Inc.

Genta, G. (2008). *Vibration Dynamics and Control.* New York City: Springer.

Greenhill, L. M., & Cornejo, G. A. (1995). Critical Speeds Resulting from Unbalance Excitation of Backward Whirl Modes. *1995 Design Engineering Technical Conferences. 3 - Part B*, pp. 991-1000. New York: ASME.

Johnson, D. (1962). Synchronous Whirl of a Vertical Shaft Having Clearance in One Bearing. *Journal of Mechanical Engineering Science*, 85 - 93.

Khan, A. H., & Khan, A. A. (2003). Estimation Of Linearised Fluid Film Coefficients In A Rotor Bearing System Subjected To Random Excitation. *11th National Conference on Machines and Mechanics*, (p. 380). Aligarh.

Pestel, E., & Leckie, F. A. (1963). *Matrix Methods in Elastomechanics.* New York City: McGraw-Hill.

Sam Samarasekera, H. (2005). *Vibration and Shock Handbook.* CRC Press.

Sterling, F. W. (1920). *Marine Engineers' Handbook.* New York City: McGraw-Hill Book Company, Inc.

Thordon Bearings Inc. (2006). Engineering Manual Version E2006.1. Burlington, Canada: Thordon.

Weisstein, E. W. (2012). *Overdamped Simple Harmonic Motion.* Retrieved 11 26, 2012, from Wolfram Mathworld: http://mathworld.wolfram.com/OverdampedSimpleHarmonicMotion.html

APPENDIX A: DRAWINGS

Drawings of the various modified test rig geometries are provided in this section. A reference table is provided below for convenience. Note that none of the drawings of the original test rig have been provided for reasons of conciseness. The drawings provided in this appendix were considered the most relevant.

REFERENCE

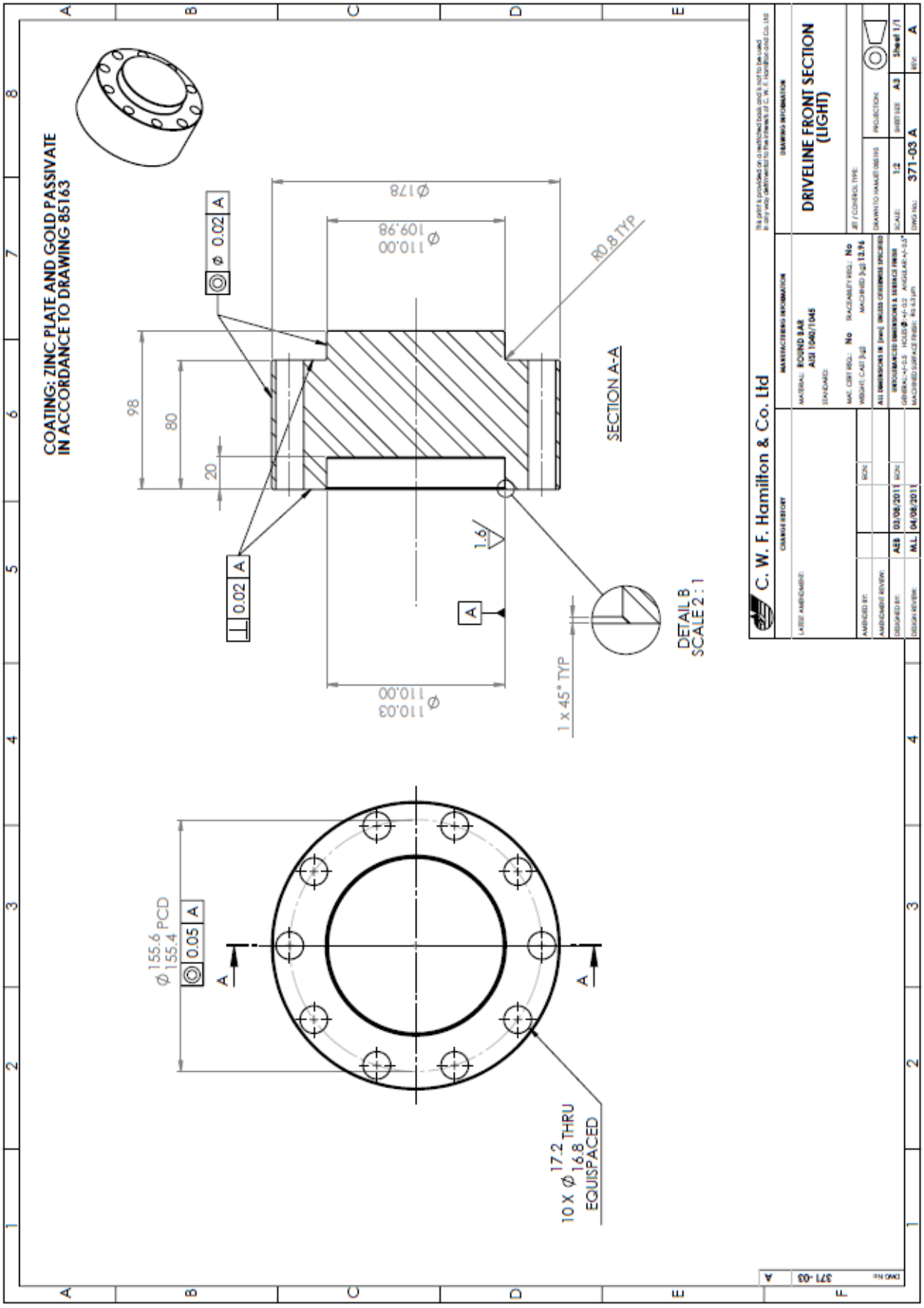

Figure A1.1 – Alternative Driveline Mass Drawing

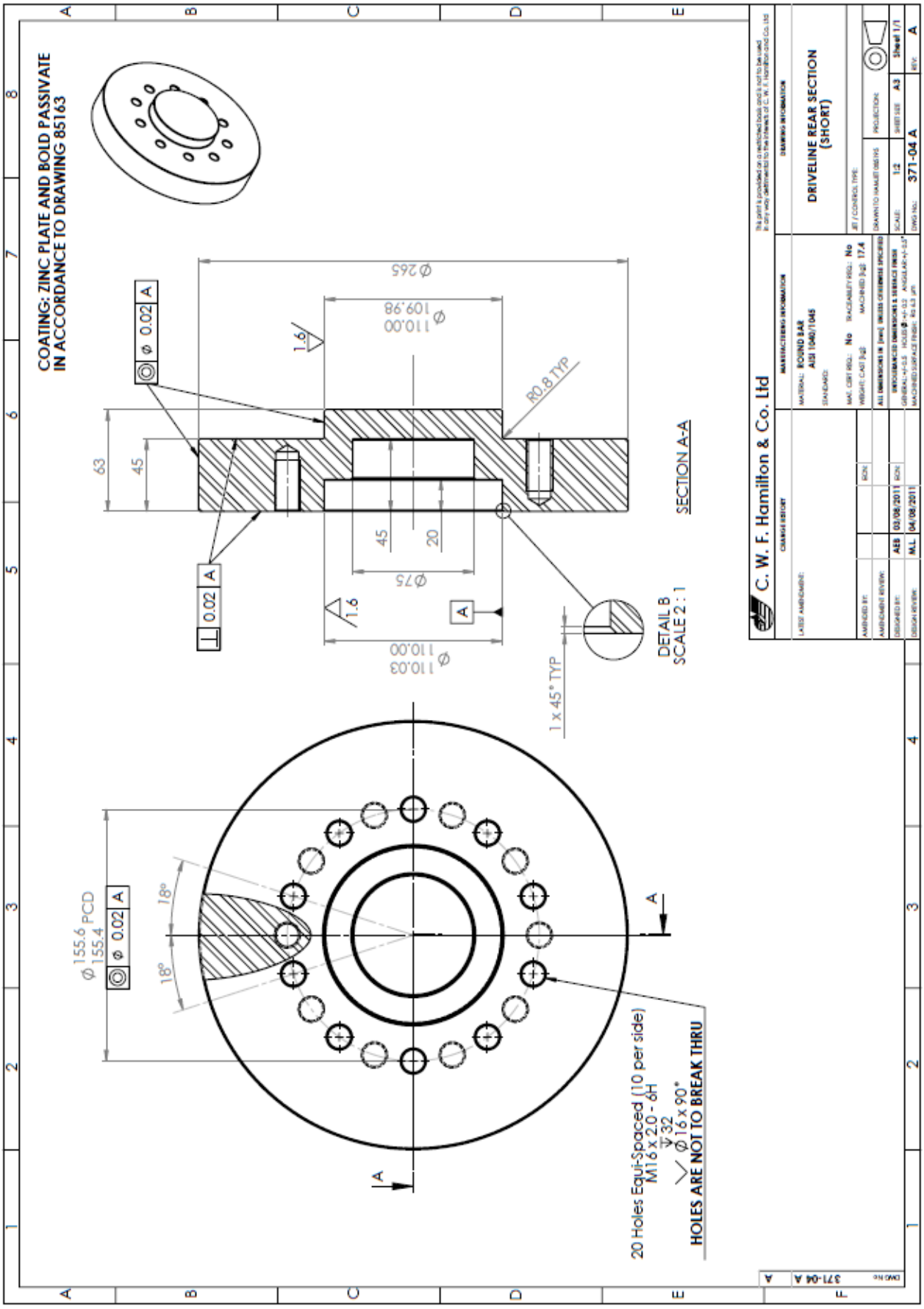

Figure A1.2 – Alternative Driveline Overhang Drawing

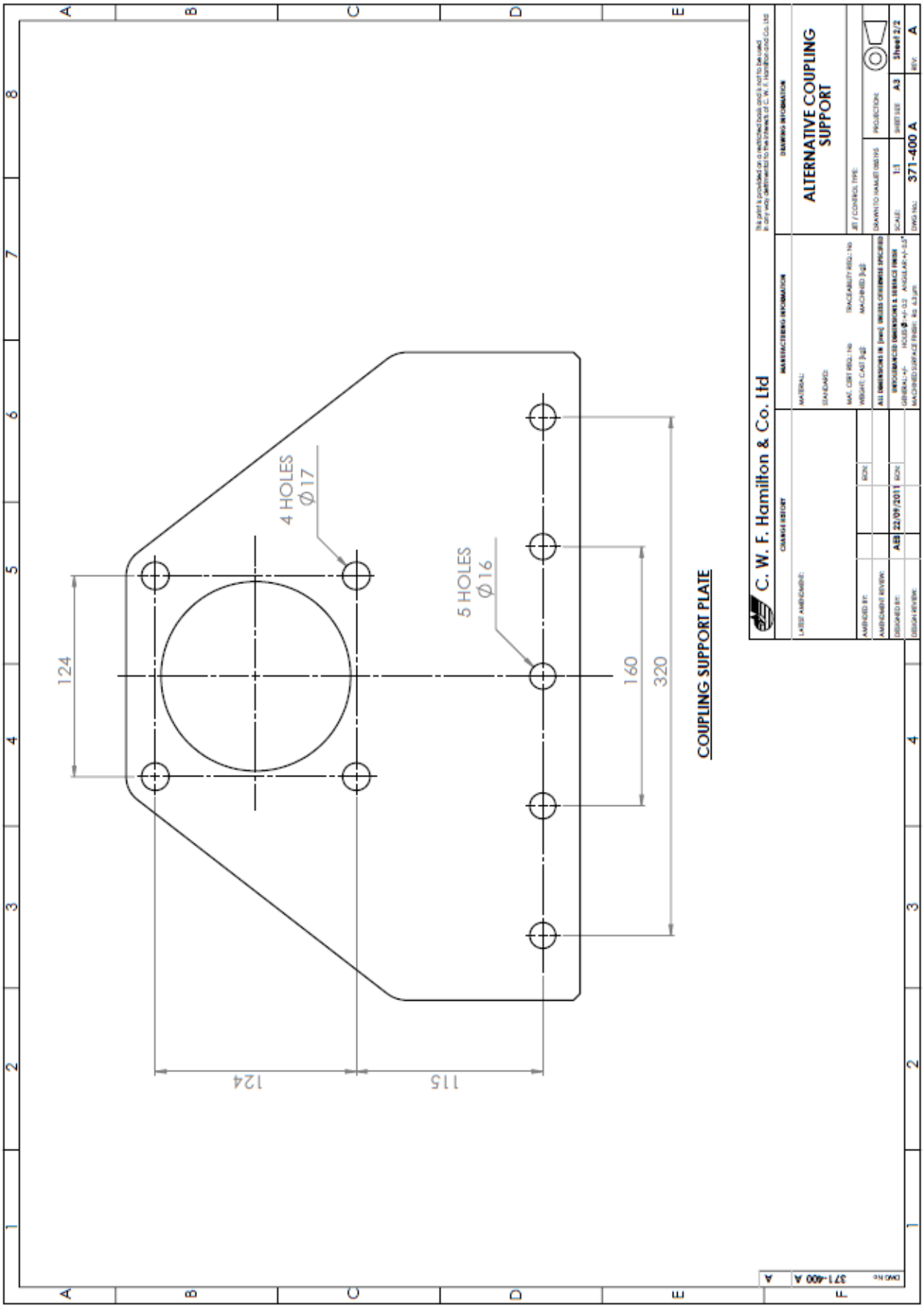

Figure A1.3 – Thrust Bearing Housing Stiffener Plate Drawing

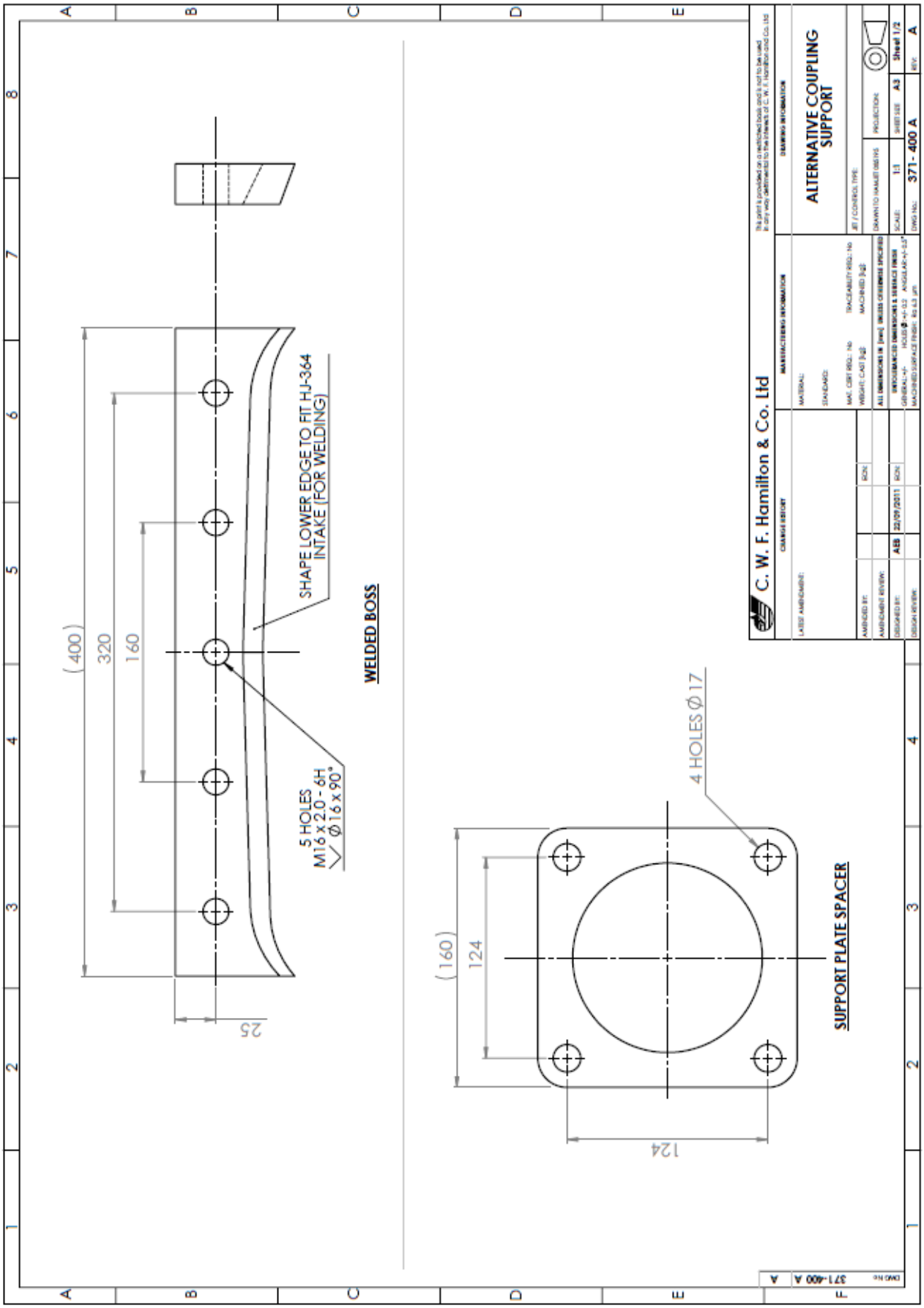

Figure A1.4 – Thrust Bearing Housing Welded Boss and Spacer Drawing

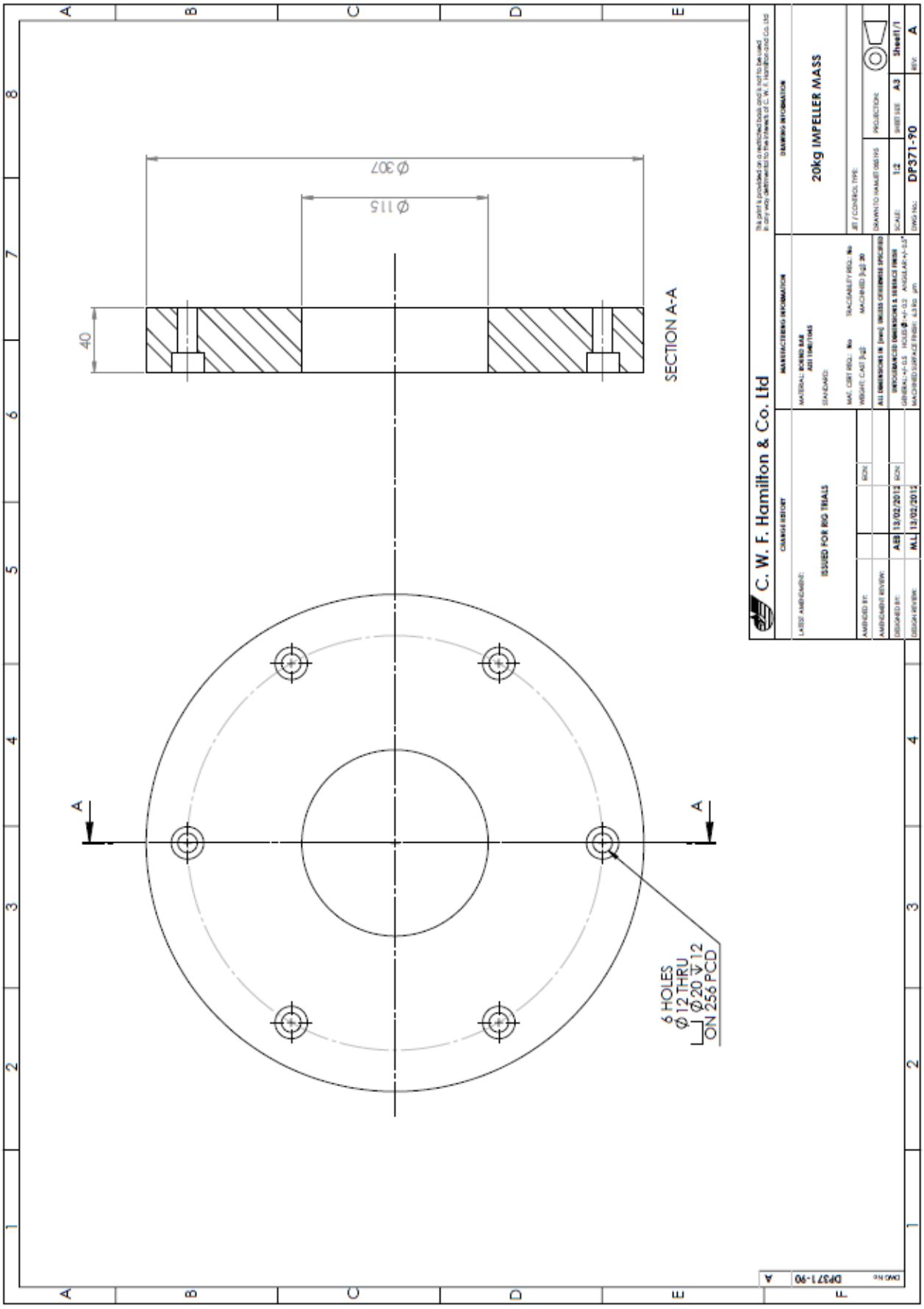

Figure A1.5 – Alternative Impeller Mass Drawing

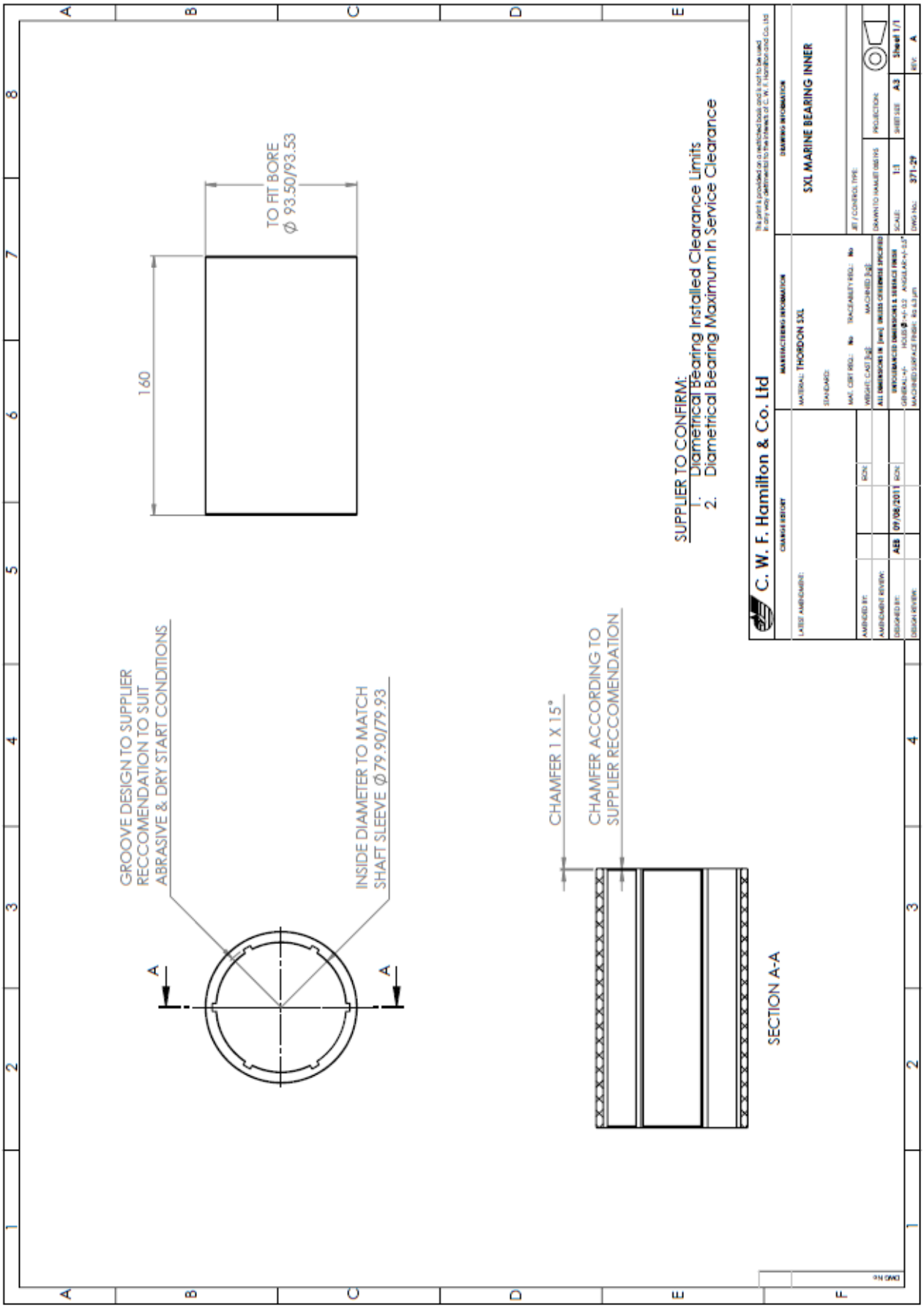

Figure A1.6 – Alternative Marine Bearing Overview (Supplied to Manufacturer)

Thordon Bearings Sizing Calculation Program

No: 205283DS36 V 2006.2
Printed Date: 12/08/2011

THORDON BEARINGS INC.
3225 Mainway Drive, Burlington, Ontario, Canada L7M 1A6
Tel: 905-335-1440 Fax: 905-335-0209, www.thordonbearings.com

General Information

Thordon Distributor:	Pacific Driveline
Customer:	Hamilton Jet
Project Reference:	HamJet Dwg 371-29 Rev A
Calculated By:	Vic
Checked By:	
Comments:	Use F31086 to machine from
Drawing Number:	371-29 Rev A
MRP Number:	

Results

-= ATTENTION =-
Means of axial retention required.
Positive flow of lubricant is required.
Amount of interference increased to increase bearing retention.

	Designed at 21 °C	Machined at 21 °C	
Machined Bearing Inside Diameter:	81.02	81.02 mm	+0.08, -0.00
Machined Bearing Outside Diameter:	94.21	94.21 mm	+0.08, -0.00
Calculated Machined Bearing Length:	158.39	158.39 mm	+0.00, -0.5
Bearing Wall Thickness:	6.60	6.60 mm	(For reference only)
Amount Of Interference:	0.68 mm		
Bore Closure Factor:	1.093		
Bore Closure Amount:	0.81 mm		
Minimum Installed Diametrical Clearance:	0.28 mm		
Diametric Running Clearance:	0.12 mm		
Diametric Thermal Expansion:	0.06 mm		
Diametric Absorption Allowance:	0.10 mm		
Axial Thermal Expansion:	0.81 mm		
Axial Absorption Allowance:	0.80 mm		
Number of Grooves:	8		
Width of Grooves:	6.00 mm		
Depth of Grooves:	3.00 mm		
Pressure on Bearing:	0.077 MPa		
Peripheral Velocity:	25.13 m/sec		
Outside Diameter After Dry Ice Cooling:	93.35 mm		
Outside Diameter After Nitrogen Cooling:	92.30 mm		

Input Data

Dimension Scale:	Metric
Temperature Scale:	Celsius
Maximum Operating Temperature:	45 °C
Minimum Operating Temperature:	-2 °C
Machine Shop Ambient Temperature:	21 °C
Maximum Shaft Diameter:	79.93 mm
Maximum Housing Diameter:	93.53 mm
Minimum Housing Diameter:	93.50 mm
Housing Length:	160.00 mm
Type of Lubrication:	Water
Grade of Thordon Used:	SXL
Type of Service:	Ind. Vertical Pump
Type of Installation:	Interference Freeze Fit
Grooved Bearing Style:	Grooved
Load on Bearing:	100 kg
Shaft RPM:	6000

Figure A1.7 – Properties of the SXL Marine Bearing as provided by the Manufacturer

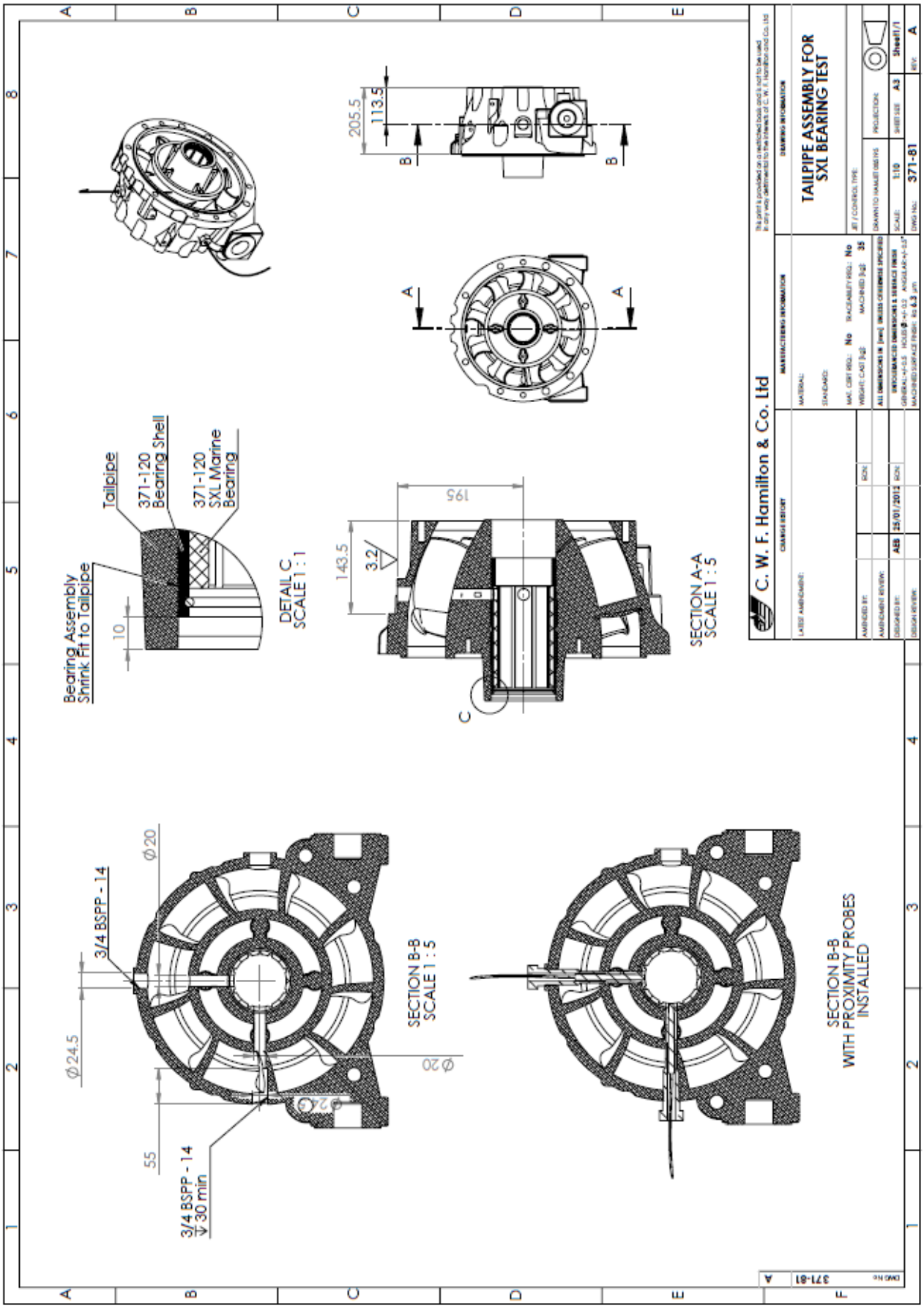

Figure A1.8 – Drawing of SXL Marine Bearing Fitted to Tailpipe

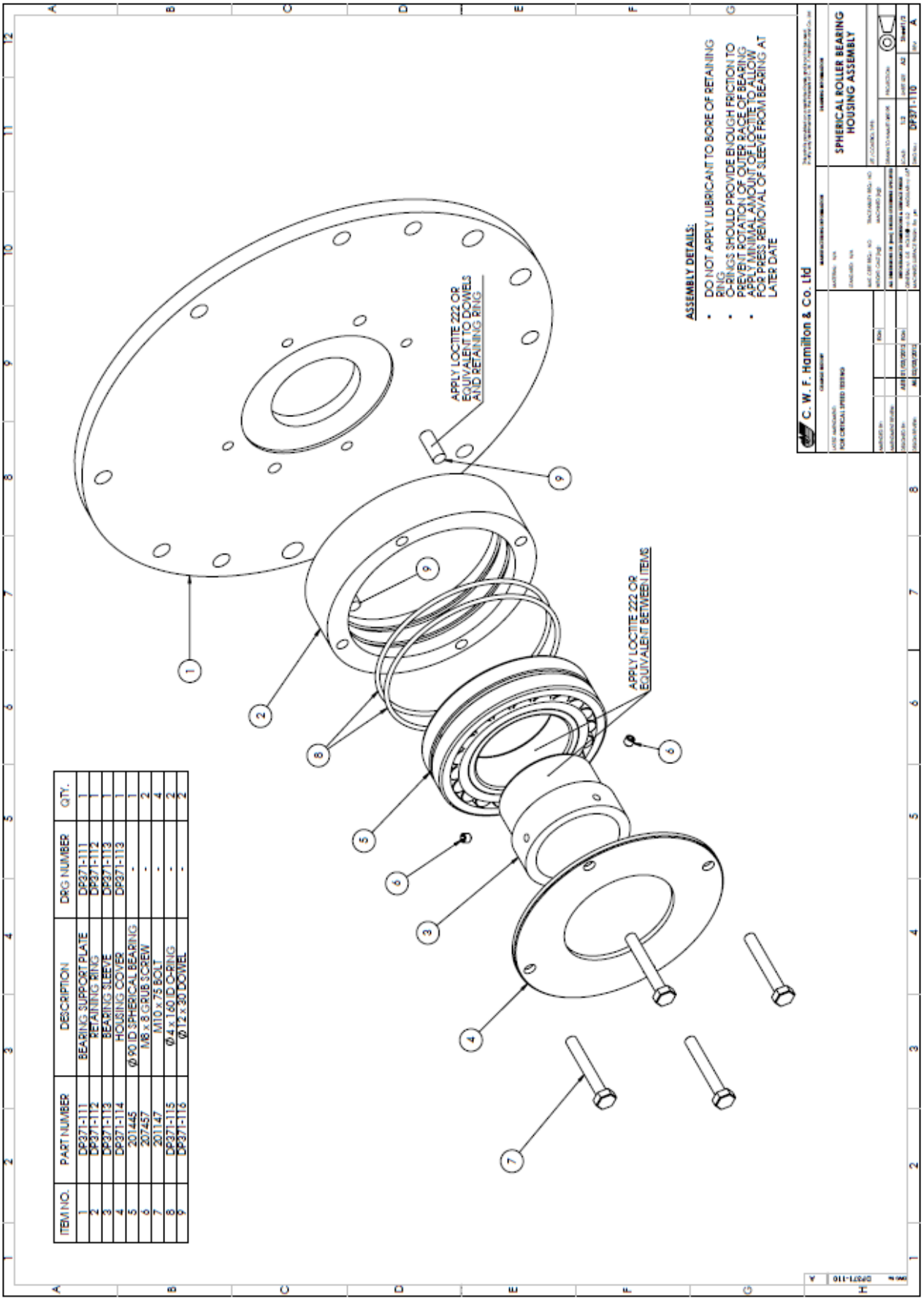

ITEM NO.	PART NUMBER	DESCRIPTION	DRG NUMBER	QTY.
1	DP371-111	BEARING SUPPORT PLATE	DP371-111	1
2	DP371-112	RETAINING RING	DP371-112	1
3	DP371-113	BEARING SLEEVE	DP371-113	1
4	DP371-114	HOUSING COVER	DP371-113	1
5	201445	Ø 90 ID SPHERICAL BEARING	-	1
6	207457	M8 x 8 GRUB SCREW	-	2
7	201147	M10 x 75 BOLT	-	4
8	DP371-115	Ø 4 x 160 ID O-RING	-	2
9	DP371-116	Ø 12 x 30 DOWEL	-	2

Figure A1.9 – Spherical Bearing Housing Exploded View Drawing

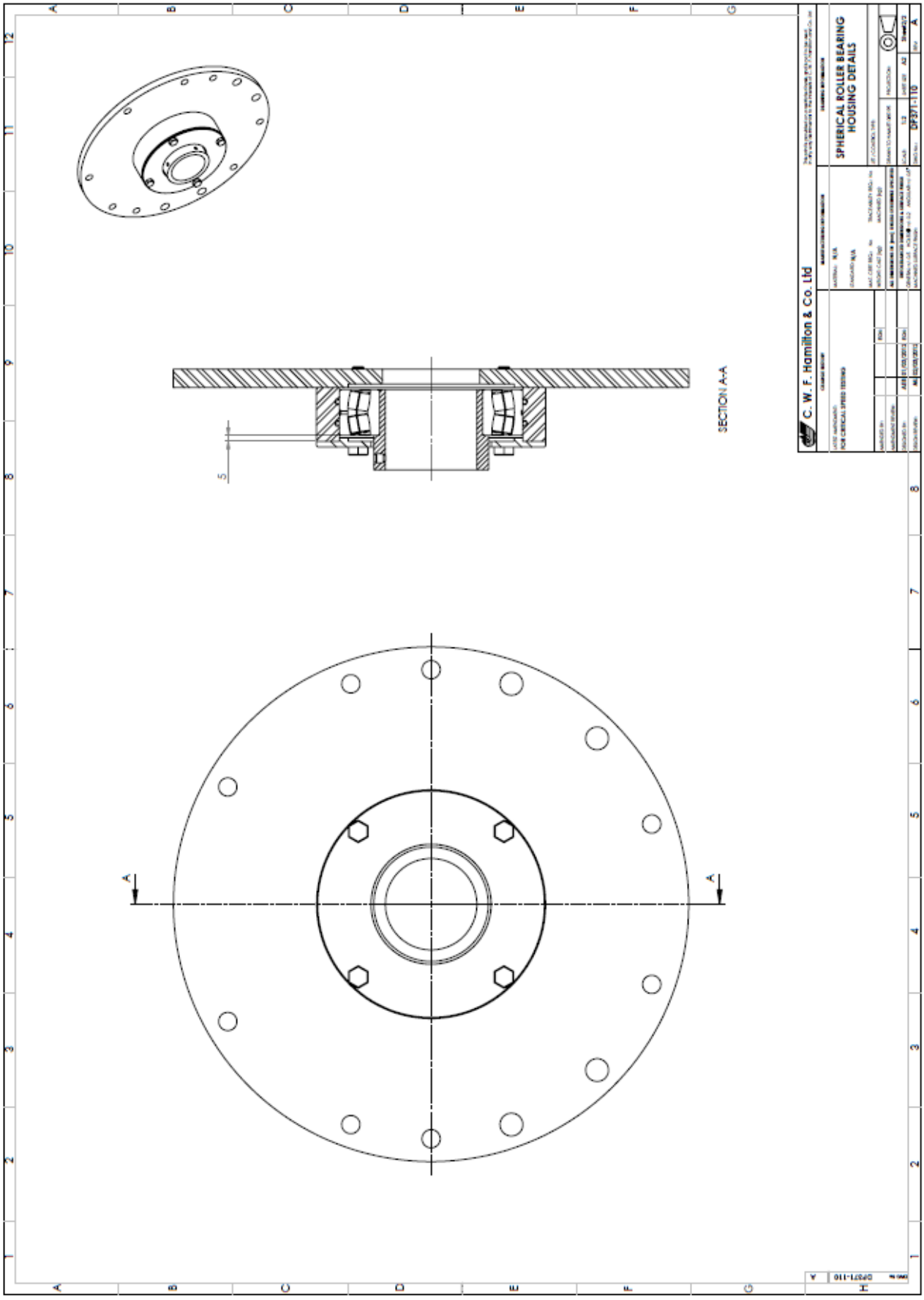

Figure A1.10 – Assembled Spherical Bearing Housing Drawing

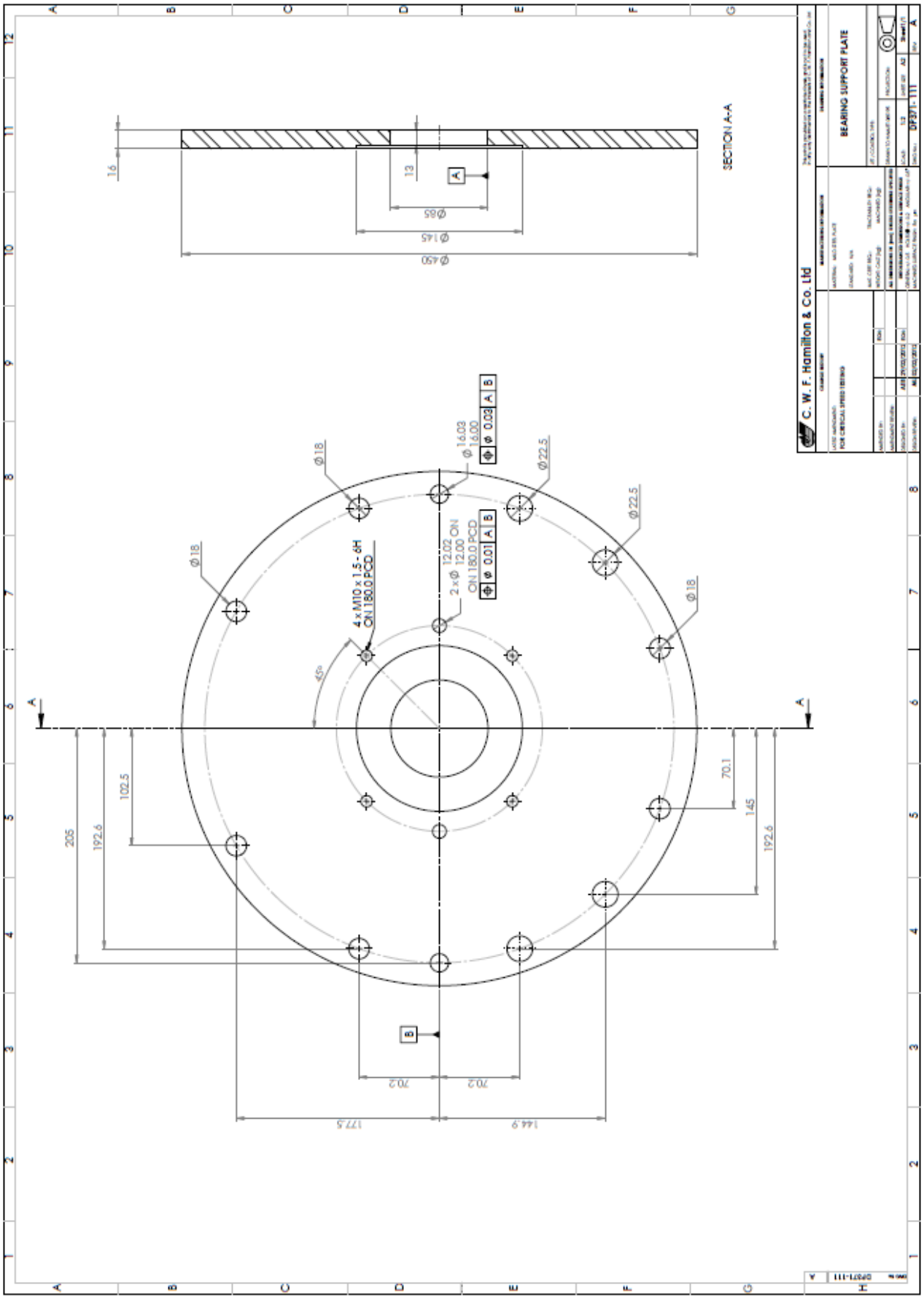

Figure A1.11 – Drawing of the Spherical Bearing Housing Support Plate

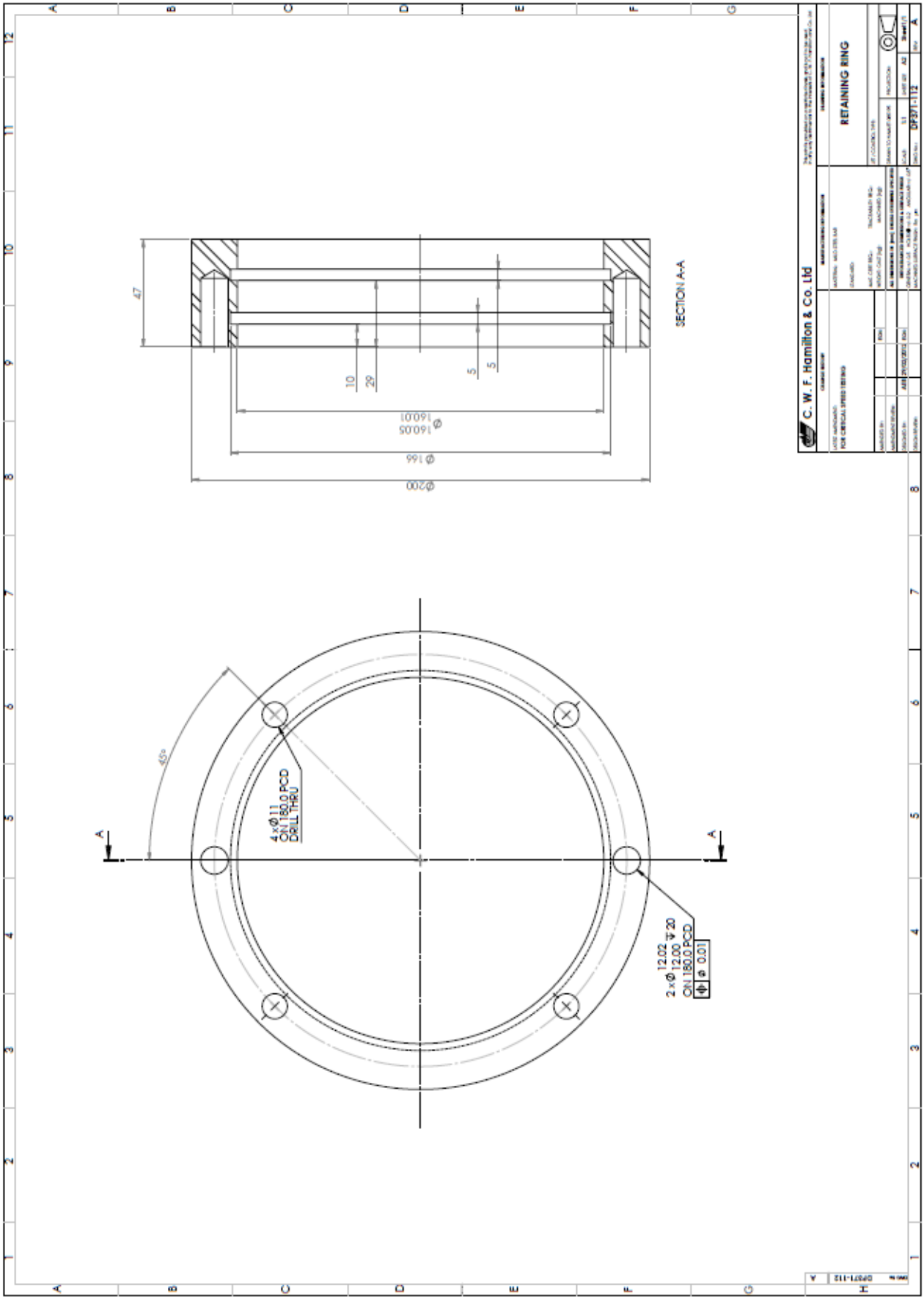

Figure A1.12 – Drawing of the Spherical Bearing Housing Retaining Ring

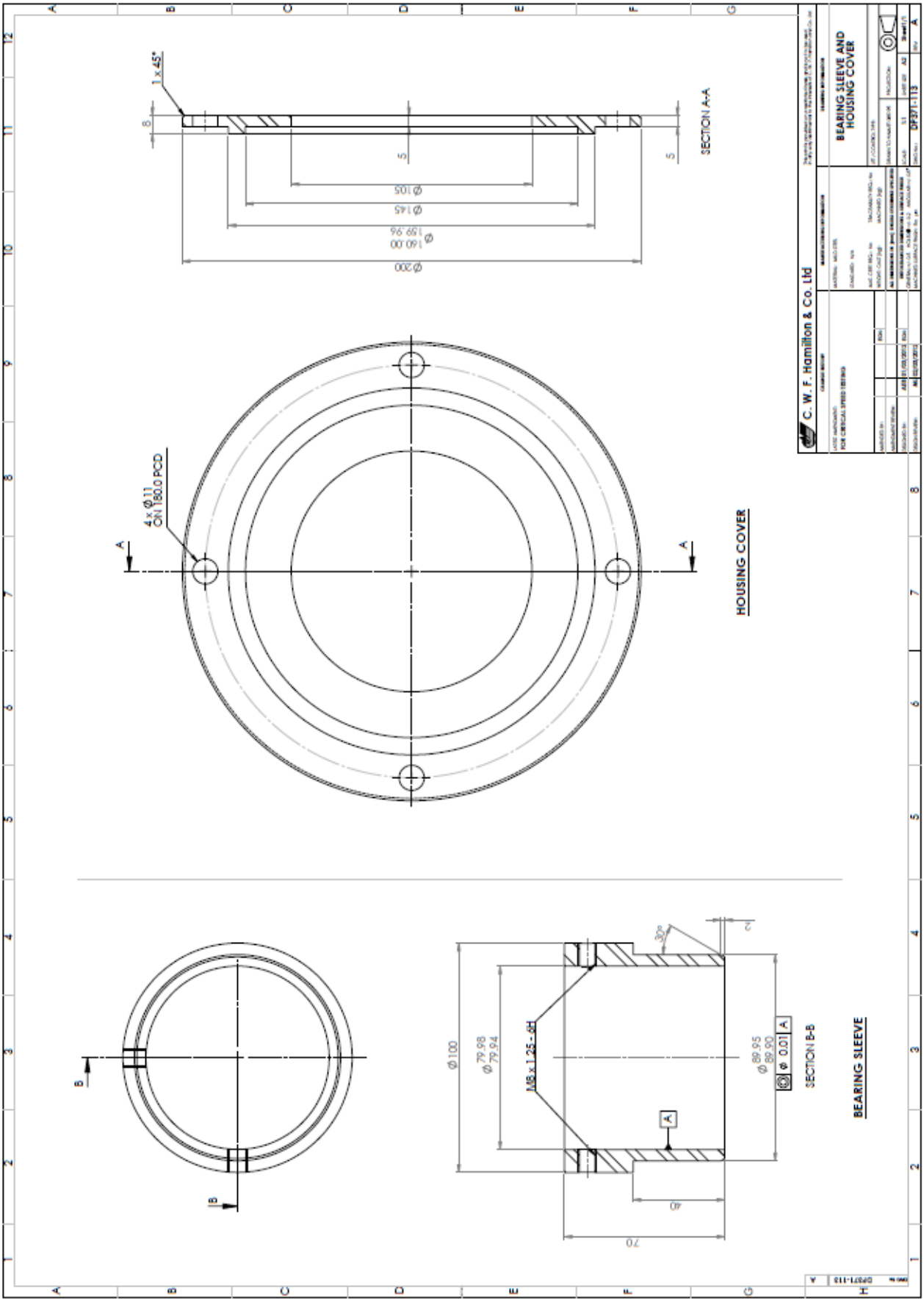

Figure A1.13 – Drawing of the Spherical Bearing Housing Sleeve and Cover

APPENDIX B: MATLAB SCRIPTS

In this section, the various scripts generated for use in Matlab are provided. On page B2, the 'Output Conversion' script is provided .This received the output data from the LabVIEW Acquisition VI and converted it into a native Matlab format. This data was then processed using the script provided on page B5 entitled 'Data Analysis'. Various figures were generated in this script; critical speeds were extracted from these.

On page B21, the script that received two first order Fourier fits and output the properties of a the resulting ellipse is provided. This was used by the 'Data Analysis' script to determine the properties of the orbit of the driveline mass.

On page B23, the 'Transfer-Matrix' script is provided. It was written to receive the properties of a shaft with known internal and external properties, apply dummy end sections and determine the first critical speed iteratively. This was discussed in Section 2 of this thesis.

Finally, on page B29, the script to evaluate critical speeds based on Timoshenko-Beam theory is provided. This is the script used to generate the Timoshenko plots provided in this thesis. It was also discussed in Section 2.

REFERENCE

B1: OUTPUT CONVERSION

```
%%%%%%%%%%%%%%%%%%%%%%%%%%%%%%%%%%%%%%%%%%%%%%%%%%%%%%%%%%%%%%%%%%%%%%%%%%%%%%%%
%%
%                       CRITICAL SPEED RIG - PRE PROCESSING
%%%%%%%%%%%%%%%%%%%%%%%%%%%%%%%%%%%%%%%%%%%%%%%%%%%%%%%%%%%%%%%%%%%%%%%%%%%%%%%%
%%

%                           Author: Ashley Brittenden

% A script that converts .csv data as output by LabVIEW. Data and headers
are % separated and data saved in a native Matlab format. Time data is
converted
% into the appropriate format.

clear
clc

folder_name = {'Test_55'};     % Input the folder name
Max_rpms =     [  4000 ];      % Input the rpm values to be converted
Min_rpms =     [  200 ];
rpm_step_size = 20;


for folder_number = 1:length(folder_name)     % Loop through folder_name
array

    % Calculate the rpm array
    RPM_Array
=Min_rpms(folder_number):rpm_step_size:Max_rpms(folder_number);

    % Operating flags
    Acc_flag = 1;
    Bearing_prox_flag = 0;
    Coupling_prox_flag = 1;

    % File load and save paths
    load_path = ['…\Data\' folder_name{folder_number} '\Raw Data\'];
    save_path = ['…\Data\' folder_name{folder_number} '\Renamed Data\'];

    % Check save paths
    if exist(save_path,'dir')
    else
        mkdir(save_path);
    end

    %% Change Accelerometer Data Names
        if Acc_flag == 1;
        for file_index = 1:length(RPM_Array)

            % Extract data into 'Output' array
            Output = lvm_import([load_path 'Accelerometer_Data_'

            % Create save path
            num2str(RPM_Array(file_index)) 'rpm.lvm']);
            handle = [save_path 'Accelerometer_Data_'
            num2str(RPM_Array(file_index)) 'rpm.mat'];
```

```
        % Calculate time and data arrays
        Acc_Data = Output.Segment1.data;
        StartTime = Output.Segment1.Comment;
        hours = str2num(StartTime(1:2));
        minutes = str2num(StartTime(3:4));
        seconds = str2num(StartTime(5:end));
        Acc_Data(:,1) = Acc_Data(:,1) + seconds + minutes*60 +
        hours*3600;

        % Save data and print status
        save (handle , 'Acc_Data' );
        clc
        fprintf('Current RPM Value is %g.\n', RPM_Array(file_index))
    end
    clc
    disp('Acceleration Data Name Changing Complete')
end



%% Change Bearing Prox Data Names
if Bearing_prox_flag == 1;
    for file_index = 1:length(RPM_Array)

        % Extract data into 'Output' array
        Output = lvm_import([load_path 'Bearing_Prox_Data_'

        % Create save path
        num2str(RPM_Array(file_index)) 'rpm.lvm']);
        handle = [save_path 'Bearing_Prox_Data_'
        num2str(RPM_Array(file_index)) 'rpm.mat'];

        % Calculate time and data arrays
        Bearing_Prox_Data = Output.Segment1.data;
        StartTime = Output.Segment1.Comment;
        hours = str2num(StartTime(1:2));
        minutes = str2num(StartTime(3:4));
        seconds = str2num(StartTime(5:end));
        Bearing_Prox_Data(:,1) = Bearing_Prox_Data(:,1) + seconds +
        minutes*60 + hours*3600;

        % Save data and print status
        save (handle , 'Bearing_Prox_Data' );
        clc
        fprintf('Current RPM Value is %g.\n', RPM_Array(file_index))
    end
    clc
    disp('Bearing Proximity Data Name Changing Complete')
end




%% Change Coupling Prox Data Names
if Coupling_prox_flag == 1;
    for file_index = 1:length(RPM_Array)
```

```
        % Extract data into 'Output' array
        Output = lvm_import([load_path 'Coupling_Prox_Data_'

        % Create save path
        num2str(RPM_Array(file_index)) 'rpm.lvm']);
        handle = [save_path 'Coupling_Prox_Data_'
        num2str(RPM_Array(file_index)) 'rpm.mat'];

        % Calculate time and data arrays
        Coupling_Prox_Data = Output.Segment1.data;
        StartTime = Output.Segment1.Comment;
        hours = str2num(StartTime(1:2));
        minutes = str2num(StartTime(3:4));
        seconds = str2num(StartTime(5:end));
        Coupling_Prox_Data(:,1) = Coupling_Prox_Data(:,1) + seconds +
        minutes*60 + hours*3600;

        % Save data and print status
        save (handle , 'Coupling_Prox_Data' );
        clc
        fprintf('Current RPM Value is %g.\n', RPM_Array(file_index))
    end
    clc
    disp('Coupling Proximity Data Name Changing Complete')
end
```

B2: DATA ANALYSIS

```
%%%%%%%%%%%%%%%%%%%%%%%%%%%%%%%%%%%%%%%%%%%%%%%%%%%%%%%%%%%%%%%%%%%%%%%%%%%%%%%%
%                    CRITICAL SPEED RIG - POST PROCESSING                       %
%%%%%%%%%%%%%%%%%%%%%%%%%%%%%%%%%%%%%%%%%%%%%%%%%%%%%%%%%%%%%%%%%%%%%%%%%%%%%%%%

%                          Author: Ashley Brittenden

% The following code takes the recorded LabVIEW data from the Critical
% Speed Test Rig and performes frequency analysis on the data to create
% 3D response curves. It also creates 3D orbital plots for both the
% water bearing and coupling. These plots are used to illustrate the
% behaviour of the HJ364 shaft.


% This script is will generate all figures and automatically close them
% after.

clc
clear all
close all

% Locate the base path of the converted data
base_path = 'C:\Users\aeb74.UOCNT\Rotordynamic test\Acquired Data\';

% Load a summary file entitled 'summary_of_critical_speeds'
load ([base_path 'Summary_of_Critical_Speeds']);

folder_name = {'Test_55'};    % Input the folder name
for folder_number = 1:length(folder_name)


% ------------------------------------------------------------------------ %
%%                              1. INPUTS
% ------------------------------------------------------------------------ %


% --------------------- FOLDERS AND FILE PATHS ---------------------- %

    Max_rpms =    [  4000 ];  % Input the rpm values to be converted
    Min_rpms =    [  200 ];
    rpm_step_size = 20;

    Accel_File_Path = [base_path folder_name{folder_number} '\Renamed
Data\Accelerometer_Data_'];
    Bearing_Prox_Path = [base_path folder_name{folder_number} '\Renamed
Data\Bearing_Prox_Data_' ];
    Coupling_Prox_Path = [base_path folder_name{folder_number} '\Renamed
Data\Coupling_Prox_Data_'];

    % ------------------------ OPERATING FLAGS ------------------------ %

    %   Accelerometer
    accel_freq_flag = 0;            % Analyse the accelerometer data
    accel_freq_plot_flag = 0; % Extract waterfall plots from data
    extraction_ratio_flag = 0;      % Extract the peak accelerometer values
```

```
    campbell_plot_flag = 0;          % Create Campbell diagram

    %   Bearing Proximity Probes
    bearing_prox_flag = 0;           % Analyse the water bearing  data
    bearing_prox_plot_flag = 0;      % Extract displacement data and plot

    %   Coupling Proximity Probes
    coupling_prox_flag = 1;          % Analyse the coupling displacement
data
    coupling_prox_plot_flag = 0;     % Extract displacement data and plot
    peak_response_detection_flag = 1;  % Extract peak displacement values


    % ----------------------- DATA POINT SELECTION ---------------------- %

    Max_response_frequency = 10000;       % Max frequency for plotting
    Acc_data_min = 1;                % Select the number of accel data
points
    Acc_data_max = 10000;
    Acc_data_points = (Acc_data_max - Acc_data_min + 1);

    Bearing_prox_data_points = 3000;      % Select bearing data points
    Coupling_prox_data_points = 3000;     % Select coupling data points

    % --------------------------- OTHER INPUTS ------------------------- %

    % Properties of Marine Bearing
    bearing_centre = [1.22,-0.72];
    diametral_clearance = 0.5;

    % Select file extensions for figures and concatenate with '.'
    filetype = 'bmp';
    ext = strcat('.',filetype);
    filetype2 = 'fig';
    ext2 = strcat('.',filetype2);
    fullscreen = get(0,'ScreenSize');    % Determine screen size for
plotting

    % Determine position in 'crit_speeds' array for data to be inserted
    for ttl_tests = 1:length(crit_speeds)-1;
        tf =
strfind(crit_speeds{ttl_tests+1,1},folder_name{folder_number});
        if tf == 1
            crit_speed_row = ttl_tests+1;
            break
        end
    end

    % ------------------------------------------------------------------ %
    %%                          2. INITIALISATION
    % ------------------------------------------------------------------ %

    % Select the RPM values of interest

RPM_Values=Min_rpms(folder_number):rpm_step_size:Max_rpms(folder_number);

    % Display status of running folder
    disp(['Running ' folder_name{folder_number}])

    % Open or create a path to save any generate figures
```

```
    path = ([base_path folder_name{folder_number} '\Figures\']);
    if exist(path,'dir')
    else
        mkdir(path);
    end


    % ------------------------------------------------------------------- %
    %%                      3. ACCELEROMETER PROCESSING
    % ------------------------------------------------------------------- %

    % Accelerometer data from the critical speed rig is analysed via FFT to
    % observe the constituent frequencies. Peaks in the frequency response
    % indicate synchronous or asynchronous vibrations.

    if accel_freq_flag == 1

        %Initialise matrices
        Acc_Time = zeros(Acc_data_points,length(RPM_Values));
        Acc_x = zeros(Acc_data_points,length(RPM_Values));
        Acc_y = zeros(Acc_data_points,length(RPM_Values));
        MagXk = zeros(floor(Acc_data_points/2),length(RPM_Values));
        MagYk = zeros(floor(Acc_data_points/2),length(RPM_Values));
        frngx = zeros(floor(Acc_data_points/2),length(RPM_Values));
        frngy = zeros(floor(Acc_data_points/2),length(RPM_Values));
        dt = zeros(1,length(RPM_Values));

        for ii = 1:length(RPM_Values)

            % Load the file for each RPM value. %Accelerometer data is in
the
            % format [time, x_acceleration, y_acceleration]
            load([Accel_File_Path,num2str(RPM_Values(ii)),'rpm.mat']);
            Acc_Data = Acc_Data;

            % Break the loaded data into the corresponding arrays
            Acc_Time(:,ii) = Acc_Data(Acc_data_min:Acc_data_max,1);
            Acc_x(:,ii) = Acc_Data(Acc_data_min:Acc_data_max,3);
            Acc_y(:,ii) = Acc_Data(Acc_data_min:Acc_data_max,2);

            % Calculate time step
            dt(ii) = Acc_Time(2,ii) - Acc_Time(1,ii);

            % Perform FFT and calculate magnitudes and frequencies
            [Mx,f] = DFT(Acc_x(:,ii),dt(ii));
            MagXk(:,ii) = Mx(1:floor(Acc_data_points/2));
            frngx(:,ii) = f(1:floor(Acc_data_points/2));

            [My,f] = DFT(Acc_y(:,ii),dt(ii));
            MagYk(:,ii) = My(1:floor(Acc_data_points/2));
            frngy(:,ii) = f(1:floor(Acc_data_points/2));

            % Clear the DC Offsets
            MagXk(1,ii) = 0;
            MagYk(1,ii) = 0;

        end
    end
```

```
    % ---------------------------------------------------------------------- %
    %%                 4. BEARING PROXIMITY PROBE PROCESSING
    % ---------------------------------------------------------------------- %

    % Proximity probes are installed on the rig, and are to be used to
    % determine the orbit plots of the shaft. This will illustrate if any
    % elliptical whirling is occuring, or rubbing is occuring in the water
    % bearing.

    if bearing_prox_flag == 1

        % Initialise time and data arrays

Bearing_Prox_Time=zeros(Bearing_prox_data_points,length(RPM_Values));
        Bearing_Prox_1 =
zeros(Bearing_prox_data_points,length(RPM_Values));
        Bearing_Prox_2 =
zeros(Bearing_prox_data_points,length(RPM_Values));

        % Initialise whirl orbit property arrays
        Bearing_A = zeros(length(RPM_Values),1);     % Major axis of
ellipse
        Bearing_B = zeros(length(RPM_Values),1);     % Minor axis of
ellipse
        Bearing_THETA = zeros(length(RPM_Values),1); % Rotation of ellipse
        Bearing_Fourier_Centre = zeros(length(RPM_Values),2);   % Centre

        for ii = 1:length(RPM_Values)

            load([Bearing_Prox_Path,num2str(RPM_Values(ii)),'rpm.mat']);
            Bearing_Prox_Data = Bearing_Prox_Data;

            % Extracting and renaming data (for clarity)
            Bearing_Prox_Time(:,ii)=Bearing_Prox_Data(1:Bearing_prox_data_p
            oints,1)- Bearing_Prox_Data(1,1);
            Bearing_Prox_1(:,ii)=Bearing_Prox_Data(1:Bearing_prox_data_poin
            ts,2) - bearing_centre(1);
            Bearing_Prox_2(:,ii)=Bearing_Prox_Data(1:Bearing_prox_data_poin
            ts,3) - bearing_centre(2);

            % Applying a first order fourier fit to extracted data
            f1
            =fit(Bearing_Prox_Time(:,ii),Bearing_Prox_1(:,ii),'fourier1');
            Bearing_Prox_1(:,ii) = f1(Bearing_Prox_Time(:,ii));

            f2
            =fit(Bearing_Prox_Time(:,ii),Bearing_Prox_2(:,ii),'fourier1');
            Bearing_Prox_2(:,ii) = f2(Bearing_Prox_Time(:,ii));

            % Maintain continuity in Bearing_THETA array
            if ii == 1
                theta_close = 0;
            else
                theta_close = Bearing_THETA(ii-1);
            end

            % Extract major axis, minor axis, angle and centre from
            % 'ellipse_from_fourier' function
            [Bearing_A(ii),Bearing_B(ii),Bearing_THETA(ii),Bearing_Fourier_
            Centre(ii,:)] = ellipse_from_fourier(f1,f2,theta_close);
```

```
        end
    end


    % ------------------------------------------------------------------- %
    %%                  5. COUPLING PROXIMITY PROBE PROCESSING
    % ------------------------------------------------------------------- %

    % Proximity probes are installed on the rig, and are to be used to
    % determine the orbit plots of the shaft. This will illustrate if any
    % elliptical whirling is occuring, or rubbing is occuring in the water
    % bearing.

    if coupling_prox_flag == 1

        % Initialise time and data arrays

Coupling_Prox_Time=zeros(Coupling_prox_dat_points,length(RPM_Values))
        Coupling_Prox_1=
zeros(Coupling_prox_data_points,length(RPM_Values));
        Coupling_Prox_2=
zeros(Coupling_prox_data_points,length(RPM_Values));

        % Initialise whirl orbit property arrays
        Coupling_A = zeros(length(RPM_Values),1);
        Coupling_B = zeros(length(RPM_Values),1);
        Coupling_THETA = zeros(length(RPM_Values),1);
        Coupling_Fourier_Centre = zeros(length(RPM_Values),2);

        for ii = 1:length(RPM_Values)

            load([Coupling_Prox_Path,num2str(RPM_Values(ii)),'rpm.mat']);
            Coupling_Prox_Data = Coupling_Prox_Data;

            %Extracting and renaming data (for clarity)
            Coupling_Prox_Time(:,ii)=Coupling_Prox_Data(1:Coupling_prox_dat
            a_points,1)- Coupling_Prox_Data(1,1);
            Coupling_Prox_1(:,ii)=Coupling_Prox_Data(1:Coupling_prox_data_p
            oints,2);
            Coupling_Prox_2(:,ii)=Coupling_Prox_Data(1:Coupling_prox_data_p
            oints,3);

            % Applying a first order fourier fit to extracted data
            f3=fit(Coupling_Prox_Time(:,ii),Coupling_Prox_1(:,ii),'fourier1
            ')
            Coupling_Prox_1_F(:,ii) = f3(Coupling_Prox_Time(:,ii));
            f4=fit(Coupling_Prox_Time(:,ii),Coupling_Prox_2(:,ii),'fourier1
      ')
            Coupling_Prox_2_F(:,ii) = f4(Coupling_Prox_Time(:,ii));



            % Maintain continuity in Coupling_THETA array
            if ii == 1
                theta_close = 0;
            else
                theta_close = Coupling_THETA(ii-1);
            end
```

```
            % Extract major axis, minor axis, angle and centre from
            % 'ellipse_from_fourier' function
            [Coupling_A(ii),Coupling_B(ii),Coupling_THETA(ii),Coupling_Four
            ier_Centre(ii,:)] = ellipse_from_fourier(f3,f4,theta_close);

            % Compensate for angle of proximity probes
            Coupling_THETA(ii) = Coupling_THETA(ii) - pi/4;

        end
    end


% ------------------------------------------------------------------- %
%%                      6. 3D FREQUENCY ANALSYIS PLOTS
% ------------------------------------------------------------------- %

    if accel_freq_plot_flag == 1

        num_freq_points = ceil(Max_response_frequency/(60*frngx(2,1)));

        % If data at only one rpm has been selected, create 2D plot
        if length(RPM_Values) == 1

            % Create 2D plot of horizontally aligned accelerometer data
            figure('Position',[fullscreen(3)/2-600 fullscreen(4)/2-350 1200
            700])
            plot(frngx(1:num_freq_points)*60 , MagXk(1:num_freq_points));
            title(['Frequency Response X ',num2str(RPM_Values),
            'rpm'],'FontSize',18)
            xlabel('Frequency Response (rpm)','FontSize',16)
            ylabel('Magnitude','FontSize',16)
            grid on

            % Create 2D plot of vertically aligned accelerometer data
            figure('Position',[fullscreen(3)/2-600 fullscreen(4)/2-350 1200
            700])
            plot(frngy(1:num_freq_points)*60 , MagYk(1:num_freq_points));
            title(['Frequency Response Y ',num2str(RPM_Values),
            'rpm'],'FontSize',18)
            xlabel('Frequency Response (rpm)','FontSize',16)
            ylabel('Magnitude','FontSize',16)
            grid on







        else
            % Create 3D 'Waterfall Plots' of the accelereometer data

            close all   % Close all figure windows

            % Create Waterfall plot of horizontally aligned accelerometer
            figure('Position',[fullscreen(3)/2-600 fullscreen(4)/2-350 1200
            700])
            waterfall(frngx(25:num_freq_points,1)*60 , RPM_Values ,
            MagXk(25:num_freq_points,:)')
```

```
            view(12,30)
            title('X Response Surface','FontSize',18)
            xlabel('Frequency Response (rpm)','FontSize',16)
            ylabel('Driven Frequency (rpm)','FontSize',16)
            zlabel('Magnitude [mm/s^2]','FontSize',16)
            saveas(gcf,[path, 'X Waterfall Plot', ext], filetype)
            saveas(gcf,[path, 'X Waterfall Plot', ext2], filetype2)
            close

            % Create Waterfall plot of vertically aligned accelerometer
            figure('Position',[fullscreen(3)/2-600 fullscreen(4)/2-350 1200
            700])
            waterfall(frngy(25:num_freq_points,1)*60 , RPM_Values ,
            MagYk(25:num_freq_points,:)')
            view(12,30)
            title('Y Response Surface','FontSize',18)
            xlabel('Frequency Response (rpm)','FontSize',16)
            ylabel('Driven Frequency (rpm)','FontSize',16)
            zlabel('Magnitude [mm/s^2]','FontSize',16)
            saveas(gcf,[path, 'Y Waterfall Plot', ext], filetype)
            saveas(gcf,[path, 'Y Waterfall Plot', ext2], filetype2)
            close

        end
    end


% ------------------------------------------------------------------- %
%%                   6. 3D FREQUENCY RATIO EXTRACTION
% ------------------------------------------------------------------- %

% Extract data along the synchronous peak from each waterfall plot to
% determine the peak response and therefore determine the first critical
% speed from accelerometers due to unbalance

      if extraction_ratio_flag == 1

        % Determine the number of points in the frequency data
        num_freq_points = ceil(Max_response_frequency/(60*frngx(2,1)));


        % Extracting Data from Horizontally Aligned Accelerometer Waterfall
        for ratio = 1         % Synchronous excitation ratio


            %Intialise arrays
            response_freq = frngx(1:num_freq_points,1)*60;
            magnitudes = MagXk(1:num_freq_points,:)';
            magnitudes(:,1:25) = 0;

            % Create string for save path
            save_name = ['X Response Comparisons along excitation ratio '
            num2str(ratio)];

            % Constant to generalise the script (not used here)
            constant = 0;

            % Perform the search process by comparing the search_rpms with
            % those in the waterfall plot
            for ii = 1:length(RPM_Values)
```

```
        for jj = 1:length(ratio)
            search_rpm = RPM_Values(ii) * ratio(jj) + constant(jj);
            [~,base_index] = min(abs(response_freq - search_rpm));
            for kk = 1:6
                break_loop = 0;
                if base_index+kk-3 > num_freq_points
                    break_loop = 1;
                    break
                end
                possible_maximum(kk) = magnitudes(ii,base_index+kk-
                3);
            end

            value_array(ii,1) = RPM_Values(ii);

            if break_loop ~= 1
                [~,actual_index] = min(abs(magnitudes(ii,:)-
                max(possible_maximum)));
                value_array(ii,jj+1) = magnitudes(ii,actual_index);
            else
                value_array(ii,jj+1) = 0;
            end
        end
    end

    % Open a figure, plot the extracted data and compare to the
    % original data stored in 'X_RATIO1_NOM'
    figure('Position',[fullscreen(3)/2-600 fullscreen(4)/2-350 1200
    700])
    axes('FontSize',12)
    load X_RATIO1_NOM
    plot(value_array(:,1),value_array(:,2:length(ratio)+1),'b-
    ',X_RATIO1_NOM(:,1),X_RATIO1_NOM(:,2),'r-','LineWidth',5)
    title(['Magnitude Comparisons along excitation ratio '
    num2str(ratio) ' from X Waterfall'],'FontSize',18)
    xlabel('Rotational Velocity (rpm)','FontSize',16)
    ylabel('Response mm/s^2','FontSize',16)
    legend('Current Test','Original Test','Location','NorthWest')
    xlim([1000 4000])
    grid on

    % Extract the peak value from this figure
    [magnitude,location] = max(value_array(:,2:length(ratio)+1));
    text(value_array(location,1),magnitude,[num2str(magnitude) ' at
    ' num2str(value_array(location,1)) 'rpm
    \rightarrow'],'FontSize',16,'HorizontalAlignment','right')

    % Save the figure under the filetypes specified earlier
    saveas(gcf,[path, save_name, ext], filetype)
    saveas(gcf,[path, save_name, ext2], filetype2)
    close

    % Store the peak values in the 'crit_speeds' storage array
    if ratio == 1
        crit_speeds{crit_speed_row,6} = value_array(location,1);
        crit_speeds{crit_speed_row,7} = magnitude;
    end

end
```

```
% Extracting Data from Vertically Aligned Accelerometer Waterfall
for ratio = 1

    %Intialise arrays
    response_freq = frngy(1:num_freq_points,1)*60;
    magnitudes = MagYk(1:num_freq_points,:)';
    magnitudes(:,1:25) = 0;

    % Create string for save path
    save_name = ['Y Response Comparisons along excitation ratio '
    num2str(ratio)];

    % Constant to generalise the script (not used here)
    constant = 0;

    % Perform the search process by comparing the search_rpms with
    % those in the waterfall plot
    for ii = 1:length(RPM_Values)
        for jj = 1:length(ratio)
            search_rpm = RPM_Values(ii) * ratio(jj) + constant(jj);
            [~,base_index] = min(abs(response_freq - search_rpm));
            for kk = 1:6
                break_loop = 0;
                if base_index+kk-3 > num_freq_points
                    break_loop = 1;
                    break
                end
                possible_maximum(kk) = magnitudes(ii,base_index+kk-
                3);
            end

            value_array(ii,1) = RPM_Values(ii);



            if break_loop ~= 1
                [~,actual_index] = min(abs(magnitudes(ii,:)-
                max(possible_maximum)));
                value_array(ii,jj+1) = magnitudes(ii,actual_index);
            else
                value_array(ii,jj+1) = 0;
            end
        end
    end

    % Open a figure, plot the extracted data and compare to the
    % original data stored in 'Y_RATIO1_NOM'
    figure('Position',[fullscreen(3)/2-600 fullscreen(4)/2-350 1200
    700])
    axes('FontSize',12)
    load Y_RATIO1_NOM
    plot(value_array(:,1),value_array(:,2:length(ratio)+1),'b-
    ',Y_RATIO1_NOM(:,1),Y_RATIO1_NOM(:,2),'r-','LineWidth',5)
    title(['Magnitude Comparisons along excitation ratio '
    num2str(ratio) ' from Y Waterfall'],'FontSize',18)
    xlabel('Rotational Velocity (rpm)','FontSize',16)
    ylabel('Response mm/s^2','FontSize',16)
    legend('Current Test','Original Test','Location','NorthWest')
```

```
            xlim([1000 4000])
            grid on

            % Extract the peak value from this figure
            [magnitude,location] = max(value_array(:,2:length(ratio)+1));
            text(value_array(location,1),magnitude,[num2str(magnitude) ' at
            ' num2str(value_array(location,1)) 'rpm
            \rightarrow'],'FontSize',16,'HorizontalAlignment','right')

            % Save the figure under the filetypes specified earlier
            saveas(gcf,[path, save_name, ext], filetype)
            saveas(gcf,[path, save_name, ext2], filetype2)
            close

            % Store the peak values in the 'crit_speeds' storage array
            if ratio == 1
                crit_speeds{crit_speed_row,8} = value_array(location,1);
                crit_speeds{crit_speed_row,9} = magnitude;
            end

        end

    end
```

```
% ------------------------------------------------------------------- %
%%                        7. 3D BEARING ORBIT PLOTS
% ------------------------------------------------------------------- %

% Create a plot of the bearing data by combining the output of the two
% proximity probes.

    if bearing_prox_plot_flag == 1

        if length(RPM_Values) == 1

            % Create a 2D Orbit Plot of the data if only one RPM is
            required % simply by combining the output data (independent of
            time - data % is that obtained with the fourier fit
            figure('Position',[fullscreen(3)/2-600 fullscreen(4)/2-350 1200
            700])
            plot(Bearing_Prox_1,Bearing_Prox_2)
            title(['Bearing Orbit Plot at
            ',num2str(RPM_Values),'rpm'],'FontSize',18)
            xlabel('X Coordinate (mm)','FontSize',16)
            ylabel('Y Coordinate (mm)','FontSize',16)
            axis equal
            grid on

        else
```

```
% Create a 3D Orbit Plot of the data simply by combining the
output data (independent of time - data is that obtained with
the fourier fit

% Initialise an array
[xx,yy] = size(Bearing_Prox_1);
X = zeros(xx*yy,1);
Y = zeros(xx*yy,1);

% Combine the data into two vectors and a 2D array (required by
% the scatter3 plot function).
for ii = 1:yy
    X(ii*xx-xx+1:ii*xx,1) = Bearing_Prox_1(:,ii);
    Y(ii*xx-xx+1:ii*xx,1) = Bearing_Prox_2(:,ii);
    Z(ii*xx-xx+1:ii*xx,1) = RPM_Values(ii);
end

% Create a figure and then make a 3D plot using the inbuilt
% scatter3 function
figure('Position',[fullscreen(3)/2-600 fullscreen(4)/2-350 1200
700])
scatter3(Z,X,Y,5)
title(['Bearing Orbit Plot from ',num2str(RPM_Values(1)),'rpm
to ',num2str(RPM_Values(end)),'rpm'],'FontSize',18)
xlabel('Shaft Speed (rpm)','FontSize',16)
ylabel('X Coordinate (mm)','FontSize',16)
zlabel('Y Coordinate (mm)','FontSize',16)
view(-10,40)      % View the plot from an appropriate angle


% Save the figure under the filetypes specified earlier
saveas(gcf,[path, 'Bearing Orbit Plot (Perspective)', ext],
filetype)
saveas(gcf,[path, 'Bearing Orbit Plot (Perspective)', ext2],
filetype2)

% View the end of the 3D plot to examine orbit shape; Save the
% figure under the filetypes specified earlier
view(-90,0)
saveas(gcf,[path, 'Bearing Orbit Plot (End View)', ext],
filetype)
saveas(gcf,[path, 'Bearing Orbit Plot (End View)', ext2],
filetype2)
close

% Create a 2 part subplot of top down and front view of scatter
% plot to check peak displacement in each of these planes; save
% the figure under the filetypes specified earlier
figure('Position',[fullscreen(3)/2-600 fullscreen(4)/2-350 1200
700])
subplot(2,1,1)
scatter3(Z,X,Y,5)
view(0,90)
title('Bearing Orbit Components','FontSize',18)
ylabel('X Displacement (mm)','FontSize',16)
xlim([1000 4000])

subplot(2,1,2)
scatter3(Z,X,Y,5)
view(0,0)
zlabel('Y Displacement (mm)','FontSize',16)
```

```
            xlabel('Shaft Speed (rpm)','FontSize',16)
            xlim([1000 4000])
            saveas(gcf,[path, 'Bearing Orbit Components', ext], filetype)
            saveas(gcf,[path, 'Bearing Orbit Components', ext2], filetype2)
            close

        end
    end
```

```
% ------------------------------------------------------------------- %
%%                        8. 3D COUPLING ORBIT PLOTS
% ------------------------------------------------------------------- %

% Create a plot of the bearing data by combining the output of the two
% proximity probes.

    if coupling_prox_plot_flag == 1

        if length(RPM_Values) == 1

            % Create a 2D Orbit Plot of the data if only one RPM is
            required % simply by combining the output data (independent of
            time - data % is that obtained with the fourier fit
            figure('Position',[fullscreen(3)/2-600 fullscreen(4)/2-350 1200
            700])
            plot(Coupling_Prox_1,Coupling_Prox_2,'b',Coupling_Prox_1_F,Coup
            ling_Prox_2_F,'r','linewidth',2)
            title([‘Coupling Orbit Plot at
            ',num2str(RPM_Values),'rpm'],'FontSize',18)
            xlabel('X Coordinate (mm)','FontSize',16)
            ylabel('Y Coordinate (mm)','FontSize',16)
            axis equal
            grid on

        else

            % Create a 3D Orbit Plot of the data simply by combining the
            output data (independent of time - data is that obtained with
            the fourier fit

            % Initialise an array
            [xx,yy] = size(Coupling_Prox_1);
            X = zeros(xx*yy,1);
            Y = zeros(xx*yy,1);
```

```
            Z = zeros(xx*yy,1);

            % Combine the data into two vectors and a 2D array (required by
            % the scatter3 plot function).
            for ii = 1:yy
                X(ii*xx-xx+1:ii*xx,1) = Coupling_Prox_1(:,ii);
                Y(ii*xx-xx+1:ii*xx,1) = Coupling_Prox_2(:,ii);
                Z(ii*xx-xx+1:ii*xx,1) = RPM_Values(ii);
            end

            % Create a figure and then make a 3D plot using the inbuilt
            % scatter3 function
            figure('Position',[fullscreen(3)/2-600 fullscreen(4)/2-350 1200
            700])
            scatter3(Z,X,Y,5)
            title(['Coupling Orbit Plot from ',num2str(RPM_Values(1)),'rpm
            to ',num2str(RPM_Values(end)),'rpm'],'FontSize',18)
            xlabel('Shaft Speed (rpm)','FontSize',16)
            ylabel('X Coordinate (mm)','FontSize',16)
            zlabel('Y Coordinate (mm)','FontSize',16)
            view(-10,40)      % View the plot from an appropriate angle
            % Save the figure under the filetypes specified earlier
            saveas(gcf,[path, 'Coupling Orbit Plot (Perspective)', ext],
            filetype)
            saveas(gcf,[path, 'Coupling Orbit Plot (Perspective)',
            ext2],filetype2)

            % View the end of the 3D plot to examine orbit shape; Save the
            % figure under the filetypes specified earlier
            view(-90,0)
            saveas(gcf,[path, 'Coupling Orbit Plot (End View)', ext],
            filetype)
            saveas(gcf,[path, 'Coupling Orbit Plot (End View)', ext2],
            filetype2)
            close

            % Create a 2 part subplot of top down and front view of scatter
            % plot to check peak displacement in each of these planes; save
            % the figure under the filetypes specified earlier
            figure('Position',[fullscreen(3)/2-600 fullscreen(4)/2-350 1200
            700])
            subplot(2,1,1)
            scatter3(Z,X,Y,5)
            view(0,90)
            title('Coupling Orbit Components','FontSize',18)
            ylabel('X Displacement (mm)','FontSize',16)
            xlim([1000 4000])

            subplot(2,1,2)
            scatter3(Z,X,Y,5)
            view(0,0)
            zlabel('Y Displacement (mm)','FontSize',16)
            xlabel('Shaft Speed (rpm)','FontSize',16)
            xlim([1000 4000])
            saveas(gcf,[path, 'Coupling Orbit Components', ext], filetype)
            saveas(gcf,[path, 'Coupling Orbit Components', ext2],
filetype2)
            close

        end
    end
```

```
% ------------------------------------------------------------------- %
%%                    9. PEAK RESPONSE DETECTION
% ------------------------------------------------------------------- %

% Determine the peak displacements of the driveline mass and shaft sleeve
% inside the marine bearing to determine critical speeds

    if peak_response_detection_flag == 1

        % Extracting Peak Displacement of Shaft Sleeve in Marine Bearing %



        % Create a figure and plot the maximum and minimum displacement
        % values (determined earlier) against rpm. This will create plot of
        % displacement vs rpm to indicate critical speeds
        figure('Position',[fullscreen(3)/2-600 fullscreen(4)/2-350 1200
700])
        axes('FontSize',12)
        plot(RPM_Values,Bearing_A,'r-',RPM_Values,Bearing_B,'b-
        ','LineWidth',5)
        title(['Peak Reponse Values (Bearing) from
        ',num2str(RPM_Values(1)),'rpm to
        ',num2str(RPM_Values(end)),'rpm'],'FontSize',18)
        xlabel('Shaft Speed (rpm)','FontSize',16)
        ylabel('Radial Displacements (mm)','FontSize',16)
        grid on
        legend('Major Axis','Minor Axis','Location','NorthWest');
        xlim([1000 4000])
        saveas(gcf,[path, 'Peak Response (Bearing)', ext], filetype)
        saveas(gcf,[path, 'Peak Response (Bearing)', ext2], filetype2)
        close

        % Create a figure and plot the angle of the elliptical response of
        % the driveline mass(determined earlier) against rpm. This will
        % create a form of 'phase' plot.
        figure('Position',[fullscreen(3)/2-600 fullscreen(4)/2-350 1200
700])
        axes('FontSize',12)
        plot(RPM_Values,Bearing_THETA*180/pi,'g-
        ',RPM_Values,0*ones(length(RPM_Values)),'k—
        ',RPM_Values,90*ones(length(RPM_Values)),'k--','LineWidth',5)
        title(['Phase Plot (Bearing) from ',num2str(RPM_Values(1)),'rpm to
        ',num2str(RPM_Values(end)),'rpm'],'FontSize',18)
        grid on
        xlabel('Shaft Speed (rpm)','FontSize',16)
        ylabel('Phase Angle (deg)','FontSize',16)
        xlim([1000 4000])
        saveas(gcf,[path, 'Phase Plot (Bearing)', ext], filetype)
        saveas(gcf,[path, 'Phase Plot (Bearing)', ext2], filetype2)
        close

        % Store the peak values into the crit_speeds storage array
        [magnitude,location] = max(Bearing_A);
        crit_speeds{crit_speed_row,4} = RPM_Values(location);
        crit_speeds{crit_speed_row,5} = magnitude;
```

```
        % Extracting Peak Displacement of Shaft Sleeve in Marine Bearing %

        % Create a figure and plot the maximum and minimum displacement
        % values (determined earlier) against rpm. This will create plot of
        % displacement vs rpm to indicate critical speeds
        figure('Position',[fullscreen(3)/2-600 fullscreen(4)/2-350 1200
700])
        axes('FontSize',12)
        plot(RPM_Values,Coupling_A,'r-',RPM_Values,Coupling_B,'b-
        ','LineWidth',5)
        title(['Peak Reponse Values (Coupling) from
        ',num2str(RPM_Values(1)),'rpm to
        ',num2str(RPM_Values(end)),'rpm'],'FontSize',18)
        xlabel('Shaft Speed (rpm)','FontSize',16)
        ylabel('Radial Displacements (mm)','FontSize',16)
        grid on
        legend('Major Axis','Minor Axis','Location','NorthWest');
        xlim([1000 4000])
        saveas(gcf,[path, 'Peak Response (Coupling)', ext], filetype)
        saveas(gcf,[path, 'Peak Response (Coupling)', ext2], filetype2)
        close

        % Create a figure and re-plot the above figure against the data
from
        % the 'standard config'
        figure('Position',[fullscreen(3)/2-600 fullscreen(4)/2-350 1200
700])
        axes('FontSize',12)
        load Coupling_A_NOM
        plot(RPM_Values,Coupling_A,'r-',1000:20:3900,Coupling_A_NOM,'b-
        ','LineWidth',5)
        title(['Peak Reponse Comparison (Coupling) from
        ',num2str(RPM_Values(1)),'rpm to
        ',num2str(RPM_Values(end)),'rpm'],'FontSize',18)
        xlabel('Shaft Speed (rpm)','FontSize',16)
        ylabel('Radial Displacements (mm)','FontSize',16)
        grid on
        legend('Current Test','Standard','Location','NorthWest');
        xlim([1000 4000])
        saveas(gcf,[path, 'Peak Response Comparisons(Coupling)', ext],
        filetype)
        saveas(gcf,[path, 'Peak Response Comparisons(Coupling)', ext2],
        filetype2)
        close

        % Create a figure and plot the angle of the elliptical response of
        % the driveline mass(determined earlier) against rpm. This will
        % create a form of 'phase' plot.
        figure('Position',[fullscreen(3)/2-600 fullscreen(4)/2-350 1200
700])
        axes('FontSize',12)
        load Coupling_THETA_NOM
        plot(RPM_Values,Coupling_THETA*180/pi,'b-
        ',1000:20:3900,Coupling_THETA_NOM*180/pi,'r-
        ',RPM_Values,0*ones(length(RPM_Values)),'k—
        ',RPM_Values,90*ones(length(RPM_Values)),'k--','LineWidth',5)
        title(['Phase Comparison (Coupling) from
        ',num2str(RPM_Values(1)),'rpm to
        ',num2str(RPM_Values(end)),'rpm'],'FontSize',18)
```

```
    grid on
    xlabel('Shaft Speed (rpm)','FontSize',16)
    ylabel('Phase Angle (deg)','FontSize',16)
    legend('Current Test','Original Test','Location','NorthWest');
    xlim([1000 4000])
    saveas(gcf,[path, 'Phase Comparison (Coupling)', ext], filetype)
    saveas(gcf,[path, 'Phase Comparison (Coupling)', ext2], filetype2)
    close

    [magnitude,location] = max(Coupling_A);
    crit_speeds{crit_speed_row,2} = RPM_Values(location);
    crit_speeds{crit_speed_row,3} = magnitude;

end
```

B3: PROPERTIES OF ELLIPSE FROM DUAL FFT

```
function [A,B,THETA,Centre] = ellipse_from_fourier(f1,f2,theta_close)

% This is a function that takes input from two first order fourier fits
(with % the same periods); functions are plotted against each other and the
% properties of the resulting ellipse are extracted and returned.

% Function of the form:
%
%   [A,B,THETA,Centre] = ellipse_from_fourier(f1,f2)
%
% Where:
%
%   A is the major axis of the ellipse
%   B is the minor axis of the ellipse
%   THETA is the angle from the x-axis to the major axis from 0 to pi
%   (anti-clockwise)
%   f1 is a first order fourier fit to the x-values of a set of data
%   f2 is a first order fourier fit to the y-values of a set of data
%   theta_close is the closest angle (rads) to THETA wanted



%                     Author:     Ashley Brittenden



a1=f1.a1;   % Extract parameters from fourier fit
b1=f1.b1;
a2=f2.a1;
b2=f2.b1;
w=f1.w;

% Set the centre of ellipse to zero for convenience
Centre = [f1.a0,f2.a0];
f1.a0 = 0;
f2.a0 = 0;

% Extract angles using the transform obtained through use of 'Maple v14'
wt(1) =  atan((1/2)*(- a1^2 + b1^2 - a2^2 + b2^2 + sqrt( a1^4 + 2*a1^2*b1^2
+ 2*a1^2*a2^2 - 2*a1^2*b2^2 + b1^4 - 2*a2^2*b1^2 + 2*b1^2*b2^2 + a2^4 +
2*a2^2*b2^2 + b2^4 + 8*a1*b1*a2*b2))/(a1*b1 + a2*b2));

wt(2) =  atan((1/2)*(- a1^2 + b1^2 - a2^2 + b2^2 - sqrt( a1^4 + 2*a1^2*b1^2
+ 2*a1^2*a2^2 - 2*a1^2*b2^2 + b1^4 - 2*a2^2*b1^2 + 2*b1^2*b2^2 + a2^4 +
2*a2^2*b2^2 + b2^4 + 8*a1*b1*a2*b2))/(a1*b1 + a2*b2));

wt(3) = (atan((1/2)*(- a1^2 + b1^2 - a2^2 + b2^2 + sqrt( a1^4 + 2*a1^2*b1^2
+ 2*a1^2*a2^2 - 2*a1^2*b2^2 + b1^4 - 2*a2^2*b1^2 + 2*b1^2*b2^2 + a2^4 +
2*a2^2*b2^2 + b2^4 + 8*a1*b1*a2*b2))/(a1*b1 + a2*b2))+pi);

wt(4) = (atan((1/2)*(- a1^2 + b1^2 - a2^2 + b2^2 - sqrt( a1^4 + 2*a1^2*b1^2
+ 2*a1^2*a2^2 - 2*a1^2*b2^2 + b1^4 - 2*a2^2*b1^2 + 2*b1^2*b2^2 + a2^4 +
2*a2^2*b2^2 + b2^4 + 8*a1*b1*a2*b2))/(a1*b1 + a2*b2))+pi);

% Convert angles to times so they can be inserted into fourier fit
t = wt./w;
```

```
for angles = 1:length(wt)
    x_m(angles) = f1(t(angles));
    y_m(angles) = f2(t(angles));
    radius(angles) = sqrt(x_m(angles)^2 + y_m(angles)^2);
    theta(angles) = atan2(y_m(angles),x_m(angles));
end

% Evaluate the angle, major axis and minor axis by sorting the radius and
% angle arrays into descending order
sorted_radii = sort(radius,'descend');
theta_A(1) = theta(find(radius==sorted_radii(1),1,'first'));
theta_A(2) = theta(find(radius==sorted_radii(2),1,'last' ));

[value,position] = min(abs(theta_A-theta_close));
THETA = theta_A(position);

A = max(radius);
B = min(radius);
```

B4: TRANSFER MATRIX METHOD

```
% ------------------------------------------------------------------------ %
%                     GENERAL TRANSFER MATRIX METHOD                       %
% ------------------------------------------------------------------------ %

% This is a script to determine the critical speeds of a circular shaft
% with flexible supports and point masses along the length (takes into
% account self mass, inertia and gyroscopic terms). It uses the General
% Transfer Matrix Method (TMM) (based on a combination of Prohl and
% Mykelsted's methods).

% Input shaft geometry, slices, material properties and the discretisation
% length

%                          Author:  Ashley Brittenden

clear

%% -------------------------  1. INPUTS  ------------------------------- %%

% Input shaft geometry (Locations of a change in shaft geometry including
start and end locations)
geom_posn_array = [0, 0.221, 0.315, 1.1344, 1.1595, 1.161, 1.168, 1.206,
1.254, 1.264, 1.278, 1.280, 1.293, 1.373];

% Number of sections incorporating a dummy section at each end
num_geom_secs = length(geom_posn_array)+1;

% Diameters at the start and finish of each geometry interval (defined in
% geom_posn_array)
diam_array = [    0.08 0.08 ; 0.06025 0.070 ; 0.070 0.070 ; 0.060 0.060 ;
0.060 0.0568 ; 0.0568 0.0568 ; 0.085 0.085 ;  0.110 0.110 ; 0.110 0.130 ;
0.180 0.180 ;  0.110 0.110 ; 0.050 0.050 ; 0.020 0.020];

% Input geometry slices and the properties at each slice (for supports,
external masses etc) from left to right along the geometry

% locations of slices along the length [m] - note that slices should be
% applied in ascending order
slice_posn  =  [ 0 ; 0.110 ; 0.244 ; 1.033  ; 1.373];
% Mass at each slice [kg]
slice_mass  =  [ 0 ; 0     ; 22.3  ; 0      ; 39.1 ];
% Polar moment of inertia at each slice [kgm^2]
slice_j_pol =  [ 0 ; 0     ; 0.27  ; 0      ; 0.21 ];
% Diametral moment of inertia at each slice [kgm^2]
slice_j_diam = [ 0 ; 0     ; 0.14  ; 0      ; 0.19 ];
% Linear (radial) stiffness at each slice [N/m]
slice_k_lin =  [ 0 ; 9.22e6 ; 0     ; 1e12   ; 0    ];
% Rotational (diametral) stiffness at each slice [N/m]
slice_k_rot =  [ 0 ; 0     ; 0     ; 0      ; 0    ];


% Input Material Properties
shaft_dens = 7900;      % shaft density [kg/m3]
youngs_mod = 200e9;     % GPa
```

```
% Create arrays of density and stiffness values and set end locations to
rigid and weightless (for use later)
dens_array = shaft_dens * ones(length(diam_array),1);
dens_array(end) = 0;
stiff_array = youngs_mod * ones(length(diam_array),1);
stiff_array(end) = 1e15;

% Input approximate discretisation length
dL = 0.001;               % [m]

% Flag to indicate whether the approximated shaft geometry should be
plotted
geomplotflag = 1;


%% ------------------  2. CONVERT SHAFT GEOMETRY ---------------------- %%


% Determine total size of discretisation

% Initialise 'num_intervals'
num_intervals = [1;zeros(length(slice_posn)-1,1);1];
% Initialise slice length vector including dummy length at start and finish
dL_actual = [dL;zeros(length(slice_posn)-1,1);dL];

for slice_counter = 2:length(slice_posn)
    % Calculate number of slices in section
    num_intervals(slice_counter) = round(    (slice_posn(slice_counter) -
    % Calculate actual slice length
    slice_posn(slice_counter-1)) / dL);    dL_actual(slice_counter) =
    (slice_posn(slice_counter) - slice_posn(slice_counter-
    1))/num_intervals(slice_counter);
end


% Initialisations

tot_intervals = sum(num_intervals); % Determine the number of intervals
tot_slices = tot_intervals - 1; % Determine and initialize the no. of
slices

% Initialise density array making end sections massless
dens = [0;shaft_dens*ones(tot_intervals-2,1);0];
% Initialise various other arrays
interval_diam = zeros(tot_intervals,1);            % interval diameter
interval_dens = zeros(tot_intervals,1);            % interval density
interval_stiff = zeros(tot_intervals,1);           % interval stiffness
posn = zeros(tot_slices + 2,1);                    % interval position
mass = zeros(tot_slices,1);                        % interval mass
j_pol = zeros(tot_slices,1);                       % interval polar inertia
j_diam = zeros(tot_slices,1);                      % interval diametral
inert
k_rot = zeros(tot_slices,1);                       % slice rot. stiffness
k_lin = zeros(tot_slices,1);                       % slice linear stiffness

% Counters & Flags
tot_int_num = 1;        % Initialise tot_int_num at '1'
sliceflag = 0;          % Set sliceflag to '0'
```

```
% ---------------------- Interval Lengths ---------------------------- %

% Calculate the lengths of intervals by dividing each section into an
integer % number of intervals with lengths as close to dL as possible.
interval_length_array = zeros(tot_intervals,1);

interval_num = 0;
for sec_num = 1:length(dL_actual)
    for subinterval_num = 1:num_intervals(sec_num)
        interval_num = interval_num + 1;
        interval_length_array(interval_num,1) = dL_actual(sec_num);
    end
end

% ---------------------- Interval Diameters ----------------------------%

% Determine the diameter at each slice position (linearly interpolate for
% tapered sections) by iteration.
sec_num = 1;
position = 0;
for interval_num = 2:tot_intervals-1
    position = position + 0.5*interval_length_array(interval_num);
    length_ratio = position / (geom_posn_array(sec_num+1)-
    geom_posn_array(sec_num));

    if length_ratio > 1;
        sec_num = sec_num + 1;
        position = 0.5*interval_length_array(interval_num);
        length_ratio = position / (geom_posn_array(sec_num+1)-
        geom_posn_array(sec_num));
    end

    interval_diam(interval_num,1) = length_ratio * (diam_array(sec_num,2)-
    diam_array(sec_num,1)) + diam_array(sec_num,1);
    position = position + 0.5*interval_length_array(interval_num);
    interval_dens(interval_num) = dens_array(sec_num);
    interval_stiff(interval_num) = stiff_array(sec_num);

end

% Set the properties of the end sections to have constant diameter and be
% rigid and weightless
interval_diam(1) = interval_diam(2);
interval_diam(end) = interval_diam(end-1);
interval_dens(1) = 0;
interval_dens(end) = 0;
interval_stiff(1) = 1e15;
interval_stiff(end) = 1e15;



% ------------------------- Slice Positions --------------------------- %

% Determine the locations of each slice in absolute terms (from LH end)
slice_position = zeros(tot_slices,1);
for slice_num = 2:tot_slices
    slice_position(slice_num) = slice_position(slice_num-1) +
    interval_length_array(slice_num);
end
```

```
% -------------------------- Plot Geometry ------------------------------ %

% Create a plot of the geometry as approximated by the interval diameters
and % lengths determined earlier
if geomplotflag == 1
    plot(slice_position,interval_diam(2:end)/2 ,  slice_position,-
    interval_diam(2:end)/2 , 'b-' ,  slice_position ,
    zeros(length(slice_position)), 'k--','linewidth', 2 )
    axis equal
    axis([-inf inf -0.2 0.2])
    grid on
    xlabel('distance [m]');
    ylabel('radius [m]');
end


%% ----------------------  3. DISCRETISE  --------------------------- %%

% Discretise the shaft and apply the mass and inertial properties of each
% shaft interval to the slices (include the additional properties specified
% at the start of this script

slice_sum = 0;
for slice_counter = 1:length(num_intervals)-1
    slice_sum = slice_sum + num_intervals(slice_counter);
    mass(slice_sum) = slice_mass(slice_counter);
    j_pol(slice_sum) = slice_j_pol(slice_counter);
    j_diam(slice_sum) = slice_j_diam(slice_counter);
    k_lin(slice_sum) = slice_k_lin(slice_counter);
    k_rot(slice_sum) = slice_k_rot(slice_counter);
end

slice_counter = 1;      % Reset counters
position = 0;
for slice_num = 1:tot_slices
    % Determine mass on left hand side at each slice
    lhs_mass = interval_dens(slice_num) * pi * interval_diam(slice_num)^2 /
4
    *  interval_length_array(slice_num)/2;
    % Determine mass on right hand side at each slice
    rhs_mass = interval_dens(slice_num+1) * pi *
interval_diam(slice_num+1)^2
    / 4  *  interval_length_array(slice_num+1)/2;
    mass(slice_num) = mass(slice_num) + lhs_mass + rhs_mass;
    % Determine polar inertia at each slice
    j_pol(slice_num) = 0.5 * lhs_mass * (interval_diam(slice_num)/2) ^ 2 +
    0.5 * rhs_mass * (interval_diam(slice_num)/2) ^ 2;


    % Determine diametral inertia on left hand side at each slice
    lhs_j_diam = 0.25 * (2*lhs_mass) * ((interval_diam(slice_num)/2)^2 +
    (2*interval_length_array(slice_num))^2/3);
    % Determine diametral inertia on left hand side at each slice
    rhs_j_diam = 0.25 * (2*rhs_mass) * ((interval_diam(slice_num+1)/2)^2 +
    (2*interval_length_array(slice_num+1))^2/3);
    % Determine diametral inertia
    j_diam(slice_num) = 0.5*(lhs_j_diam + rhs_j_diam);
end
```

```
%% -------------------------    4. SOLVE    ------------------------------ %

% With the discretised shaft geometry, apply the transfer matrix method (as
% described in Dara Child's 'Rotordynamics') to determine the first
critical % speeds of the shaft assembly

w_max = 1000;               % Maximum angular frequency [rad/s]
w_step = w_max/100;         % Initial frequency step size [rad/s]
w_tol = .001;               % Solution tolerance [rad/s]

% Initialise the 3D field matrix
field_mat = zeros(4,4,tot_intervals);
% Initialise the 3D point matrix
point_mat = zeros(4,4,tot_slices);
% Area moment of inertia of circular shaft [m^4]
inertia_mat = 0.25*pi*(interval_diam/2).^4;
% Define the rotational velocity vector
rot_mat = 0:w_step:w_max;

for n_refinements = 1:ceil(log(w_step/w_tol)/log(10))+1

    for count = 1:length(rot_mat)

        % -------------- Calculate Field Matrices --------------- %

        for ii = 1:tot_intervals

            field_mat(:,:,ii) =

                  [1,interval_length_array(ii),interval_length_array(ii)^2
                  / (2*interval_stiff(ii)*inertia_mat(ii)),-
                  interval_length_array(ii)^3 /
                  (6*interval_stiff(ii)*inertia_mat(ii)); 0,
                  1,interval_length_array(ii) /
                  (interval_stiff(ii)*inertia_mat(ii)), -
                  interval_length_array(ii)^2 /
                  (2*interval_stiff(ii)*inertia_mat(ii));0,0,1,-
                  interval_length_array(ii);0,0,0,1];
        end




        % -------------- Calculate Point Matrices --------------- %

        for ii = 1:tot_slices

            point_mat(:,:,ii) =
                  [1,0,0,0; 0,1,0,0; 0,(k_rot(ii)-(j_diam(ii)+j_pol(ii)) *
                  rot_mat(count)^2),1,0; (k_lin(ii)-
                  mass(ii)*rot_mat(count)^2) , 0, 0, 1];
        end

        % -------------- Calculate Transfer Matrix --------------- %

        U = field_mat(:,:,1);
        for ii = 1:tot_slices
            U = point_mat(:,:,ii) * U;
```

```
            U = field_mat(:,:,ii+1) * U;
        end

        % -------------- Obtain Determinant -------------- %

        % Evaluate the determinant assuming the shaft has free ends
(achieved
        % through the rigid and weightless sections attached earlier)
        detmtx = [U(3,1) , U(3,2) ; U(4,1) , U(4,2)];
        determ(count) = (det(detmtx));

    end

    % Establish zero-values of the determinant (which occur at critical
    % speeds)
    clear('crit_speeds')
    count = 1;
    for crit_speed_counter = 1:length(rot_mat)-1
        if determ(crit_speed_counter) * determ(crit_speed_counter+1) <= 0
            crit_speeds(count) = rot_mat(crit_speed_counter);
            count=count+1;
        end
    end

    critical_speed_guess = min(abs(crit_speeds));

    % Refine steps around this value and re-iterate
    w_step = w_step/10;
    w_new = [critical_speed_guess-10*w_step : w_step :
    critical_speed_guess+10*w_step];
    clear('w');
    rot_mat = w_new;
    clear('determ')

end

% Print evaluated critical speed
fprintf('  Critical Speed is: %10.3f rad/s    or %10.3f Hz    or %8.0f RPM
\n',critical_speed_guess,critical_speed_guess/(2*pi),critical_speed_guess*6
0/(2*pi) )
```

B5: TIMOSHENKO BEAM METHOD

```
%%%%%%%%%%%%%%%%%%%%%%%%%%%%%%%%%%%%%%%%%%%%%%%%%%%%%%%%%%%%%%%%%%%%%%%%%%%%%%%%
%%
%                              TIMOSHENKO BEAM METHOD
%%%%%%%%%%%%%%%%%%%%%%%%%%%%%%%%%%%%%%%%%%%%%%%%%%%%%%%%%%%%%%%%%%%%%%%%%%%%%%%%
%%

%                           Author: Ashley Brittenden

% A script that receives various geometry properties of a shaft with rigid
% supports and returns critical speeds based on Timoshenko Beam theory
% (described in Marks & Labberton)

% Shown here is the effect of changing impeller mass on critical speeds.
% Minor changes can be made to test the effects of driveline mass and
% overhang.

clear
clc
close all

fullscreen = get(0,'ScreenSize');

b  = 855.6;        % Distance from thrust bearing to impeller mass
Wo = 3.7;          % Weight of overhanging shaft
Wc = 6;            % Weight of coupling
c3 = 141.4;        % Distance to overhanging shaft COM
Wd = 37;           % Weight of driveline mass
c1 = 163.2;        % Distance to coupling COM
c2 = 95;           % Distance 2
W1 = 25;           % Mass of shaft section between bearings
W2 = 41.2;         % Combined weight of shaft and impeller between bearings
L  = 998.8;        % Distance between marine and spherical bearing
c  = 273.2;        % Combined COM of overhanging shaft, coupling and mass
d  = 70;

npoints = 200;     % Number of discretization points
Wi_min = 0;        % Minimum impeller mass
Wi_max = 60;       % Maximum impeller mass

Wi_array = linspace(Wi_min,Wi_max,npoints);

% Calculate the critical speed for each impeller mass using Timoshenko
method % Described in Marks and Labberton
for Wi_new = 1:npoints;

    Ws = pi/4 * 7.8 * d^2 * L * 0.625 / 1000000;
    Wo = pi/4 * 7.8 * d^2 * c1 * 0.75 / 1000000;
    W1 = Wi_new * 2 * (L - b) / L + Ws;
    W2 = Wc * c3 / c + Wo * c1 / (2 * c) + Wd;
    A = 1 - (9/16) * L / (L + c);
    U = 207114.52 * d^2 / (L * sqrt(W1*L));
    V = 51778.63 * d^2 / (c * sqrt(W2*(L+c)));
```

```
    N(Wi_new) = sqrt(0.5/A * (U^2 + V^2 - sqrt((U^2 + V^2)^2 - 4 * A * U^2
    *V^2)));

end

% Create a figure and plot critical speeds across the full range of
impeller % masses defined.
figure('Position',[fullscreen(3)/2-600 fullscreen(4)/2-350 1200 700])
plot(Wi_array,N(:,1),'b-',Wi_array,N(:,2),'b-','LineWidth',3);
hold on

% Plot a line showing the standard impeller mass and its corresponding
% critical speed
h1 = line([21.9,21.9],[0,5000]);
set(h1,'color','r','linestyle','--','LineWidth',3);
title('Impeller Mass Effects (Timochenko)','FontSize',18)
xlabel('Impeller Mass [kg]','FontSize',16)
ylim([0 4000]);
xlim([0 inf]);
ylabel('Critical Speed [rpm]','FontSize',16)
grid on
```

APPENDIX C: WATER BEARING WORK

A section of work was carried out in parallel to the preparation of this thesis in regards to the operating characteristics of the marine bearing. The results and implications from this work were critical in determining how to model the properties of the marine bearing; critical speeds could only be evaluated once this was known.

Ashley Brittenden
98693248
Department of Mechanical Engineering
University of Canterbury

OPERATING CHARACTERISTICS OF A WATER LUBRICATED HYDRODYNAMIC JOURNAL BEARING

ABSTRACT

Investigation into the operating characteristics of a water lubricated hydrodynamic journal (HDJ) bearing with ten equi-spaced axial grooves was carried out on a Hamilton Jet HJ-364 Jet Assembly. It was determined that the bearing is not operating in a stable manner and that significant rubbing is occurring. Boat trials should be carried out to validate these findings.

1 INTRODUCTION

A number of characteristics can be used to determine whether a hydrodynamic journal (HDJ) bearing is operating satisfactorily. However, the two most important characteristics include the eccentricity ratio and the journal stability during operation. The eccentricity ratio is defined as the ratio of shaft eccentricity to radial clearance inside the journal (an eccentricity ratio of unity or greater would indicate rubbing).

This testing was carried out on a Hamilton Jet HJ364 Jet Assembly. It is to be used as preparation for subsequent work involving non-standard lubricants.

2 DESCRIPTION OF APPARATUS

The apparatus consisted of a Hamilton Jet HJ364 Jet assembly (as shown in **Figure 1**), instrumented with:

- three 1psi pressure transducers (RS – 228-8533) at tappings 1, 2 and 10 on the HDJ bearing (see **Figure 4**);
- two 1psi pressure transducers (RS – 228-8533) equi-spaced along the axis of the HDJ bearing with a 20mm spacing between each;
- five 15psi pressure transducer (RS – 286-664) at tappings 3, 4, 5, 9 and 13;
- three 30 psi pressure transducer (RS – 286-670) at tappings 6, 7, 8;
- two sets of two non-contacting linear displacement transducers (Brüel and Kjær IN – 081) to measure vertical and horizontal displacements of the shaft at the tailpipe (see **Figure 3**) and the Driveshaft Mass.
- two general purpose ceramic shear accelerometers (Brüel and Kjær 352C03) attached to the top of the thrust bearing housing.

Drawings of the instrumented tailpipe are provided in **Figure 2** and **Figure 3** and a detailed view of the bearing is shown in **Figure 4** (not to scale). Output of the pressure transducers were individually amplified with Burr-Brown INA126 instrument amplifiers to give a full scale output of 10V. The output signal was acquired with a National Instruments 'NI 9205' 32 channel module and recorded through LabVIEW.

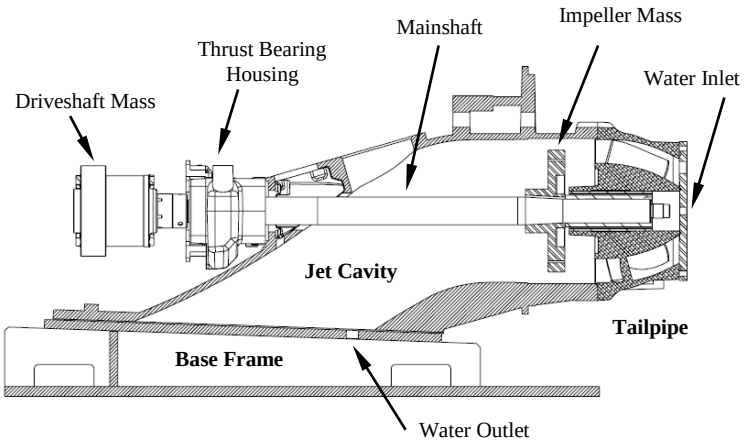

Figure 1 - Overview of Test Rig Schematic, labelling tailpipe, bearings, impeller, overhung mass, water inlet and outlets

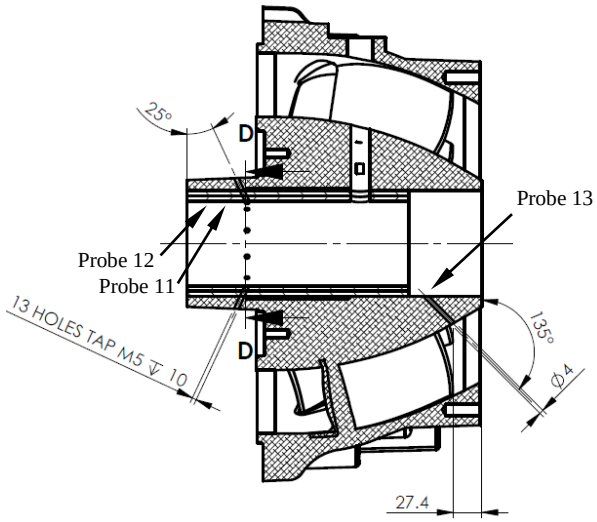

Figure 2 - Position of Pressure Transducers on Tailpipe

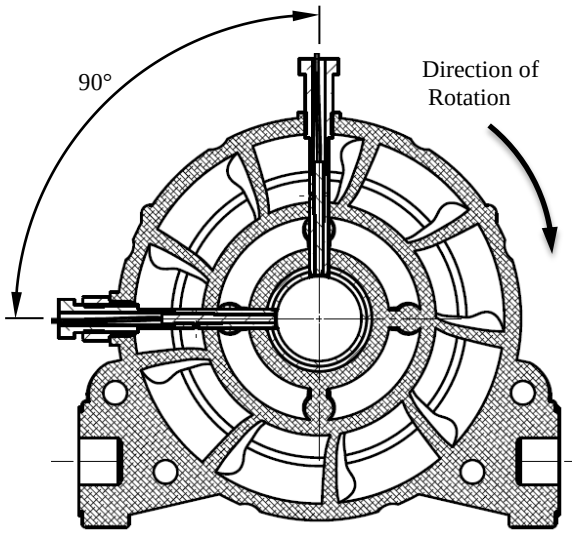

Figure 3 - Position of Displacement Transducers on Tailpipe

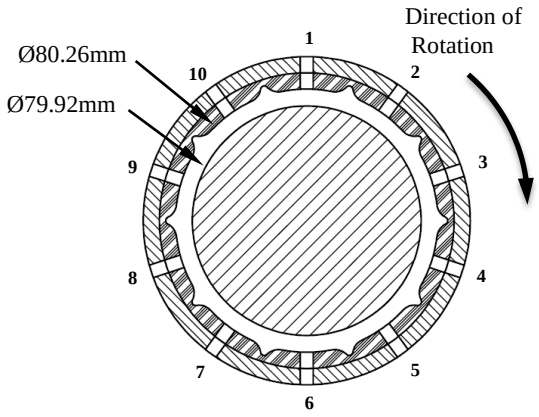

Figure 4 - Image of Bearing Groove/Tapping Configuration (Section **D**-**D** - not to scale)

3 CALIBRATION

Individual calibration of the 1psi pressure transducers was carried out with a 1.5m water filled manometer. Three readings were taken and the method of least-squares was used to determine the linear relationship between pressure and output voltage. A nominal uncertainty of ±10mm H_20 was noted and was attributed to transducer and amplifier instability with temperature. Calibration of the 15psi and 30psi transducers was carried out with an industrial dead weight tester and a nominal uncertainty of ±3kPa was recorded.

Calibration of the Displacement Transducers was performed by creating an output voltage vs. displacement plot for each transducer and extracting the gradients. These gradients were then used to scale data during the acquisition process. The two accelerometers were provided with calibration data from the manufacturer. Hence, no further calibration of these was required.

Analogue to digital conversion was performed using the following National Instruments equipment:

- A 'CompactDAQ' 8-slot chassis
- A 'NI 9205' (32-channel, 250 kS/s) analogue input module to measure the output signal from the pressure transducers
- Two 'NI 9234' (4-channel, 24-bit, 51.2 kS/s) analogue input module to measure the output signals from the displacement transducers and accelerometers

Data acquisition was performed using a script prepared in National Instruments LabVIEW (2009 release) and run on a Dell 'Latitude D630' laptop computer. All sampling was performed at a rate of 5 kHz.

4 TESTING PROCEDURE

Testing was initially trialled with water trickling through the HDJ bearing. The journal showed relatively good stability in this configuration. However, air was released along with water from most of the pressure tappings indicating that there was incomplete lubrication acting around the bearing. Therefore, the jet assembly was completely filled with water before testing was undertaken.

Data acquisition was performed at test speeds from 200rpm to 1800rpm in 200rpm intervals (significant instability was noted above this limit and pressure readings all tended towards zero). With the jet cavity filled with water and vented to atmospheric pressure, the mainshaft was run at each test speed until all pressures had stabilised to within 1kPa/min. A three second segment of data was then acquired from each of the transducers.

5 RESULTS

In **Figure 5 - a, b** and **c**, the pressure readings after 5, 10 and 15 minutes are provided respectively (note that pressure probes 1, 2, 3, 10, 11 and 12 are not displayed due to pressures less than atmospheric). It is expected that the magnitude of these neglected pressures is relatively small and therefore insignificant. In **Figure 6**, the output from the displacement transducers on the tailpipe is provided. Similarly, the output from the transducers at the coupling is provided in **Figure 7**.

Detailed views of the HDJ bearing performance at 200rpm, 600rpm, 1200rpm and 1800rpm are provided in **Figure 8**, **Figure 9**, **Figure 10** and **Figure 11** respectively. These figures aim to show how the pressure distribution and the shaft location as a function of its total clearance vary with speed. Note that a shaft position outside the black circle indicates that the rubber bearing is being compressed and/or rubbing is occurring.

Each pressure was subsequently integrated over one tenth of the bearing surface area and resolved into vertical and horizontal force components. This surface area is difficult to determine in this configuration; however it can be bounded by the area of the bearing 'lands' and the total normal surface area of the bearing (3261 mm^2 and 5295 mm^2 respectively). From these areas, maximum and minimum force acting on the mainshaft inside the HDJ bearing are shown in **Figure 12** and **Figure 13**.

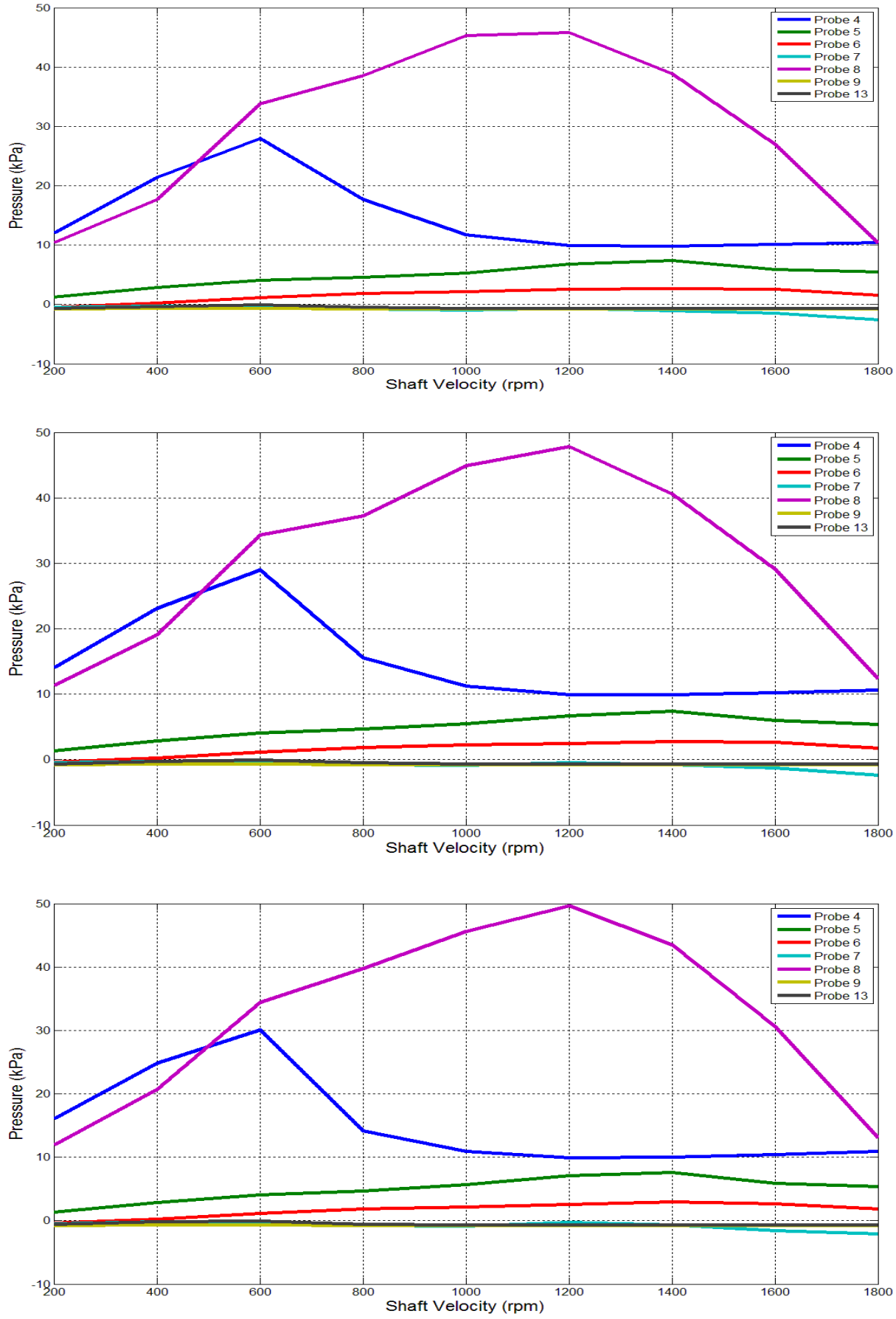

Figure 5 - Pressure Measurements at 5, 10 and 15 Minute Settling Times Respectively

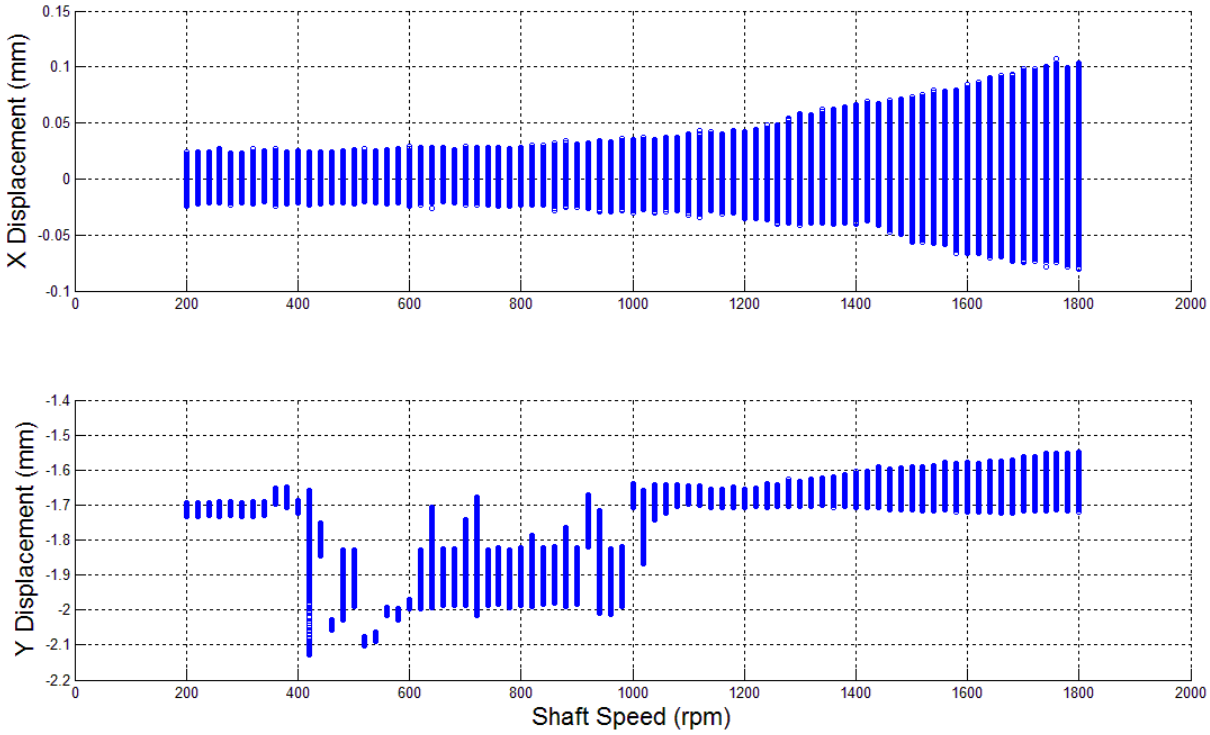

Figure 6 – Proximity measurements as a function of speed within the HDJ bearing
(note that 'X Displacement' is horizontal; 'Y Displacement' vertical)

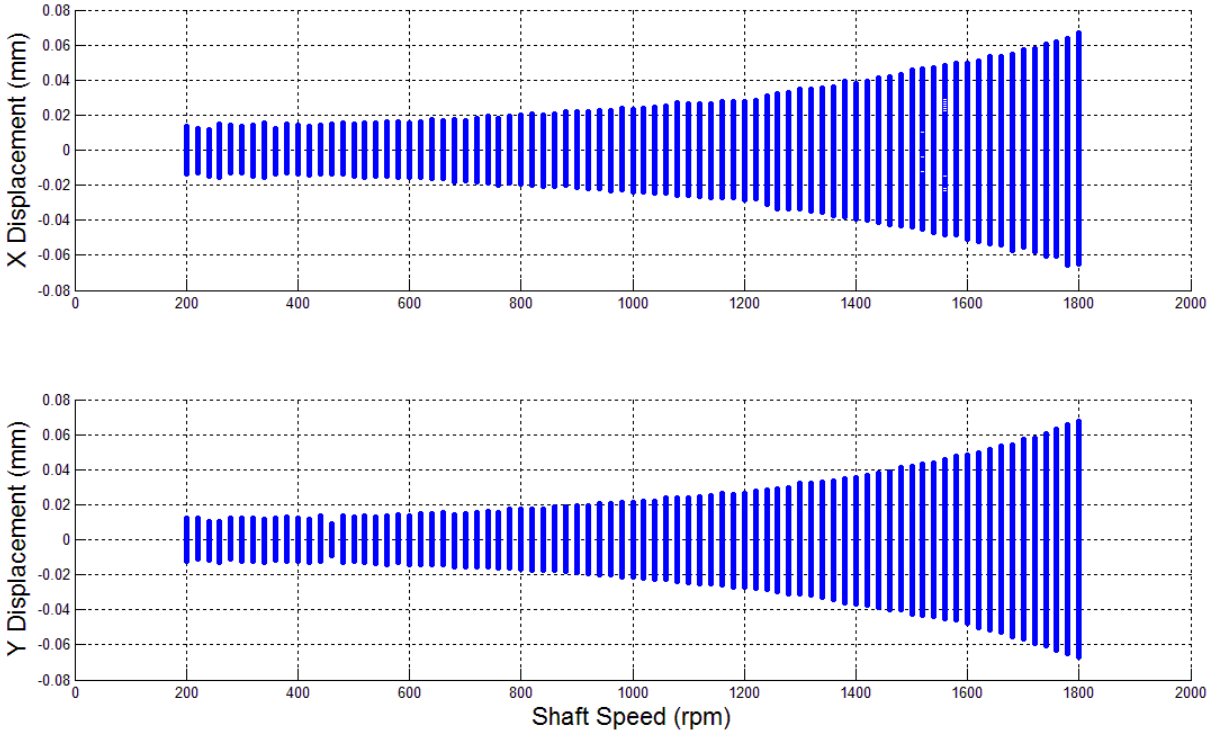

Figure 7 – Proximity measurements as a function of speed on the coupling

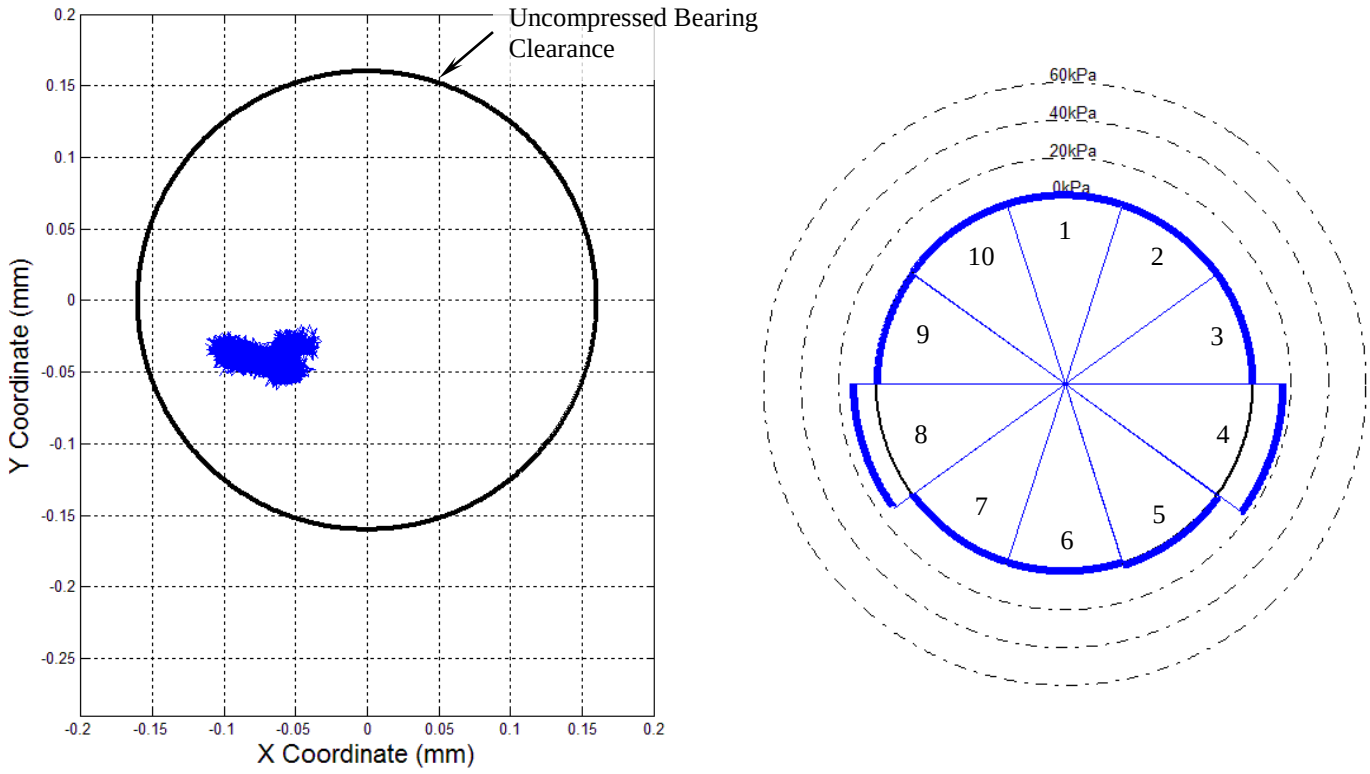

Figure 8 – **(a)** Shaft position as a function of uncompressed clearance in HDJ bearing over time at 200rpm
(b) Pressures within HDJ bearing averaged over time at 200rpm

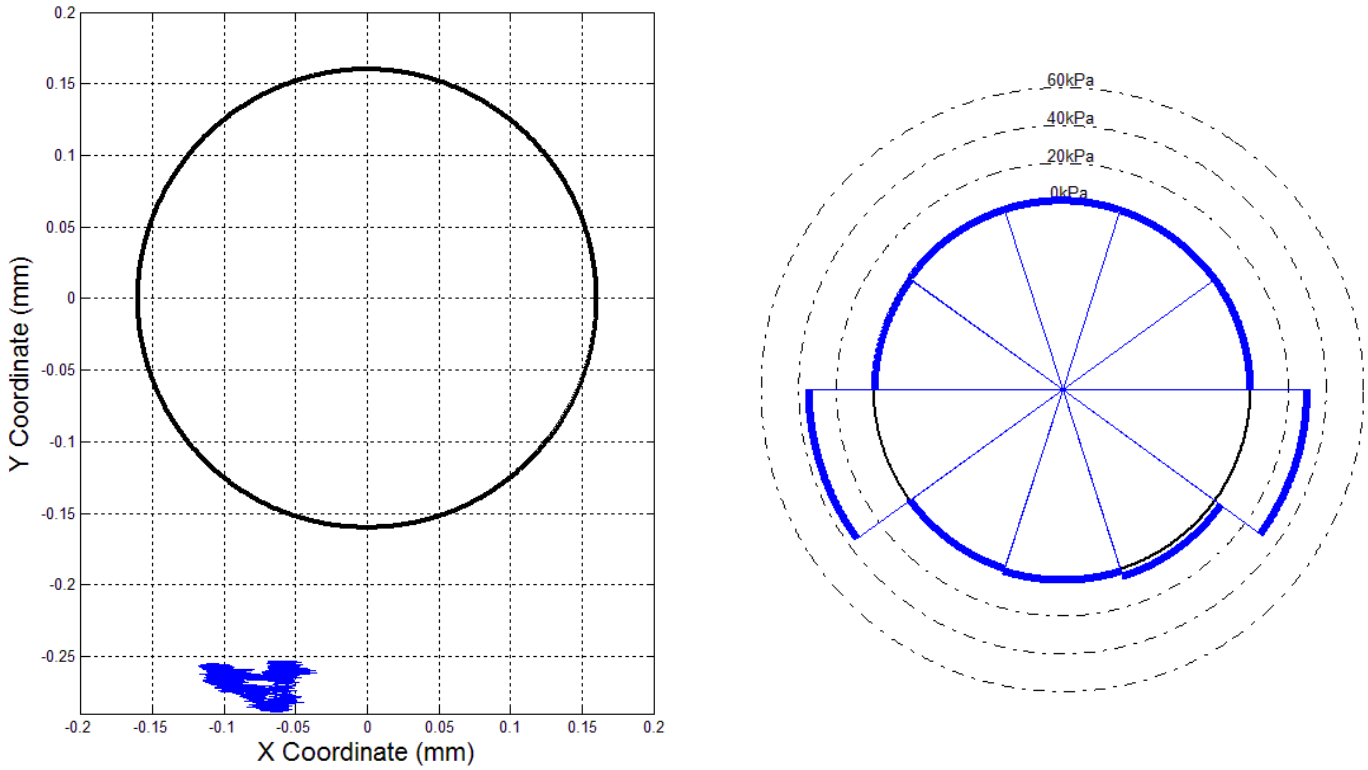

Figure 9 - **(a)** Shaft position as a function of uncompressed clearance in HDJ bearing over time at 600rpm
(b) Pressures within HDJ bearing averaged over time at 600rpm

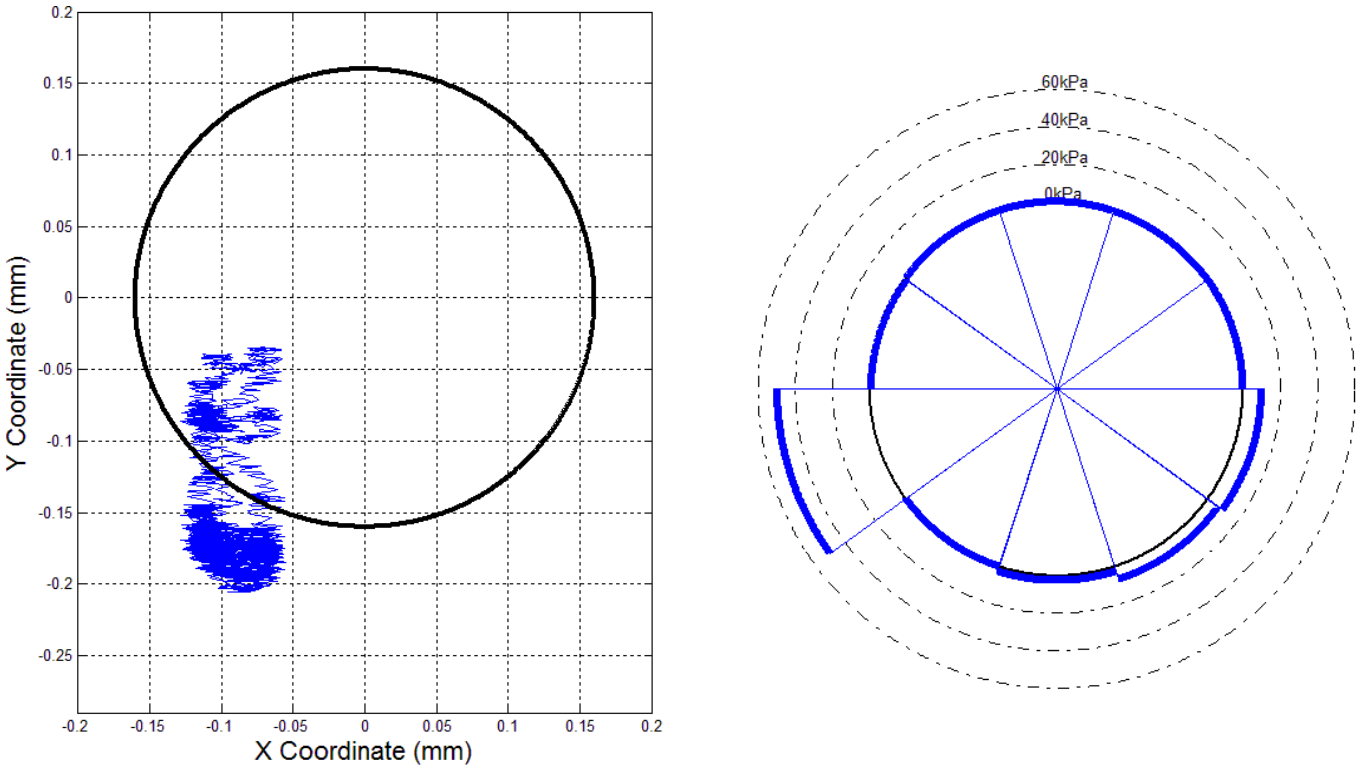

Figure 10 - **(a)** Shaft position as a function of uncompressed clearance in HDJ bearing over time at 1200rpm
(b) Pressures within HDJ bearing averaged over time at 1200rpm

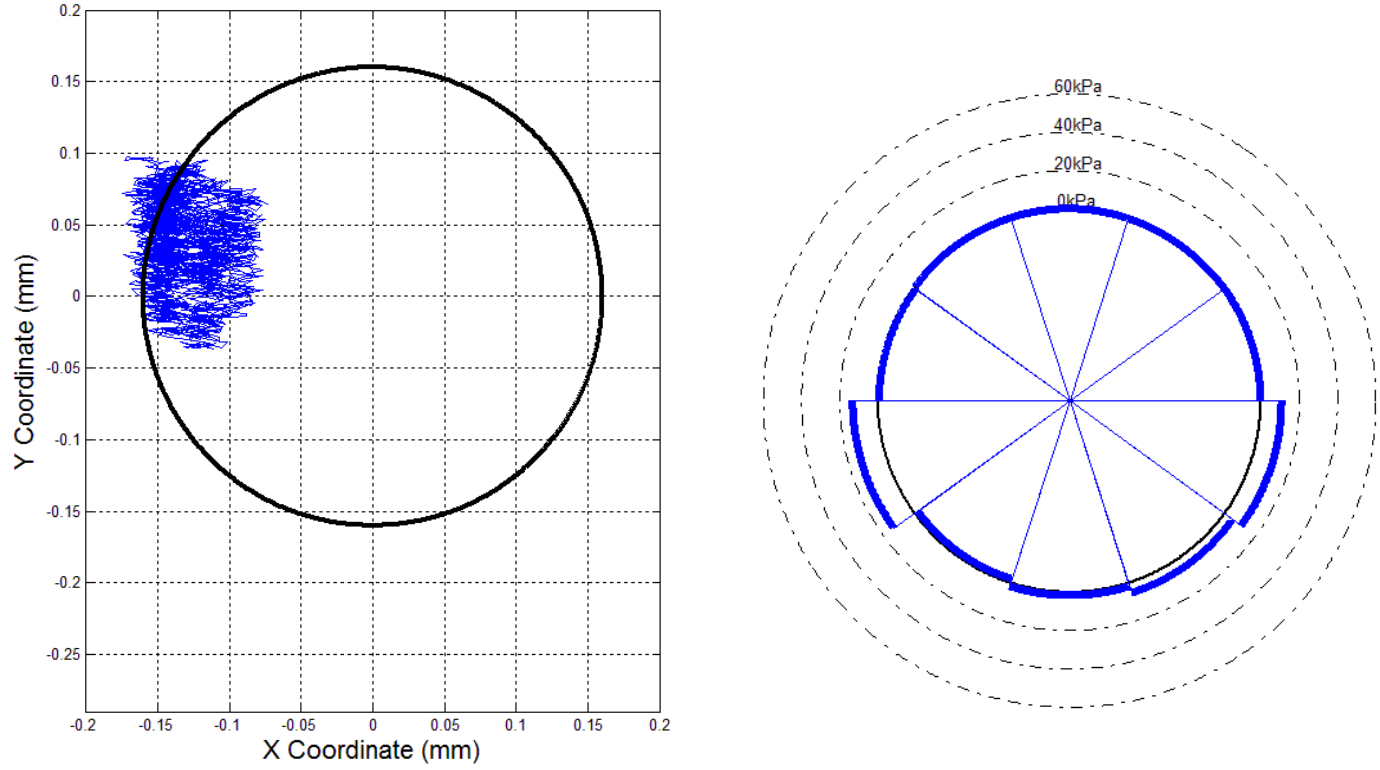

Figure 11 - **(a)** Shaft position as a function of uncompressed clearance in HDJ bearing over time at 1800rpm
(b) Pressures within HDJ bearing averaged over time at 1800rpm

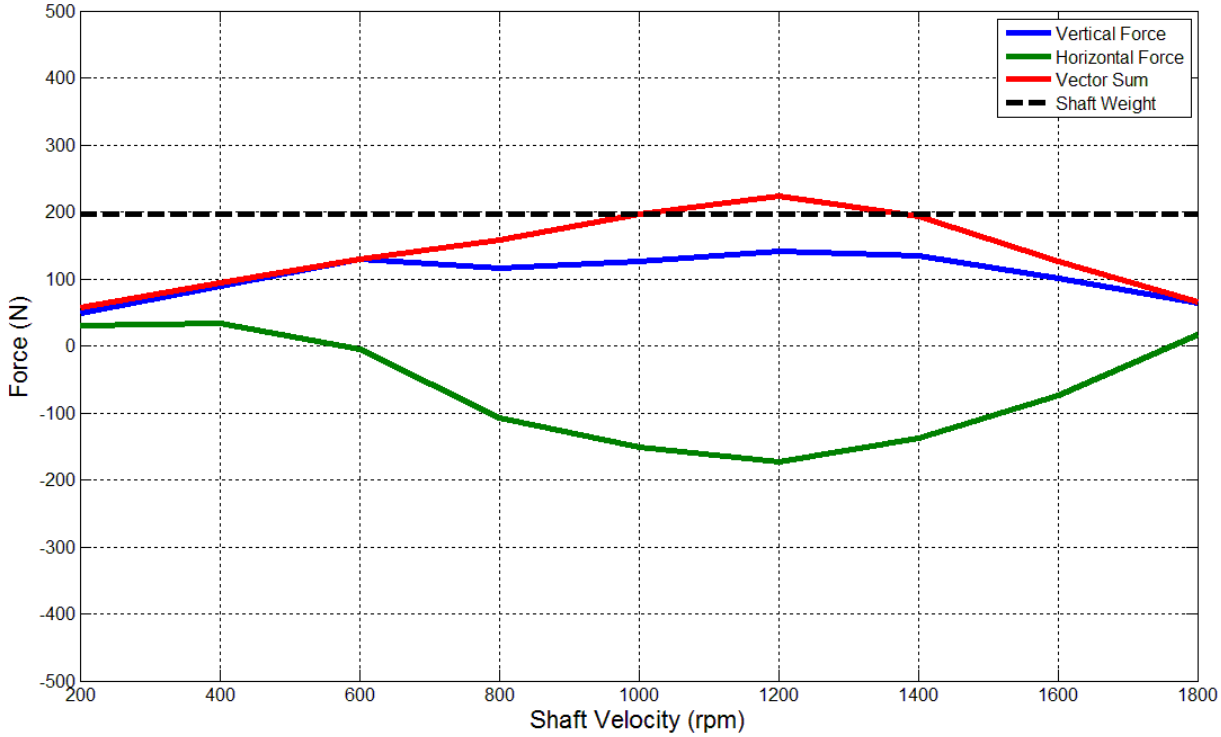

Figure 12 – Maximum Force
Resolved vertical, horizontal and total force acting on journal from integration of measured pressures (each pressure integrated over 1/10th of the total bearing surface area - 529.5mm^2)

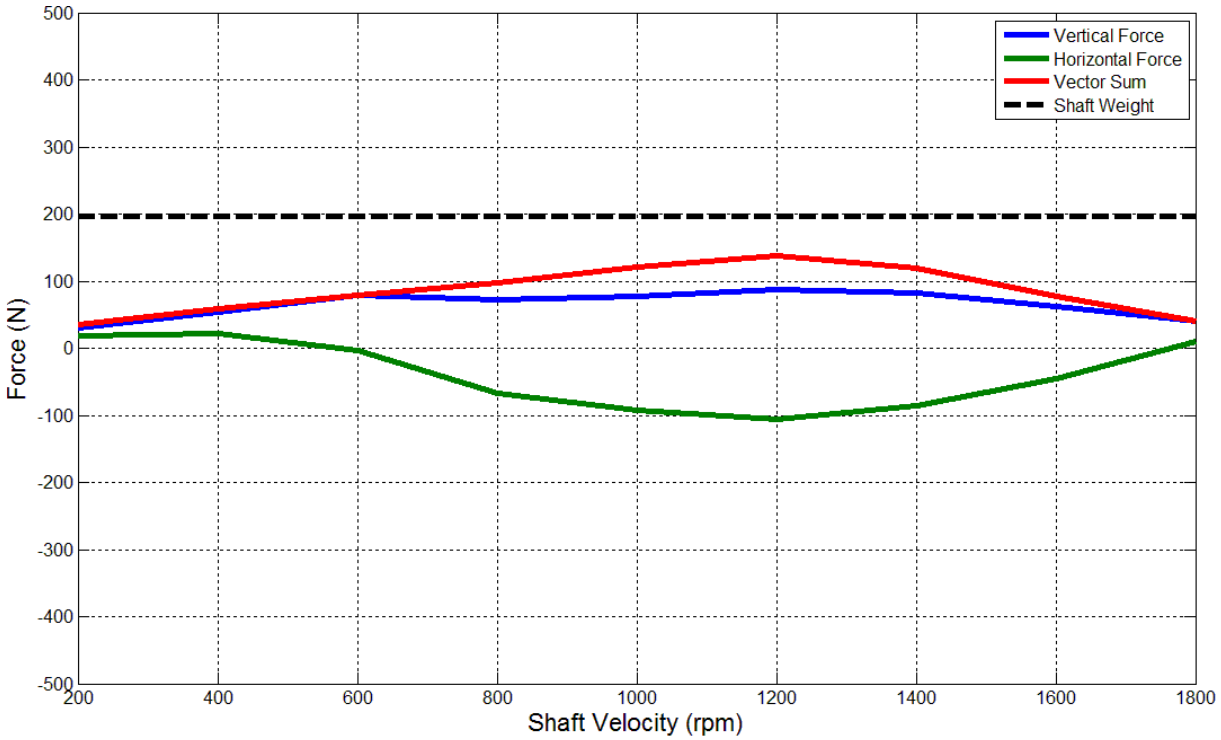

Figure 13 - Minimum Force
Resolved vertical, horizontal and total force acting on journal from integration of measured pressures (each pressure integrated over the area of one bearing 'land' – 326.1mm^2)

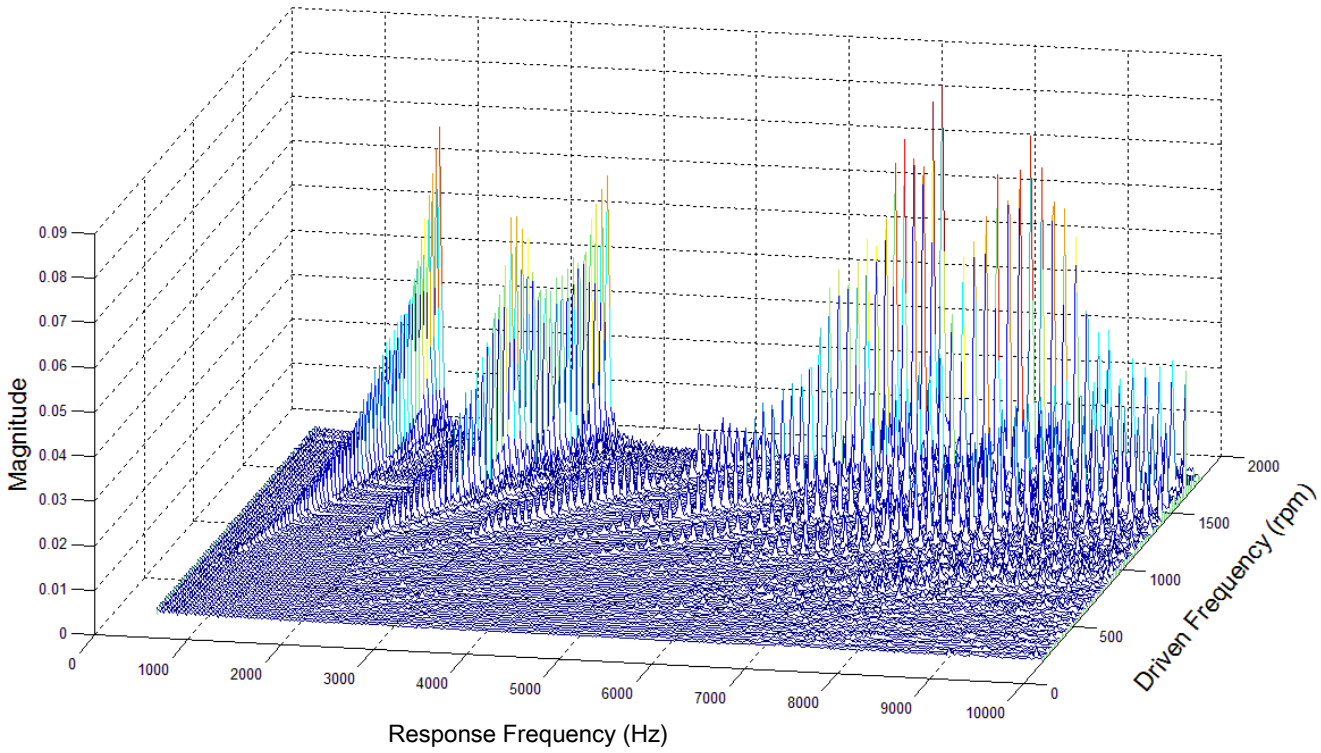

Figure 15 - Waterfall Plot in Vertical Plane (Perpendicular to Mainshaft)

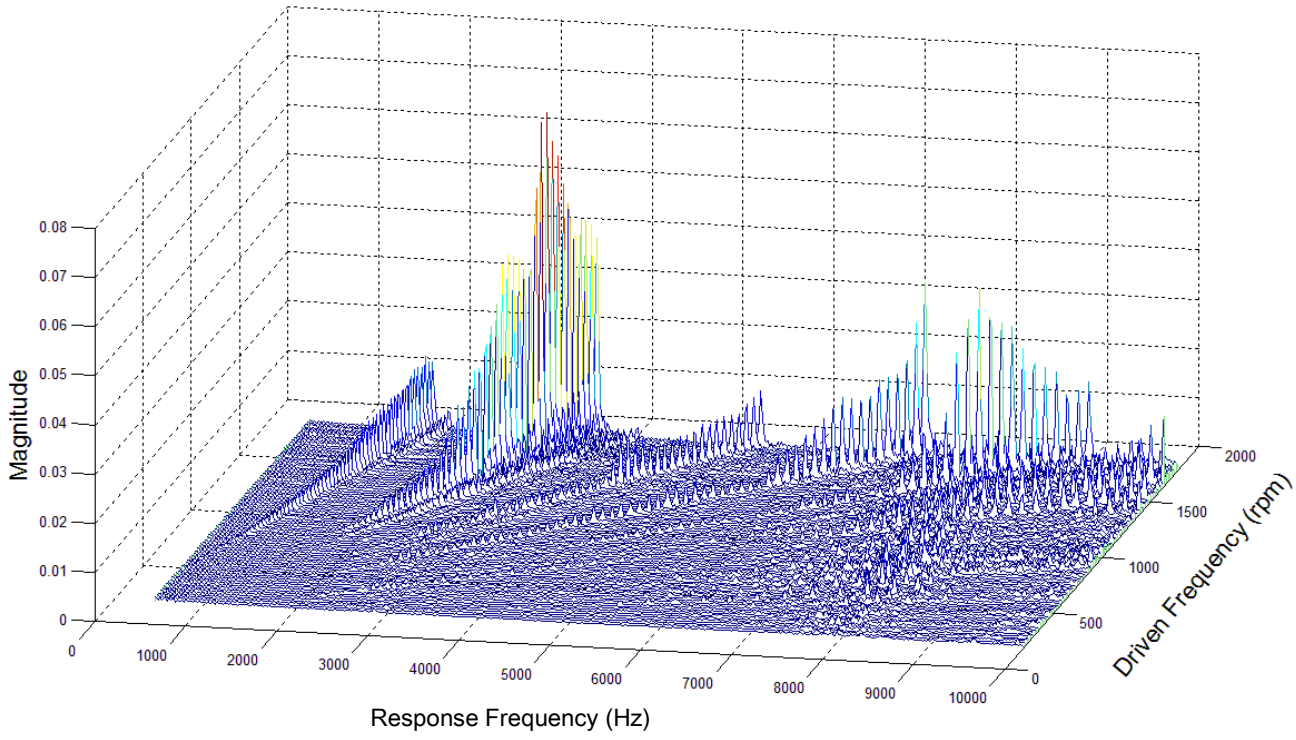

Figure 14 - Waterfall Plot in Horizontal Plane (Perpendicular to Mainshaft)

6 DISCUSSION

In **Figure 5** the pressure profile establishes almost completely within the first five minutes. However, pressure readings still haven't stabilised after 15 minutes. This is attributed to a combination of factors:

- small clearance at some of the journal - bearing interfaces causing very low flow rates through the pressure tappings
- residual air in the tubes between the pressure tappings and pressure probes which increases settling time (compressibility)
- random variations of shaft position with time within the HDJ bearing

It is immediately evident that the pressure profiles in **Figure 5** are not typical of an ideal journal bearing. From 200rpm to 600rpm, pressure readings increase with angular velocity which would be expected during film development (Probe 4, however, is unusually high in this region). From 600rpm to 1200rpm, pressures increase further still apart from Probe 4 which decreases rapidly. This would tend to indicate that the hydrodynamic film within the bearing is still developing or whirling inside the bearing is occurring. At 1200rpm, Probe 8 indicates its highest value. Above this, the pressure at Probe 8 decreases rapidly indicating a loss of stability within the bearing and rubbing of the journal against the bearing wall.

Observation of **Figure 6** further indicates that the HDJ bearing is not operating ideally. Below 400rpm, slight whirling is observed but the bearing appears to be operating relatively normally. From 400rpm to approximately 1000rpm, the journal destabilises from its film and the centre of rotation drops by approximately 0.2mm and is highly unstable. Above 1000rpm, the centre of rotation re-stabilises to its original value and whirling inside the bearing increases with rotational speed. This increase in whirling can be attributed to a combination of bearing instability and unbalance force from the coupling (see **Figure 7**).

The data in **Figure 5** and **Figure 6** is re-plotted as comparisons of shaft position and pressure profile in **Figure 8** through **Figure 11**. This provides an easier visual assessment of the bearing behaviour. Note that the measured bearing clearance and the bearing centre have a relatively high associated uncertainty due to the low stiffness of the rubber. Therefore these results are only indicative of the journal behaviour and strong limitations are placed on the conclusions drawn.

In an ideal HDJ bearing, pressure would increase with a reduction in clearance between the journal and the bearing. This is due to the compression of water in this region (Liu, Li, & Ganeriwala, 2006). An ideal pressure distribution and shaft position is provided in In **Figure 8**, this behaviour is mildly evident aside from the deviation at Probe 4. In **Figure 9**, the shaft appears to be compressing the rubber bearing substantially. However, pressure measurements don't change significantly. In **Figure 10**, the instability of the journal is strongly evident. This instability is also observed in **Figure 11**.

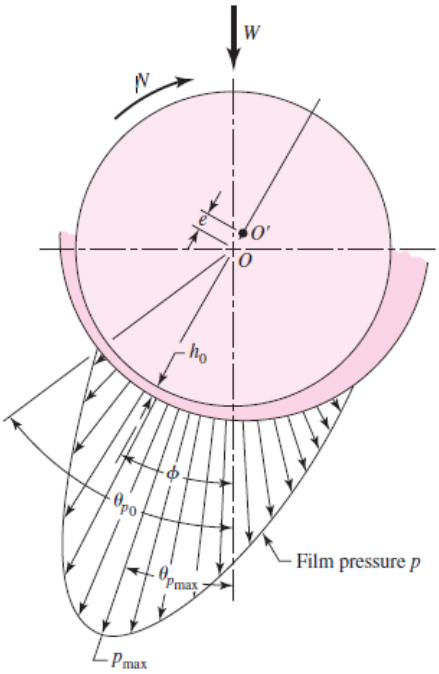

Figure 16 - Pressure Distribution and Shaft Position in an Ideal HDJ Bearing **(Budynas-Nisbett, 2006)**
Where: 'W' is the shaft weight; 'N' is the direction of rotation; 'e' is the journal eccentricity; 'h0' is the minimum clearance and 'φ' is the angle between minimum clearance and the shaft weight

Finally, **Figure 12** and **Figure 13** strongly indicate that the bearing is not performing correctly. For complete support of the journal, 'Vertical Force' and 'Shaft Weight Force' should be equal. As neither plots reach this value, it is evident that rubbing is occurring within the HDJ bearing.

These results show that there are a number of characteristics that deviate from an ideal HDJ bearing. This poor performance could be due to a number of factors. Lubricant 'whirl' is commonly caused by (Berry, 2005):

- Light dynamic and preload forces
- Excessive bearing wear or clearance
- A change in lubricant properties (primarily shear viscosity)
- An increase or decrease in lubricant temperature or pressure; improper bearing design (over design for actual shaft loading)
- Fluid leakage
- Change in internal damping
- Gyroscopic effects, especially on overhung rotors with excessive overhang

Light shaft loading, fluid leakage, bearing wear and gyroscopic effects are all issues with the current design. Further reasons for non-ideal bearing behaviour are potentially due to theory limitations. Major HDJ bearing theory relates to rigid, non-grooved bearings. In this bearing, turbulence may be occurring in the grooves. At high angular velocities, this turbulent water may be dragged onto the bearing 'lands' and upsetting pressure measurements.

Interestingly, further testing (not shown) indicated that the same bearing with water trickling through it is far more stable. With this incomplete lubrication, the bearing possibly acts more like a 'partial journal'. Partial journal bearings are inherently more stable than their 'full journal' equivalents.

Table 1 - PV Values for Each Test Speed

Rotational Speed [RPM]	**PV Value** [MPa – m/min]
200	0.010
400	0.021
600	0.031
800	0.041
1000	0.051
1200	0.062
1400	0.072
1600	0.082
1800	0.092

In **Table 1**, PV values are provided for each test speed. These are calculated from the projected area of the bearing and the 20kg radial load obtained from a moment-balance about the coupling bearing.

7 FURTHER WORK

This testing has given rise to a number of questions regarding the bearing performance. Testing limitations have also reduced the number of conclusions that can be drawn. Ideally, testing would be re-performed with an isolated test rig in which the radial load on the journal can be increased. In addition to this: more pressure probes should be placed around the bottom of the bearing; suction probes should be placed along the top of the bearing; and probes should be placed along the length of the bearing to detect axial pressure variations. Finally, boat trials should be performed to view the effects of water flow on the bearing's operation.

8 CONCLUSION

Pressure and journal location measurements were taken on an 80mm ID rubber hydrodynamic-journal bearing on a Hamilton Jet HJ-364 Jet Assembly. Results indicated that the bearing is not performing correctly and that significant whirling and rubbing is occurring. The lack of observed wear is attributed to the smooth surface of the water bearing sleeve and the very low coefficient of friction of the wet rubber bearing. Boat testing and correspondence with the bearing manufacturer in regards to the bearing design should be performed to complete this research. Furthermore, analysis of other jet sizes is recommended as the issues observed are unlikely to be isolated to the HJ364 model.

9 REFERENCES

Aitken, M. (1993). *Investigation of the Dynamic Characteristics of Water Lubricated Bearings: Hamilton Jet Model 273.* Christchurch, New Zealand: Industrial Research Limited.

Berry, J. E. (2005). Oil Whirl and Whip Instabilities Within Journal Bearings. *Machinery Lubrication*, 72-75.

Budynas-Nisbett. (2006). *Shigley's Mechanical Engineering Design, 8th Edition.* New York City: McGraw-Hill.

Donohue, B. (2001). *Investigation of Shaft Dynamic Displacements CWF Hamilton & Co Limited.* Christchurch, New Zealand: Engineerin Dynamics Consultancy Limited.

Lengoc, L., Donahue, B., Baxter, C., & Aitken, M. (1992). *Investigation on the Dynamic Characteristics of Water Lubricated Bearings.* Christchurch, New Zealand: Industrial Research Limited.

Liu, L., Li, Z., & Ganeriwala, S. (2006). *Interesting Rotor Dynamics Observations on Oil Whirl and Whip.* Virginia: SpectraQuest Inc.